Roadmap to a mutually consistent set of offshore vertical reference frames

D. C. Slobbe

Roadmap to a mutually consistent set of offshore vertical reference frames

Proefschrift

ter verkrijging van de graad van doctor
aan de Technische Universiteit Delft,
op gezag van de Rector Magnificus prof. ir. K.C.A.M. Luyben,
voorzitter van het College voor Promoties,
in het openbaar te verdedigen op vrijdag 6 september 2013 om 10:00 uur

door
Dirk Cornelis SLOBBE,
Master of Science in Geomatics,
geboren te Capelle aan den IJssel.

Dit proefschrift is goedgekeurd door de promotor:
Prof. Dr.-Ing. habil. R. Klees

Samenstelling promotiecommissie:

Rector Magnificus,	voorzitter
Prof. Dr.-Ing. habil. R. Klees,	Technische Universiteit Delft, promotor
Prof. dr. D.T. Sandwell,	Scripps Institution of Oceanography
Prof. dr. M. Ziebart,	University College London
Prof. dr. J. Pietrzak,	Technische Universiteit Delft
Prof. dr. ir. M.J.F. Stive,	Technische Universiteit Delft
Dr. ir. M. Verlaan,	Deltares
Dr. F.J. Simons,	Princeton University
Prof. dr. ir. R.F. Hanssen,	Technische Universiteit Delft, reservelid

ISBN 978-94-6203-389-4

Printed by Wöhrmann Print Service, Zutphen, The Netherlands

Contents

Preface

The book in front of you is the result of more than 5.5 years work to the development and implementation of a procedure that enables to derive a consistent set of offshore vertical reference surfaces. I hope this procedure enables users of the derived vertical reference surfaces to meet the ever-increasing accuracy requirements they face in their daily practice. I also hope that the established and till now fruitful cooperation among the disciplines of geodesy, hydrography, and hydrodynamics will be continued, as I believe that it provides a real synergy.

I am very much indebted to my promotor and daily supervisor Roland Klees. The freedom to extend the scope of my thesis is thanks to the freedom he provided me. Besides this, his involvement, support, criticism, quick response, and the flexibility he provided to direct my work in my own way during the entire project are greatly acknowledged and were essential for the realization of this thesis.

Although formally there were no other supervisors, I consider Martin Verlaan as such, by which I hope to express something of his commitment to this project. His support in understanding hydrodynamic modeling, the setting up and implementation of the many experiments carried out with the Dutch Continental Shelf Model form the basis of the contents of two journal papers/chapters of this thesis, for which I thank him.

Together with Martin Verlaan, I would like to thank Herman Gerritsen. Thanks to him, the cooperation with Deltares was established. Furthermore, I appreciate his critical look at my results and two journal papers.

Also the other colleagues at Deltares are thanked for their involvement and support to this project and, of course, for their hospitality during the period I worked one day a week at the Deltares office.

The Hydrographic Service of the Royal Netherlands Navy was, especially in the person of Leendert Dorst, involved from the beginning of this project. It was not the first time Leendert helped me; during my graduation project at the University of Applied Sciences Utrecht in 2005 he invited me to discuss a number of issues related to Kriging interpolation I could not solve myself. At the end of this research, I want to thank him again for his openness and the care he has taken to disseminate the result

of this research within the international hydrographic community. Moreover, for his support to the realization of the paper/chapter about the computation of LAT and for his critical look at the introduction and summary of my thesis.

For the realization of the "Slepian paper" (Chapter 6) I am, besides Roland Klees, very much indebted to Frederik Simons from the Department of Geosciences of Princeton University. It is fair to say that thanks to his tireless efforts, the paper finally appears in Journal of Geodesy. His open and pleasant way of working, his support during the programming and writing of the paper were crucial and are gratefully acknowledged.

I am also grateful to Wouter Goedhart who, as a student of the University of Applied Sciences Utrecht, conducted an internship and graduation project that aimed to compose a database with unique and high-quality shipboard and terrestrial gravity data. For this, he compared and combined data from different providers and applied a crossover adjustment to all shipboard data in order to eliminate mutual biases. The reconstruction of the sailed tracks from point cloud data, required to determine the crossovers is indeed a monkish work. However, his vast knowledge of programming helped to finish this work and thanks to him we have access to a clean and mutually consistent set of gravity data.

I also acknowledge the support of Pavel Ditmar in the estimation of the signal and noise power spectral densities and Brian Gunter for his out-of-core solver that was needed to estimate the NLGEO2013 quasi-geoid. Despite their busy schedules, both of them were ready to help what I greatly appreciate. Brian Gunter is also acknowledged for his help in English writing.

My brother and colleague Arthur Slobbe and my travel partner Johannes van Wingerden are acknowledged for their careful check of the Dutch summary of this thesis.

Besides the people who actively contributed to one or more papers/chapters of this thesis, I would like to thank those whose contribution is may be less tangible, but not less essential. First of all, my (former) colleagues within the research group of Physical and Space Geodesy for fruitful discussions and sharing of software. Especially, Tobias Wittwer for his support in working with his wonderful radial basis function software. Special thanks also to Riccardo Riva, Marcin Glegola, Hassan Hashemi Farahani, and Junchao Shi with whom I have shared a room during the past years. Furthermore, I would like to mention Remko Scharroo and Marc Naeije for providing me access to the Radar Altimeter Database System and their support in using it.

I also gratefully acknowledge funding from the Interreg IVB North Sea Region Programme, project "Bringing Land and Sea Together" (BLAST), and the Netherlands Geodetic Commission (NCG).

Gravity data were kindly provided by the British Geological Service; the Geological Survey of Northern Ireland; the Nordic Geodetic Commission; Bundesamt für Kar-

tographie und Geodäsie (Germany); Institut für Erdmessung (Germany); the Bureau Gravimétrique International (France); the Banque de données Gravimétriques de la France; and the Bureau de Recherches Géologiques et Minières (France).

Tide gauge data were kindly provided by the Vlaamse Hydrografie, Agentschap voor Maritieme Dienstverlening en Kust, afdeling Kust (Belgium); Danish Coastal Authority; Danish Meteorological Institute; Danish Maritime Safety Administration; Service Hydrographique et Océanographique de la Marine (France); Bundesamt für Seeschifffahrt und Hydrographie (Germany); Marine Institute, Ireland; Rijkswaterstaat (the Netherlands); Norwegian Hydrographic Service; Swedish Meteorological and Hydrological Institute; and U.K. National Tidal and Sea Level Facility (NTSLF) hosted by POL.

P. A. M Berry is acknowledged for providing retracked ERS-1 radar altimeter data and O.B. Andersen for providing the mean sea surface heights, mean dynamic topography, and altimeter-derived gravity anomaly grids to the community and his help in answering some questions.

I would also like to gratefully acknowledge the support of the Proudman Oceanographic Laboratory (POL) for providing the results of the Atlantic — European North West Shelf — Ocean Physics Hindcast to the community and their help in answering some questions.

Finally, I would like to thank my family for their unfailing interest and encouragement. Especially, my wife Janneke I cannot thank enough. Without her understanding, support, and help to convert handwritten text to digital text, I doubt whether this work would have been completed. You forced me from time to time to put all “problems” in their proper perspective, which I really appreciate.

Soli Deo Gloria!

Cornelis Slobbe, August 14, 2013.

Summary

Roadmap to a mutually consistent set of offshore vertical reference frames

Dutch waters lack an accurate and easily accessible 3D description of the lowest astronomical tide (LAT) surface, i.e., a so-called "separation model". This tidal datum, defined as "the lowest tide level that can be predicted to occur under average meteorological conditions and under any combination of astronomical conditions" (International Hydrographic Organization 2011*a*, Technical Resolution 3/1919), is, in those regions where tides have an appreciable effect on the water level, adopted as chart datum (CD) by the International Hydrographic Organization (IHO). Having an accurate separation model of LAT provides numerous benefits to a variety of commercial and non-commercial users, including faster, cheaper, and more accurate hydrographic survey data for nautical charts; more precise navigation, even over areas with submarine hazardous objects; merging of depth data with height data for coastal zone management; and an accurate planning of depth maintenance in port approach areas.

The current practice to obtain a coastal-waters-inclusive continuous (CWIC) separation model of LAT is to express it as the sum of LAT values derived from a global/regional ocean tide model and an altimeter-derived mean sea level (MSL) model, complemented by LAT values derived from water level observations and GNSS ellipsoidal heights at tide gauges. The latter are the sole information source for deriving the separation model of LAT in coastal waters. This is due to the lack of information about the MSL in these waters as a consequence of the degrading accuracy of radar altimeter data in the vicinity of land (e.g., Andersen & Knudsen 2000, Deng et al. 2002). To obtain a continuous surface in coastal waters out of these point data, strong interpolation is required. This interpolation is not trivial as the tidal behavior at a particular tide gauge location, and hence the LAT value, is not necessarily representative for nearby locations. Furthermore, significant gaps may exist between the tide gauge locations. Alternatively, information about the MSL can be derived from GNSS surveys (e.g., Pineau-Guillou & Dorst 2011). These are, however, expensive and therefore this approach is not preferable.

To derive an accurate and continuous separation model of LAT in Dutch waters including the coastal waters, Wadden Sea, and Eastern and Western Scheldt estuaries, avoiding interpolation, we developed an alternative approach. In this approach, the ellipsoidal heights of LAT are computed as the sum of the quasi-geoid heights and the heights of LAT relative to this quasi-geoid. The latter can be derived from modeled water levels of a vertically referenced hydrodynamic model, which comprise the tide and the time-averaged meteorological and steric contributions.

In this study, a new quasi-geoid model is estimated that covers the whole Netherlands Continental Shelf and the Dutch mainland, because the European Gravimetric Geoid 2008 (EGG08) lacks accuracy for two reasons. First, EGG08 does not include data acquired by the Gravity field and steady-state Ocean Circulation Explorer (GOCE) satellite; these data have become publicly available in May 2010. Second, in the estimation of EGG08, satellite radar altimeter data have been corrected for using a global ocean tide model. In this study, we use a shallow water hydrodynamic model which provides apart from tides also the surge and steric contributions to the dynamic topography corrections. The fact that all contributions are obtained from the same model has the additional advantage that any non-linear interaction between the three contributions (e.g., between tide and surge (Prandle & Wolf 1978)) is accounted for.

The fact that we have to use a hydrodynamic model both in deriving the separation between the quasi-geoid and LAT and in estimating the quasi-geoid itself requires a small, but important, change of our approach to derive a separation model of LAT. Instead of a one-way link between the quasi-geoid and the hydrodynamic model, a two-way link exists. This two-way link results in a chicken-and-egg problem. On the one hand, we aim to use a hydrodynamic model to derive a proper quasi-geoid, while on the other hand this quasi-geoid needs to be the model's reference surface. The development of a methodology that solves this problem is our main research objective.

In this thesis, we first present the overall procedure by means of a flowchart. Three steps can be distinguished: (i) the data preprocessing; (ii) the estimation of the quasi-geoid and the realization of a hydrodynamic model that provides water levels relative to this quasi-geoid; and (iii) the realization of the LAT and mean dynamic topography (MDT) surfaces once the final quasi-geoid and the vertically referenced hydrodynamic model are available. The latter surface can be used to produce the ellipsoidal heights of the MSL (as the sum of quasi-geoid and MDT), which is often used as a vertical reference surface in the offshore industry. The model used in this study is the Dutch Continental Shelf Model version 5 (DCSM), which is a 2D storm surge model. In the remainder of the thesis, we elaborate on four key elements of this procedure.

Vertical referencing of a shallow water model

First, we treat the question how a shallow water hydrodynamic model can be vertically referenced to a given (quasi-)geoid and to which extent such a model benefits from an improved (quasi-)geoid. In addition, we assessed the accuracy of the obtained modeled (mean) water levels.

A prerequisite to reference a hydrodynamic model vertically is that the model includes all forcing terms needed to represent the instantaneous water levels. The main missing forcing term in DCSM is the baroclinic forcing. Adding this term is realized by adding the depth-averaged horizontal baroclinic pressure gradients to the model equations. These are derived from 4D salinity and temperature fields of the Atlantic — European North West Shelf — Ocean Physics Hindcast provided by the Proudman Oceanographic Laboratory (POL), hereafter referred to as POL's hindcast. The vertical datum of the extended DCSM model is fixed to that of EGG08. This is done by an adjustment of the hydrodynamic model parameters that depend on the choice of the reference surface (e.g., bathymetry) and by referring the water levels along the open sea boundaries to this quasi-geoid.

Using different numerical experiments we investigated the effects on the water levels of several approximations we made during the implementation. From the experiments, we conclude that the (quasi-)geoid is only weakly constrained by prescribed water levels along the open sea boundaries. Hence, if another (quasi-)geoid is chosen as the reference surface, the water levels along the open sea boundaries change accordingly, but this change will not propagate much inside the model domain. This suggests that from a model quality perspective the hydrodynamic model hardly profits from an improved (quasi-)geoid.

The ability of the model to reproduce both the MDT and instantaneous water levels is assessed by a comparison with the MDT derived from POL's hindcast, as well as with instantaneous water levels acquired by various radar altimeter satellites. From this comparison, we conclude that our model-derived MDT is in good agreement with the MDT derived from POL's hindcast: the standard deviation of the differences is below 2 cm. Larger differences in MDT are observed when comparing the model output with the MDT derived from radar altimeter data. They are attributed to either errors in the EGG08 quasi-geoid or errors in the used salinity and temperature fields. The root mean square (rms) differences between observed and modeled instantaneous water levels over the whole model domain vary from 9 cm for data acquired by the TOPEX satellite to 11 cm for data acquired by the GFO-1 satellite. These rms differences improve to 8–10 cm on the North Sea, for data acquired by the TOPEX and ERS-2 satellites, respectively. These numbers are a factor two to three larger than the expected accuracy of water levels derived from radar altimeter data (which is $\sim$4 cm (Chelton et al. 2001, Sandwell & Smith 2009)). About 25% of these differ-

ences can be explained by a bias between the modeled water levels and the observed water levels acquired during a single satellite pass. These biases are, among others, attributed to errors in the applied correction for the net steric expansion/contraction of the global oceans. This effect is not captured by DCSM that makes use of the Boussinesq approximation.

Added value of a shallow water hydrodynamic model in quasi-geoid computations

Second, we focus on the actual estimation of the quasi-geoid. In particular, we evaluated the added value of using a shallow-water hydrodynamic model for the reduction of radar altimeter sea surface heights (SSHs) to quasi-geoid heights in the estimation of a quasi-geoid for the North Sea. Here, we separately evaluated the contribution of the tide to the dynamic topography (DT) corrections and the contributions induced by surge and steric water level variations. As a reference, we used tidal corrections derived from the global ocean tide model GOT4.7, surge corrections derived from the MOG2D model, and corrections for the time-averaged steric contribution computed as differences between the DTU10 mean sea surface model (DTU10-MSS) and the EGG08 quasi-geoid.

The actual analysis consists of two parts. First, we compared for nine TOPEX passes the mean signal and noise power spectral densities (PSDs) of the residual along-track deflections of the vertical (DoV) obtained after applying different sets of DT corrections to the SSHs. From this analysis, we conclude that both the steric and surge parts mainly contribute to improvements in the signal-to-noise-ratios at longer wavelengths (a few hundred km) and that the improvements increase towards the southern North Sea. For shorter wavelengths, no significant differences are observed between the PSDs obtained after applying DT corrections *with* the surge and steric contributions and those *without* them (irrespective from which source they are derived). For some passes, the PSDs even suggest that including the surge and steric contributions increases the noise level. This especially applies to the surge corrections obtained from the MOG2D model. Also the improved representation of the astronomical tide by DCSM shows up at longer wavelengths, and also here the added value of using DCSM instead of GOT4.7 is increasing towards the southern North Sea. In this region, improvements are visible over almost the entire spectrum. The improvements associated with an improved representation of the tide by DCSM are dominant compared to those associated with an improved representation of the surge and steric contributions.

In the second part of the analysis, the added value is quantified in terms of quasi-geoid heights. Using the different sets of DT corrections, different quasi-geoids are estimated. Based on their mutual differences we conclude that, if shipboard gravity

data are included in the estimation, the added value of using a shallow water model for the reduction of SSHs to quasi-geoid heights is negligible. This is explained by the fact that radar altimeter data hardly contribute at all to the estimated quasi-geoid if shipboard gravity data are included. Except at some isolated spots along the coasts of Belgium, Denmark, France, Great Britain, and the Shetland Islands, and a feature along the Norwegian coast aligned with the Norwegian Trench, the differences are below ± 1 cm. Without shipboard gravity data the differences are much larger. By a comparison of the solutions obtained with and without shipboard gravity data, but after applying the same set of DT corrections, we conclude that the systematic differences between the quasi-geoids have been reduced if we use a shallow water model, especially along the coasts of the Netherlands and Great Britain and in the English Channel.

To compute the NLGEO2013 quasi-geoid, the along-track DoV obtained after applying the DT corrections of the extended, vertically referenced DCSM model are combined with terrestrial, shipborne, and airborne gravity data, and EGG08-derived DoV in north and east directions. The quality of NLGEO2013 is assessed by comparing it with both the EGG08 quasi-geoid and the gravimetric quasi-geoid solution underlying NLGEO2004 (NLGEO2004-grav). We conclude that NLGEO2013 best fits to EGG08: the rms difference over the Netherlands is 1.42 cm. The obtained differences have many causes, among which are the use/preprocessing of different gravity data sets, differences in the applied computational strategy, and differences in the weights assigned to the various observation groups. By comparing the NLGEO2013, EGG08, and NLGEO2004-grav quasi-geoids with geometric height anomalies at 81 GPS/leveling points over the Netherlands, it was shown that NLGEO2013 has the best performance. Only for this model, the standard deviation is below 1 cm, which is within the uncertainty of the 81 geometric height anomalies.

Deriving LAT relative to the quasi-geoid

Next, we treat the question how, and to which level of accuracy, we can derive the separation between the quasi-geoid and LAT from a shallow water hydrodynamic model. Deriving LAT from a shallow water hydrodynamic model relative to the quasi-geoid is realized by an explicit modeling of the average meteorological and steric conditions. Numerical experiments show that significant differences between the traditional (deriving LAT relative to MSL) and the pursued approach exist if average monthly variations in MSL are accounted for. The obtained LAT surface is validated using LAT values at 92 onshore and 10 offshore tide gauges. For the 92 onshore tide gauges, we found a mean of 0.5 cm and a standard deviation of 21.5 cm. The obtained differences between observation- and model-derived LAT reveal a mixture of errors in both model and control data. We found that systematic errors in the representation of the tidal amplitude by DCSM dominate. We have also investigated

whether the sense of safety evoked by using LAT as CD is justified. Indeed, since LAT is computed as a once per 18.6 years event under average meteorological conditions, the use of LAT as CD suggests that the instantaneous water depth is rarely smaller than the charted depth. We showed that the probability that the water level drops below LAT is high, with a maximum frequency of once per week in the eastern North Sea. In that region, the magnitude of LAT relative to the quasi-geoid is low due to the existence of two complete amphidromic systems and one degenerating one. Indeed, in this region the contribution of the surge dominates the water level variations and hence it is reasonable to expect a high probability that the instantaneous water level drops below LAT. Therefore, we propose to reconsider the deterministic concept of LAT by a probabilistic CD concept, and we quantified the differences between them.

Solving spectral inconsistencies using a Slepian basis

The last question treated in this thesis is whether a spherical Slepian basis representation enables to obtain spectral consistency between a high- and low-resolution data set. Spectral consistency between the quasi-geoid and the model-derived separation between this quasi-geoid and LAT is required if we compute the ellipsoidal heights of LAT as the sum of both. Following recent studies, this question is treated in the context of MDT estimation using the so-called "geodetic approach", i.e., by computing the difference between a MSL model obtained from satellite altimetry and a gravimetric geoid. Doing so, requires that both data sets are spectrally consistent. In practice, it is quite common that the resolution of the geoid data is less than the resolution of the MSL data. Hence, the latter need to be low-pass filtered before the MDT is computed. For this purpose, conventional low-pass filters are inadequate as they fail in coastal regions where they run into the undefined MSL signal on the continents.

To study whether the use of a bandlimited, spatially concentrated Slepian basis enables to obtain a low-resolution approximation of the MSL signal, we computed Slepian functions for the oceans and parts of the oceans and compared the performance of calculating the MDT via this approach with other methods. In particular, we compared the approach with the iterative spherical harmonic approach in combination with Gaussian low-pass filtering, and various modifications.

Based on the numerical experiments, we conclude that none of these methods provide a low-resolution MSL approximation at the sub-decimeter level. In particular, we showed that Slepian functions are not appropriate basis functions for this problem, and a Slepian representation of the low-resolution MSL signal suffers from broadband leakage. We also showed that a meaningful definition of a low-resolution MSL over incomplete spherical domains involves orthogonal basis functions with addi-

tional properties that Slepian functions do not possess. A low-resolution MSL signal, spectrally consistent with a given geoid model, is obtained by a suitable truncation of the expansions of the MSL signal in terms of these orthogonal basis functions. We compute one of these sets of orthogonal basis functions using the Gram-Schmidt orthogonalization for spherical harmonics. For the oceans, we could construct an orthogonal basis only for resolutions equivalent to a spherical harmonic degree 36. The computation of a basis with a higher resolution failed due to inherent instabilities. Regularization reduced the instabilities but destroyed the orthogonality and, therefore, provided unrealistic low-resolution MSL approximations. More research is needed to solve the instability problem, perhaps by finding a different orthogonal basis that avoids it altogether.

Principal innovations

In this thesis, the principal innovations developed and tested by the author are:

- An approach to realize a coastal-waters-inclusive continuous (CWIC) separation model of LAT where interpolation is avoided (Chapters 1, 2, and 5);
- An approach to include the depth-averaged baroclinic forcing into a 2D shallow water hydrodynamic model (Section 3.3);
- A method to vertically reference a 2D shallow water hydrodynamic model to a particular (quasi-)geoid (Section 3.4);
- The reduction of altimeter-derived SSHs to geometric quasi-geoid heights using a 2D shallow water hydrodynamic model that includes astronomical tidal forcing, atmospheric wind and pressure forcing, and baroclinic forcing, together with a detailed analysis of signal and noise in dynamic topography corrections for the North Sea and an assessment of the added value of using such a model in quasi-geoid computations (Sections 4.4 and 4.5);
- A pragmatic approach to select the bandwidth and density of the radial basis functions (Chapter 4);
- Harmonize various gravity data sets by including bias parameters into the functional model (Chapter 4);
- Application of modeling the average surge and steric contributions in deriving LAT relative to the quasi-geoid (Sections 5.3.2 and 5.3.3);
- Probabilistic design of chart datum (Section 5.4);
- An attempt to obtain spectral consistency between a high- and low-resolution data set using a Slepian approach (Chapter 6).

Samenvatting

Roadmap naar een onderling consistente set van offshore verticale referentievlakken

Voor het Nederlandse deel van de Noordzee ontbreekt een nauwkeurige en toegankelijke 3D-beschrijving van het laagste astronomische getij (LAT) verticale referentievlak. Dit referentievlak, gedefinieerd als het laagste getijdenniveau dat voorspeld kan worden onder gemiddelde meteorologische omstandigheden en onder elke combinatie van astronomische omstandigheden (International Hydrographic Organization 2011*a*, Technische Resolutie 3/1919), is in de gebieden waar het getij een aanzienlijk effect op de waterbeweging heeft door de Internationale Hydrografische Organisatie (IHO) aangenomen als het reductievlak voor dieptes in zeekaarten (chart datum (CD)). De beschikbaarheid van een nauwkeurige 3D-beschrijving van het LAT-referentievlak levert een groot aantal voordelen op voor uiteenlopende commerciële en niet-commerciële organisaties, waaronder een snellere, goedkopere en nauwkeurigere inwinning van bathymetrische data ten behoeve van zeekaarten; een preciezere navigatie, vooral in gebieden met gevaarlijke ondiepten; een vereenvoudigde combinatie van diepte en hoogte data ten behoeve van kustzonemanagement; en het maakt een nauwkeurigere planning mogelijk van de baggerwerkzaamheden die worden uitgevoerd om de aanvaarroutes naar de havens op diepte te houden.

De gangbare praktijk om een continue 3D-beschrijving van het LAT-referentievlak te verkrijgen dat de kustwateren omvat (hier aangeduid als een coastal-waters-inclusive continuous (CWIC) model) is om het uit te drukken als de som van LAT-waarden afgeleid met behulp van een mondiaal of regionaal getijmodel en een van radar altimetrie afgeleid model van het gemiddeld zeeniveau (MSL), aangevuld met LAT-waarden afgeleid van waargenomen waterstanden en GNSS-hoogtes op getijdestations. Laatstgenoemde dataset is de enige bron van informatie om een continue 3D-beschrijving van het LAT-referentievlak af te leiden in de kustwateren. Dit als gevolg van een gebrek aan informatie over de ligging van het MSL-referentievlak, wat op zijn beurt weer het gevolg is van de lagere nauwkeurigheid van uit radar altimetrie afgeleide waarnemingen van de hoogte van het zeeniveau in de buurt van land (bv.

Andersen & Knudsen 2000, Deng et al. 2002). Om uit deze puntwaarnemingen een continue beschrijving van het LAT-referentievlak te verkrijgen, moet er sterk geïnterpoleerd worden. Deze interpolatie is niet triviaal, omdat de getijbeweging op een bepaalde meetlocatie, en daarmee ook de LAT-waarde, niet noodzakelijk representatief is voor de omgeving van deze locatie. Daar komt bij dat er behoorlijke afstanden kunnen zijn tussen de locaties waar getijmeters zijn geïnstalleerd. Als alternatief kan de ligging van het MSL-referentievlak bepaald worden uit GNSS-hoogtes van het zeeniveau die met een schip zijn opgenomen (bv. Pineau-Guillou & Dorst 2011). Vanwege de hoge kosten heeft deze aanpak echter niet de voorkeur.

Om een nauwkeurige en continue 3D-beschrijving van het LAT-referentievlak af te leiden voor de Nederlandse zeewateren (waaronder de kustwateren, Waddenzee en de Ooster- en Westerschelde), waarbij interpolatie wordt vermeden, hebben wij een alternatieve aanpak ontwikkeld. In deze aanpak worden de ellipsoïdische hoogtes van het LAT-referentievlak berekend als de som van de quasi-geoïdehoogtes en de hoogtes van LAT ten opzichte van deze quasi-geoïde. Laatstgenoemde hoogtes kunnen worden afgeleid van waterstanden die de bijdragen van het getij en de tijdsgemiddelde meteorologische en sterische componenten bevatten, en die afkomstig zijn van een ondiepwatermodel waarvan de ligging van het verticale referentievlak is vastgelegd.

In deze studie is een nieuw quasi-geoïdemodel geschat dat het gehele Nederlandse deel van de Noordzee en het vaste land omvat. Reden hiervoor is dat het beschikbare state-of-the-art quasi-geoïdemodel, de European Gravimetric Geoid 2008 (EGG08), de minimaal vereiste nauwkeurigheid mist. Hiervoor zijn twee redenen te noemen. Ten eerste is in de berekening van EGG08 geen gebruik gemaakt van data afkomstig van de Gravity field and steady-state Ocean Circulation Explorer (GOCE) satelliet; deze data waren pas beschikbaar in mei 2010. Ten tweede zijn in de schatting van EGG08 de radar altimeter waarnemingen gecorrigeerd voor de dynamische zeetopografie met behulp van een mondiaal getijmodel. In deze studie gebruiken we een ondiepwatermodel waarin naast het getij ook de bijdragen van de windopzet en sterische waterstandsvariaties worden meegenomen. Het feit dat al deze drie bijdragen worden bepaald met hetzelfde model heeft als bijkomend voordeel dat elke niet-lineaire interactie tussen de drie bijdragen (bv. tussen getij en windopzet (Prandle & Wolf 1978)) wordt meegenomen.

Het gebruik van een ondiepwatermodel voor zowel het afleiden van de hoogte van het LAT-referentievlak ten opzichte van de quasi-geoïde als voor de schatting van de quasi-geoïde, vereist een kleine, maar wel belangrijke verandering in de voorgestelde aanpak om een continue 3D-beschrijving van het LAT-referentievlak te verkrijgen. Dit resulteert in een “kip-en-ei” probleem: enerzijds willen we het ondiepwatermodel gebruiken om een goede quasi-geoïde te berekenen, terwijl anderzijds deze quasi-geoïde het verticale referentievlak van het model moet zijn. De ontwikkeling van een methode die dit probleem oplost is het belangrijkste doel van dit onderzoek.

In dit proefschrift wordt eerst de algehele procedure gepresenteerd. Drie stappen worden onderscheiden: (i) de voorbewerking van alle benodigde data; (ii) de schatting van de quasi-geoïde en de realisatie van een ondiepwatermodel dat waterstanden levert ten opzichte van deze quasi-geoïde; en (iii) de realisatie van het LAT-referentievlak en de gemiddelde dynamische zeetopografie (mean dynamic topography (MDT)) zodra de uiteindelijke quasi-geoïde en het model waarvan de ligging van het verticale referentievlak is vastgelegd beschikbaar zijn. Dit laatste referentievlak kan worden gebruikt om de ellipsoïdische hoogtes van het MSL-referentievlak uit te rekenen (als de som van de quasi-geoïde en de MDT), wat gebruikt wordt door de offshore industrie als verticaal referentievlak. Het model dat we in deze studie gebruiken is het Dutch Continental Shelf Model versie 5 (DCSM). Dit is een 2D-model voor windopzet en getijberekeningen. In het resterende deel van dit proefschrift worden vier sleutelelementen uit de procedure uitgewerkt.

Het vastleggen van het verticale referentievlak van een ondiepwatermodel

In de eerste plaats gaan we in op de vraag hoe van een ondiepwatermodel het verticale referentievlak kan worden gerelateerd aan een gegeven (quasi-)geoïde, en in welke mate een dergelijk model voordeel heeft van een nauwkeuriger (quasi-)geoïdemodel. Verder bepalen we de nauwkeurigheid van de gemodelleerde waterstanden.

Een eerste vereiste aan een ondiepwatermodel waarvan we het verticale referentievlak vast willen leggen, is dat het model alle bijdragen aan de momentane waterstanden modelleert. De belangrijkste ontbrekende component in het DCSM model is de sterische. De toevoeging hiervan is gerealiseerd door het opnemen van de dieptegemiddelde horizontale barokliene drukgradiënten in de modelvergelijkingen. Deze zijn afgeleid van 4D saliniteit- en temperatuurvelden van de Atlantic — European North West Shelf — Ocean Physics Hindcast uitgevoerd door het Proudman Oceanographic Laboratory (POL), hierna duiden we deze dataset aan als POL's hindcast. Het verticale referentievlak is gerelateerd aan de EGG08 quasi-geoïde. Dit is gerealiseerd door aanpassing van die modelparameters die afhangen van de keuze van het referentievlak (bv. de bathymetrie) en door de waterstanden die als open randvoorwaarden worden voorgeschreven te refereren aan deze quasi-geoïde.

Middels verschillende numerieke experimenten zijn de effecten onderzocht van verscheidene aannames die we hebben gedaan tijdens de implementatie. Uit deze experimenten concluderen we dat het referentievlak niet goed wordt vastgelegd door waterstanden langs de open randen van het model voor te schrijven. Als een ander (quasi-)geoïdemodel wordt gekozen als referentievlak zullen de waterstanden langs de open randen daarom meeveranderen, maar deze verandering zal zich niet ver in het modeldomein voortplanten. Dit suggereert dat, vanuit het oogpunt van modelkwaliteit, het ondiepwatermodel nauwelijks profiteert van een verbeterde (quasi-)geoïde.

De mate waarin het model in staat is om de MDT en de momentane waterstanden te reproduceren is bepaald door een vergelijking met de MDT afgeleid uit POL's hindcast en ook met momentane waterstanden afkomstig van meerdere radar altimeter satellieten. Op basis van de eerste vergelijking concluderen wij dat de uit het model afgeleide MDT goed overeenkomt met de MDT afgeleid uit POL's hindcast: de standaardafwijking is kleiner dan 2 cm. Wanneer we de model-output vergelijken met de MDT afgeleid uit radar altimeter data nemen we grotere verschillen waar. Deze schrijven we toe aan fouten in de EGG08 quasi-geoïde of aan fouten in de gebruikte saliniteit- en temperatuurvelden. Het kwadratisch gemiddelde van de verschillen (rms) tussen de waargenomen en gemodelleerde momentane waterstanden over het gehele modeldomein variëren van 9 cm voor data afkomstig van de TOPEX-satelliet tot 11 cm voor data afkomstig van de GFO-1 satelliet. Over de Noordzee verbeteren deze rms verschillen tot 8–10 cm voor data afkomstig van respectievelijk de TOPEX- en ERS-2-satellieten. Deze getallen zijn een factor twee tot drie groter dan de nauwkeurigheid die we verwachten van waterstanden afgeleid van radar altimeter data (deze is $\sim$4 cm (Chelton et al. 2001, Sandwell & Smith 2009)). Ongeveer 25% van deze verschillen kan worden verklaard door een gemiddelde afwijking tussen de gemodelleerde waterstanden en de waterstanden die worden waargenomen gedurende een enkele overkomst van de satelliet. Deze gemiddelde afwijkingen schrijven we onder andere toe aan fouten in de toegepaste correctie voor de netto sterische uitzetting/krimp van alle oceanen wereldwijd. Dit effect wordt niet meegenomen in DCSM, omdat dit model gebruik maakt van de Boussinesq-benadering.

De toegevoegde waarde van een ondiepwatermodel voor ondiepe wateren in quasi-geoïde berekeningen

Ten tweede richten we ons op de eigenlijke schatting van de quasi-geoïde. In het bijzonder hebben we geëvalueerd wat de toegevoegde waarde is van het gebruik van een ondiepwatermodel voor de reductie van radar altimeter zeespiegelhoogtes (sea surface heights (SSHs)) naar quasi-geoïdehoogtes in de schatting van een quasi-geoïde voor de Noordzee. Hier hebben we apart gekeken naar de bijdrage van het getij aan de correcties voor de dynamische topografie (DT) en de bijdragen als gevolg van windopzet en sterische waterstandsvariatie. Als referentie hebben we gebruik gemaakt van getijdecorrecties afkomstig van het mondiaal getijmodel GOT4.7, windopzet correcties afkomstig van het MOG2D model en correcties voor de tijdsgemiddelde sterische bijdrage berekend als verschillen tussen het DTU10 gemiddeld zeeniveaumodel (DTU10-MSS) en de EGG08 quasi-geoïde.

De eigenlijke analyse bestaat uit twee delen. In het eerste deel hebben we voor negen TOPEX-passes de gemiddelde spectrale dichtheden (power spectral densities (PSDs)) van het signaal en de ruis vergeleken van de residuele, langs de satellietbaan berekende schietloodafwijkingen verkregen na toepassing van verschillende

DT-correcties op de SSHs. Uit deze analyse concluderen we dat het toevoegen van zowel de sterische als windopzet-componenten vooral bijdraagt aan verbeteringen van de signaal/ruis verhouding in de langere golflengtes (een paar honderd km) en dat de verbeteringen naar het zuiden van de Noordzee toenemen. Voor kortere golflengtes zijn geen significante verschillen waargenomen tussen de PSDs verkregen na toepassing van DT-correcties *inclusief* de windopzet en sterische bijdragen, en de PSDs *exclusief* deze bijdragen. Voor enkele passes suggereren de PSDs zelfs dat het opnemen van de windopzet en sterische bijdragen het ruisniveau verhoogt. Dit geldt in het bijzonder voor de windopzet-correcties die zijn verkregen uit het MOG2D model. De betere representatie van het astronomisch getij door DCSM is ook zichtbaar in de langere golflengtes en ook hier neemt de toegevoegde waarde van het gebruik van DCSM in plaats van GOT4.7 toe naar het zuiden van de Noordzee. In de zuidelijke Noordzee zien we verbeteringen over bijna het hele spectrum. De verbeteringen die zijn te associëren met een betere representatie van het getij door DCSM zijn dominant vergeleken met de verbeteringen van de windopzet en sterische bijdragen.

In het tweede deel van de analyse is de toegevoegde waarde gekwantificeerd in termen van quasi-geoïdehoogtes. Gebruikmakend van de diverse sets van DT-correcties zijn verschillende quasi-geoïdemodellen geschat. Op basis van hun onderlinge verschillen concluderen we dat, als de zwaartekrachtmetingen op zee worden meegenomen in het schattingsproces, de toegevoegde waarde van het gebruik van een ondiepwatermodel verwaarloosbaar is. De reden hiervan is dat in dit geval de radar altimeter data zelf nauwelijks bijdragen aan de geschatte quasi-geoïde. Behalve op geïsoleerde locaties langs de kusten van België, Denemarken, Frankrijk, Groot Brittannië en de Shetland eilanden, en voor een lijn langs de Noorse kust parallel aan de Noorse Geul, zijn de verschillen kleiner dan ± 1 cm. Tussen de quasi-geoïdes geschat zonder zwaartekrachtmetingen op zee zijn de verschillen veel groter. Op basis van een vergelijking van de oplossingen verkregen met en zonder zwaartekrachtmetingen op zee, maar na toepassing van dezelfde set van DT-correcties, concluderen wij dat de systematische verschillen tussen de quasi-geoïdes zijn afgenomen als we een ondiepwatermodel gebruiken, met name langs de kusten van Nederland en Groot Brittannië, en in het Kanaal.

Om de NLGEO2013 quasi-geoïde te berekenen, zijn de langs de satellietbaan berekende schietloodafwijkingen verkregen na toepassing van de DT-correcties uit het uitgebreide DCSM model gecombineerd met zwaartekrachtmetingen op land en zee, vliegtuiggravimetriegegevens en van EGG08 afgeleide schietloodafwijkingen in de noord-zuid en oost-west richtingen. De kwaliteit van NLGEO2013 is beoordeeld door een vergelijking met zowel de EGG08 quasi-geoïde als met de gravimetrische quasi-geoïde die de basis vormt van NLGEO2004 (NLGEO2004-grav). We concluderen dat NLGEO2013 het beste past bij EGG08: het rms verschil over Nederland is 1.42 cm. De verkregen verschillen hebben vele oorzaken, waaronder het gebruik/de voorbewerking van verschillende zwaartekrachtmetingen, verschillen in de toegepas-

te berekeningsstrategie, en verschillen in de gewichten die zijn toegekend aan de diverse waarnemingsgroepen. Door het vergelijken van NLGEO2013, EGG08 en NLGEO2004-grav met geometrische hoogte-anomalieën op 81 GPS/waterpaspunten in Nederland is aangetoond dat NLGEO2013 de beste oplossing is. Alleen voor dit model is de standaarddeviatie lager dan 1 cm. Dit valt binnen de onzekerheid van de 81 geometrische hoogte-anomalieën.

Het bepalen van LAT ten opzichte van de quasi-geoïde

Ten derde behandelen we de vraag hoe en met welke nauwkeurigheid we de hoogtes van LAT ten opzichte van de quasi-geoïde kunnen bepalen met behulp van een ondiepwatermodel. Het afleiden van deze hoogtes is gerealiseerd met behulp van een expliciete modellering van de gemiddelde meteorologische en sterische omstandigheden. Numerieke experimenten tonen significante verschillen aan tussen de traditionele (het afleiden van de hoogtes van LAT ten opzichte van MSL) en voorgestelde aanpak als we de gemiddelde maandelijkse variaties in MSL meenemen. Het uit het model afgeleide LAT-referentievlak is gevalideerd met behulp van 92 onshore en 10 offshore getijreeksen. Voor de 92 onshore getijmeters komen we uit op een gemiddelde van 0.5 cm en een standaard afwijking van 21.5 cm. De verkregen verschillen tussen de uit waarnemingen en uit het model afgeleide LAT-waarden laten een mix van fouten zien in beiden. Het is gebleken dat systematische fouten in de modelrepresentatie van de getij-amplitude domineren.

Daarnaast hebben we onderzocht of het gevoel van veiligheid dat wordt opgeroepen door LAT als CD te gebruiken gerechtvaardigd is. Omdat LAT berekend is als een gebeurtenis die eens per 18.6 jaar optreedt onder gemiddelde meteorologische omstandigheden, suggereert het gebruik van LAT als CD dat de momentane diepte zelden kleiner is dan de gekarteerde waterdiepte. Wij laten zien dat de kans toch groot is dat de waterstand lager is dan LAT, met een maximale frequentie van eens per week in de oostelijke Noordzee. In dit deel van de Noordzee is het verschil tussen LAT en de quasi-geoïde klein als gevolg van drie amfidromische punten. In dit deel van de Noordzee domineert de windopzet de waterstandsvariaties en daarom is het aannemelijk dat de kans groot is dat de momentane waterstand onder LAT komt. Omdat de kans zo groot is, stellen wij voor het deterministische concept van LAT te vervangen door een probabilistisch concept, en hebben we de verschillen tussen de realisaties van deze concepten gekwantificeerd.

Het wegwerken van spectrale inconsistenties met behulp van een Slepian basisrepresentatie

De laatste onderzoeksvraag die we in dit proefschrift behandelen is de vraag of een sferische Slepian basisrepresentatie ons in staat stelt spectrale consistentie te verkrijgen tussen data met hoge en lage resolutie. Spectrale consistentie tussen de quasi-geoïde en de uit het model afgeleide hoogtes van LAT ten opzichte van deze quasi-geoïde is vereist als we de ellipsoïdische hoogtes van LAT uitrekenen als de som van beiden. In navolging van recente studies behandelen we deze vraag in de context van MDT schatting met behulp van de zogenoemde geodetische aanpak, namelijk door het berekenen van het verschil tussen een MSL-model verkregen uit radar altimeter data en een gravimetrische geoïde. Het op deze manier berekenen van de MDT vereist spectrale consistentie tussen beide datasets. In de praktijk is gewoonlijk de resolutie van de geoïde lager dan de resolutie van het MSL-model. Daarom zal de laatste eerst gefilterd moeten worden met een low-pass filter voordat de MDT kan worden berekend. Hiervoor zijn conventionele filters niet toereikend: in de kustgebieden is het probleem dat MSL niet is gedefinieerd op de continenten.

Om na te gaan of het gebruik van een bandgelimiteerde, in het ruimtelijke domein geconcentreerde Slepian basis in staat is een lage resolutie benadering van het MSL-signaal te verkrijgen, hebben we Slepian functies voor de oceanen en delen van de oceanen berekend, en hebben we de prestatie van de berekening van de MDT via deze methode vergeleken met andere methoden. In het bijzonder met de "iteratieve sferisch harmonische aanpak" in combinatie met toepassing van een Gaussisch low-pass filter en verschillende varianten op deze aanpak.

Op basis van numerieke experimenten concluderen wij dat geen van deze methodes een benadering levert van het lage resolutie MSL-signaal op sub-decimeterniveau. In het bijzonder hebben we laten zien dat Slepian functies geen geschikte basisfuncties zijn voor dit probleem en dat een Slepian representatie van het lage resolutie MSL-signaal onderhevig is aan "broadband leakage". Verder hebben we laten zien dat een zinvolle definitie van het lage resolutie MSL-signaal over een deel van de bol moet worden uitgedrukt in orthogonale basisfuncties met extra eigenschappen die de Slepian functies niet hebben. Een laag resolutie MSL-signaal, spectraal consistent met een gegeven geoïdemodel, kan worden verkregen door een geschikte afbreking van de uitdrukking van het MSL-signaal in termen van deze orthogonale basisfuncties. Een van deze sets van orthogonale basisfuncties hebben wij berekend door gebruik te maken van de Gram-Schmidt orthogonalisatie van sferisch harmonische functies. Voor de oceanen waren we slechts in staat een orthogonale basis te construeren met een resolutie die equivalent is aan een sferisch harmonische graad 36. De berekening van een basis met een hogere resolutie lukt niet als gevolg van inherente instabiliteit. Regularisatie reduceert de instabiliteit, maar vernietigt de orthogonaliteit en levert daarom onrealistische benaderingen van het lage resolutie MSL-signaal. Meer on-

derzoek is nodig om het instabiliteitsprobleem op te lossen. Mogelijk is het probleem te omzeilen door de keuze van een andere orthogonale basis.

Overzicht van de belangrijkste innovaties

De belangrijkste, door de auteur van dit proefschrift, ontwikkelde en geteste innovaties zijn:

- Een methode voor de realisatie van een continue 3D-beschrijving van het LAT-referentievlak dat de kustwateren omvat, waarbij interpolatie wordt vermeden (Hoofdstukken 1, 2 en 5);
- Een methode voor het opnemen van de diepte-gemiddelde barokliene forcering in een 2D-ondiepwatermodel (Sectie 3.3);
- Een methode voor het relateren van het verticale referentievlak van een 2D-ondiepwatermodel aan een gegeven (quasi-)geoïde (Sectie 3.4);
- Het reduceren van uit radar altimetrie afgeleide SSHs naar geometrische quasi-geoïdehoogtes met behulp van een 2D-ondiepwatermodel waarmee het getij en de bijdragen als gevolg van windopzet en sterische waterstandsvariaties zijn gemodelleerd. Dit omvat een gedetailleerde analyse van het signaal en de ruis in DT-correcties voor de Noordzee en een beoordeling van de toegevoegde waarde van het gebruik van een dergelijk model in quasi-geoïde berekeningen (Secties 4.4 en 4.5);
- Een pragmatische aanpak voor de selectie van de bandbreedte en de dichtheid van de radiale basisfuncties (Hoofdstuk 4);
- Het harmoniseren van verschillende zwaartekrachtdatasets door het opnemen van bias parameters in het functionele model (Hoofdstuk 4);
- Toepassing van het modelleren van de gemiddelde windopzet en sterische bijdragen in het afleiden van LAT ten opzichte van de quasi-geoïde (Secties 5.3.2 en 5.3.3);
- Probabilistisch ontwerp voor een reductievlak voor dieptes in zeekaarten (Sectie 5.4);
- Een poging om spectrale consistentie te krijgen tussen data met hoge en lage resolutie met behulp van een Slepian basisrepresentatie (Hoofdstuk 6).

Chapter 1

Introduction

1.1 Background

Offshore vertical reference surfaces are part of the geometric infrastructure of all coastal countries. In general, they are tidal surfaces, i.e., surfaces defined by a certain phase of the tide (Gill & Schultz 2001). The reason why this type of vertical datum (VD) is used rather than the gravity-based VDs commonly used on land, follows, on the one hand, from user requirements. For example, safe navigation in shallow tidal waters requires accurate knowledge of the bathymetry and submerged hazards at a low-water phase of the tidal cycle, and passage underneath bridges requires knowledge of the clearance at a high-water phase of the tide. On the other hand, their use emerged from the possibilities available in the past to realize a VD and to reduce observed water depths to the adopted VD. If a tidal datum is used as the adopted VD, both can be achieved using observed water levels only.

As shown by the examples above, different applications require depths/heights relative to different tidal datums. For the hydrographic offices responsible for the acquisition, storage, and distribution of bathymetric data, this requires the realization of accurate transformations from the datum the stored depths/heights refer to, i.e., the chart datum (CD), to the ones requested by the users. However, nowadays one needs not only to realize transformations between different tidal datums. Due to the ever-increasing interest in the coastal zones as areas of particular ecological, social, and economic value, there is a growing group of users who need to merge bathymetric and topographic data. Such a merge requires transformations between tidal and gravity-based VDs. Moreover, the possibilities offered by the ever-increasing accuracy of 3D positioning with GNSS systems, such as GPS, Galileo, GLONASS, and/or COMPASS (about which more is to follow below), and the advent of light

detection and ranging (LiDAR) technology, has brought the need for transformations between ellipsoidal and tidal VDs.

These changing needs have put into question relative to which type of VD offshore depth/height data should be stored. As noticed by the FIG Commission 4 Working Group 4.2 (2006), CD is not a *seamless* reference surface as it varies from location to location, where a seamless reference surface is considered to be one that does not vary significantly either over time or area. In answering the question what the Canadian Hydrographic Service should do to bring their VDs into a consistent digital database taking into account current and future Differential Global Positioning System (DGPS) capabilities, Wells et al. (1996) recommended to adopt a reference ellipsoid as the vertical reference surface. The motivation was that a reference ellipsoid is simple and can easily be made temporally invariant by convention, since it is defined by adopting numerical values for certain parameters. Its use, of course, requires the realization of transformations between the reference ellipsoid and the reference surfaces used in practice (tidal or gravity-based VDs), i.e., it requires a proper 3D description of these reference surfaces. The latter is sometimes referred to as "separation model" (FIG Commission 4 Working Group 4.2 2006).

Despite a large and ever-increasing demand from both public and private sectors, Dutch waters lack an accurate 3D description of most relevant vertical offshore reference surfaces and a well-defined and accurate relation to the national height system. In particular, Dutch waters lack an accurate 3D description of the lowest astronomical tide (LAT). This tidal datum, defined as "the lowest tide level that can be predicted to occur under average meteorological conditions and under any combination of astronomical conditions" (International Hydrographic Organization 2011*a*, Technical Resolution 3/1919), is, in those regions where tides have an appreciable effect on the water level, adopted as CD by the International Hydrographic Organization (IHO). As such, it is the vertical reference surface used in nautical charts, i.e., charts that provide, among others, information about the water depths and navigational hazards. Obviously, such charts are crucial for safe navigation in the shallow waters of the Netherlands Continental Shelf.

For the Netherlands Continental Shelf, the generation and updating of nautical charts is one of the primary tasks of the Hydrographic Service of the Royal Netherlands Navy (RNLN). Updating nautical charts is a costly affair, mainly due to the high surveying costs. In times of budget cuts and delays in the updating cycle, innovative approaches are required to reduce the costs and to accelerate the process while maintaining the quality requirements. One way to achieve this is that the RNLN started to make use of a sophisticated resurvey planning where the resurvey frequency depends, among others, on the behavior of the sea floor (Dorst 2004, 2009, Van Dijk et al. 2011). Another development that allows to realize efficiency improvements and hence cost reduction is offered by the already mentioned increasing accuracy of

3D positioning with GNSS. Due to this, GNSS is more often used for the vertical positioning of hydrographic data collection platforms known as "ellipsoidally referenced surveying" (Dodd & Mills 2011). Ellipsoidally referenced surveying enables to derive seabed heights relative to the reference ellipsoid after which the reduction to CD is trivial, provided CD is known relative to the same reference ellipsoid. One major advantage of this so-called "water level reduction with GNSS procedure" is that it eliminates the reliance on temporary, expensive tide gauge observations. For the RNLN, however, this is not the main benefit as the use of temporary tide gauges has been strongly reduced by the use of the PREdiction MOdule (PREMO) (Versteeg 2000, Hounjet et al. 2012) for the water level reduction. In PREMO, the reduction to CD is carried out by combining a tide correction derived from a shallow water hydrodynamic model and a correction for the surge interpolated from nearby tide gauges. The main benefit for the RNLN stems from the expected reduction of the vertical positioning error contribution to the total error budget. Due to this, the contribution of other error sources are allowed to increase without violating the accuracy constraints specified by the IHO S44 standards (International Hydrographic Organization 2008). One of these, directly related to the survey efficiency, is the sounding accuracy of the multi-beam echo sounder. This accuracy is, among others, dependent on the beam angle of the received signals; the larger this angle, the lower the accuracy, but also the larger the swath width (width of area measured). When the swath width becomes larger, less time is needed to cover the whole survey area, which improves the efficiency and hence reduces the costs.

Besides faster, cheaper, and more accurate hydrographic survey data for nautical charts, other benefits of having accurate 3D descriptions of all relevant vertical offshore reference surfaces covering the Dutch waters are that they enable a more precise navigation, even over areas with submarine hazardous objects; merging of bathymetric data with topographic data to improve the protection of the coastal zone; and more accurate planning of depth maintenance in port approach areas. Furthermore, they are crucial in sea level rise studies, eco-system studies, integrated coastal zone management, and pro-active disaster-mitigation planning. In addition, they provide the necessary geometric infrastructure (in line with the Infrastructure for Spatial Information in Europe (INSPIRE) initiative) for maritime vertical positioning tasks such as preventing vessel grounding, and they allow the output of data and products on the VD requested by the user. Finally, they may pave the way to a more realistic, time-varying representation of under keel clearances in response to increasing demands from the shipping industry to load a ship as full as allowable by safety regulations.

So, to meet the demands from practice and by that the requirements imposed on modern vertical reference systems, this project aims to derive an accurate 3D description of CD (LAT) for the Dutch waters. Before we explain the motivation and formulate the research questions of this study, in the next section we provide a concise summary of previous work in the development of ellipsoidal heights of CD.

1.2 Previous work

The development of models that describe the ellipsoidal heights of CD was pioneered by the Canadian Hydrographic Service in 1996 (Wells et al. 1996, O'Reilly et al. 1996). Since then, many countries have followed their example, among which are the US (VDatum), Germany, Australia, France (BATHYELLI), and the UK (VORF).

A description of the basic procedure that should be implemented to realize separation models is provided by the *FIG Guide on the Development of a Vertical Reference Surface for Hydrography* (FIG Commission 4 Working Group 4.2 2006). Two main steps are considered: (i) derivation of the difference between CD and the reference ellipsoid at discrete points (usually tide gauge stations) and (ii) interpolation of the difference between those discrete points and extrapolation of the model for a reasonable distance offshore. To perform the extrapolation, so-called co-tidal and co-range charts can be used. These charts are constructed based on historical data, hydrodynamic models, and/or other information sources, and show lines of equal times and equal range of tides. This approach is known as "zoning". If the co-tidal charts lack accuracy, the FIG Commission 4 Working Group 4.2 (2006) proposes to obtain separation values at some offshore locations by, e.g., GNSS using the approach outlined by the International Hydrographic Organization (2005).

In most countries, however, the separation models are realized by a combination of hydrodynamic modeling and separation values derived from a tidal analysis of tide gauge records and/or sea surface heights (SSHs) provided by radar altimeter satellites. Without claiming to be exhaustive, in the remainder of this section we provide an overview of the procedures applied in different countries. Here, we also include a description of the procedure applied in the Netherlands to derive the separation between mean sea level (MSL) and LAT, which can be considered as a first step to obtain the separation between the reference ellipsoid and LAT.

1.2.1 US: VDatum (2000–)

VDatum is a software tool jointly developed by the US National Oceanic and Atmospheric Administration, the National Geodetic Survey/Remote Sensing Division, and the Center for Operational Oceanographic Products and Services. It allows users to transform geospatial data among a variety of ellipsoidal, orthometric, and tidal VDs (Parker et al. 2003, Myers et al. 2005). It was first developed for the Tampa Bay region (Milbert & Hess 2001) in 2000 and since then for other US near-coastal waters (e.g., Spargo & Woolard 2005, Dhingra et al. 2008, Yang et al. 2012). It is expected that by 2013 the software provides seamless coverage for all of the US coastal areas.

Within each of the three groups of VDs (ellipsoidal, orthometric, and tidal), there is a *primary* datum. This is the North American Datum of 1983 (NAD 83) for the ellip-

soidal VDs, the North American Vertical Datum of 1988 (NAVD 88) for the orthometric VDs, and the MSL for the tidal VDs. Transformations between VDs belonging to a different group are carried out via these primary datums. For the transformation between NAD 83 and NAVD 88, VDatum makes use of one of the National Geodetic Survey's GEOID models (National Geodetic Survey 2012), while for the transformation between the geoid and MSL a mean dynamic topography (MDT) model is used. This MDT model is constructed by interpolating MDT values derived from observed water levels at benchmarked tide gauges to a grid (Myers et al. 2005).

The tidal datums, including mean lower low water, mean higher high water, and mean tide level, relative to MSL are derived by hydrodynamic modeling (Myers et al. 2010). As part of the effort to adopt standard procedures for each regional application of VDatum, the primary hydrodynamic model used is the ADvanced CIRCulation model (Luettich et al. 1992). This hydrodynamic model, which can be run in 2D or 3D mode, uses unstructured grids in its solution of the hydrodynamic equations. For each regional application of VDatum, such a grid is constructed. After calibration, the model is forced by tides only and the tidal water levels are modeled over, normally, 37 days with a time step that accords with the smallest size of triangles in the grid (typically it is on the order of a few seconds or less). From the time series of tidal water levels, the tidal datums are derived. Note that the MSL (induced by tidal forcing only) is also derived. Other tidal datums are reduced to this model-derived MSL. As a final step, the model-derived grids are adjusted by the tidal datum realizations derived from tide gauge records. For this adjustment, the so-called "tidal constituent and residual interpolation" method is used (Hess et al. 2004). This method uses a set of weighting functions (generated by solving numerically Laplace's equation) to quantify the local contributions from each of the tide gauges, taking into account the effects of islands and complex shorelines. The same method is also used to derive a continuous surface of the separations between all tidal datums and MSL if no hydrodynamic model is available at all but only tide gauge records.

For each regional application of VDatum, the random uncertainties in both the VDs and of the mutual transformations are quantified. We refer to National Ocean Service (2012) for these values and an overview of the methods used to derive them.

1.2.2 Germany (2002–2006)

The derivation of a model describing the ellipsoidal heights of CD (LAT) for the German North Sea sector is carried out by the Bundesamt für Seeschifffahrt und Hydrographie (Ellmer & Goffinet 2006). Here, LAT is derived relative to the ETRF89 ellipsoid, which is the same ellipsoid used by the German satellite positioning service SAPOS.

Input data used to derive the separation model are: (i) ellipsoidal heights of CD at about 140 tide gauges distributed over the German North Sea coast and rivers under tidal influence; (ii) heights of the European Gravimetric Geoid 1997 (EGG97), used as a preliminary reference surface for MSL determination; and (iii) LAT values relative to MSL at 32,000 grid nodes of a finite element model for the area of the German Bight, provided by the Bundesanstalt für Wasserbau. The latter were derived from tidal water levels modeled over one year with a time step of one hour. The ellipsoidal heights of the tide gauge bench marks were derived from GPS data collected at the bench marks.

Ellmer & Goffinet (2006) do not provide any information about the uncertainty of the derived separation model.

1.2.3 Australia (2004–)

The first Australian project to derive a 3D description of CD (LAT) was the AUSHYDROID project (Martin & Broadbent 2004, Todd et al. 2004). During this project, carried out in 2004, a model of the height of LAT relative to the WGS84 ellipsoid was developed for Queensland waters. This surface is referred to as the "AUSHYDROID". AUSHYDROID was developed by extrapolating offshore the ellipsoidal heights of LAT at the tide gauge locations using the so-called "zoning" process. Here, the area is divided into a number of zones, referred to as "co-tidal zones", which are defined small enough for the curved surface of LAT within each zone to be regarded as planar. Depending on the number of tide gauges available within a co-tidal zone, an interpolation is performed using the so-called "linear" or "planar" method (Todd et al. 2004).

In February 2009, the Cooperative Research Centre for Spatial Information with support from Landgate and the Western Australian Department of Planning and Infrastructure, conducted a pilot project to develop a general approach to VD transformation across the littoral zone, i.e., the part of the ocean closest to the shore. The intention was to obtain topographic and bathymetric LiDAR data relative to a reference ellipsoid and to investigate strategies for creating a seamless ellipsoidal height-based digital elevation model. Following this, methods for transformation to other relevant vertical reference frames including tidal datums were to be considered. However, at the time the researchers were unable to obtain reliable and accurate ellipsoidal elevation data from the data providers.

A new project followed in 2011, which main objective was "to facilitate the creation of seamless elevation data sets across the littoral zone" (Keysers et al. 2012). This involved developing a method to enable the transformation between ellipsoidal height data and other types of VDs. These datums include the GRS80 ellipsoid realized through the Geocentric Datum of Australia 1994 and the Australian Height

Datum (AHD), CD (LAT), MSL, mean high water springs (MHWS), and the highest astronomical tide (HAT). Due to (i) the limited number of tide gauges around the Australian coast, (ii) the number of existing gauges which lack MSL and/or ellipsoid data, and (iii) the lack of metadata to determine the reliability and accuracy of available tide gauge records, it was concluded that "an accurate and effective VD transformation tool cannot be readily produced".

Despite these limitations, a demonstration tool was developed for a small study area as a proof of concept. For this area, gridded separation models have been created of MSL, LAT, MHWS, HAT, and AHD. The MSL surface was derived from satellite altimetry enhanced by MSL values derived from onshore tide gauge records. The ellipsoidal heights of the other tidal datums were obtained by summing the ellipsoidal heights of MSL and the separations of these tidal datums relative to MSL. The latter were derived by hydrodynamic modeling, for which the Global Environmental Modeling Solutions tide model was used. A comparison of the model-derived tidal datums with their realizations derived from 16 tide gauge records reveals average differences of 0.22, -0.15, and -0.02 m and standard deviations of 0.32, 0.22, and 0.21 m for the HAT, LAT, and MHWS datums, respectively.

1.2.4 France: BATHYELLI (2005–)

The BATHYmetry referenced to the ELLIpsoid (BATHYELLI) project, commenced in 2005 and led by the Service Hydrographique et Océanographique de la Marine (SHOM), aims to derive the offshore vertical reference surfaces (including MSL, LAT, and CD) for the entire French coastline relative to the GRS80 ellipsoid of réseau géodésique français 1993 (RGF93).

Offshore, the MSL is derived from satellite altimetry, while along the coast it is derived from tide gauges. To fill the gap between the open sea and the coast left by the radar altimeter data (see Section 1.3.1 for the reasons of this gap), a series of GPS survey campaigns were conducted by SHOM at 20 sites (Pineau-Guillou & Dorst 2011). Here, the MSL is obtained by correcting the observed ellipsoidal heights of the instantaneous water levels along the tracks of the ship for the contributions of tide and surge. In a final step, the data from these sources are merged using a least-squares collocation interpolation.

The separations MSL–LAT and MSL–CD are derived by tidal modeling. Unfortunately, no further details about this part of the procedure are available to the author.

A second phase of the project was initiated in mid-2011. The goals for this phase include validation and improvement of the VDs by including additional GPS measurements and the development of a transformation software.

1.2.5 UK: Vertical Offshore Reference Frame project (2005–)

One of the most recent efforts to the realization of models that describe the ellipsoidal heights of CD is the UK Vertical Offshore Reference Frame (VORF) project. This project aimed to integrate all VDs and reference surfaces used in the UK and Ireland (Ziebart et al. 2007); particularly the datums used in marine charting (CD, LAT, mean low water springs, MSL, mean high water springs, and HAT), the land datums used for expressing height above sea level (e.g., Newlyn), and the reference frame used for GNSS positioning. All reference surfaces are modeled as a grid of heights above the GRS80 ellipsoid referenced to both ETRF89 and ITRF2000, and estimated at epoch 2000.0. Besides the reference surfaces, VORF is also a software package that enables transformation of data sets between the modeled reference surfaces.

A grid of LAT values was computed by adding the heights of LAT relative to MSL to the ellipsoidal heights of MSL. The MSL grid was computed by merging point values of MSL at tide gauge stations with the Danish National Space Center mean sea surface 2006 (DNSC06-MSS) grid (Andersen & Knudsen 2007) from which all grid points within 14 km of the coastline were excluded. Prior to the actual merging, the geoid heights were subtracted from the MSL heights. The reason is that the resulting MDT is smoother and hence better suited to perform the merging step. For this merging, a least-squares collocation interpolation was applied. Note that this interpolation only affected the MSL model in the zone 14–30 km from the coast; beyond 30 km it is solely determined by DNSC06-MSS. Another feature of the computational strategy used to derive the MSL model is that separations between points were computed as "sea-distances"; the distance between two points is not the straight-line distance, but the shortest distance that it would be necessary to travel between the points by sea. For more details, we refer to Iliffe et al. (2007*a*).

LAT relative to MSL was computed using three different data sets (Turner et al. 2010). Beyond 30 km from the coast, LAT is solely derived from the Center for Space Research version 4.0 (CSR4.0) satellite altimetry ocean tide model. Within 30 km of the coast, the LAT values derived from CSR4.0 were supplemented by those derived from the North and Irish Sea and English Channel (NISE10) hydrodynamic tide-surge model and LAT values derived from observed water levels at tide gauge stations. The NISE10 model is a 2D, depth-averaged numerical model with a horizontal resolution of 3.5 km. To derive LAT relative to MSL, it is forced by tidal input only, realized by prescribing the 26 largest tidal constituents to the open sea boundaries of NISE10. The final LAT surface is obtained by merging all data using a thin plate spline interpolation method. As in the computation of the MSL model, distances between points were computed as "sea-distances". After merging, the root mean square (rms) agreement between the observation-derived LAT values at approximately 700 onshore tide gauges sourced from the Admiralty Tide Tables and the obtained LAT surface is 5.81 cm. All these data, however, have been used in the

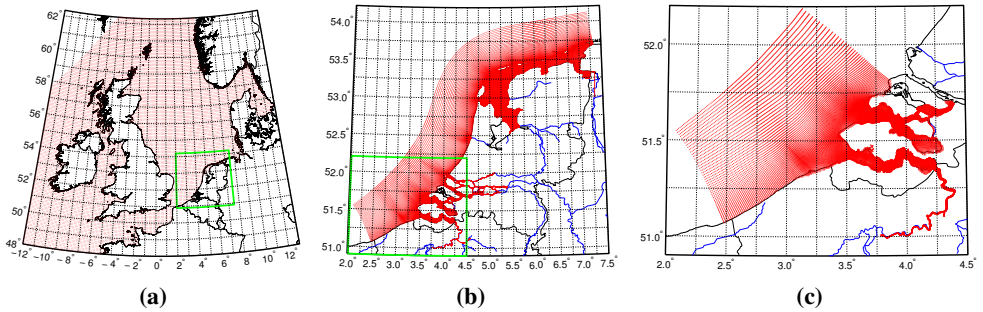

Figure 1.1: Model grids of the Dutch Continental Shelf Model (a), the "Kuststrook-Fijn" model (b), and the "Kustzuid" model (c). The green boxes in Figs. (a) and (b) indicate the geographical extent of the model plotted next to it.

computation of the LAT surface. By some kind of cross-validation, it was shown that the rms agreement between observation-derived and predicted LAT values in areas where no in-situ tidal data were available is 20 cm (Turner et al. 2010).

1.2.6 The Netherlands (2006)

Dutch waters lack a 3D description of LAT. Available, however, is a model of the separation between MSL and LAT as the procedure to reduce observed water depths to LAT currently applied by the RNLN involves a reduction of MSL to LAT. This model is referred to as the "LAT reduction matrix". It should be noted that in the coastal areas, the Wadden Sea, and the Eastern and Western Scheldt estuaries, this matrix provide the separation between LAT and the Normaal Amsterdams Peil (NAP), i.e., the Dutch height datum.

The LAT reduction matrix is computed as a blend of separations between MSL/NAP and LAT derived with three nested shallow water hydrodynamic models (Kwanten 2007): (i) the Dutch Continental Shelf Model (DCSM) (Gerritsen et al. 1995, Verlaan et al. 2005); (ii) the "Kuststrook-Fijn" model (Rijkswaterstaat-Waterdienst & Deltares 2009*a*); and (iii) the "Kustzuid" model (Rijkswaterstaat-Waterdienst & Deltares 2009*b*). We refer to Figs. 1.1a–1.1c for the model grids.

DCSM (Fig. 1.1a) is the largest and coarsest model; it covers the area of the northwest European continental shelf to at least the 200 m depth contour, i.e., 12°W to 13°E and 48°N to 62.3°N. It has a horizontal resolution of $1/8^\circ \times 1/12^\circ$ (approximately 8×9 km) in east-west and north-south directions, respectively. For each grid point, LAT is computed as the lowest modeled tidal water level (astronomical tide is the only driving force) that occurred during the period 1999 to 2018. The astronomical

tide is prescribed at the open sea boundaries of DCSM in the form of water levels computed from a harmonic expansion using a set of 11 tidal constituents.

The domain of the "Kuststrook-Fijn" model (Fig. 1.1b) comprises the entire Dutch coast and the main inland waters. In seaward direction, the grid extends to approximately 60–70 km from the coast. While the model has a curvilinear grid, its spatial resolution varies strongly; along the open sea boundary the resolution is 300–800 m by 2.5 km, which reduces to a few hundred meters along the coast and in the inland waters. For each grid point, LAT is computed as the lowest modeled tidal water level that occurred during the first six months of 2005, the period in which DCSM predicted the LAT event to occur. The open sea boundary conditions are derived from the "Zuidelijke Noordzee" model (Roelvink et al. 2001), whose open sea boundary conditions are, in turn, derived from DCSM. Along the coast, the model provided the separation between LAT and NAP, while west of the 20 m depth contour line, LAT is provided relative to MSL.

The "Kustzuid" model (Fig. 1.1c), which is a cut-out of the Kuststrook-Fijn model, is, compared to the latter model, extended by one additional cell at the land-sea boundary and it has a three times higher resolution in the Nauw van Bath. LAT was derived similarly as with the Kuststrook-Fijn model.

After computing the three separate LAT surfaces, they were merged. In regions where the model domains overlap, the LAT values were used from the model that best fit to the LAT values computed at nearby tide gauge stations. Besides some cosmetical changes, at some locations the merged grid was adjusted to the LAT values derived from tide gauge records.

A validation of the obtained LAT reduction matrix is carried out by comparing model-derived LAT values with observation-derived ones (the same as used in the manual adjustment step). The estimated precision is $\sim$7 cm (95% confidence level), while the mean of the residuals is close to zero. On the Netherlands continental shelf and in the Belgian waters, the expected precision is approximately 10 cm. Our study, however, suggests that the accuracy is much lower (Slobbe et al. 2013b).

1.3 Motivation

In this section, we provide the motivation for this research from a hydrographic, geodetic, and hydrodynamic modeling perspective. The overview of previous work shows that in all recent projects more or less the same procedure is applied to derive a separation model of CD; all combine the ellipsoidal heights of CD at tide gauges with those derived as the sum of model-derived separations between MSL and CD and the ellipsoidal heights of MSL. Here, we motivate why this approach is not adequate for the Netherlands. In short the reason is that this approach relies on the

MSL, which is not available with sufficient accuracy in the Dutch coastal waters, the Wadden Sea, and the Eastern and Western Scheldt estuaries. An alternative approach is proposed in which the ellipsoidal heights of CD (LAT) are derived as the sum of quasi-geoid heights and model-derived separations between the quasi-geoid and LAT. Next, we motivate why we chose to estimate a new quasi-geoid model rather than using a state-of-the-art, publicly available quasi-geoid, which is the research motivation from a geodetic perspective. Finally, we show that a hydrodynamic model that provides water levels relative to a particular (quasi-)geoid also serves the needs of the hydrodynamic community, which is the research motivation from a hydrodynamic modeling perspective.

1.3.1 A hydrographic perspective

In the North Sea, no coastal-waters-inclusive continuous (CWIC) 3D description of LAT can be derived purely from observations. Doing so requires time series of the instantaneous water levels relative to a reference ellipsoid over a sufficiently long time period and the measurement locations should have sufficient spatial coverage. Moreover, these time series also should have sufficient temporal resolution to resolve all relevant tidal constituents needed to reconstruct the tidal water levels from which LAT is derived, especially in the shallow parts of the North Sea. From the existing measurement techniques that provide time series of instantaneous water levels: radar altimetry, tide gauges, and GNSS buoys, the first provides time series over a sufficiently long period and, in open sea, with sufficient spatial resolution. The data lack, however, the required temporal resolution. Tide gauges and GNSS buoys, on the other hand, provide time series that are sufficiently long and do have sufficient temporal resolution, but their spatial coverage is poor. Therefore, the current practice to obtain a CWIC model of the ellipsoidal heights of LAT in shallow waters is to derive them as the sum of LAT values derived from a global/regional ocean tide model and an altimeter-derived MSL model, complemented by LAT values derived from tide gauge records plus GNSS measurements. Schematically, this approach is illustrated in Fig. 1.2.

However, due to a degrading accuracy of radar altimeter data in coastal regions (e.g., Andersen & Knudsen 2000, Deng et al. 2002), coastal waters lack information about the MSL. Even when using the most advanced retracking schemes (Deng 2003, Gommenginger et al. 2011), the data gap along the coastline will still be a few kilometers (Gommenginger et al. 2011). Therefore, in these waters the ellipsoidal heights of LAT can be solely derived from tide gauge records in combination with GNSS measurements. To obtain a CWIC surface from these point data, strong interpolation is required, unless the data gap is closed by GNSS surveys as in the BATHYELLI project (Section 1.2.4). The latter, however, is expensive and hence not preferable. The interpolation, on the other hand, is not trivial. Remember that the tidal behavior

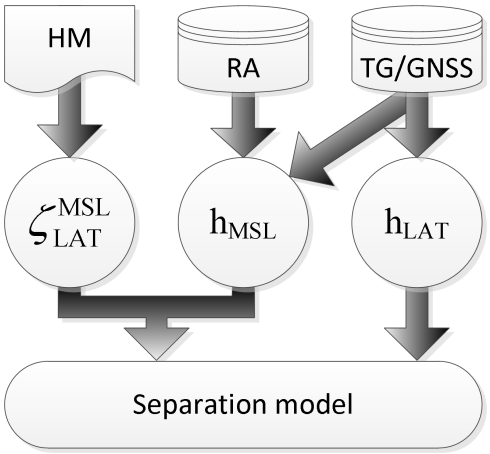

Figure 1.2: Schematic representation of current practice in deriving separation models of CD (LAT), where ζ^{MSL}_{LAT} is the model-derived separation between the MSL and LAT, and h_{MSL}, h_{LAT} the ellipsoidal heights of MSL and LAT, respectively. The abbreviations HM, RA, and TG, stand for hydrodynamic model, radar altimetry, and tide gauges, respectively.

at a particular tide gauge location, and hence the LAT value, is not necessarily representative for nearby locations. Furthermore, the distance between neighboring tide gauge locations may be tens of kilometers.

To derive an accurate and continuous 3D description of LAT in Dutch waters including the coastal areas, the Wadden Sea, and the Eastern and Western Scheldt estuaries, avoiding interpolation, two alternative approaches are possible. Schematically, these approaches are illustrated in Fig. 1.3. Both approaches differ from each other by the reference surface used as intermediate surface to which the model-derived LAT values refer and, related to that, by the way the average meteorological conditions, under which the LAT events are supposed to occur (International Hydrographic Organization 2011*a*, Technical Resolution 3/1919), are accounted for.

The first approach (Fig. 1.3a) determines the ellipsoidal heights of LAT as the sum of the ellipsoidal heights of MSL and the heights of LAT relative to MSL. The ellipsoidal heights of MSL are derived by adding the quasi-geoid heights to the hydrodynamic model-derived MDT expressed relative to that quasi-geoid, while LAT relative to MSL is derived from modeled tidal water levels.

In the second approach (Fig. 1.3b), the ellipsoidal heights of LAT are computed as the sum of the quasi-geoid heights and the heights of LAT relative to this quasi-geoid. The latter can be derived from modeled water levels which comprise the tide and the time-averaged meteorological and steric contributions, provided that the modeled water levels refer to the quasi-geoid.

In this study, the second approach is preferred. The reason for this is twofold: (i) this approach is conceptually clearer since the model's reference surface, as well as the quasi-geoid, is an equipotential surface of the Earth's gravity field (Hughes & Bingham 2008) (indeed, in a strict sense the quasi-geoid is not an equipotential surface, but at sea the differences between the geoid and quasi-geoid are negligible) and (ii) this

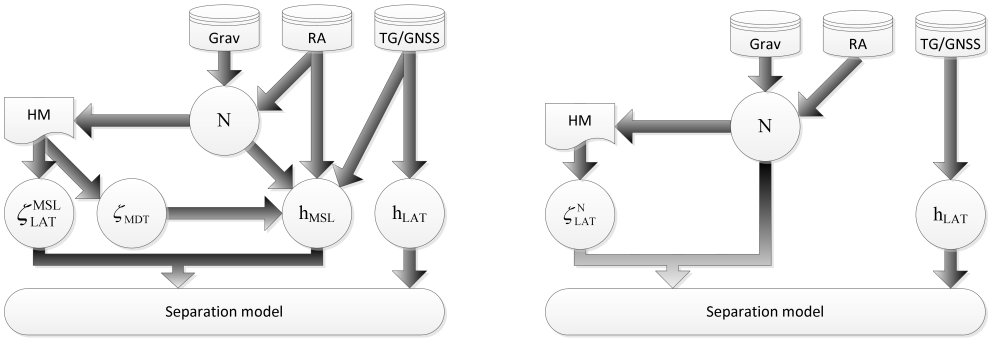

Figure 1.3: Schematic representations of two alternative approaches to derive a separation model of CD (LAT). Both alternatives differ from each other by the reference surface used as intermediate surface to which the model-derived LAT values refer and, related to that, by the way the average meteorological conditions, under which the LAT events are supposed to occur (International Hydrographic Organization 2011*a*, Technical Resolution 3/1919), are accounted for. In the first alternative (a) the MSL is used as intermediate surface, while in the second alternative (b) the quasi-geoid is used. In the schemes, we use ζ^{MSL}_{LAT} for the model-derived separation between the MSL and LAT, ζ_{MDT} for the model-derived MDT, N for the quasi-geoid heights, h_{MSL}, h_{LAT} for the ellipsoidal heights of MSL and LAT, respectively, and ζ^{N}_{LAT} for the model-derived separation between the quasi-geoid and LAT. The abbreviations HM, Grav, RA, and TG, stand for hydrodynamic model, gravimetry, radar altimetry, and tide gauges, respectively.

approach allows to include the average dominating variations (i.e., seasonal) of the meteorological and steric conditions/MSL in the realization of LAT. The error introduced by not taking into account that the model's reference surface is an equipotential surface, is illustrated by the results of Prandle (1978); the contribution of the M_2 tide to MSL in the southern North Sea varies from -1 to 8 cm, with maximum values along the Dutch coast. The latter reason follows from a more precise interpretation of the LAT definition as the lowest water level to occur under *average meteorological conditions* and under any combination of astronomical conditions. Indeed, since the average meteorological conditions in, e.g., spring differ from those in, e.g., fall, it makes sense to include the average seasonal variations into the definition of the LAT.

Anyway, regardless of which approach we use, both for the first and the second approach a method needs to be developed to vertically reference a hydrodynamic model to a particular quasi-geoid. As such a method is not available, its development is part of this research. Thereafter, LAT relative to the quasi-geoid needs to be realized and its accuracy should be assessed. This realization and assessment is also part of this research.

1.3.2 A geodetic perspective

Another motivation for this research arises when we ask whether we do have a quasi-geoid model available that is adequate for our purpose. To be considered as adequate, such a quasi-geoid model should at least cover our domain of interest; the Netherlands Continental Shelf and the Dutch mainland. Based on this criterion, several "candidates" drop out. In particular, the EDIN2000 geoid (Hipkin et al. 2004) as this geoid does not cover the Dutch mainland. As noted by Hipkin et al. (2004): "the EDIN2000 model was primarily developed to estimate the MDT, so that, onshore, the computation only has to estimate the geoid reliably enough for comparison with coastal tide gauges, and for errors on land not to leak into marine areas". We have three other candidates: (i) the GEONZ97 North Sea geoid (De Bruijne et al. 1997), (ii) the quasi-geoid synthesized from the Earth Gravitational Model 2008 (EGM2008) spherical harmonic coefficients (Pavlis et al. 2012), and (iii) the European Gravimetric Geoid 2008 (EGG08) (Denker et al. 2008).

The GEONZ97 North Sea geoid was computed as a preliminary geoid model in 1997, but is still in use in the Netherlands. There are two main reasons why this geoid is not adequate for our purpose. Starting with a gravimetric geoid, corrections to this geoid were derived on land from differences at GPS/leveling points and at sea from differences with TOPEX along-track mean sea surface heights. In this way, they tried to correct the gravimetric geoid for long-wavelength errors. Hence, at sea GEONZ97 is closer to the MSL than to a geoid. This is the first reason why this "geoid" is not adequate for our purpose. The second reason is that this geoid was just a *preliminary* model (originally, the revision of GEONZ97 was even one of the primary motivations to start this research). As recommended by De Bruijne et al. (1997), a revision of GEONZ97 should include among others: (i) improved gravity data from the British Geological Service and new shipboard gravity data in the German Bight; (ii) improved processing of the radar altimeter data (e.g., improved orbits and ocean tide corrections); (iii) radar altimeter data from other altimetry missions than TOPEX/POSEIDON; and (iv) improved modeling of the MDT.

Of the two remaining candidates, EGG08 has the best performance. Although not specifically computed for the North Sea area, it is currently the best, publicly available quasi-geoid model covering the whole North Sea and Dutch mainland. It makes use of an extensive database of terrestrial, airborne, and shipboard gravity data (most of these data are classified) combined with satellite gravity data (CHAMP + GRACE) and radar altimeter data (the Danish National Space Center altimeter-derived gravity anomaly grid 2008 (Andersen et al. 2010)). The older shipboard gravity data were edited and crossover adjusted (Denker & Roland 2005). The model is made available on a $1' \times 1'$ grid, though the real spatial resolution maybe somehow less. A validation of EGG08 using independent GPS and leveling data suggests a sub-decimeter accu-

racy at continental scales to an accuracy of a few centimeters over distances of a few hundred kilometers.

There are two reasons why the accuracy of EGG08 can be further improved. The first reason is that EGG08 does not include data acquired by the GOCE (Gravity field and steady-state Ocean Circulation Explorer) satellite (Journal of Geodesy 2011) as these data are just publicly available from May 2010. Undoubtedly, including these data will further improve the quality of the quasi-geoid. The use of satellite gravity data in (regional) (quasi-)geoid computations is a topic of ongoing research.

The second reason is that in the estimation of EGG08 one did not exploit the full potential of satellite radar altimeter data. This data set is considered as a key data set to obtain an accurate, high-resolution quasi-geoid. Indeed, most existing shipboard gravity data sets are old and have varying accuracies, which are often hard to assess. According to Wessel & Watts (1988), errors up to a few tens of mGal occur that mainly originate from the incorrect computation of the Eötvös effect, a direct consequence of the poor ship positioning quality in the pre-GNSS era. Depending on the used measurement technology, other error sources mentioned by Wessel & Watts (1988) are: off-leveling, cross-coupling, non-linear drift, and a mechanical "tare" or "jar" of the gravity sensor. All these sources give rise to mostly systematic errors that can be partially removed by, e.g., a crossover analysis (e.g., Wessel & Watts 1988, Denker & Roland 2005). Since surveying is time consuming and expensive, no systematic gravity re-survey of the whole North Sea is foreseen. Although airborne data are less expensive to acquire, existing data sets lack complete coverage over the whole North Sea. Moreover, they are not always publicly available. Radar altimeter data, however, are not classified and provide accurate information with a uniform coverage. The use of radar altimeter data requires, among others, a correction of the observed SSHs for the dynamic sea surface topography. The latter consists of three components: tides, surge, and steric water level variations. Astronomical tide corrections are commonly derived from global ocean tide models. Several authors (e.g., Andersen & Knudsen 2000, Hwang et al. 2006, Sandwell & Smith 2009) have suggested that these corrections lack accuracy in shallow waters. Much better corrections can be obtained by using dedicated shallow water tide models. In the computation of EGG08, 951,251 anomalies from the KMS2002 global marine gravity field were used (Andersen et al. 2005), for which a slightly modified version of the GOT00.2 global ocean tide model (Ray 1999) was used to correct for the astronomical tide. Therefore, applying astronomical tide corrections derived from a shallow water tide model is the second expected improvement that can be achieved compared to EGG08. The real added value of using a shallow water tide model for the astronomical tide corrections needs to be investigated. The assessment is part of this research.

From a conceptual point of view, also the surge and steric contributions to the instantaneous water levels need to be removed, before the corrected SSHs can be

identified with (quasi-)geoid heights, referred to as *geometric* (quasi-)geoid heights. While in most (quasi-)geoid computations, however, the gradients of the geometric (quasi-)geoid heights (i.e., the DoV) rather than the geometric (quasi-)geoid heights themselves are used, these contributions are assumed to be negligible, except for the slopes associated with eddies and mesoscale variability, and western boundary currents (Sandwell & Smith 2009). This assumption is motivated by comparing the magnitude of the gradients associated with non-tidal water level variations to the precision with which the DoV can be derived. The outcome of this comparison is, however, explicitly dependent on the distance between the two geometric (quasi-)geoid heights used to compute the DoV, i.e., it is dependent on the wavelength. Indeed, application of the error propagation law shows that the propagated standard deviation of the DoV is inversely proportional to this distance (Hwang et al. 2002, Eq. 5). We agree that over 7 km (1 s of flight along the satellite track) the contribution of non-tidal water level variations to the DoV might be negligible, i.e., for these wavelengths the signal-to-noise-ratio (SNR) is less than one. However, over wavelengths of tens to hundreds of kilometers, the SNR may be more favorable, meaning that these contributions are not negligible anymore. Sandwell & Smith (2009) found that the measured noise for wavelengths > 80 km is less than the estimated errors in the sea surface slope. Therefore, we conclude that as long as it is allowed that radar altimeter data contribute to determine the (quasi-)geoid's medium-wavelengths, the added value of proper corrections for the non-tidal water level variations should not be limited to the very short-wavelengths.

Several authors (e.g., Brennecke & Groten 1977, Rapp & Yi 1997) have shown that applying a MDT correction to the observed SSHs has a limited impact on the estimated gravity anomalies and the (quasi-)geoid. Rapp & Yi (1997), who carried out a number of experiments in the Gulf Stream region, provide two reasons to explain this lack of improvement. First, their computations were carried out after removing the mean difference between the SSHs and the reference geoid from the observations. While this removal was not restored to the computed anomalies and the MDT is almost constant in the region they considered, this "data centering" effectively removed the MDT effect. The second reason is that they did not account for the seasonal MDT variations that exist in the non-repeat ERS-1 geodetic mission (GM) data used in their study. Our study, however, differs from the study of Rapp & Yi (1997) in that we will evaluate the impact of the *instantaneous* dynamic topography corrections rather than those of the *mean* dynamic topography. In the North Sea, which is known for its frequent storm surges, the gradients associated with the MDT are somewhat small compared to the gradients that can show up during a surge event. During such an event, sea level can be raised or lowered by several meters over a period ranging from a few hours to 2–3 days (Pugh 1996, Flather 2000). The argument that this contribution averages out and, therefore, is of little importance for (quasi-)geoid computations, is not valid. It might be true for the exact repeat mission (ERM) data, but not for the

GM data. In fact, the GM data are of utmost importance for gravity field recovery due to their spatially dense ground tracks (Sandwell & Smith 2009). For these data, we cannot compute average values.

Sandwell & Smith (2009) removed the long-wavelength SSH gradient iteratively: in each iteration, the long-wavelength components are removed from the observations by subtracting the low-pass filtered differences (0.5 gain at 180 km) between the observed SSH gradients and the gradients of the geoid obtained in the previous iteration. In the initial run they used a geoid computed from the EGM96 spherical harmonic coefficients. Although they showed that this method provides good results, it is not very practical for the semi-enclosed North Sea basin. Indeed, while there are no data on land, the performance of this filter operation decreases in coastal waters. In addition, low-pass filtering also removes signal, i.e., after filtering radar altimeter data in fact only contribute to the determination of the (quasi-)geoid's short-wavelengths.

Therefore, in this study we also consider the importance of the time-varying non-tidal water level variation corrections for the computation of the quasi-geoid. The inverted barometer correction, as for example applied by Hwang et al. (2006), lacks accuracy in shallow water to properly remove the sea level signal induced by atmospheric wind and pressure forcing. The reason is that the dominating acceleration term related to wind stress is ignored in the inverted barometer correction. This also holds for the quasi-stationary corrections for the water level variations induced by water density variations derived from the Levitus climatological data set (e.g., Hwang 1997); according to Wunsch & Stammer (1998) their accuracy is limited to the 10–25 cm level. Both correction terms can be improved by using a shallow water hydrodynamic model. Here, we will use the same model as used to improve the astronomical tide corrections, which has the additional advantage that any non-linear interaction between the separate contributions (e.g., between tide and surge (Prandle & Wolf 1978)) will be included as well. This means that just one correction is applied instead of three separate ones.

So, the hydrodynamic model used to derive the separation between the quasi-geoid and LAT, will also be used to estimate the quasi-geoid. This requires a small, but important change of the schematic representation of our approach to derive a separation model of LAT as given in Fig. 1.3b; instead of a one-way link between the quasi-geoid and the hydrodynamic model, a two-way link exists (cf. Fig. 1.4, which is an update of Fig. 1.3b). This two-way link results in a chicken-and-egg problem; on the one hand, we aim to use a hydrodynamic model to derive a proper quasi-geoid, while on the other hand this quasi-geoid needs to be the model's reference surface. The development of a methodology that solves this problem is a part of this research.

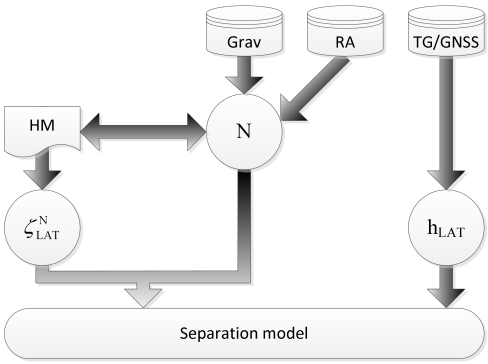

Figure 1.4: Schematic representation of the approach used in this study to derive a separation model. Compared to Fig. 1.3b, we included an arrow from the hydrodynamic model to the quasi-geoid, as the hydrodynamic model will also be used to estimate the quasi-geoid. In the scheme, we use ζ^{N}_{LAT} for the model-derived separation between the quasi-geoid and LAT, N for the quasi-geoid heights, and h_{LAT} for the ellipsoidal heights of LAT. The abbreviations HM, Grav, RA, and TG, stand for hydrodynamic model, gravimetry, radar altimetry, and tide gauges, respectively.

1.3.3 A hydrodynamic modeling perspective

A hydrodynamic model that provides proper estimates of the instantaneous water levels expressed relative to a (quasi-)geoid does not only serve hydrographic and geodetic needs. The increasing accuracy requirements demanded from hydrodynamic models expose the need to abandon modeling practice that leaves the model's reference surface undefined and use some work-arounds if modeled water levels need a proper reference. Indeed, the reference surface of a model that enables to reduce observed SSHs to the (quasi-)geoid is the (quasi-)geoid. Hence, such a model perfectly matches the need of the hydrodynamic community.

Finally, the properly referenced hydrodynamic model we aim to develop in this study paves the way to new applications. One of them is a probabilistic approach to realize CD, i.e., an approach where CD is defined as the level below which the water falls with a given probability. Such an approach to realize CD may be preferred above LAT if the probability that the instantaneous water level drops below LAT is significantly higher than once per 18.6 years. Indeed, if this is the case, mariners might take more risk than they realize. In this study, these probabilities will be assessed.

1.4 Research objectives

The overall goal of this study is the realization of the offshore vertical reference surface LAT in the ETRS89/GRS80 system and linked to the onshore height system. As seen above, a shallow water hydrodynamic model takes a key role in the realization of this surface. First, it is needed to correct radar altimeter SSHs for the contribution of the dynamic sea surface topography, which is needed to realize an accurate high-resolution quasi-geoid. Second, it is needed to realize LAT expressed relative to this estimated quasi-geoid. We have identified a chicken-and-egg problem; on the

one hand, we aim to use a hydrodynamic model to derive a proper quasi-geoid, while on the other hand this quasi-geoid needs to be the model's reference surface. Hence, the main objective of this study is to *develop a procedure that enables to derive a consistent set of offshore vertical reference surfaces; a quasi-geoid based on, among others, radar altimeter data combined with a shallow water hydrodynamic model and LAT relative to this quasi-geoid, obtained using a shallow water hydrodynamic model*.

From this objective, four specific research questions are derived.

1. *How can a shallow water model be vertically referenced to a given (quasi-) geoid and to which extent does such a model benefit from an improved (quasi-) geoid? What accuracy can be expected of the modeled instantaneous and mean dynamic topography?*

Vertical referencing of a shallow water hydrodynamic model comprises all tasks needed to refer the modeled instantaneous water levels to a particular equipotential surface of the Earth's gravity field. Once known how to reference such a model, we can assess the impact of quasi-geoid errors on the modeled water levels. This, in turn, will answer the question to which extent a more accurate quasi-geoid improves the quality of modeled water levels. In this study, we use the Dutch Continental Shelf Model version 5 (DCSM), which is a 2D storm surge model. This model will be extended to include the effect of horizontal water density variations on the modeled water levels.

2. *What is the added value of using a shallow-water hydrodynamic model for the reduction of radar altimeter SSHs to quasi-geoid heights when estimating a quasi-geoid for the Netherlands Continental Shelf?*

The reduction of SSHs to quasi-geoid heights implies the removal of the *full* dynamic topography signal, i.e., the contributions associated with tides, surge, and steric water level variations. While the last two contributions are in most areas assumed to be negligible (at least for the short wavelengths), in our analysis we will quantify the impact of including them into the dynamic topography corrections separately. For an unambiguous interpretation, the analysis will be split into two parts. First, we perform a spectral analysis of the residual along-track DoV and the associated noise, obtained after applying different sets of dynamic topography corrections. Second, we quantify the impact of different sets of dynamic topography corrections on the estimated quasi-geoid. To estimate the quasi-geoid, we use a radial basis function parameterization of the disturbing potential. This parameterization was used successfully for the most recent realization of the Dutch land quasi-geoid NLGEO2007 (Klees et al. 2008). Note that in this thesis, we do not distinguish between the geoid

and the quasi-geoid as they are nearly identical in the Dutch coastal regions and at the open sea.

3. *How, and to which level of accuracy, can we derive the separation between the quasi-geoid and LAT from a shallow water hydrodynamic model?*

To obtain the highest accuracy of the LAT surface, LAT values at the tide gauges need to be integrated in the model-derived LAT surface (cf. Turner et al. 2010). This can be achieved in several ways. Turner et al. (2010) merged LAT values derived from observed water levels and hydrodynamic models in a post-processing step. Alternatively, one might consider an online assimilation of tidal water levels into the model. In this study, we rely on the model calibration that has been carried out using both tide gauge and radar altimeter data. Furthermore, to reduce the numerical complexity, we exclude a detailed modeling of the LAT surface in the estuaries and the Wadden Sea as was done to obtain the current "LAT reduction matrix" (Section 1.2.6). This will be done in the future once a refined DCSM model has become available. For operational use of the LAT surface, a number of practical issues need to be addressed. First, the issue of how to achieve a continuous transition from those waters where LAT is used as the vertical reference surface to the rivers where a non-tidal datum is used. Second, the issue of impounded waters, i.e., waters that are not dynamically connected to the open sea. Both issues are out of the scope of this thesis. Regarding the first one, it is worth to mention that in the Netherlands the vertical datum used in the rivers that are connected to the waters where LAT is used, is defined (i) relative to NAP (i.e., the quasi-geoid) and (ii) such that it smoothly transits to LAT. Hence, the first issue does not seem to be a concern.

4. *Does the use of a Slepian basis representation provides a solution of the spectral inconsistency between a high- (e.g., MSL) and low-resolution (e.g., geoid) data set?*

One facet of the aim to obtain a consistent set of vertical reference frames is that the frames are consistent in terms of spectral resolution. While, in general, this is not the case, we have to enforce "spectral consistency" by, e.g., the application of a suitable low-pass filter. Here, conventional low-pass filters are inadequate since we have to deal with signals that are not defined on land (MSL, MDT, and LAT). A recent study of Albertella et al. (1999) suggests that the use of a Slepian basis representation may solve this problem. While so far this has not been proven, in this study we will elaborate the Slepian basis representation solution and demonstrate (by numerical experiments) that it does not solve the spectral consistency problem. Because this "spectral consistency problem" recently emerged in computing the MDT by subtracting a gravimetric geoid from an altimeter-derived MSL model, our experiments are presented in the same context.

1.5 Outline

This thesis is organized as follows.

In Chapter 2, we present the flowchart of the overall procedure developed and implemented in this study to estimate, on the one hand, a quasi-geoid and to obtain, on the other hand, a hydrodynamic model that provides water levels relative to this quasi-geoid. This chapter will guide the reader through the remaining chapters of the thesis.

In Chapter 3, we describe the approach developed to obtain a 2D storm surge model that provides estimates of the instantaneous water level relative to a particular quasi-geoid.

In Chapter 4, we assess the added value of the use of this model in computing the dynamic topography corrections needed to reduce the altimeter-derived SSHs to geometric quasi-geoid heights. Furthermore, we present and validate the estimated quasi-geoid.

Chapter 5 treats two closely related but distinct topics. The first topic is the derivation of LAT in the North Sea from a vertically referenced shallow water model. The second topic is the assessment of the suggested sense of safety of the use of LAT as CD.

In Chapter 6, we treat the question whether a spherical Slepian basis representation enables to obtain spectral consistency in the context of MDT estimation using the so-called “geodetic approach”, i.e., by computing the difference between a mean sea surface model obtained from satellite altimetry and a gravimetric geoid.

Chapter 7 comprises the conclusions and recommendations for future research.

Chapter 2

Overall approach to offshore vertical reference frame realization

In Chapter 1, we showed that to obtain a coastal-waters-inclusive continuous (CWIC) surface of the ellipsoidal heights of LAT, LAT needs to be derived relative to the quasi-geoid. Moreover, it was shown that in the North Sea an accurate realization of both the quasi-geoid and the LAT surface requires the use of a shallow water hydrodynamic model: (i) to correct the altimeter sea surface heights (SSHs) for the contribution of the dynamic sea surface topography and (ii) to obtain the separations between the quasi-geoid and the LAT surface. Obviously, the computation of the ellipsoidal heights of LAT as the sum of the quasi-geoid heights and the model-derived separation between the quasi-geoid and LAT can only be applied if the hydrodynamic model's reference surface can be identified with the quasi-geoid. The quasi-geoid, however, is not known, and the hydrodynamic model is needed to estimate the quasi-geoid. In this chapter, we present the flowchart of the procedure developed and implemented in this study to estimate, on the one hand, a quasi-geoid and to obtain, on the other hand, a hydrodynamic model that provides water levels relative to this quasi-geoid. The hydrodynamic model, in turn, can be used to realize the commonly used offshore vertical reference surfaces LAT and MSL, or separations between these surfaces such as the mean dynamic topography (MDT). The overall procedure can be divided in three steps: (i) the data preprocessing; (ii) the estimation of the quasi-geoid and the realization of a hydrodynamic model that provides water levels relative to this quasi-geoid; and (iii) the realization of the LAT and MDT surfaces (spectrally consistent with the quasi-geoid) once the final quasi-geoid and the vertically referenced hydrodynamic model are available. In the remainder of this chapter, these three steps

are briefly discussed. References are included to the corresponding sections of this thesis that provide more detailed information about the individual sub-steps.

2.1 Step 1: data preprocessing

The first step comprises the preprocessing of the various data sets required to estimate the quasi-geoid (satellite, airborne, shipboard, and terrestrial gravity data and radar altimeter data (Section 4.3)) and/or required as input for the hydrodynamic model (mean sea level pressure fields, wind speed fields, salinity and temperature fields, radar altimeter data, and tide gauge data (Sections 3.5.2, 3.5.3, 3.5.4, and 5.2)). The preprocessing aims to harmonize the data and prepare them for further processing. In general, this includes a harmonization of the horizontal and vertical datums to which the various data refer. The horizontal datum used in this study is the European Terrestrial Reference System 1989 (ETRS89) that is based on the GRS80 ellipsoid. Any height data (e.g., observed water levels at tide gauges, SSHs from radar altimetry, and heights of the terrestrial/airborne gravity observation points) are transformed to ellipsoidal heights in ETRS89 as well. In the remainder of this section, we provide for each data set a concise overview of the applied preprocessing.

As shown in the flowchart, the way used to transform *tide gauge water levels* to ellipsoidal heights depends on the available information (Section 5.2). If GNSS measurements at a tide gauge are available, the transformation is straightforward. If not, but the tide gauge station is connected to the national height datum, we add the national (quasi-)geoid height or we transform the heights to the European Vertical Reference Frame 2007 (EVRF2007) after which we add the height of the quasi-geoid EVRF2007 refers to, which is the European Gravimetric Geoid (EGG08). If the tide gauge station is not connected to the national height datum, which applies to most offshore stations, the data are usually provided relative to MSL. Hence, ellipsoidal heights can be obtained by adding the ellipsoidal height of the MSL. In this study, they are derived from the mean sea surface computed by the Danish National Space

Figure 2.1 ***(following page)*****:** Flowchart of the procedure developed and implemented in this study to obtain ellipsoidal heights of LAT and to establish the connection with the onshore height system. The different colors of the blocks refer to the different steps in the overall procedure: (i) green refers to the data preprocessing step, (ii) yellow refers to the step where we estimate the quasi-geoid and realize a hydrodynamic model that provides water levels relative to this quasi-geoid, and (iii) the light coral color refers to the step where we realize the LAT and MDT surfaces. The different colors of the arrows refer to the different data flows: tide gauge data (blue); radar altimeter data (green); gravity data (red); and salinity, temperature, and meteorological data (black). Grey is used if the arrow refers to a non-data flow or when two or more data groups are involved.

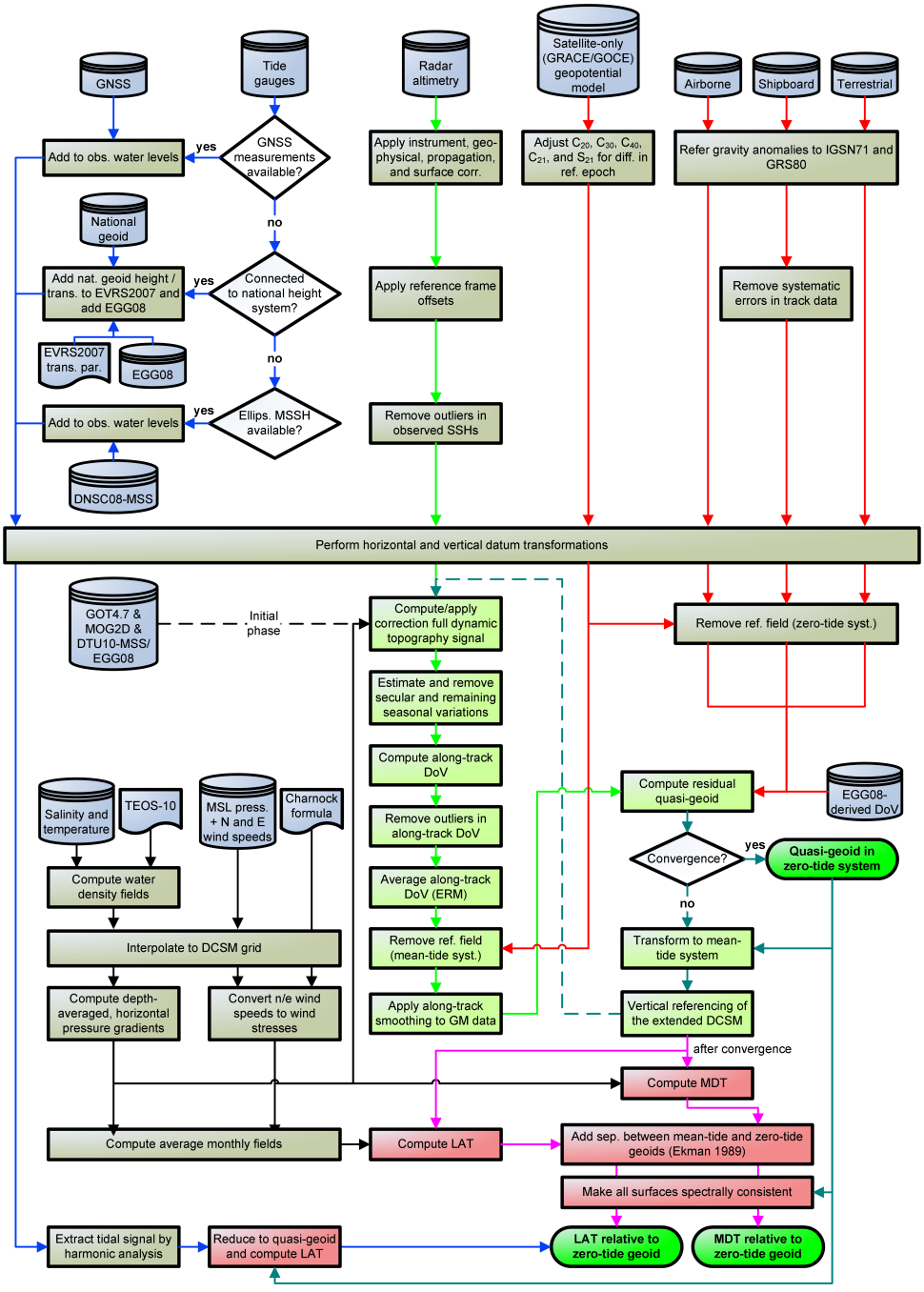
GNSS
Tide gauges
Radar altimetry
Satellite-only (GRACE/GOCE) geopotential model
Airborne
Shipboard
Terrestrial
Add to obs. water levels
yes
GNSS measurements available?
no
Apply instrument, geo-physical, propagation, and surface corr.
Adjust C_{20}, C_{30}, C_{40}, C_{21}, and S_{21} for diff. in ref. epoch
Refer gravity anomalies to IGSN71 and GRS80
National geoid
Add nat. geoid height / trans. to EVRS2007 and add EGG08
yes
Connected to national height system?
Apply reference frame offsets
Remove systematic errors in track data
EVRS2007 trans. par.
EGG08
no
Add to obs. water levels
yes
Ellips. MSSH available?
Remove outliers in observed SSHs
DNSC08-MSS
Perform horizontal and vertical datum transformations
GOT4.7 & MOG2D & DTU10-MSS/ EGG08
Initial phase
Compute/apply correction full dynamic topography signal
Remove ref. field (zero-tide syst.)
Estimate and remove secular and remaining seasonal variations
Compute along-track DoV
Salinity and temperature
TEOS-10
MSL press. + N and E wind speeds
Charnock formula
Remove outliers in along-track DoV
Compute residual quasi-geoid
EGG08-derived DoV
Convergence?
yes
Quasi-geoid in zero-tide system
Compute water density fields
Average along-track DoV (ERM)
no
Interpolate to DCSM grid
Remove ref. field (mean-tide syst.)
Transform to mean-tide system
Compute depth-averaged, horizontal pressure gradients
Convert n/e wind speeds to wind stresses
Apply along-track smoothing to GM data
Vertical referencing of the extended DCSM
after convergence
Compute MDT
Compute average monthly fields
Compute LAT
Add sep. between mean-tide and zero-tide geoids (Ekman 1989)
Make all surfaces spectrally consistent
Extract tidal signal by harmonic analysis
Reduce to quasi-geoid and compute LAT
LAT relative to zero-tide geoid
MDT relative to zero-tide geoid

Center in 2008 (DNSC08-MSS) (Andersen & Knudsen 2009). The preprocessing of the tide gauge data is concluded by extracting the astronomical tide signal from the observed water levels, which is realized by a harmonic analysis (see Eq. (5.1)).

Harmonizing the *airborne, shipboard, and terrestrial gravity data* (Sections 4.3.4, 4.3.3, and 4.3.2, respectively), furthermore involves harmonizing the gravity datums and, for shipboard gravity data in particular, a removal of systematic errors (Section 4.3.3.2). Note that, when specific information is missing, the gravity data are supposed to be in the zero-tide system. For the *satellite gravity data* (Section 4.3.1), we need to adjust the low-degree coefficients (C_{20}, C_{30}, C_{40}, C_{21}, and S_{21}) for secular variations introduced by differences in the reference epoch adopted in the estimation of the geopotential model and the one adopted in our study (January 1, 1999).

In those continental areas of the computational domain where we do not have terrestrial/airborne gravity data or which are characterized by strong variations in topography (note that we do not apply terrain corrections (Section 4.3.2)), we use *DoV in north and east direction derived from the EGG08 quasi-geoid* (Section 1.3.2). These data do not need any preprocessing.

Besides gravity data, *radar altimeter data* are used to estimate the quasi-geoid. The preprocessing of these data involves applying all instrument and propagation corrections (e.g., corrections for dry and wet troposphere refraction). In addition, we need to remove the geophysical corrections for solid earth tide, loading tide, and pole tide and the surface correction for the electromagnetic bias. Reference frame differences among the various altimeters are accounted for by applying reference frame offsets to the data, using TOPEX as reference. Finally, outliers in SSHs have to be removed.

The *meteorological forcing input* to DCSM comprises the (time-varying) mean sea level pressure and wind speed fields in north and east direction (Section 3.5.2). After interpolation to the DCSM model grid (GRS80 ellipsoid in the ETRS89 (Section 3.2)), the wind speeds need to be converted to wind stresses for which we make use of Charnock's relation (see Eq. (3.4)). For the computation of the LAT surface, we also need to compute the average monthly variations in mean sea level pressure and wind stress (Section 5.3.3). These variations represent the "average meteorological conditions" referred to in the definition of LAT (International Hydrographic Organization 2011*a*, Technical Resolution 3/1919).

The preprocessing of the 4D *salinity and temperature fields* (Section 3.5.3) starts with the computation of 4D water density fields for which we use the international thermodynamic equation of seawater 2010 (TEOS-10) (IOC, SCOR and IAPSO 2010). After interpolating the water densities to the DCSM model grid, we compute the associated pressure gradients for each depth layer and integrate over depth to obtain the depth-averaged horizontal pressure gradient fields (see Eq. (3.5)). Finally, the computation of the LAT surface requires average monthly fields to be computed (Section 5.3.3).

2.2 Step 2: iterative estimation of the quasi-geoid and vertical referencing of the hydrodynamic model

After preprocessing all data, the procedure continues with the iterative estimation of the quasi-geoid (see Chapter 4) and the subsequent vertical referencing of the *extended* DCSM model (Section 3.3 for the extension we made to the DCSM model). Here, vertical referencing refers to all steps needed to obtain a hydrodynamic model that provides instantaneous water levels relative to a (quasi-)geoid (Section 3.4).

First, the *full* dynamic topography signal needs to be removed from the altimeter SSHs (Section 4.3.5). In the initial run, these corrections are derived as the sum of the ocean tide (GOT4.7), dynamic atmosphere (MOG2D), and the time-averaged steric (difference between the DTU10-MSS mean sea surface and the EGG08 quasi-geoid) contributions. In all subsequent iterations, these corrections are replaced by instantaneous water levels relative to the estimated quasi-geoid of the previous iteration obtained from the extended and vertically referenced DCSM model.

Next, we estimate and remove secular and remaining seasonal variations in the radar altimeter sea level data (Section 4.3.5). In general, the secular variations induced by, e.g., eustatic and steric sea level changes, self-gravitation, and glacial isostatic adjustment, are not included in the modeled water levels. The remaining seasonal variations are mainly associated with the net steric expansion/contraction of the global oceans that cannot be represented by the extended DCSM model since it makes use of the Boussinesq approximation (Section 3.3). After removing these variations, we obtain "geometric" quasi-geoid heights up to some long-wavelength errors, which are likely dominated by radial orbit errors.

To suppress the long-wavelength errors, we compute the along-track derivatives of the obtained geometric quasi-geoid heights, i.e., the along-track deflections of the vertical (DoV) (see Eq. (4.54)). After removing the outliers, for the exact repeat mission (ERM) data we continue to compute the time-averaged along-track DoV. Next, we remove the reference quasi-geoid (in the mean-tide system) and apply to the geodetic mission GM data an along-track low-pass filter to suppress high-frequency noise (Section 4.3.5).

The quasi-geoid is estimated using the classical remove-compute-restore technique (RCR); the quasi-geoid is obtained by the sum of the global field contribution (spherical harmonic expansion of the satellite-only geopotential model) and the contribution of the residual gravity field (Section 4.2.1). The latter contribution is estimated from the residual terrestrial, shipboard, and airborne gravity data, the EGG08-derived DoV in north and east direction, and the altimeter-derived residual along-track DoV. The residual gravity field is parameterized using a linear representation of radial basis functions (Section 4.2.2).

In the initial run, we continue with the vertical referencing of the extended DCSM model, after which we start the first iteration. In all iterations, it will be evaluated whether the root mean square (rms) difference relative to the last solution is lower than a certain threshold. If not, the extended DCSM model will be vertically referenced to the latest quasi-geoid and a new iteration is started. Otherwise, the extended DCSM model will be vertically referenced to the latest quasi-geoid and the iteration stops.

2.3 Step 3: computation of vertical reference surfaces

In the final step of the procedure, we compute the LAT (Section 5.3.3) and MDT (Section 3.6.1) surfaces relative to the estimated quasi-geoid using the extended and vertically referenced DCSM model. The MDT at each model grid point is computed as the time-averaged modeled water level over the entire simulation period (1984–2004), where the model is forced by astronomical tides, atmospheric wind and pressure forcing, and baroclinic forcing.

The LAT at each model grid point is derived as the minimum water level over the entire time series of modeled water levels (1984–2004). Here, the time-varying wind stress and water density pressure gradient fields are replaced by their average monthly values. The model-derived LAT values are validated using LAT values at tide gauges. They are derived from the observed water levels as the minimum water level over the reconstructed astronomical tide signal, after reducing them to the estimated quasi-geoid.

Finally, the obtained surfaces are made spectrally consistent with the quasi-geoid, for which we will try the use of a Slepian basis representation (see Chapter 6).

Chapter 3

Vertical referencing of a shallow water hydrodynamic model

An earlier version of this chapter is published in Continental Shelf Research under the title "Obtaining instantaneous water levels relative to a geoid with a 2D storm surge model" (Slobbe et al. 2013a). In this chapter, we present an approach to obtain a 2D storm surge model that provides estimates of the instantaneous water level relative to a particular quasi-geoid (the European Gravimetric Geoid 2008 model (EGG08)), i.e., an approach to vertically reference a 2D storm surge model. Using different numerical experiments, we investigate the effects on the (mean) water levels of several approximations we made during the implementation. The ability of the model to reproduce both the mean dynamic topography (MDT) and instantaneous water levels is assessed by a comparison with the MDT derived from the Atlantic-European North West Shelf- Ocean Physics Hindcast, as well as with instantaneous water levels acquired by various radar altimeter satellites. Furthermore, the chapter includes an experiment where we assess the impact of quasi-geoid errors on the model-derived MDT, which in turn answers the question to which extent expected quasi-geoid improvements improve the model.

3.1 Introduction

In this chapter, we aim to obtain proper estimates of the instantaneous water levels in a uniquely defined 3D coordinate system (e.g., the European Terrestrial Reference System ETRS89 in combination with the GRS80 ellipsoid) from a 2D storm surge model. In the North Sea, characterized by strong tides and storm surges, such models are often used for real-time prediction of tides and surges. The models typically solve the depth-integrated shallow water equations, assuming that the water density

is uniform in both space and time (Heaps 1983, Engedahl 1995, Vested et al. 1995, Flather 2000). Ignoring this so-called baroclinic forcing is motivated by the fact that both the magnitude and temporal variability of the associated steric sea level changes in the North Sea are much lower than the dominant tide and surge signals. Hence, these variations are not relevant to short-term storm surge predictions, though some pragmatic approaches exist which attempt to account for them (see Section 3.3 for an example).

A further "limitation" is that storm surge models, usually, do not provide absolute water levels, i.e., water levels in a 3D coordinate system. Such water levels can be easily obtained as soon as the model's reference surface is uniquely described in a 3D coordinate system. Often, this surface is identified with the mean sea level (MSL) (e.g., Mouthaan et al. 1994, Heemink et al. 2002, Iliffe et al. 2007*b*, Dodd et al. 2010). MSL can be described in a 3D coordinate system by making use of radar altimeter data. However, while the dynamics of the models usually assume zero horizontal gravity components, this interpretation is strictly spoken not correct. Indeed, vanishing horizontal gravity components imply the model's vertical reference surface is an equipotential surface of the Earth's gravity field (a so-called geop). This has already been noticed by Hughes & Bingham (2008). Geops close to MSL (so-called geoids) are often used as natural reference surface for onshore height systems, see Hofmann-Wellenhof & Moritz (2005) for a thorough introduction or Meyer et al. (2006) for a brief summary. Like the MSL, a geoid is an observable reference surface that can be uniquely described in a 3D coordinate system. Since both the model's reference surface and a geoid are geops, the most natural way to obtain a model that provides absolute water levels is when the model is adjusted such that its reference surface can be identified with a geoid.

Until now, one dealt with this issue in a pragmatic way if properly referenced water levels are required. For example, to assess the predicted height of the water level induced by a predicted storm surge to decide whether or not storm surge barriers need to be closed, absolute water levels relative with respect to the onshore height system reference surface are necessary. These are obtained by adding, at the locations of nearby tide gauges, the predicted surge to the tide predicted by a harmonic synthesis using tidal constituents, including the zero-frequency one, estimated from observed water levels that refer to the onshore height system. Here, the predicted surge is computed as the difference between two model runs with as driving forces (i) astronomical tide and meteorology (wind and mean sea level pressure variations) and (ii) astronomical tide. Indeed, since the constituents are estimated from observed water levels (that contain the sum of all effects including steric), the estimated zero-frequency constituent represents the total MSL expressed relative to the vertical reference surface of the observed water levels. Moreover, this approach even accounts for a part of the time-varying steric sea level changes, since this variability has energy at the same frequencies of some tidal constituents used in the harmonic analysis.

Although such pragmatic approaches to account for steric water level variations and to obtain absolute water levels suffice for storm surge applications, they are not adequate or accurate enough for some applications in coastal engineering, hydrography, and geodesy. For example, one major drawback of the above described workaround to obtain absolute water levels is that it can only be applied at those tide gauge stations whose benchmarks are fixed in a 3D coordinate system. For some applications this is not sufficient; they need estimates of the instantaneous water levels expressed relative to a well-defined (quasi-)geoid everywhere. Of course, other workarounds can be found (see below for one example), but from a conceptual point of view this is not satisfactory. It is much clearer if any workaround can be avoided and the definition of the model's vertical datum becomes an intrinsic feature of the model itself. Moreover, avoiding workarounds is needed to satisfy the higher and ever increasing accuracy requirements. The following examples of applications require sub-decimeter accuracy for instantaneous and mean water levels.

One hydrographic application, thoroughly treated in Chapter 5, is the derivation of the separation between the chart datum (CD) and a reference ellipsoid in coastal waters and estuaries. In deep water, the ellipsoidal heights of CD are obtained by adding to the ellipsoidal heights of MSL the separation between MSL and CD derived from a global ocean tide model. Along the coast and in estuaries, however, no ellipsoidal heights of MSL are available due to a lack of reliable radar data. Since the (quasi-) geoid is globally defined, the most straightforward approach to obtain the ellipsoidal heights of CD is by "modeling" CD directly relative to the (quasi-)geoid and add this separation to the (quasi-)geoid heights. In Chapter 5, it is also shown that in the North Sea the low water levels frequently deviate from the adopted CD. As suggested by technical resolution 3/1919 of the International Hydrographic Organization (IHO) (International Hydrographic Organization 2011*a*), in such a case another surface might be used as CD. In Chapter 5, a CD is proposed that is defined as a level which is exceeded with a prescribed probability. To compute the ellipsoidal heights of this surface, a model is required that provides instantaneous water levels expressed relative to a (quasi-)geoid. Another application, relevant to a broader community, is to reference water levels at offshore locations properly. Currently, these water levels refer to MSL, which is realized by adjusting them to the mean computed over the measurement period. This period, however, needs to be sufficiently long before the initial mean can be computed and the data can be used. Furthermore, while only by averaging over longer time spans the mean gets closer to the actual MSL, the datum is commonly recalculated over time, resulting in discontinuities in the time series. By using a properly referenced model that includes steric effects, the water levels can be expressed relative to the (quasi-)geoid from the first measurement day.

To a first approximation, instantaneous water levels relative to a particular (quasi-) geoid can be obtained in a post-processing step by adding to the modeled water levels the time-averaged steric water levels expressed relative to that (quasi-)geoid (the

dominant time-variable steric water level variations can be added using conventional workarounds (Section 3.3)). This contribution needs to be derived from an ocean circulation model (hydrodynamic model developed to simulate the large scale movements of waters (spatial scales of 50–500 km, time scales of 10–100 days)) whose model domain comprises that of the 2D storm surge model being used (it cannot be derived from radar altimeter data as no reliable radar data are available in coastal zones and estuaries). However, irrespective of whether observations or a model are used, the main problem is that all contributions to the MDT other than steric (mainly astronomical tide and the contribution induced by atmospheric wind and pressure forcing) need to be excluded. This is straightforward as long as the contributions of the astronomical tide and the atmospheric wind and pressure forcing, on the one hand, and the steric contribution, on the other hand, are linearly additive. However, this is not the case. Anyway, unless we have access to the model used to derive the full MDT, we cannot obtain the contributions induced by tide and atmospheric wind and pressure forcing only. Deriving them using our 2D storm surge model reduces to a replacement of its mean water levels by those obtained from the ocean circulation model. As a consequence, any contribution of the 2D storm surge model to an improved representation of the MDT is ignored, which is undesirable. Besides that, another important disadvantage of this approach is that the steric contribution is assumed to be static. This means not only that the modeled water levels lack the time-varying contribution of the water density gradients, but also that the modeled water levels become dependent on the time span used to compute the time-mean steric water levels.

In this chapter, we present an alternative approach to obtain a 2D storm surge model that provides estimates of the instantaneous water level relative to a particular (quasi-) geoid. Essentially, the approach involves two steps. First, we explicitly add to the model the baroclinic forcing by adding the depth-averaged baroclinic pressure gradient terms as diagnostic variables. They are computed from 4D temperature and salinity fields obtained from a 3D hydrodynamic model. Second, we adjust the model parameters that depend on the choice of the reference surface (e.g., bathymetry) and also refer the water levels along the open sea boundaries to the (quasi-)geoid. The most attractive aspect of this approach is that, in a relatively simple manner, more physics is added to the model so that the model becomes conceptually clearer and workarounds can be avoided. This will, among others, increase the transparency if observed water levels are assimilated into the model. Indeed, no additional corrections are needed to exclude a part of the observed signals in an attempt to make the observed water levels consistent with the modeled ones. Also the interoperability of modeled water levels will be improved. This is useful, e.g., in flood studies where water level simulations are integrated with digital elevation models that usually refer to the (quasi-)geoid, or in support of off-shore works and shipping, since the provided forecasts can be properly transformed to any height that is needed (e.g., ellipsoidal

heights). Besides a description of the applied procedure, this chapter investigates the effect on the modeled water levels of several approximations we make during the implementation. The procedure is described for the Dutch Continental Shelf Model version 5 (DCSM). This is a 2D storm surge model used operationally at the Royal Netherlands Meteorological Institute KNMI (De Vries 2011) to predict the water levels along the Dutch coast.

In this chapter, we first introduce the DCSM. Second, we describe the extension of this model to account for the horizontal variations in water density. Following this, we address the issue of how to define the model's vertical datum. Next, we describe the data sets used in our numerical experiments, which were designed to investigate the ability of the referenced model to represent the MSL and instantaneous water levels. Thereafter, we present and discuss the results of the numerical experiments. Finally, we provide a brief summary of the work that has been done and we conclude by emphasizing the main findings.

3.2 The Dutch Continental Shelf Model

The numerical model used in this study is the Dutch Continental Shelf Model version 5 (DCSM) described by Gerritsen et al. (1995) and Verlaan et al. (2005). It was developed to make tide and surge forecasts over the full tidal cycle to support the operational management of the Eastern Scheldt storm surge barrier. The model is based on the WAQUA software package (Leendertse 1967, Stelling 1984) for depth-integrated flow. WAQUA includes the non-linear surge-tide interaction and is based on the depth-integrated shallow water equations. DCSM covers the area of the north-west European continental shelf to at least the 200 m depth contour, i.e., 12°W to 13°E and 48°N to 62.3°N, and has a horizontal resolution of $1/8^\circ \times 1/12^\circ$ (approximately 8×9 km) in east-west and north-south directions, respectively. For a graphical outline of the model domain we refer to Fig. 1.1a.

To obtain a unique solution of the depth-integrated shallow water equations, a set of boundary conditions is prescribed. Through *closed* boundaries, where neither inflow nor outflow can occur, the flow velocity normal to the boundary is set equal to zero. At the *open* sea boundaries, water levels are prescribed as discussed in detail in Section 3.4. Note that if water enters the model domain, prescription of water levels is supplemented by the condition that the velocity parallel to the open sea boundary is zero.

Although spherical coordinates are used to solve the equations, during the development of the model the horizontal coordinates were assumed to be ellipsoidal latitude and longitude referring to the GRS80 ellipsoid (Moritz 2000) in the European Terrestrial Reference System 1989 (ETRS89). This implies that all features of the model,

e.g., coastlines, openings, and bathymetry, are expressed in ellipsoidal geographic coordinates, which in turn are treated as spherical geographic coordinates. In addition, distances between the model grid points are computed on the surface of a sphere rather than on the surface of the ellipsoid. The errors introduced in this way are negligible compared to the model uncertainties (H. Gerritsen, personal communication, 2012). To remain consistent, we assume that the model output is geo-referenced in ellipsoidal geographic coordinates as well.

To limit the propagation of uncertainty of the used model parameters and parameterizations to the model output, extensive calibrations of the model have been carried out; both by off- and on-line data assimilation of observed water levels (Verboom et al. 1992, Mouthaan et al. 1994, Gerritsen et al. 1995, Philippart et al. 1998). Here, by changing the bathymetry, bottom friction coefficients, open boundary conditions, and the Charnock coefficient the differences between modeled and observed water levels over a certain time period are minimized. The length of this period varies for the different calibrations that have been conducted. For instance, Philippart et al. (1998) used a period of 2.5 months.

Note that the internal tide generation can be neglected, because the model domain mainly consists of shelf seas.

3.3 The extension of the Dutch Continental Shelf Model

In the original model formulation, the water density was assumed to be uniform. One only accounts for the seasonal variations by including a seasonal term in the formulation of the water levels prescribed at the open sea boundaries, about which more is to follow in Section 3.4. The amplitude and phase of these seasonal terms are calibrated such that the model properly reproduces the spatially averaged remaining seasonal variations in the water level, i.e., the signal not captured by seasonal mean sea level pressure/wind variations. Obviously, it cannot be expected that such a pragmatic approach fully accounts for a missing forcing term; the time-mean contribution is not included at all, while also the inter- and intra-annual variations are ignored (although the latter can be accounted for by repeating the calibration from time to time, at least approximately).

In this study, the baroclinic forcing is explicitly added to the model. This is realized by treating the water density as a diagnostic variable computed from temperature and salinity values derived from a 3D hydrodynamic model using the international thermodynamic equation of seawater 2010 (TEOS-10) (IOC, SCOR and IAPSO 2010). The reason why we treat the water density as a diagnostic variable is that in the North Sea the horizontal variations in water density induce a 3D flow structure that cannot be handled by a 2D shallow water model. In the extended model equations, this

contribution shows up as the depth-averaged baroclinic pressure gradient terms in x (east-west) and y (north-south) directions; Γ_x and Γ_y, respectively. Following the Boussinesq hypothesis the influence of variable density appears only in these terms, while in the other terms a constant reference density ρ_0 is assumed. In Cartesian coordinates, used here for simplicity, the three model equations become

$$\frac{\partial \zeta}{\partial t} + \frac{\partial Hu}{\partial x} + \frac{\partial Hv}{\partial y} = 0, \tag{3.1}$$

$$\frac{\partial u}{\partial t} + u\frac{\partial u}{\partial x} + v\frac{\partial u}{\partial y} - fv + g\frac{\partial \zeta}{\partial x} + gu\frac{\sqrt{u^2+v^2}}{C^2 H} = \frac{\tau_x}{\rho_0 H} - \frac{1}{\rho_0}\frac{\partial P}{\partial x} - \Gamma_x, \tag{3.2}$$

$$\frac{\partial v}{\partial t} + u\frac{\partial v}{\partial x} + v\frac{\partial v}{\partial y} + fu + g\frac{\partial \zeta}{\partial y} + gv\frac{\sqrt{u^2+v^2}}{C^2 H} = \frac{\tau_y}{\rho_0 H} - \frac{1}{\rho_0}\frac{\partial P}{\partial y} - \Gamma_y, \tag{3.3}$$

where τ_x and τ_y are

$$\tau_x = \rho_a C_d W_x \sqrt{W_x^2 + W_y^2}, \quad \tau_y = \rho_a C_d W_y \sqrt{W_x^2 + W_y^2}, \tag{3.4}$$

and represent the wind stresses in x (east-west) and y (north-south) directions, respectively. Γ_x and Γ_y are defined as

$$\begin{aligned}
\Gamma_x &= \sum_{l=1}^{L} \frac{h_l}{d}\left(\frac{g}{\rho_l}\left\{\frac{h_l}{2}\frac{\partial \rho_l}{\partial x} + \sum_{j=1}^{l-1}\left(h_j\frac{\partial \rho_j}{\partial x} + (\rho_j - \rho_l)\frac{\partial h_j}{\partial x}\right)\right\}\right), \\
\Gamma_y &= \sum_{l=1}^{L} \frac{h_l}{d}\left(\frac{g}{\rho_l}\left\{\frac{h_l}{2}\frac{\partial \rho_l}{\partial y} + \sum_{j=1}^{l-1}\left(h_j\frac{\partial \rho_j}{\partial y} + (\rho_j - \rho_l)\frac{\partial h_j}{\partial y}\right)\right\}\right).
\end{aligned} \tag{3.5}$$

The description of the other variables is provided in the list below.

x, y	Cartesian coordinates in horizontal plane
u, v	depth-averaged currents in x, y direction
t	time
R	Earth radius (6371 km)
ζ	water elevation above reference surface
d	depth below reference surface
H	total water depth ($d + \zeta$)
g	gravity acceleration (9.813 m/s^2)
C	Chézy bottom friction coefficient
f	parameter of Coriolis
W_x, W_y	10 m wind velocity components in x, y direction
C_d	wind drag coefficient
ρ_a	density of air (1.205 kg/m^3)
ρ_0	constant reference density of water (1023 kg/m^3)

P	surface atmospheric pressure
L	number of depth layers in 3D model from which temperature and salinity fields are derived
j, l	layer indices
h_j, h_l	thickness of layers j and l
ρ_j, ρ_l	mean water density of layers j and l

Since the model currently only features a static depth-averaged baroclinic pressure field, the baroclinic forcing is added to the model as if it was wind forcing. This can be done by converting the depth-averaged baroclinic pressure gradients to "pseudo-wind stresses" using Eq. (3.4) after replacing W_x and W_y by Γ_x and Γ_y, respectively. Then we scale these "pseudo-wind stresses" by $\rho_0 d$ and add them to the actual wind stresses. The scaling by $\rho_0 d$ is needed to account for the fact that in the model equations the wind stresses are divided by $\rho_0 H$. The errors in ζ introduced by using d rather than H appear to be on the order of sub-millimeters and hence are negligible.

It should be noted that models that make use of the Boussinesq approximation (as most models do), and therefore conserve volume and not mass, can never represent the steric effect properly (Greatbatch 1994). In a global model, at least two contributions are lacking: a contribution mainly attributed to the so-called Goldsbrough Stommel gyres that is unknown and ignored as a small error and a spatially uniform but time-varying contribution that accounts for the net expansion/contraction of the global oceans. Mellor & Ezer (1995) showed that in case of a regional model there is an additional contribution that accounts for either the Boussinesq or non-Boussinesq transport through the open boundaries of the model. Practically, the correction for the net expansion/contraction can be treated in the water levels prescribed at the open boundaries. The approach followed in this chapter will be discussed in Section 3.4.3.

Note that in the model the gravity acceleration (g) is treated as a constant value, although in reality it varies with location (mainly due to the Earth's meridional flattening). Hughes & Bingham (2008) pointed out that the effect of the meridional flattening gives rise to errors in water levels of about 0.5%. Hence, we conclude that for the domain of the DCSM model the errors introduced by using this assumption are negligible as well.

3.4 Vertical referencing of the DCSM

To ensure that water levels of the extended DCSM model refers to the quasi-geoid, we need to (i) express the bathymetry used in the model relative with respect to the quasi-geoid and (ii) prescribe water levels along the open sea boundaries referring to the quasi-geoid. The two steps are referred to as "vertical referencing" of DSCM. Note that the latter of the two steps can be unambiguously realized only if all of

the relevant physics is included. Furthermore, it should be noted that in principle also the water levels within the model's domain at initial epoch should be referenced, but in our model setup the influence of the initial water levels on the water levels at later epochs vanishes after a few days of spin-up and, therefore, this step is skipped. Moreover, for models that do include special hydrodynamic features such as barriers, weirs, and sluices (not included in DCSM), also the overflow-heights need to be expressed relative to the quasi-geoid.

In the past, bathymetry was interpreted as given relative with respect to MSL. Hence, referring bathymetric data to the quasi-geoid reduces to apply a correction for the separation between MSL and the quasi-geoid (i.e., the MDT). For DCSM this is not possible because the original bathymetric data set is no longer available, only the adjusted bathymetry obtained after applying subsequent model calibrations (Section 3.2). Moreover, even if it was available, after applying the reduction we would need to recalibrate DCSM again, which is a very elaborate procedure and out of the scope of this study. By still applying the reduction from MSL to the quasi-geoid to the current bathymetry we can, however, get an idea of the impact of such a correction on the modeled water levels (see Experiment III in Section 3.6.3).

Direct observations of the instantaneous water level in the neighborhood of the open sea boundaries are provided by radar altimetry. However, the spatial-temporal resolution of radar altimetry is not sufficient to derive the open boundary conditions entirely. Alternatively, the water levels along the open sea boundaries can be derived from a larger hydrodynamic model that includes all the required contributions in the modeled water levels, i.e., astronomical tide, surge, and steric effects. Although embedding DCSM into such a model is foreseen in the future, this is not implemented yet. Hence, we still use the current approach where the open boundary conditions are derived as the sum of the separate contributions that make up the full instantaneous water levels expressed relative to the quasi-geoid: the astronomical tide (ζ_a), surge (ζ_u), and steric height (ζ_s). In the following, we discuss how these three contributors are quantified for DCSM. In particular, we discuss how the steric contribution has been computed along the open sea boundaries.

3.4.1 Astronomical tide

ζ_a is derived by a harmonic expansion using 12 constituents, namely M_2, S_2, N_2, K_2, O_1, K_1, Q_1, P_1, NU_2, L_2, Mf, and Mm

$$\zeta_a(\vartheta,\lambda,t) = \sum_{i=1}^{12} f_i H_i \cos(\omega_i t + (V_0+u)_i - G_i), \tag{3.6}$$

where ϑ is the latitude, λ is the longitude, $f_i H_i$, ω_i, and G_i are the amplitude, angular velocity, and phase of harmonic constituent i, respectively, and $(V_0+u)_i$ links the

local time basis to the orbital positions of the Sun, Moon, and Earth. Except for *Mf* and *Mm*, the amplitudes and phases of the other constituents are the same as used in the operational version of DCSM. These were originally derived from a global ocean tide model, but modified during the subsequent tidal model calibrations. The amplitudes and phases of the lunar fortnightly *Mf* and lunar monthly *Mm* are taken from the FES2004 tidal atlas solution (Lyard et al. 2006). The 18.6 year nodal tide cycle is approximated by the nodal coefficients $f_i(t)$ and $u_i(t)$. The remaining long-period constituents, e.g., the solar annual (*SA*), the solar semi-annual (*Ssa*), and the 14-month pole tide, are believed to be negligible (H. Gerritsen, personal communication, 2012).

3.4.2 Surge

Water level variations induced by atmospheric wind and pressure forcing (ζ_{u}) are approximated by the inverted barometer (IB) equation given as (Wunsch & Stammer 1997)

$$\zeta_{\mathrm{u}}(\vartheta,\lambda,t) = -\frac{1}{\rho_0 g}\left(P(\vartheta,\lambda,t) - \bar{P}_{\Omega_o}(t)\right), \tag{3.7}$$

where $\bar{P}_{\Omega_o}(t)$ is the spatial average of $P(\vartheta,\lambda,t)$ over the global oceans Ω_o at epoch t.

In many studies, time dependencies in $\bar{P}_{\Omega_o}(t)$ are neglected (e.g., De Vries et al. 1995, Heemink et al. 2002) and $\bar{P}_{\Omega_o}(t)$ is replaced by the global mean pressure $\bar{P}_{\Omega}$. Then, however, one needs to correct for the bias in the modeled water levels introduced by the fact that the time-mean spatially averaged pressure over the global oceans is not equal to the global mean pressure $\bar{P}_{\Omega}$.

3.4.3 Steric heights

In this study, we consider two possibilities of how to compute the steric contribution to instantaneous water levels along the open sea boundaries of DCSM: (i) we use available monthly mean water levels from a larger ocean circulation model, with a domain that comprises the model domain of DCSM and subtract the astronomical tide and the surge components; (ii) we interpolate in space and time instantaneous water level observations provided by radar altimeter satellites after subtracting the astronomical tide and the surge components (see Section 3.5.4 for more details).

If the first approach is used, we need to account for a different vertical reference of the larger ocean circulation model compared to the one we aim at, i.e., the used ocean circulation model needs to be vertically referenced as well. While usually the vertical datum of the model is unknown, the only feasible way to obtain the datum shift $\delta W_{\mathrm{G,P}}$ between the quasi-geoid and the model's equipotential reference surface is by comparing observed and modeled water levels. In absence of errors, $\delta W_{\mathrm{G,P}}$

can be obtained by comparing the observed and modeled water levels at a particular location for a certain epoch. Obviously, however, there will be errors and the question is how to limit their impact in the computation of $\delta W_{\mathrm{G,P}}$. In this study, we applied four measures:

1. We use the time-averaged water levels (MDT) rather than the water levels at one particular epoch.
2. $\delta W_{\mathrm{G,P}}$ is computed as a spatially integrated difference rather than using the water levels at one particular location.
3. To suppress high-frequency noise in both the observation- and model-derived MDT's, the MDT's are smoothed with a Gaussian filter ($\mathscr{W}^G$).
4. Regions prone to errors both in the observation- and model-derived MDT's (coastal regions and regions along the open boundaries of the used ocean circulation model) are excluded.

So, the equation used to compute $\delta W_{\mathrm{G,P}}$ is

$$\delta W_{\mathrm{G,P}} = \frac{1}{\Omega_{\delta W}} \iint\limits_{\Omega_{\delta W}} \mathscr{W}^G(\psi) \left(\overline{\zeta_{\mathrm{O}}}(\vartheta,\lambda) - \overline{\zeta_{\mathrm{M}}}(\vartheta,\lambda) \right) d\Omega, \tag{3.8}$$

where $\Omega_{\delta W}$ is the actual region used to compute $\delta W_{\mathrm{G,P}}$, ψ is the distance between the computation point and the data point, and $\overline{\zeta_{\mathrm{O}}}$ and $\overline{\zeta_{\mathrm{M}}}$ are the observation- and model-derived MDT, respectively. It should be noted that the reference epoch of the observation-derived MDT should correspond to that of the model-derived one. The reason is that the radar altimeter data used to derive the observation-derived MDT include the spatially varying secular changes due to e.g., melting of the ice sheets. Hence, any discrepancy between the reference epochs causes spatially varying differences between the observation- and model-derived MDT that contribute to $\delta W_{\mathrm{G,P}}$.

In addition, we need to account for the fact that the steric contribution to the instantaneous water levels derived from an ocean circulation model, in general, is not the full steric signal. Indeed, since most ocean circulation models make use of the Boussinesq approximation, the net steric expansion/contraction of the global oceans is lacking. If we use observed water levels (e.g., from radar altimeter data) to validate DCSM's output, we need to add this correction to the observed water levels before the validation is done. Note that for the approach (ii) such a correction is not needed; the net expansion/contraction signal is contained in the observed water levels used to derive the steric contribution and hence becomes a part of the water levels prescribed at the open sea boundaries. The corrections ($\delta_{\zeta_{\mathrm{s}}}$) are computed using (Bouffard et al. 2008)

$$\delta_{\zeta_{\mathrm{s}}}(t) = \frac{1}{\Omega_{\mathrm{D}}} \iint\limits_{\Omega_{\mathrm{D}}} \left(\zeta_{\tilde{\mathrm{s}}}(\vartheta,\lambda,t) - \overline{\zeta_{\tilde{\mathrm{s}}}(\vartheta,\lambda)} \right) d\Omega, \tag{3.9}$$

where Ω_{D} is DCSM's model domain and $\zeta_{\mathrm{s}}(\vartheta,\lambda,t)$ and $\overline{\zeta_{\mathrm{s}}(\vartheta,\lambda)}$ the steric height and its time average, estimated by integrating the density anomalies, computed from the salinity (S) and temperature (T), over the whole water column (Tomczak & Stuart 1994):

$$\zeta_{\mathrm{s}}(\vartheta,\lambda,t) = \int_{-d}^{0} \frac{\rho(\vartheta,\lambda,z,35,0) - \rho(\vartheta,\lambda,z,t,S,T)}{\rho(\vartheta,\lambda,z,35,0)}\, dz, \tag{3.10}$$

with $\rho(\vartheta,\lambda,z,35,0)$ is the water density at the standard salinity $S = 35.0$ and temperature $T = 0°\mathrm{C}$.

3.5 Experimental setup

To demonstrate the vertical referencing procedure developed in this study, we referenced the extended DCSM model to the European Gravimetric Geoid 2008 model (EGG08) (Denker et al. 2008), which is the state-of-the-art quasi-geoid model for Europe. In this section, we briefly introduce the data sets used, and the applied preprocessing required to carry out the experiments presented in Section 3.6.

3.5.1 The European Gravimetric Geoid 2008 (EGG08)

The EGG08, briefly introduced in Section 1.3.2, is a zero-tide quasi-geoid model. This means that the potential value assigned to the quasi-geoid does not include the tide-generating potential but still includes the potential of the permanent deformation of the Earth due to the tides (e.g., Ekman 1989, Hughes & Bingham 2008, Mäkinen & Ihde 2008). While the tide generating forces in the hydrodynamic model do not include any contribution at the zero frequency, the quasi-geoid must be expressed in the mean-tide system for consistency. This implies that the time-averaged tide-generating potential has to be restored, for which we use the approximation given by Ekman (1989)

$$N_m = N_z + 9.9 - 29.6 \sin^2 B \ [\mathrm{cm}], \tag{3.11}$$

where B is the ellipsoidal geographic latitude and N_m and N_z are the quasi-geoid heights in the mean- and zero-tide system, respectively.

3.5.2 Wind and mean sea level pressure

For operational storm surge forecasting, DCSM uses forecasts of the wind and air pressure fields provided by the meteorological high-resolution limited area model (HiRLAM) (Cats & Wolters 1996). HiRLAM has a spatial resolution of 5–15 km. Unfortunately, we cannot make use of these data as our simulation period is January

1, 2000 to January 1, 2003, while the HiRLAM data are not continuously available prior to 2007. Hence, we need to derive the wind and air pressure data from other sources. In this study, we use the publicly available data of the interim reanalysis project ERA-Interim provided by the European Centre for Medium-Range Weather Forecasts (ECMWF). ERA-Interim covers the period from January 1, 1979 onwards and provides three-hourly grids with a spatial resolution of $1.5^\circ \times 1.5^\circ$. The data are available from the ECMWF data server. For a description of the model, the data assimilation method, and the input data sets used in ERA-Interim, we refer to Dee et al. (2011).

The wind and air pressure fields are interpolated to the DCSM grid using the Generic Mapping Tools (GMT) `greenspline` routine (Wessel 2009) with a tension factor of 0. To account for the differences between on- and offshore wind regimes, we only use the grid cells that are flagged as sea in the ERA-Interim land/sea mask.

3.5.3 Monthly mean salinity, temperature, and water levels

Salinity and temperature fields used in computing the depth-averaged baroclinic pressure gradients are obtained from the Atlantic — European North West Shelf — Ocean Physics Hindcast provided by the Proudman Oceanographic Laboratory (POL), hereafter referred to as POL's hindcast (Holt et al. 2005). This hindcast over 45 years (1960–2004) was carried out with a coupled hydrodynamic-ecosystem model. The hydrodynamics are provided by the POL 3D baroclinic model (POL3DB) (Holt & James 2001, Holt et al. 2001), which is part of the POL Coastal Ocean Modeling System. The model fully covers the northwest European continental shelf; its domain ranges from 20°W to 13°E and 40°N to 65°N. The horizontal resolution is comparable to that of DCSM; $1/6^\circ \times 1/9^\circ$ in east-west and north-south directions, respectively. The model has 42 terrain-following coordinate levels in the vertical. The output, provided as monthly mean fields, include the sea surface height, potential temperature, and salinity of the sea water. All products are interpolated onto 24 standard vertical levels distributed over the range of 0 to 5000 m such that the resolution decreases with increasing depth. In the remainder of this chapter, we refer to these products by, e.g., POL's monthly mean water levels.

Since the model does not include the formation of sea ice, water temperatures below zero degrees Celsius have been masked out. Hence, for these grid points, no water density can be computed. Since this only affects the upper layers and occurs in small subregions of the model domain, the empty values are filled using the non-empty grid points of the same depth level during the interpolation to the DCSM grid. This interpolation is performed using GMT's `surface` routine (Wessel & Smith 1995) with the default tension factor. As discussed in Section 3.3, the depth-averaged pressure gradients induced by the spatial variations in water density are converted into

"pseudo-wind stresses" and added to the actual wind stress fields. Since the latter are updated every three hours, we interpolate the monthly fields to three-hourly values using a cubic spline interpolation, for which we assign the monthly means to the mid-epochs of each month.

The steric contribution to the instantaneous water levels along the open sea boundaries is derived after subtracting the monthly mean water levels induced by astronomical tide and meteorological forcing from POL's monthly mean water levels. Note that this steric contribution does not include the net expansion/contraction of the oceans since the POL3DB model makes use of the Boussinesq hypothesis. Ideally, the astronomical tide and meteorological forcing contributions have to be derived using the POL3DB model as well. However, while we do not have access to this model to run it, we subtracted the monthly mean astronomical tide and IB correction computed using Eqs. (3.6)–(3.7). As discussed in Section 3.1, this implies that "our" monthly mean water levels at the open sea boundaries are replaced by those from POL. To reference these water levels to EGG08, we add the datum shift ($\delta W_{\mathrm{G,P}}$) between EGG08 and the zero water level surface of POL3DB that is empirically derived using the approach outlined in Section 3.4.3 (see Eq. (3.8)). Here, $\overline{\zeta_{\mathrm{O}}}$ is the DNSC08 mean sea surface (DNSC08-MSS) not corrected for the inverted barometer effect (Andersen & Knudsen 2009) expressed relative to EGG08, and $\overline{\zeta_{\mathrm{P}}}$ is the MDT derived from POL's monthly mean water levels computed over the same time span as DNSC08-MSS (1993–2004). The reference epoch of DNSC08-MSS is January 1, 1999, i.e., the mid-epoch of the time span over which the mean sea surface is computed. For the filter operation applied to suppress possible noise in $\overline{\zeta_{\mathrm{O}}}$ and $\overline{\zeta_{\mathrm{P}}}$, we use a Gaussian filter with a half-width of 29.4 km. This is about three times the half-wavelength data resolution. Here, the actual choice of the filter half-width hardly affects the computed datum shift; doubling the half-width decreases $\delta W_{\mathrm{G,P}}$ by only 1.2 mm. Fig. 3.1 shows a geographical map of the smoothed differences. Since the MDT signal is not defined on land, this filter operation fails in coastal regions and hence all grid points closer than 150 km from the coastline were excluded from the computation of $\delta W_{\mathrm{G,P}}$. In this way, we also eliminate remaining errors in the coastal region in both $\overline{\zeta_{\mathrm{O}}}$ and $\overline{\zeta_{\mathrm{P}}}$. Furthermore, we excluded those grid points that were within 3° from the open boundaries of the POL3DB model. We refer to Fig. 3.1 for an outline of the regions used to compute $\delta W_{\mathrm{G,P}}$ ($\Omega_{\delta W}$). We can neglect the spatial variability of gravity over $\Omega_{\delta W}$ and obtain for the datum difference $\delta W_{\mathrm{G,P}}$ a value of 3.837 $\mathrm{m^2/s^2}$, which is equivalent to 0.391 in metric units.

3.5.4 Radar altimeter data

Radar altimeter data are used to derive time series of the steric heights at the open boundaries, as well as to validate the modeled water levels obtained with the extended, vertically referenced DCSM model. The data acquired by the ERS-2, Envisat,

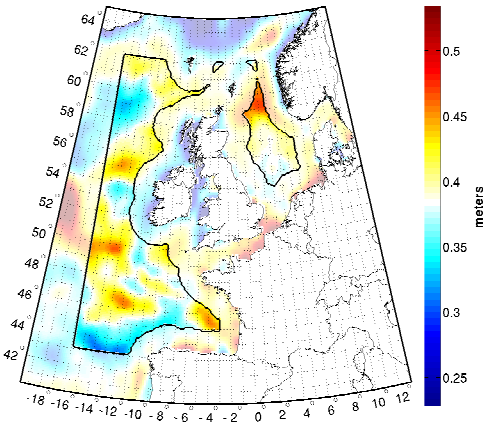

Figure 3.1: Differences between the smoothed DNSC08-MSS not corrected for the inverted barometer effect expressed relative to EGG08 and the smoothed MDT derived from POL's monthly mean modeled water levels over the same time span for which DNSC08-MSS is computed (1993–2004). The data inside the regions bounded by the thick black line are used to compute $\delta W_{\mathrm{G,P}}$.

GFO-1, Jason-1, and TOPEX/POSEIDON (T/P) satellites are taken from the Radar Altimeter Database System (Scharroo 2013). Table 3.1 shows the main characteristics of those missions together with an overview of the used orbits and background models used to compute the ellipsoidal heights of the instantaneous sea surface. They are computed by correcting the observed sea surface heights (SSHs) for dry and wet tropospheric refraction, ionospheric refraction, and the sea state bias. In addition, we applied corrections for solid earth tide, loading tide, and pole tide, since none of these signals are included in WAQUA. Reference frame differences among the various altimeters are accounted for by applying reference frame offsets to the data using TOPEX as reference (see Andersen & Scharroo (2011) for details about the computation).

Outliers in the observed SSHs are removed using the iterative procedure described in Hwang & Hsu (2008). Smoothing of the along-track height differences with a 1D Gaussian filter using a filter half-width of 5.5 km is repeated until the largest residual between observed and smoothed height differences is smaller than three times the residual standard deviation. Errors in the water levels derived from radar altimeter data are caused by measurement noise and systematic errors introduced by mismodeling in all applied corrections. Moreover, secular changes in sea level due to, e.g., eustatic and steric sea level changes, self gravitation, and glacial isostatic adjustment also contribute to the error budget. In general, they are not included in the modeled water levels (Boussinesq approximation!) unless they are explicitly added to the open boundary conditions. Here, we remove the secular changes by detrending the observed water levels. We estimate a trend in observed water levels per grid point from T/P, Jason-1, and Jason-2 data over the entire measurement period (1992–2011). The corrections are centered at the mid-epoch of the period over which the observation- and model-derived MDT are computed when deriving the datum shift ($\delta W_{\mathrm{G,P}}$), i.e., the reference epoch of DNSC08-MSS.

Table 3.1: Main characteristics of the radar altimeter missions from which data are used in this study together with an overview of the orbits and background models used to compute the ellipsoidal heights of the instantaneous sea surface and an overview of the number of data points derived over the whole DCSM domain (Ω_D) and North Sea (Ω_{NS}) only. Note that the data of the Envisat and ERS-2 missions, as well as the data of the Jason-1 and T/P missions, are combined.

	Envisat	ERS-2	GFO-1	Jason-1	POSEIDON	TOPEX
ID	n1	e2	g1	j1	pn	tx
Start	9/2002	4/1995	1/2000	1/2002	10/1992	10/1992
End	4/2012	7/2011	9/2008	7/2013	1/2006	1/2006
Inclination	98.5°	98.5°	108°	66°	66°	66°
Cycle [days]	35	35	17	10	10	10
Orbit	EIGEN-GL04S	DGM-E04	GDR-C Prime	idem n1	idem g1	idem g1
Dry Tropo.	ECMWF	idem n1	NCEP	idem n1	idem n1	idem n1
Wet Tropo.	MWR (NN)	idem n1	MWR	enhanced JMR	TMR	TMR
Ionosphere	smth. dual-freq.	JPL GIM	JPL GIM	idem n1	NIC09	idem n1
Sea State Bias	CLS	BM3	hybrid	CLS	BM4	CLS
Load tide	GOT4.7	idem n1	idem n1	idem n1	idem n1	idem n1
Nr. pnts Ω_D	12,720	182,093	258,853	82,136	10,833	204,338
Nr. pnts Ω_{NS}	5,735	79,330	105,435	33,481	4,669	88,602
Mode nr. of cycles per pass	31	31	60	122	122	122

Finally, the detrended ellipsoidal heights of the observed instantaneous water levels are reduced to EGG08 by subtracting the EGG08 quasi-geoid heights. Note that errors in the EGG08 quasi-geoid become part of the error budget.

3.5.4.1 Time series of steric heights along the open sea boundaries

A time series of steric heights along the open sea boundaries is derived as the difference between observed water levels expressed relative to EGG08, computed astronomical tides, and water levels due to atmospheric pressure variations. Note that contrary to the time series of steric heights derived from POL's hindcast, these include the net expansion/contraction signal of the oceans. The values along the open sea boundaries have been interpolated using this information at the data points. The time series of astronomical tides is taken from the GOT4.7 global ocean tide model (Ray 1999), which includes the major eight diurnal and semi-diurnal constituents (K_1, O_1, P_1, Q_1, M_2, S_2, K_2, N_2), long-period tides, and the largest quarter diurnal shallow water constituent $M4$ (Andersen & Scharroo 2011). The time series of water levels caused by atmospheric pressure variations is taken from the MOG2D model (Carrère & Lyard 2003). Besides the low-frequency periods (>20 days), the barotropic, non-linear and time-stepping MOG2D model provides also the high-frequency periods (<20 days) response to atmospheric wind and pressure forcing, which is not accounted for when using the standard IB correction (Eq. (3.7)).

To remain consistent with POL's salinity and temperature fields, only a monthly resolution is required. The weighted average steric height for month m ($\overline{\zeta_s^m}$) is computed on a $1^\circ \times 1^\circ$ grid by computing (i) the arithmetic mean ($\overline{\zeta_s^p}$) of all measurements inside the grid cell belonging to the same pass p of a particular satellite and (ii) the weighted mean steric height $\overline{\zeta_s^m}$ by

$$\overline{\zeta_s^m} = \sum_{p=1}^{N} w_p \overline{\zeta_s^p}, \tag{3.12}$$

where the weighting factors w_p account for the inhomogeneous distribution of satellite passes over time

$$w_p = \begin{cases} \frac{\frac{1}{2}(t_{p+1}-t_p)-t_s}{T_m} & \text{if } p = 1, \\ \frac{t_{p+1}-t_{p-1}}{2T_m} & \text{if } 1 < p < N, \\ \frac{t_e-\frac{1}{2}(t_p-t_{p-1})}{T_m} & \text{if } p = N, \end{cases} \tag{3.13}$$

with N the total number of satellite passes over a grid cell, t_s and t_e the start and end time of month m, t_p the measurement time of the p^{th} pass, and T_m the time interval of one month. Finally, these monthly grids are interpolated to the locations of the open sea boundaries using GMT's `greenspline` routine (Wessel 2009) with a tension factor of 0.

3.5.4.2 Observed dynamic topography used for validation

The last preprocessing step required to enable a proper validation of the modeled water levels is only required if the steric contribution to the instantaneous water levels prescribed along the open sea boundaries of DCSM is derived from POL's hindcast. Indeed, since the POL3DB model makes use of the Boussinesq approximation, the net expansion/contraction of the global oceans signal should be removed from the observed water levels to maintain consistency. The corrections ($\delta_{\zeta_s}(t)$) are computed using Eq. (3.9).

When validating the modeled instantaneous water levels and the derived MDT, we compute the time-averaged differences over all exact repeat mission (ERM) measurements. Here, we combined the data of all missions that share the same orbit, i.e., we combined the data of the T/P and Jason-1 missions and the data of the ERS-2 and Envisat missions. See Table 3.1 for an overview of the derived number of data points and the mode number of cycles per pass (a cycle is one full completion of the repeat period and a pass spans half an orbital revolution and is either ascending (South-North) or descending (North-South)).

Table 3.2: Summary of the experiments. Column OBC (open boundary conditions) provides information of how the water levels along the open boundaries of DCSM have been computed in the model run.

Exp.	Objective	Bathymetry	OBC	Source ζ_s	Wind
Ia	Reference case remaining exp.	d	$\zeta_a(\vartheta,\lambda,t)+\zeta_u(\vartheta,\lambda,t)+\zeta_s(\vartheta,\lambda,t)+\delta W_{G,P}$	POL	ERA-Int.
Ib	ERA-40 versus ERA-Interim	d	$\zeta_a(\vartheta,\lambda,t)+\zeta_u(\vartheta,\lambda,t)+\zeta_s(\vartheta,\lambda,t)+\delta W_{G,P}$	POL	ERA-40
II	Comparison with original DCSM model	d	$\zeta_a(\vartheta,\lambda,t)+\zeta_u(\vartheta,\lambda,t)+\zeta_s^{\overline{SA}}(t)$	n/a	ERA-Int.
III	Influence errors in bathymetry	$d-\overline{\zeta_O}$	$\zeta_a(\vartheta,\lambda,t)+\zeta_u(\vartheta,\lambda,t)+\zeta_s(\vartheta,\lambda,t)+\delta W_{G,P}$	POL	ERA-Int.
IV	Influence steric from altimeter	d	$\zeta_a(\vartheta,\lambda,t)+\zeta_u(\vartheta,\lambda,t)+\zeta_s(\vartheta,\lambda,t)$	radar alt.	ERA-Int.

3.6 Results and Discussion

In this section, we present and discuss the quality of the extended, vertically referenced model by validation of the modeled (time-averaged) water levels using (i) water levels of POL's hindcast and (ii) observed water levels from radar altimetry. In all our experiments, summarized in Table 3.2, we model the instantaneous water levels with a time step of 10 min over the period January 1, 2000 to January 1, 2003. To distinguish the results of the various experiments, they are labeled with Roman numerals, e.g., the modeled dynamic topography ($\zeta_D(t)$) for Experiment Ia is $\zeta_{D_{Ia}}(t)$, where the capital letter D refers to the source from which the water level is derived; the DCSM model. Besides D, we use O and P referring to observed and POL's modeled water levels, respectively.

3.6.1 Experiment Ia: reference case

In Experiment Ia, which serves as a reference case for the other experiments, the mean and instantaneous water levels are modeled using POL's time-varying salinity and temperature fields. The steric contribution in the water levels prescribed at the open sea boundaries are also derived from POL's hindcast. Since for POL's hindcast ERA-40 wind fields were used, Experiment Ia is repeated using these wind fields as well. This experiment, labeled as Experiment Ib, enables a fair comparison between our model-derived MDT and the one derived from POL's hindcast. Before we present the validation results, we first provide a brief overview of the main features in the model-derived MDT and depth-averaged flow velocities. The latter helps to interpret the obtained MDT and the differences between observed and modeled water levels presented in Section 3.6.1.3.

3.6.1.1 Model-derived MDT and depth-averaged flow velocities

The model-derived MDT and flow velocities over the entire simulation period are shown in Figs. 3.2 and 3.3, respectively. Many of the features shown in these maps

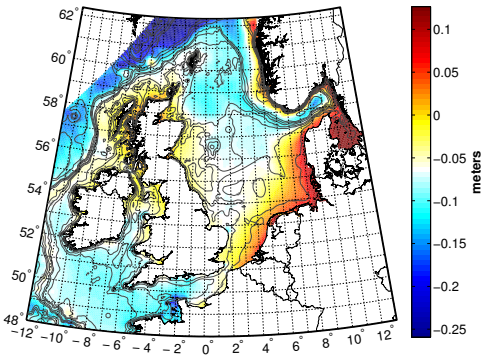

Figure 3.2: Model-derived MDT relative to EGG08 computed over the entire simulation period January 1, 2000 to January 1, 2003. The grey lines show the contour lines of the bathymetry.

are consistent with oceanographic expectations. For example, the polewards flow of the Atlantic Ocean along the shelf break is clearly visible, as well as a part of the Scottish Coastal Current which comes from the Irish Sea and flows to the north on both sides of the Western Isles of Scotland, although this is less pronounced. We also observe the inflow of mixed coastal and oceanic water through the Fair Isle Channel most of which is guided eastwards to the Norwegian Trench by the $\sim$100 m depth contour (the Fair Isle Current). The remaining part flows southwards along the Scottish and English coasts and anti-clockwise back in the southern North Sea where it finally joins the Norwegian Coastal Current in the Skagerrak. The Norwegian Coastal Current is fed by inflow of the Atlantic Ocean, which gives a flow along the western slope of the Norwegian Trench. The water re-circulates in the Skagerrak where it is joined by the water flow from the southern North Sea and fresh water from the Baltic, and flows out along the eastern side of the Norwegian Trench forming the major transport out of the North Sea. For a recent overview of these currents, we refer to (Huthnance et al. 2009, United Kingdom Marine Monitoring and Assessment Strategy (UKMMAS) 2010, and cited studies).

The MDT field (Fig. 3.2) also shows well-known features, such as the piling up against the Danish and German coasts as a response to the prevailing wind direction and the abrupt rise of the MDT in the Kattegat. The latter reflects the salinity front there, separating the brackish Baltic Sea water from the saline North Sea water, and the associated Baltic current (Ekman & Mäkinen 1996). The causes of both features are nicely illustrated by Figs. 3.4a and 3.4b, which show the separate contributions of wind and astronomical tide to $\overline{\zeta_{\mathrm{D_{Ia}}}}$ and that of horizontal variations in water density, respectively. The map shown in Fig. 3.4b is computed by subtracting from $\overline{\zeta_{\mathrm{D_{Ia}}}}$ the MDT obtained by a simulation using astronomical tide and atmospheric wind and pressure forcing only, i.e., $\overline{\zeta_{\mathrm{D_{II}}}}$ (Section 3.6.2), which is shown in Fig. 3.4a. Fig. 3.4b also gives an idea about the order of magnitude of the time-mean signal so far ignored in DCSM. The sea level increases more than 10 cm from north to south over the North Sea.

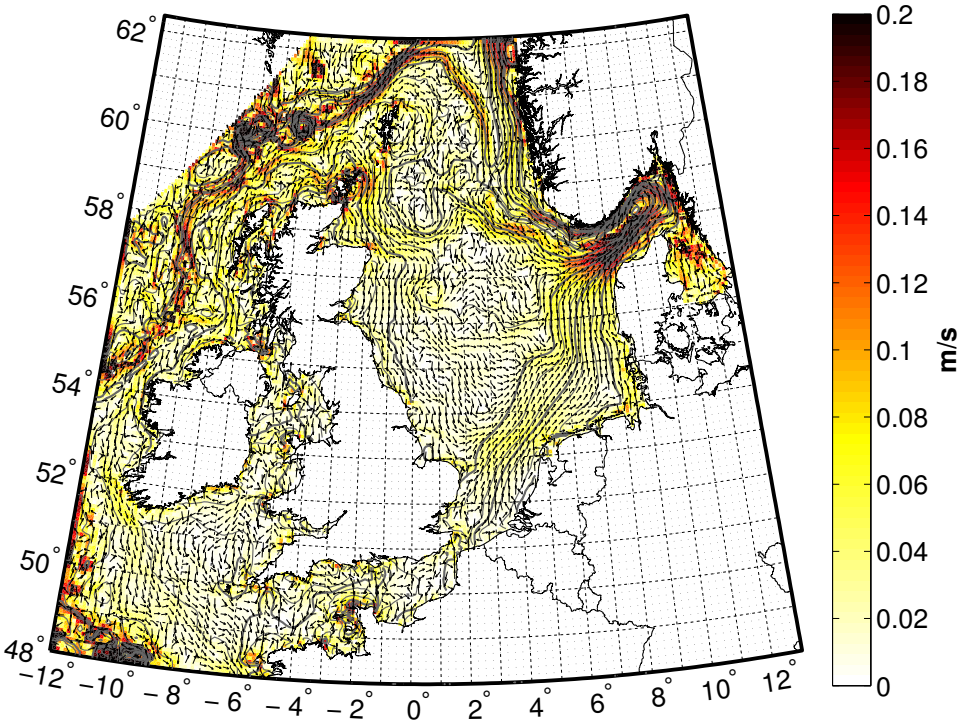

Figure 3.3: Time-averaged flow velocities computed over the entire simulation period January 1, 2000 to January 1, 2003. The grey lines show the contour lines of the model-derived MDT (Fig. 3.2). For clarity only velocity vectors at every second grid points are shown.

3.6.1.2 Comparison with POL's MDT

Fig. 3.5 shows a map of the spatial differences between POL's MDT computed over our simulation period ($\overline{\zeta_{\mathrm{P}}}$) and the MDT derived in Experiment Ia ($\overline{\zeta_{\mathrm{DIa}}}$), while Table 3.3 provides the statistics of these differences computed over the whole DCSM domain (Ω_{D}) and over the North Sea (Ω_{NS}). Compared to $\overline{\zeta_{\mathrm{P}}}$, in general $\overline{\zeta_{\mathrm{DIa}}}$ tends to overestimate the MDT, mostly on the shelf. This is also reflected by the mean difference over Ω_{D} and Ω_{NS}: -2.24 cm and -3.02 cm, respectively. The most probable explanation for these biases is that in the computation of the datum shift ($\delta W_{\mathrm{G,P}}$) between EGG08 and the zero water level surface of POL3DB we use also data over a region outside the DCSM domain. Hence, any difference between this shift and the shift that we would obtain if we only use data inside the DCSM model domain shows up as a bias between $\overline{\zeta_{\mathrm{P}}}$ and $\overline{\zeta_{\mathrm{DIa}}}$. The variability of the differences in the spatial domain is small; the standard deviations of the differences taken over Ω_{D} and Ω_{NS} are both <2 cm. The large minimum deviation (-48.85 cm) comes from a grid point in

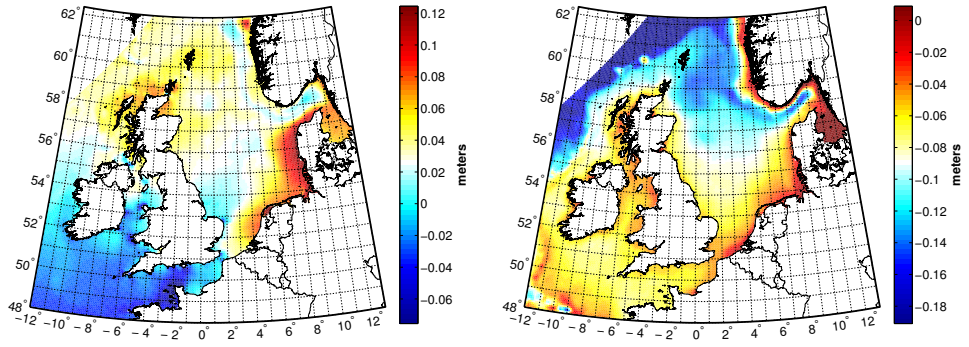

(a) **(b)**

Figure 3.4: Time-averaged water level induced by astronomical tide and surge (a) and the time-averaged water level induced by horizontal variations in water density expressed relative to EGG08 (b). Both are computed over the entire simulation period January 1, 2000 to January 1, 2003.

the Wadden Sea right next to a non-computational point. Detailed analysis showed that this point represents a small channel and is surrounded by grid points that are dry most of the time. Most likely, this "outlier" is caused by the applied drying/flooding procedure. Also along the open sea boundaries larger deviations are observed, which are attributed to boundary effects. Remaining differences should be attributed to the fact that different models are used (e.g., bathymetry, open boundary conditions) and to differences in the used wind fields.

Although the differences between the two model-derived MDT fields are small (i.e., on the order of a few centimeters), the differences between POL's monthly mean water levels and monthly mean water levels from DCSM are much larger, especially in the central North Sea. This follows directly from Fig. 3.6a, which shows the standard deviation of the differences between POL's and DCSM's monthly mean water levels per grid point. Except for some spots near the open boundaries, away from the shelf, the standard deviation of these differences is on the order of 1.0 cm, while in the North Sea they increase from $\sim$2.0 cm in the northern part to 2.5–3.5 cm in the southern part with extreme values along the Belgian/French coast ($>$ 5 cm). A detailed analysis of the differences per month reveals that the maximum differences in the central and southern part reach $\sim$10 cm for the months January 2000, February 2000, November 2000, and January 2002, while for other months the differences are on the order of centimeters (not shown).

The main explanation for these differences is the difference in atmospheric wind and pressure forcing; ERA-40 (POL) versus ERA-Interim (DCSM). This follows directly from Fig. 3.6b that shows the result of Experiment Ib. Experiment Ib differs from Experiment Ia in that the ERA-Interim wind fields were replaced by ERA-40 wind

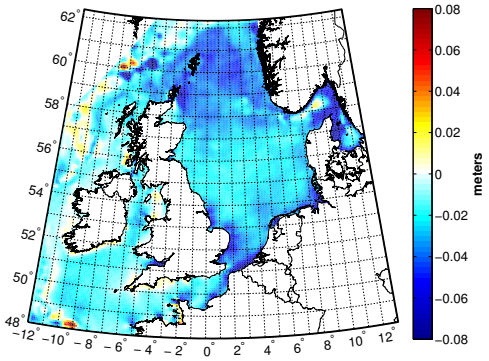

Figure 3.5: Difference between the model-derived MDT derived from POL's monthly mean water levels ($\overline{\zeta_P}$) and the MDT derived in Experiment Ia, both computed over the entire simulation period January 1, 2000 to January 1, 2003.

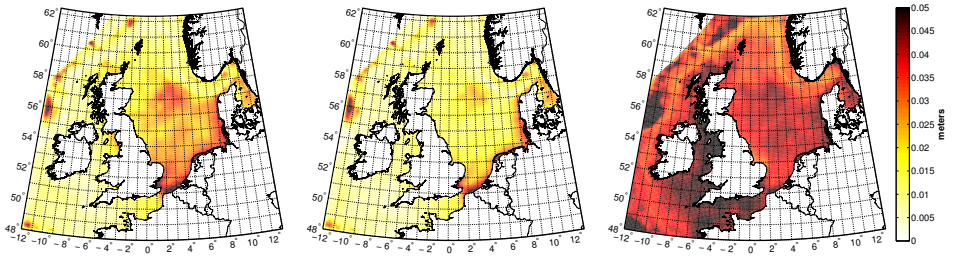

(a) **(b)** **(c)**

Figure 3.6: Standard deviations of the differences between POL's monthly mean water levels and the ones obtained in: Experiment Ia (a); Experiment Ib (computed over the first 32 months of our simulation period, ERA-40 atmospheric wind and pressure forcing) (b); and Experiment IV (c).

fields. Note that since ERA-40 is only available till September 2002 (from October 2002 operational analyses of ECMWF were used in POL's hindcast), Fig. 3.6b is computed over the first 32 months of our simulation period (this period include all 4 months for which extreme deviations were observed). Indeed, the standard deviations of the differences between POL's and DCSM's monthly mean water levels per grid point are significantly smaller; about 1.5 cm. Hence, we conclude that our model setup (2D) is able to reproduce within a few centimeters standard deviation the (monthly) mean water levels derived by POL's hindcast (3D).

3.6.1.3 Validation with observation-derived MDT

The comparison with POL's (monthly) mean water levels is not really independent since we used the same water levels to extract the steric signal prescribed at the open boundaries, as well as POL's monthly mean salinity and temperature fields to carry out this experiment. Therefore, we compare the model-derived MDT with an independent MDT derived from radar altimeter data and the EGG08 quasi-geoid. In

Table 3.3: Experiment Ia: statistics of the differences between POL's MDT and the one derived in Experiment Ia, as well as the aggregate and satellite-specific statistics of the (time-averaged) differences between the observed and modeled dynamic topography computed over both the whole model domain (Ω_D) and North Sea (Ω_{NS}). All values are provided in cm.

differences	domain	satellite	rms	min	max	mean	std
$\overline{\zeta_P} - \overline{\zeta_{D_{Ia}}}$	Ω_D	n/a	2.84	-48.85	11.29	-2.24	1.75
	Ω_{NS}	n/a	3.32	-48.85	1.39	-3.02	1.38
$\overline{\zeta_O(t) - \zeta_{D_{Ia}}(t)}$	Ω_D	all	5.77	-89.21	226.54	-0.86	5.71
	Ω_{NS}		4.18	-89.21	101.20	-1.28	3.98
$\zeta_O(t) - \zeta_{D_{Ia}}(t)$	Ω_D	all	10.45	-186.60	268.88	-1.01	10.40
	Ω_{NS}		9.31	-186.60	101.20	-1.13	9.24
	Ω_D	ERS-2	11.03	-61.52	103.51	-0.45	11.02
		GFO-1	11.27	-186.60	268.88	-2.49	10.99
		Jason-1	9.72	-65.87	92.74	-0.14	9.72
		Envisat	9.93	-29.93	48.49	2.07	9.71
		POSEIDON	9.78	-105.23	68.64	-0.16	9.78
		TOPEX	9.09	-164.89	81.68	-0.22	9.09
	Ω_{NS}	ERS-2	10.17	-61.52	50.63	-1.05	10.11
		GFO-1	9.78	-186.60	101.20	-2.86	9.35
		Jason-1	8.50	-65.87	67.13	-0.08	8.50
		Envisat	9.34	-29.84	40.88	2.73	8.94
		POSEIDON	9.30	-93.47	68.64	-0.24	9.30
		TOPEX	8.13	-76.18	49.21	0.17	8.13
$\zeta_O(t) - \zeta_{D_{Ia}}(t) - \overline{\delta\zeta^p}$	Ω_{NS}	ERS-2	6.83	-34.62	41.06	0.17	6.83
		GFO-1	7.32	-177.67	101.04	-0.13	7.32
		Jason-1	7.14	-55.39	58.17	-0.18	7.13
		Envisat	7.15	-30.66	49.53	0.00	7.15
		POSEIDON	7.44	-93.29	61.45	0.30	7.44
		TOPEX	6.03	-73.90	47.85	0.31	6.02

Fig. 3.7a, we show the pointwise differences computed as $\overline{\zeta_O(t) - \zeta_{D_{Ia}}(t)}$. To improve the readability of this map, we interpolated the differences at the grid points of the DCSM grid (using GMT's `surface` routine (Wessel & Smith 1995) with the default tension factor) and applied a moderate smoothing using a Gaussian filter with a filter half-width of 29.4 km. The obtained map is shown in Fig. 3.7b.

Besides some spurious behavior along the coasts, likely caused by unreliable radar data and interpolation errors, Fig. 3.7b shows also clear spatial patterns where significant differences occur. Along the western open boundary the sign is more or less opposite to the pattern shown in Fig. 3.5. Note that the spurious spots near 60° latitude and at the southern open boundary near $-10°$ longitude show up here as well. Besides these, deviations up to 5 cm are observed in the Celtic Sea, the English Channel, and the northern North Sea (see Fig. 3.7b that includes the bounding boxes around the features of interest in the Celtic Sea and in the northern North Sea). Since these patterns did not show up in the comparison with POL's MDT (Fig. 3.5), which model's open sea boundaries are both further to the east and north, these cannot be attributed to boundary effects. The fact that both the POL3DB model and DCSM make

use of the Boussinesq approximation provides one possible explanation for these differences. For instance, Greatbatch et al. (2001) has shown that on longer time scales the difference field between non-Boussinesq and Boussinesq models shows spatial variability of several centimeters, which is not accounted for by the applied globally uniform correction of Eq. (3.9). In the remainder, we show that here other explanations are more likely.

We obtain some insight into these discrepancies by analyzing the associated flow field implied by the differences. Such an analysis would be rather straightforward if the geostrophic assumption could be used to describe this flow. However, since we are in shallow water this cannot be expected, which is further proved by a comparison of the geostrophic velocities computed from the model-derived MDT (Fig. 3.2) with the model-derived time-averaged depth-mean flow velocities (Fig. 3.3). For some regions, the geostrophic assumption appears to be reasonable, while for others it is clearly not. On the other hand, we observe a reasonable match between the direction of the geostrophic water flow and the actual time-averaged flow field shown in Fig. 3.3. This follows already from the fact that the currents shown in Fig. 3.3 almost flow along the contours of the MDT such that the slope in the MDT perpendicular to the flow direction is positive towards the right (northern hemisphere), which is expected if the flow is geostrophic. Hence, although we cannot perform a quantitative assessment, we use this fact to interpret the differences shown in Fig. 3.7b. So, we assume that the associated water flow implied by the differences, flows along the contours of equal height such that the slope in the differences perpendicular to the flow direction is positive towards the right.

Using this assumption the pattern in the Celtic Sea would imply the existence of a clockwise flowing eddy, which should be added to the model results to match the observations. From Pingree & Lecann (1989) and Huthnance et al. (2009), we conclude that the low-frequency circulation in the Celtic Sea is generally weak, except along the shelf edge and where the flow is channeled or accelerated around promontories. This is in line with the model-derived time-averaged flow velocities (Fig. 3.3) that hardly exceed a few cm/s. From this, we believe the observed patterns originate from errors in the observation-derived MDT, i.e., errors in the observation-derived MSL and/or quasi-geoid. Here, the latter is likely to dominate since the eddy is located far enough from the continents to be associated with the degraded performance of radar altimetry in coastal regions.

The latter is probably the explanation for the observed patterns in the English Channel, where the altimeter satellites provide only a few samples when they cross from the UK to France or vice versa. Probably, the degraded performance of the radar altimeters biases the computed mean differences. In addition, the observed discrepancies might be introduced by errors in the interpolated wind speeds and mean sea level pressure values. First of all, the resolution of the ERA-Interim fields is only

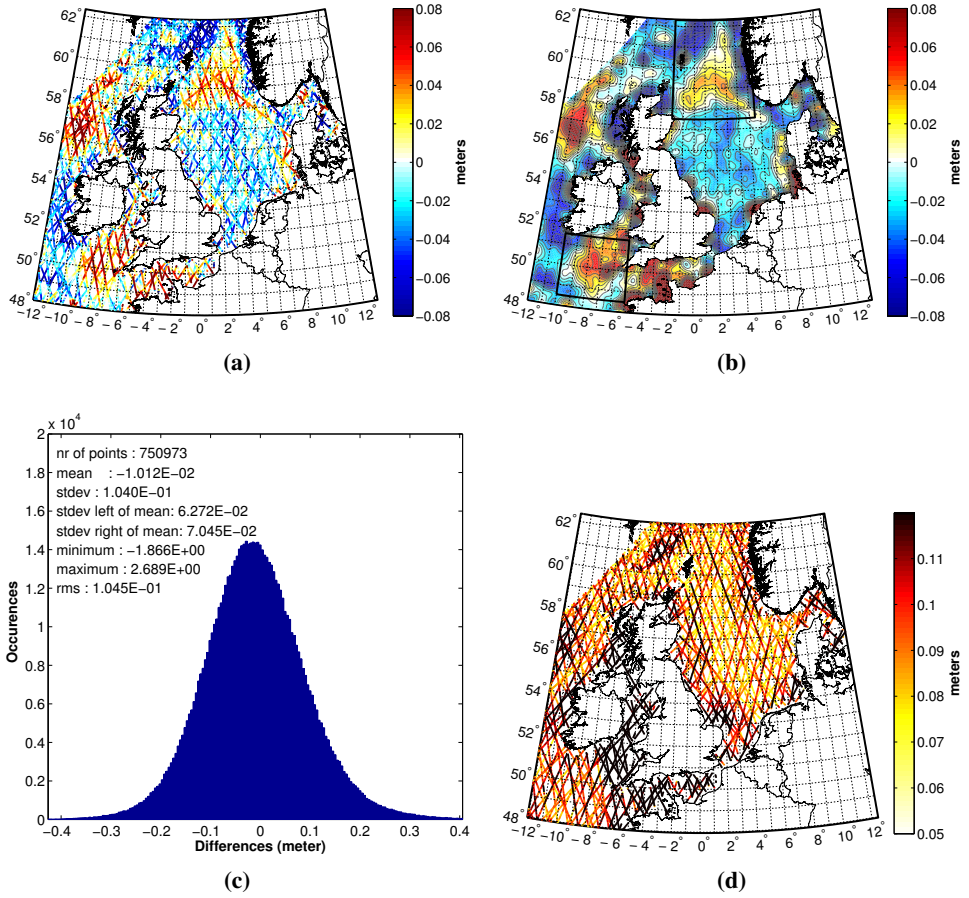

Figure 3.7: Time-averaged differences between the observed and modeled dynamic topography ($\overline{(\zeta_{\mathrm{O}}(t) - \zeta_{\mathrm{D_{Ia}}}(t))}$) at the locations of the radar altimeter data points (a) and interpolated to the DCSM grid (b). Here, a moderate Gaussian smoothing is applied using a filter half-width of 29.4 km (sigma is 25 km). On top of this map, we added in gray the contour lines of the differences for each centimeter in the range -0.08 to 0.08. The bounding boxes (bold black lines) indicate the geographic extent of the features discussed in the text. Fig. (c) shows the histogram of all differences, while Fig. (d) provides the standard deviations of the differences computed for each bin.

$1.5^\circ \times 1.5^\circ$, which is not sufficient to represent the actual wind and mean sea level pressure in this "small" channel. Moreover, we excluded all grid points masked as land in the interpolation to the DCSM grid, which implies that almost no grid points remain in this region. Consequently, the values at the grid points inside the English Channel (this holds for some other regions as well) are almost exclusively interpolated from values inside the Celtic Sea and North Sea.

When looking at Fig. 3.7b, we notice correlation between the spatial pattern of the differences $\overline{\zeta_{\mathrm{O}}(t) - \zeta_{\mathrm{DIa}}(t)}$ and the currents in the northern North Sea. First, we expect a flow that counteracts the Fair Isle Current and the inflow from the Atlantic Ocean along Shetland. Second, we expect a southwards flow on both sides of the Norwegian Trench in line with the inflow of the Atlantic Ocean (western side) and the Norwegian Coastal Current (eastern side). From this, we conclude that these differences are dominated by errors in the model-derived MDT. In particular, these results suggest that the model overestimates the inflow via the Fair Isle Current and the inflow from the Atlantic Ocean along Shetland, but underestimates the inflow along the western side of the Norwegian Trench. The first two observations support the suggestion of Holt & Proctor (2008) who conclude from a comparison of the modeled and observed volume fluxes that the North Sea inflows are overestimated in their model. In addition, we conclude that the outflow by the Norwegian Coastal Current is overestimated. A comparison of Fig. 3.4a and Fig. 3.4b indicates that the differences can mainly be explained by errors in the steric water levels. They have to come from (i) errors in the used salinity and temperature fields and (ii) errors in the steric water levels prescribed at the open boundaries.

3.6.1.4 Validation of the modeled dynamic topography

In this study, we assess the model's ability in representing the full dynamic topography over the whole model domain by differencing the modeled instantaneous water levels and the ones computed from SSHs acquired by radar altimeter satellites and the EGG08 quasi-geoid.

The results are summarized by a histogram of these differences (Fig. 3.7c) and a map that shows the standard deviation of these differences for each bin (Fig. 3.7d). Furthermore, Table 3.3 provides the aggregate and satellite-specific statistics, computed over both the whole model domain (Ω_{D}) and North Sea (Ω_{NS}). In general, these statistics should be interpreted with care. First, they represent the performance away from the coast, since we almost do not have radar altimeter observations in the first 25 km off the coast. Second, the statistics are biased toward the errors in the northern part of the domain. The reason is that due to the orbital inclination of the satellites the measurement density increases towards the poles. Therefore, we also

provided Fig. 3.7d from which we gain insight in the spatial behavior of the model performance.

The histogram in Fig. 3.7c shows that the differences are normally distributed with a mean and standard deviation of -1.01 cm and 10.40 cm, respectively. The overall quality over Ω_D in terms of the root mean square (rms) error is 10.45 cm, which decreases to 9.31 over Ω_{NS}. Fig. 3.7d, however, reveals that these latter numbers have little practical implication, since the standard deviation of the differences for each bin varies significantly over the model domain; compared to the North Sea, we observe a degraded performance in the St. George's Channel, Irish Sea, English Channel, German Bight, and Kattegat. The discrepancies can be partly attributed to the degraded performance of altimetry in coastal regions. Moreover, according to Holt et al. (2001) an accurate simulation of the processes in the St. George's Channel and the Irish Sea as a whole requires not only a finer resolution model but a model coupled to a wider area than considered here. The differences may also be partially attributed to the, already mentioned, inability of DCSM to reproduce the surge component to the instantaneous water level in these waters. This is a consequence of the limited spatial resolution of the ERA-Interim data in combination with the applied interpolation method (Section 3.6.1.3). Except for the Western Ireland Shelf, a small region around 57°N, and the area northwest to Shetland we do not observe a significant increase of the standard deviations along the open sea boundaries. This is attributed to the fact that the dominating astronomical tide signal prescribed at the open boundaries, via data assimilation into a global ocean tide model, is derived from radar altimeter data as well. There are two more regions that show degraded accuracies. One is in the southern North Sea, north of the city Norwich (around (1.5°E, 53.5°N)), where the water inflow starts to recirculate towards the North. Most likely, the strong tidal currents are not well represented by the model. The other is in the Norwegian Trench, west to Norway. This might be related to the fact that the Norwegian Coastal Current is unstable and forms large eddies (Huthnance et al. 2009), which are not resolved here.

Note that the agreement between modeled and observed dynamic topography varies significantly for the various altimeters. Table 3.3 provides the satellite-specific statistics, again both for the whole model domain and the North Sea. The observed dynamic topography derived from the TOPEX data shows the best agreement with the modeled one; the rms values are 9.09 cm over Ω_D and 8.13 cm over Ω_{NS}. Compared to the rms values obtained for the ERS-2 and GFO-1 missions, the rms for TOPEX is smaller by about ~ 2 cm over Ω_D and 1.5–2 cm over Ω_{NS}. Probably, the reduced ability of the GFO-1 mission is related to the problems with the orbit determination (Lemoine et al. 2006), which is also suggested by the relatively large mean error (orbit errors have long wavelengths) in the differences between the modeled and observed dynamic topography for this satellite (~ -3 cm). The large minimum and maximum deviations (especially those from GFO-1) come from a few isolated data

points close to the coast. Because these are isolated, they are not detected by the data editing method applied to remove outliers (Section 3.5.4). Since the accuracy of the TOPEX SSHs is $\sim$4 cm (Chelton et al. 2001), we conclude that even in those regions where the model performs best the accuracy of the modeled water levels is about two times lower than that of the observed ones. This suggests that there is still space to improve the model by, e.g., assimilation of water levels from radar altimetry and better input data.

A significant part of the spread between observed and modeled dynamic topography can be explained by a bias in each single satellite pass ($\overline{\delta\zeta^p}$). This is based on Fig. 3.8, which shows a time series of this bias and its mean value over each successive week. Here, we excluded all satellite passes that have less than 10 data points (the mean number of data points per satellite pass is 94). For all missions together, the standard deviation of the computed biases is $\sim$7 cm. However, among the various altimeters significant differences exist; for ERS-2 and GFO-1 the standard deviations are 8.3 and 7.4 cm, while for TOPEX and Jason-1 these are $\sim$6 cm. The "outliers" visible in Fig. 3.8 are mainly from the ERS-2 and GFO-1 data. To illustrate the impact of $\overline{\delta\zeta^p}$ on the statistics, we recomputed the satellite-specific statistics over Ω_{NS} after removing the bias. From Table 3.3, we observe that the rms values, compared to the values before subtraction of the bias, decreased by 1.36–3.34 cm, which is about 25%. Roblou et al. (2011) interpreted the bias as errors in the applied corrections for the net steric expansion/contraction of the global oceans. This could be one possible explanation of the observed signal, although the actual source of error should differ in our case. The correction applied by Roblou et al. (2011) contains a term that represents the model-derived mean sea surface elevation computed over the measurement epochs. Hence, these corrections are directly dependent on the water levels prescribed at the open sea boundaries of their model. Any mean error in these water levels propagates into the modeled water levels and consequently to the computed corrections. In our formulation of this correction (Eq. (3.9)), we do not have this dependency. So, the errors should be in the steric heights computed from the temperature and salinity fields derived from POL's hindcast. In addition, a Fourier analysis of the time series (not shown here) reveals peaks at some tidal frequencies, as well as peaks at monthly, semi-annual, and even intra-annual frequencies. These latter peaks indeed point to the applied corrections, but might also be caused by errors in (i) the used wind fields, (ii) pressure gradients induced by spatial variations in water density, and (iii) the prescribed water levels along the open sea boundaries. Finally, while significant differences among the various altimeters exist, a part of the biases can be explained by errors in the radar data that do not average out when computing the biases.

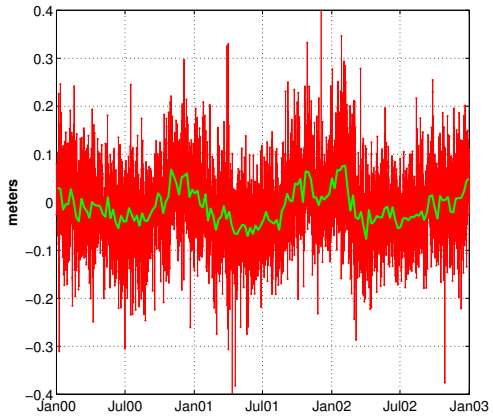

Figure 3.8: Time series of the bias between observed and modeled dynamic topography computed over the differences belonging to a single satellite pass. In green we plotted the weekly mean bias.

3.6.2 Experiment II: the extended versus the original DCSM model

In this study, we aim to obtain instantaneous water levels expressed relative to EGG08 from the 2D storm surge model DCSM. In Experiment Ia, the approach used to realize this involves (i) adding to DCSM the baroclinic forcing by adding the depth-averaged baroclinic pressure gradient terms as diagnostic variables computed from 4D temperature and salinity fields obtained from POL's hindcast and (ii) an adjustment of the water levels prescribed at the open sea boundaries such that they refer to EGG08. The purpose of Experiment II is to quantify the improvements in representing the (time-mean) water levels of the extended, vertically referenced DCSM model compared to the original DCSM model.

Therefore, Experiment Ia is repeated without adding the baroclinic forcing, where also the steric contribution to the prescribed water levels at the open sea boundaries ($\zeta_s(\vartheta,\lambda,t)$) disappears accordingly. We apply, however, the pragmatic approach described in Section 3.3 to account for the dominant time-variable part of the steric water level variations. That is, the time-variable steric contribution to the modeled water levels is approximated by adding the annual steric signal averaged over the model domain ($\zeta_s^{\overline{SA}}(t)$) to the prescribed water levels at the open sea boundaries. This signal is derived as the spatially averaged remaining annual signal estimated from the differences between observed and modeled water levels, where the latter are taken from a model run without any annual signal. So, in Experiment II the water levels are modeled both with and without including the remaining annual signal in the prescribed water levels along the open sea boundaries.

To assess whether the extended model provides any improvement compared to the original model, we apply a similar analysis as presented in Sections 3.6.1.3 and 3.6.1.4. That is, we compare the modeled (time-mean) water levels obtained in Experiment II with observed ones. The obtained statistics will be compared with those

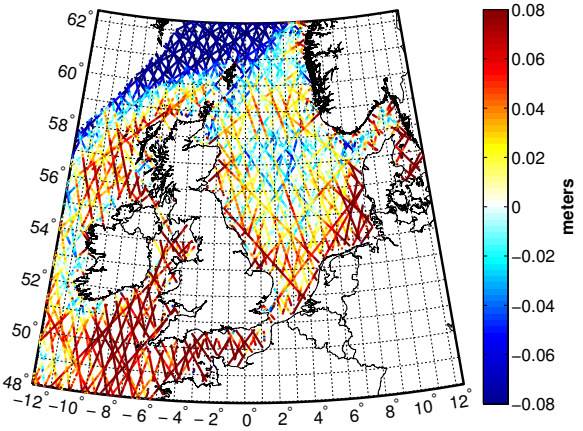

Figure 3.9: Time-averaged differences between $\zeta_{\mathrm{O}}(t)$ and $\zeta_{\mathrm{D_{II}}}(t)$ at the locations of the radar altimeter data points.

obtained in Experiment Ia. Since, however, the observed water levels ($\zeta_{\mathrm{O}}(t)$) are expressed relative to EGG08 while in Experiment II the modeled water levels ($\zeta_{\mathrm{D_{II}}}(t)$) are expressed relative to the ill-defined model's reference surface, we first remove the mean difference computed using all differences between $\zeta_{\mathrm{O}}(t)$ and $\zeta_{\mathrm{D_{II}}}(t)$) over the whole model domain. Furthermore, it should be noted that the corrections for the net expansion/contraction of the global oceans to the observed water levels are not applied (Section 3.5.4.2). Indeed, these corrections are required if the baroclinic forcing is included and the steric contribution to the prescribed water levels at the open sea boundaries is derived from a ocean circulation model (Section 3.4.3). In Experiment II, the baroclinic forcing is not included and the signal becomes, to a large extent, part of $\zeta_{\mathrm{s}}^{\overline{\mathrm{SA}}}(t)$. Table 3.4 provides the aggregate and satellite-specific statistics of the (time-averaged) differences computed over both the whole model domain (Ω_{D}) and North Sea (Ω_{NS}). We gain understanding in interpreting these statistics by Fig. 3.9, which shows, similar to Fig. 3.7a, the time-averaged differences between the observed and modeled dynamic topography ($\overline{\zeta_{\mathrm{O}}(t) - \zeta_{\mathrm{D_{II}}}(t)}$). This signal mainly represents the spatially varying contribution of horizontal water density variations to the time-mean water levels. Over Ω_{D}, this signal is 0.68 cm $\pm$8.10 cm. Over Ω_{NS}, the signal is 1.20 cm $\pm$4.40 cm. The lower standard deviation is explained by the fact that in the domain Ω_{NS} the off-shelf region is excluded where the steric signal is largest (Fig. 3.9). This is also the reason why in Experiment Ia the standard deviation of the time-averaged differences between the observed and modeled dynamic topography ($\overline{\zeta_{\mathrm{O}}(t) - \zeta_{\mathrm{D_{Ia}}}(t)}$) over Ω_{D} is significantly lower (5.71 cm), while over Ω_{NS} the standard deviation decreases only by 0.42 cm to 3.98 cm. In any case, while both for Ω_{D} and Ω_{NS} the standard deviations obtained in Experiment Ia are lower, we conclude that adding the baroclinic forcing results in an improved representation of the MDT.

One could argue, however, that the applied comparison is not fair; the modeled water levels induced by tide and atmospheric wind and pressure forcing are compared to observed water levels that also include the steric contribution. Indeed, to carry

Table 3.4: Experiment II: aggregate and satellite-specific statistics of the (time-averaged) differences between the observed and modeled dynamic topography computed over both the whole model domain (Ω_D) and North Sea (Ω_{NS}). All values are provided in cm.

differences	domain	satellite	rms	min	max	mean	std
$\overline{\zeta_O(t) - \zeta_{D_{II}}(t)}$	Ω_D	all	8.13	-74.97	239.20	0.68	8.10
	Ω_{NS}		4.56	-74.97	115.19	1.20	4.40
$\zeta_O(t) - \zeta_{D_{II}}(t)$	Ω_D	all	11.69	-186.50	275.12	-0.00	11.69
	Ω_{NS}		9.29	-186.50	115.19	1.06	9.22
	Ω_D	ERS-2	11.89	-62.25	107.98	0.32	11.89
		GFO-1	12.13	-186.50	275.12	-1.11	12.08
		Jason-1	11.79	-60.14	103.22	2.89	11.43
		Envisat	12.20	-49.80	54.92	2.40	11.96
		POSEIDON	11.41	-102.68	67.27	-0.96	11.37
		TOPEX	10.84	-164.34	86.73	-0.14	10.84
	Ω_{NS}	ERS-2	9.74	-60.22	53.52	0.94	9.69
		GFO-1	9.44	-186.50	115.19	-0.63	9.42
		Jason-1	9.83	-60.14	75.38	4.18	8.90
		Envisat	10.72	-25.56	47.32	5.14	9.40
		POSEIDON	9.04	-92.38	67.27	0.83	9.00
		TOPEX	8.34	-70.27	51.96	1.73	8.15

out a fair comparison, the time-mean steric contribution to the observed water levels should be removed. However, as discussed in Section 3.1, this is not straightforward. The bottom-line of the difficulty is that to obtain such "steric corrections" we need to use DCSM to exclude the tide and atmospheric wind and pressure forcing contributions to the MDT. Irrespective of whether the MDT is derived from observations or a model, the consequence is that DCSM will not contribute anymore to the representation of the MDT. Note that if the MDT is derived from observations, the differences in Fig. 3.9 disappear.

From Table 3.4 it also turns out that the overall ability of DCSM in the simulation of the dynamic topography in terms of the rms decreases from 10.45 cm in Experiment Ia to 11.67 cm in Experiment II. Over the North Sea, the ability improved by only 0.2 mm to 9.29 cm. Evaluated for each satellite mission, the statistics over Ω_D show a similar picture; compared to those in Experiment Ia, for all missions the rms values increase by 0.86–2.27 cm. Over Ω_{NS}, a mixed picture is observed; for ERS-2, GFO-1, and POSEIDON, we observe a decrease of 0.26–0.43 cm, while for Envisat, Jason-1, and TOPEX the rms values increase by 0.21–1.42 cm. By comparing the standard deviations, we conclude that for Envisat and Jason-1 these increased rms values are mainly caused by rather large mean errors; 5.14 cm and 4.18 cm. While over Ω_{NS} the differences are only in the order of millimeters, we conclude that the improvements in the modeled water levels by adding the time-variable baroclinic forcing are within the level of remaining model errors, and have a negligible effect on these bulk statistics.

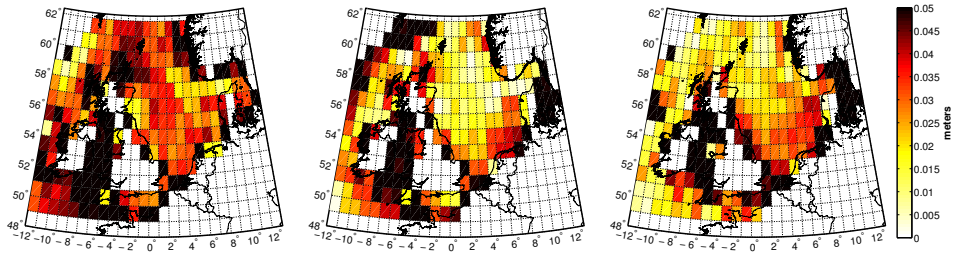

(a) **(b)** **(c)**

Figure 3.10: Amplitudes of the remaining annual cycle estimated using Eq. (3.14) on a $1^\circ \times 1^\circ$ grid for Experiment Ia (a), Experiment II (b), and Experiment IV (c).

A better picture of the difference in performance to represent the dynamic topography between Experiment Ia and Experiment II is obtained by comparing Fig. 3.10a with Fig. 3.10b. These figures show the amplitudes of the remaining annual signal estimated from the differences on all data points inside grid cells of $1^\circ \times 1^\circ$ using

$$\zeta_{\mathrm{O}}(t) - \zeta_{\mathrm{D}}(t) = x_1 + x_2 \sin\left(\frac{2\pi t}{T}\right) + x_3 \cos\left(\frac{2\pi t}{T}\right), \tag{3.14}$$

where T is one year. In Fig. 3.10b, the amplitudes are ~ 1.5 cm, except in the Irish Sea, Celtic Sea, German Bight, Skagerrak, English Channel, and along the open sea boundaries. In Fig. 3.10a, however, much larger values are observed, mainly in the North Sea. The improved description of the annual signal for Experiment II is attributed to the fact that in this experiment the entire signal that is not captured by the correction for the net expansion/contraction of the global oceans leaks to the open boundary conditions. Indeed, what still shows up as an error in Experiment Ia is accounted for in Experiment II.

3.6.3 Experiment III: influence of errors in the bathymetry

In this experiment, we want to get a rough estimate of the errors in modeled water levels introduced when bathymetry data are used which do not refer to the quasi-geoid but to MSL. Although the original bathymetry is no longer available, we can assess the impact by subtracting the MDT signal from the current bathymetry and compare the model-derived MDT ($\overline{\zeta_{\mathrm{D_{III}}}}$) with the one derived in Experiment Ia ($\overline{\zeta_{\mathrm{D_{Ia}}}}$). In this experiment, we use DNSC08-MSS (Andersen & Knudsen 2009) expressed relative to EGG08 as the MDT signal for which the current bathymetry will be corrected.

From the statistics of the pointwise differences between $\overline{\zeta_{\mathrm{D_{Ia}}}}$ and $\overline{\zeta_{\mathrm{D_{III}}}}$ provided in Table 3.5, we conclude that the impact on the water level of a correction of this order of magnitude is at most 6.65 cm. These extreme differences show up only in the

Table 3.5: Experiment III: statistics of the differences between the MDT's derived in Experiment Ia and Experiment III, as well as the aggregate and satellite-specific statistics of the differences between the observed and modeled dynamic topography computed over both the whole model domain (Ω_D) and North Sea (Ω_{NS}). All values are provided in cm.

differences	domain	satellite	rms	min	max	mean	std
$\overline{\zeta_{D_{Ia}}} - \overline{\zeta_{D_{III}}}$	Ω_D	n/a	0.10	-6.65	0.26	0.01	0.10
	Ω_{NS}	n/a	0.16	-6.65	0.26	0.01	0.16
$\zeta_O(t) - \zeta_{D_{III}}(t)$	Ω_D	all	10.45	-186.67	268.83	-1.00	10.40
	Ω_{NS}		9.30	-186.67	101.22	-1.11	9.24
	Ω_D	ERS-2	11.04	-61.37	104.73	-0.43	11.03
		GFO-1	11.27	-186.67	268.83	-2.48	10.99
		Jason-1	9.73	-65.90	92.97	-0.14	9.73
		Envisat	9.93	-30.08	48.50	2.09	9.71
		POSEIDON	9.79	-105.50	68.50	-0.17	9.79
		TOPEX	9.10	-164.87	82.08	-0.21	9.09
	Ω_{NS}	ERS-2	10.17	-61.37	50.61	-1.03	10.12
		GFO-1	9.77	-186.67	101.22	-2.85	9.35
		Jason-1	8.49	-65.90	67.55	-0.07	8.49
		Envisat	9.35	-29.71	40.95	2.76	8.94
		POSEIDON	9.30	-93.55	68.50	-0.24	9.30
		TOPEX	8.13	-76.17	49.20	0.19	8.12

Wadden Sea, which is a very small region compared to the whole model domain. This is already reflected by the rms error that is only 0.10 cm. As noted in Section 3.6.1.2, the Wadden Sea is a complicated area partly located in the intertidal zone. Changing the bathymetry means that computational cells inside this region for a shorter or longer time are wet (depending on the sign of the correction applied to the depth).

Because we have hardly any radar altimeter data inside the Wadden Sea, we cannot assess the impact of this correction on the simulation of the dynamic topography there. Over the whole model domain and North Sea, the comparison with the statistics of Experiment Ia and those provided in Table 3.5 suggest the impact is negligible compared to other errors in model and data.

3.6.4 Experiment IV: influence of deriving the steric contribution to the open sea boundary conditions from altimeter data

Steric heights expressed relative to the quasi-geoid at the open boundaries can also be obtained from radar altimeter data (see Section 3.4.3). This has the advantage that no correction is needed for the net expansion/compaction of the global oceans, since this signal becomes part of the prescribed water levels at the open sea boundaries. In Experiment IV, we evaluate whether this provides any model improvement. In addition, this experiment enables to assess the impact of quasi-geoid errors on the model-derived MDT. This, in turn, answers the question to which extent expected

quasi-geoid improvements, achieved when data provided by the Gravity field and steady-state Ocean Circulation Explorer (GOCE) mission (Drinkwater et al. 2003) are included in future updates of EGG08, improve the model. Indeed, to obtain the time series of steric heights expressed relative to EGG08, we need to subtract the quasi-geoid heights from the SSHs (Section 3.5.4). Hence, quasi-geoid errors become part of the derived steric signal. A proxy for these errors is given in Fig. 3.1, which shows a spatial rendition of the differences between $\overline{\zeta_{\mathrm{O}}}$ and $\overline{\zeta_{\mathrm{P}}}$. While these differences also contain errors in the MSL, which can be estimated with a standard deviation of 4–10 cm (Andersen & Knudsen 2009), and errors introduced by using the Boussinesq approximation (Greatbatch et al. 2001), this interpretation is somewhat pessimistic. On the other hand, it is the upper bound; although it might be that part of the actual errors cancelled out when computing the differences between $\overline{\zeta_{\mathrm{O}}}$ and $\overline{\zeta_{\mathrm{P}}}$.

Table 3.6 provides the statistics of the pointwise differences between $\overline{\zeta_{\mathrm{D_{Ia}}}}$ and $\overline{\zeta_{\mathrm{D_{IV}}}}$, while Fig. 3.11 shows a spatial rendition of these differences. From this map, we observe that the largest differences are off the shelf; $\sim$5 cm northwest to Ireland. In the Celtic Sea, Irish Sea, and English Channel the differences are $>$ 2 cm, while for the whole North Sea they are $\sim$1 cm. Therefore, we conclude that quasi-geoid errors along the open sea boundaries hardly propagate into the model domain. This also implies that any improvement in the quasi-geoid will have a limited impact on the MDT inside the model domain. Note that this result does not mean that an improved quasi-geoid does not provide any advantage. Indeed, the calibration of DCSM using radar altimeter data and quasi-geoid data would benefit directly from an improved quasi-geoid. Furthermore, the conclusion only applies to the approach of vertical referencing followed in this study (prescribing water levels relative to the quasi-geoid at the open sea boundaries). To better constrain the quasi-geoid, we could examine the possibility to also assimilate observed (radar altimetry) instantaneous water levels in the model domain (referring to the quasi-geoid) into the hydrodynamic model. The assimilation could be realized using an Ensemble Kalman Filter (Evensen 1994, 2003); model parameters to be constrained could be identified by a sensitivity analysis.

The impact of using steric heights derived from radar altimetry rather than from the POL3DB model can be nicely observed in Fig. 3.6c that shows, for each grid point, the standard deviation of the differences between the monthly mean water levels computed in this experiment and those derived from POL's hindcast. Compared to Fig. 3.6a, we observe that everywhere, but mainly along the open sea boundaries and inside the Celtic Sea, Irish Sea, and the English Channel, the standard deviations of the differences between POL's and DCSM's monthly mean water levels increase from $\sim$1.0 cm to $>$3.0 cm. This can be understood by the fact that in Experiment Ia both the pressure gradients induced by water density variations and the steric contribution to the water levels at the open sea boundaries are derived from POL's hindcast, which are fully consistent with each other. In Experiment IV, there is no consistency

Table 3.6: Experiment IV: statistics of the differences between the MDT's derived in Experiment Ia and Experiment IV, as well as the aggregate and satellite-specific statistics of the differences between the observed and modeled dynamic topography computed over both the whole model domain (Ω_D) and North Sea (Ω_{NS}). All values are provided in cm.

differences	domain	satellite	rms	min	max	mean	std
$\overline{\zeta_{D_{Ia}}} - \overline{\zeta_{D_{IV}}}$	Ω_D	n/a	2.23	-4.57	17.42	-0.42	2.19
	Ω_{NS}	n/a	0.88	-2.15	0.55	-0.77	0.43
$\zeta_O(t) - \zeta_{D_{IV}}(t)$	Ω_D	all	10.57	-183.57	267.46	-0.22	10.57
	Ω_{NS}		9.26	-183.57	103.79	-1.13	9.19
	Ω_D	ERS-2	10.95	-67.75	107.32	0.33	10.95
		GFO-1	11.43	-183.57	267.46	-2.05	11.25
		Jason-1	9.78	-64.78	89.29	1.07	9.72
		Envisat	10.26	-38.76	54.32	0.25	10.26
		POSEIDON	10.14	-104.39	66.98	1.12	10.08
		TOPEX	9.37	-159.57	82.82	0.97	9.32
	Ω_{NS}	ERS-2	9.76	-67.75	46.96	-1.10	9.70
		GFO-1	9.92	-183.57	103.79	-3.09	9.43
		Jason-1	8.65	-64.78	68.19	0.77	8.62
		Envisat	9.22	-33.23	41.45	-0.02	9.22
		POSEIDON	9.22	-89.45	66.98	0.04	9.22
		TOPEX	8.14	-74.37	50.97	0.32	8.13

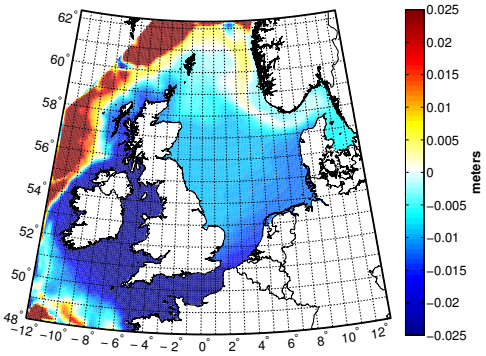

Figure 3.11: Difference in model-derived MDT computed over the entire simulation period January 1, 2000 to January 1, 2003, as derived from Experiment Ia and Experiment IV.

between those fields. Apparently, a part of these inconsistencies propagates into the model domain. This results in increased differences compared to POL's monthly mean water levels.

No significant differences are observed between the statistics obtained in Experiment IV compared to those of Experiment Ia. Over Ω_D, we obtain 10.45 cm (Experiment Ia) and 10.57 cm (Experiment IV), Over Ω_{NS}, 9.31 cm (Experiment Ia) and 9.26 cm (Experiment IV). On the other hand, compared to Experiment Ia, we obtain an improved representation of the annual signal as shown in Fig. 3.10c. Indeed, compared to Fig. 3.10a, the amplitudes of the remaining annual cycle are significantly reduced. The latter could be expected since any error in the applied corrections for the net expansion/contraction of the oceans is avoided in Experiment IV. Compared

to the representation obtained in Experiment II (Fg. 3.10b), we observe an improvement in the region off the shelf and Celtic Sea, but a slightly degraded performance in the southern North Sea.

3.7 Summary and conclusions

We developed a methodology to extend the two-dimensional DCSM such that it provides estimates of the instantaneous water levels relative to a particular (quasi-)geoid. This opens a wide range of new applications of such a model in coastal engineering, hydrography, and geodesy. The overall procedure can be applied to other 2D storm surge models as well. The method involved two steps. First, we added to DCSM the baroclinic forcing. This has been done by adding the depth-averaged baroclinic pressure gradient terms as diagnostic variables. They are computed from temperature and salinity values derived from the Atlantic- European North West Shelf- Ocean Physics Hindcast (POL's hindcast) carried out with the POL 3D baroclinic model. The steric contribution that needs to be added to the water levels prescribed at the open sea boundaries can be derived from either an ocean circulation model, as well as from radar altimeter data. In the latter case, we immediately account for the net steric expansion/contraction signal of the global oceans, which is not possible when using Boussinesq ocean circulation models. Second, we adjusted the model parameters that depend on the choice of the reference surface (e.g., bathymetry) and referred the water levels along the open boundaries to the quasi-geoid. Besides the fact that the model becomes conceptually clearer, a proper vertical reference has some benefits and is even required for some (new) applications. The benefits are, among others, that it becomes possible to link off-shore observations to an absolute reference without ignoring biases, that it enables to provide absolute referencing for off-shore locations, and that it enables to provide properly referenced off-shore forecasts. In addition, proper referencing is required to link model, tide-gauges, and altimeter data beyond current practice of ignoring biases.

In a number of numerical simulations with the extended, vertically referenced model, we quantified and analyzed the errors in the derived (mean) dynamic topography using as reference (i) (monthly) mean water levels from POL's hindcast and (ii) differences between ellipsoidal heights of the instantaneous sea surface from radar altimeter satellites and EGG08 quasi-geoid heights. We showed that the 2D model was able to reproduce POL's MDT and monthly mean water levels. The time-averaged differences between the observed and modeled dynamic topography likely reveal quasi-geoid errors in the Celtic Sea and an overestimation of the inflow from the Atlantic Ocean along Shetland, the Fair Isle Current, and of the Norwegian Coastal Current, but an underestimation of the inflow from the Atlantic Ocean along the western side of the Norwegian Trench.

Compared to the original DCSM model, the extended DCSM model provides an improved representation of the MDT. Over the whole model domain, the standard deviation of the differences between the observation- and model-derived MDT decreases from 8.10 cm to 5.71 cm, while over the North Sea it decreases from 4.40 cm to 3.98 cm. In the representation of the dynamic topography over the North Sea, no significant differences between the original and extended DCSM model are observed in the statistics; 9.29 cm (original DCSM) and 9.31 cm (extended DCSM). Apparently, the improvements are within the level of remaining model errors and have a negligible effect on the computed bulk statistics.

In addition, we showed that the order of magnitude of errors in the used bathymetry, introduced by using MSL rather than the quasi-geoid as the vertical datum, have no significant impact on the modeled instantaneous water levels and the model-derived MDT.

From the experiments, we also conclude that the quasi-geoid is only weakly constrained by prescribed water levels along the open sea boundaries. Hence, if another quasi-geoid is chosen as reference surface, the water levels along the open sea boundaries change accordingly, but this change will not propagate much into the model domain. Therefore, a better approach to vertically reference a hydrodynamic model is to assimilate instantaneous water levels in the model domain into the hydrodynamic model. These instantaneous water levels can be computed as differences between sea surface data from radar altimetry and a quasi-geoid model. The assimilation could be realized using an Ensemble Kalman Filter (Evensen 1994, 2003); model parameters to be constrained could be identified by a sensitivity analysis. Whether this improves the quality of the modeled water levels needs to be investigated. Moreover, whether it is feasible to implement such an approach needs to be investigated due to the numerical complexity of the model and the amount of input data.

The overall skill of the extended DCSM to model the dynamic topography is 9–11 cm rms, which improves to 8–10 cm on the North Sea. About 25% of these errors can be explained by a bias between the modeled water levels and the observed water levels acquired during a single satellite pass. No statistically significant differences were observed if the steric heights expressed relative to the quasi-geoid are derived from radar altimeter data. Compared to the original approach described in Section 3.3 of implicitly representing the steric signal via the open sea boundary conditions (applied in Experiment II), we observe no significant changes in the bulk statistics. We do, however, observe a worse representation of the seasonal water level cycle, in particular, in the North Sea. When using steric heights derived from radar altimeter data, the seasonal water level cycle is better represented. Nevertheless, on the North Sea the original approach still provides better results.

Chapter 4

Estimation of the quasi-geoid

4.1 Introduction

The second part of the flowchart presented in Chapter 2 is the actual estimation of the quasi-geoid. Here, our main research objective is to quantify in terms of quasi-geoid height differences the added value of the use of a shallow water hydrodynamic model for the dynamic topography (DT) corrections needed to reduce the altimeter-derived sea surface heights (SSHs) to geometric quasi-geoid heights up to some long-wavelength errors likely dominated by radial orbit errors. Since in particular the contribution of the astronomical tide to these corrections computed with such a model is expected to improve the quasi-geoid (Section 1.3.2), the analysis is carried out *with* and *without* the surge and steric contributions in the applied DT corrections. As a reference if we do not include the surge and steric contributions, we use the ocean tide corrections computed with the global ocean tide model GOT4.7 (see Ray (1999) and Section 3.5.4). If we do include them, the GOT4.7 tide corrections in the reference set are supplemented by surge corrections computed using the MOG2D model (see Carrère & Lyard (2003) and Section 3.5.4) and corrections for the time-averaged steric contribution computed as differences between the DTU10 mean sea surface model (DTU10-MSS) (Andersen 2010) and the EGG08 quasi-geoid (Denker et al. 2008).

Prior to the estimation of the different quasi-geoids, we will compare for nine passes the mean signal and noise power spectral densities (PSDs) of the residual along-track deflections of the vertical (DoV) obtained after applying different sets of DT corrections to the SSHs. Doing so helps to assess observed differences among the estimated quasi-geoids. Indeed, since the quasi-geoids need to be estimated based on a combination of heterogeneous data, differences can, for instance, also be introduced by

different estimates of the weights assigned to the observation groups. Here, we use variance component estimation (VCE) techniques to determine the weights.

Before we continue, we first need to evaluate what the implications are of our findings in obtaining a proper vertically referenced model (Chapter 3) for the proposed iterative approach (Chapter 2) to the simultaneous realization of such a model and a proper quasi-geoid. One of the most important findings is that the actual procedure to vertically reference DCSM hardly benefits from an improved quasi-geoid (Section 3.6.4). Consequently, no iterations are required. Furthermore, this implies that for the numerical experiments carried out to assess the impact of the various contributors to the DT corrections we do not need to estimate the quasi-geoid over DCSM's whole model domain. This strongly reduces the computational load. Only as a final step we estimate the quasi-geoid over the whole model domain, since we need it to compute the ellipsoidal heights of LAT and MSL. We would like to stress that this simplification is only justified for the applied vertical referencing procedure; if observed water levels expressed relative to the quasi-geoid are assimilated into the model, as proposed in Section 3.7, iterations are likely necessary. It should also be noted that since we use radar altimeter data in the form of along-track DoV, we get rid of the identified biases between the modeled and observed water levels of a single satellite pass (Section 3.6.1.4). Finally, no attempt is made to reduce the propagation of the identified errors in DCSM's DT corrections to the quasi-geoid associated with the used salinity and temperature fields (Section 3.6.1.3).

In this chapter, we first describe our computational strategy. In particular, we focus on (i) the used radial basis function (RBF) parameterization and (ii) the procedure we apply to obtain proper weight factors for the various observation groups. Next, we introduce the various data sets used in the estimation/validation of the quasi-geoid, and we describe the applied preprocessing steps. After that, we present and discuss for nine passes of TOPEX data the comparison of the mean signal and noise PSDs of the residual along-track DoV obtained after applying various sets of DT corrections. Thereafter, we use the various sets of DoV together with the other data to quantify the impact of the various DT corrections on the estimated quasi-geoid. Finally, we present and validate the quasi-geoid needed to compute the ellipsoidal heights of LAT and MSL over DCSM's model domain.

4.2 Computational strategy

4.2.1 Remove-compute-restore

In this study, the classical remove-compute-restore technique (RCR) (Sjöberg 2005, and cited studies) is used to estimate the quasi-geoid; the quasi-geoid is obtained by

the sum of the global field contribution (spherical harmonic expansion of a satellite-only geopotential model) and the contribution estimated from the residual gravity and radar altimeter data. Note that if a terrain correction was applied to the free-air gravity anomalies (FAA), a third contribution would have shown up that represents some short-wavelength components of the quasi-geoid.

We agree that the classical RCR technique is suboptimal as the variance-covariance matrix of the satellite-only geopotential model is not used in the estimation process. As shown by Wittwer (2009, Chapter 7), a joint inversion of both terrestrial and satellite data yields combined solutions that are significantly better than a solution obtained using the classical RCR technique. However, in his experiments only simulated data sets were used, and the noise in the terrestrial data was approximately white. As was concluded, the presence of colored noise could lead to a significantly lower quality of the combined solution unless a more accurate stochastic model is used. Colored noise is expected in particular for airborne and shipboard gravity data, EGG08-derived DoV, and altimeter-derived along-track DoV. While deriving a proper description of the noise model for each observation group is out of the scope of this thesis, we stick to the well-known classical RCR technique.

4.2.2 Parameterization

4.2.2.1 Background

Spherical radial basis functions, or simply radial basis functions (RBFs), are radially symmetric functions that have most of their energy confined to a spherical cap of limited size. The function depends only on the spherical distance between two points on the sphere. RBFs are often used in regional gravity field modeling (Schmidt et al. 2007, Klees et al. 2008, and cited studies). According to Klees et al. (2008), their popularity is due to the following properties:

1. When located inside the masses, the harmonicity outside the masses is guaranteed.
2. They lead to simple functional models for all relevant gravity field functionals.
3. They are suited both for global and local gravity field modeling.
4. They allow for local refinements of a global spherical harmonic representation of the gravity field.
5. They can be easily adapted to the data distribution and the signal variation.

4.2.2.2 Preliminaries

Following Wittwer (2009), we denote by σ_R the surface of the sphere of radius R, which is located completely inside the topographic masses (Bjerhammar sphere), $\sigma_R = \left\{(x_1,x_2,x_3) : x_1^2+x_2^2+x_3^2 = R^2\right\}$. Int σ_R denotes the interior and Ext σ_R denotes the exterior of the Bjerhammar sphere. Two points $\mathbf{x}$, $\mathbf{y} \in \mathbb{R}^3$, $\mathbf{y} \neq 0$, with $\mathbf{x} = (x_1,x_2,x_3)^\mathsf{T} \in$ Ext σ_R and $\mathbf{y} = (y_1,y_2,y_3)^\mathsf{T} \in$ Int σ_R with unit vectors $\hat{\mathbf{x}} = \frac{\mathbf{x}}{|\mathbf{x}|}$, $\hat{\mathbf{y}} = \frac{\mathbf{y}}{|\mathbf{y}|}$ are considered. The exterior RBF centered at $\mathbf{y}_i$ and evaluated at $\mathbf{x}$ is

$$\Psi_i(\mathbf{x},\mathbf{y}_i) = \sum_{l=0}^{\infty} \psi_l \left(\frac{R}{|\mathbf{x}|}\right)^{l+1} P_l(\hat{\mathbf{x}}^\mathsf{T}\hat{\mathbf{y}}_i^\mathsf{T}), \tag{4.1}$$

where P_l is the Legendre polynomial of degree l and ψ_l are the Legendre coefficients. The exterior RBF is a harmonic function in Ext σ_R. It is a zonal function, i.e., it is rotationally symmetric around the axis $\hat{\mathbf{y}}_i$.

4.2.2.3 Functional and stochastic models

The residual disturbing potential T is expressed as a linear combination of K RBFs

$$T(\mathbf{x}) = \sum_{i=1}^{K} \alpha_i \Psi_i(\mathbf{x},\mathbf{y}_i), \tag{4.2}$$

where the coefficients α_i need to be estimated from the data using least-squares techniques. The data are residual gravity anomalies (Δg), residual gravity disturbances (δg), and residual DoV (ε) in direction τ. After linearization and/or spherical approximation they are related to the disturbing potential as

$$\Delta g(\mathbf{x}) = -\frac{\partial T(\mathbf{x})}{\partial |\mathbf{x}|} - \frac{2}{|\mathbf{x}|} T(\mathbf{x}), \tag{4.3}$$

$$\delta g(\mathbf{x}) = -\frac{\partial T(\mathbf{x})}{\partial |\mathbf{x}|}, \tag{4.4}$$

$$\varepsilon(\mathbf{x}) = -\frac{\partial \zeta(\mathbf{x})}{\partial s} = -\frac{1}{\gamma(\mathbf{x}')}\frac{\partial T(\mathbf{x})}{\partial s} = \xi(\mathbf{x})\cos\tau + \eta(\mathbf{x})\sin\tau, \tag{4.5}$$

where $\zeta(\mathbf{x})$ is the residual height anomaly, s is the incremental distance along the satellite's ground track, γ is the normal gravity, $\mathbf{x}'$ is the point on the telluroid associated with the surface point $\mathbf{x}$ by a telluroid mapping, τ is the azimuth of the gradient (if Eq. (4.5) is applied to radar data, τ is the azimuth of the radar satellite ground track), $\xi(\mathbf{x})$ is the residual DoV in north direction, which is in spherical approxima-

tion

$$\xi(\mathbf{x}) = -\frac{1}{|\mathbf{x}|\gamma(\mathbf{x}')}\frac{\partial T(\mathbf{x})}{\partial \varphi_{\mathbf{x}}}, \tag{4.6}$$

and $\eta(\mathbf{x})$ is the residual DoV in east direction, which is in spherical approximation

$$\eta(\mathbf{x}) = -\frac{1}{|\mathbf{x}|\gamma(\mathbf{x}')\cos\varphi_{\mathbf{x}}}\frac{\partial T(\mathbf{x})}{\partial \lambda_{\mathbf{x}}}. \tag{4.7}$$

$\varphi_{\mathbf{x}}$, $\lambda_{\mathbf{x}}$, and $|\mathbf{x}|$ are the spherical coordinates of $\mathbf{x}$. Note that the minus sign in Eq. (4.5) is a convention (pp. 116–119 Hofmann-Wellenhof & Moritz 2005). To compute the quasi-geoid heights from the estimated RBF coefficients, we also need the functional model for height anomalies, which reads to the same level of approximation

$$\zeta(\mathbf{x}) = \frac{T(\mathbf{x})}{\gamma(\mathbf{x}')}. \tag{4.8}$$

Note that it does not matter whether the quantities T, ξ, and η are evaluated at the surface point ($\mathbf{x}$) or the telluroid point ($\mathbf{x}'$).

Combining Eq. (4.2) with Eq. (4.3) provides the observation equation for (residual) gravity anomalies

$$\Delta g(\mathbf{x}) = \sum_{i=1}^{K}\left(-\frac{\partial}{\partial|\mathbf{x}|}\Psi_i(\mathbf{x},\mathbf{y}_i) - \frac{2}{|\mathbf{x}|}\Psi_i(\mathbf{x},\mathbf{y}_i)\right)\alpha_i. \tag{4.9}$$

For (residual) gravity disturbances the observation equation is (combining Eq. (4.2) with Eq. (4.4))

$$\delta g(\mathbf{x}) = \sum_{i=1}^{K} -\frac{\partial}{\partial|\mathbf{x}|}\Psi_i(\mathbf{x},\mathbf{y}_i)\alpha_i. \tag{4.10}$$

For the (residual) DoV in north (Eq. (4.2) and Eq. (4.6)) and east (Eq. (4.2) and Eq. (4.7)) direction the observation equations are

$$\xi(\mathbf{x}) = \sum_{i=1}^{K} -\frac{1}{|\mathbf{x}|\gamma(\mathbf{x}')}\frac{\partial}{\partial\varphi_{\mathbf{x}}}\Psi_i(\mathbf{x},\mathbf{y}_i)\alpha_i, \tag{4.11}$$

$$\eta(\mathbf{x}) = \sum_{i=1}^{K} -\frac{1}{|\mathbf{x}|\gamma(\mathbf{x}')\cos\varphi_{\mathbf{x}}}\frac{\partial}{\partial\lambda_{\mathbf{x}}}\Psi_i(\mathbf{x},\mathbf{y}_i)\alpha_i. \tag{4.12}$$

Substituting both Eq. (4.11) and Eq. (4.12) into Eq. (4.5) provides the observation equation for DoV in an arbitrary direction τ.

These functional models can be written as general Gauss-Markov models

$$\mathbf{y}_k = \mathbf{A}_k\mathbf{x} + \mathbf{e}_k, \tag{4.13}$$

where $\mathbf{y}_k$ is the $m_k \times 1$ vector of observations of observation group k, $\mathbf{A}_k$ is the $m_k \times n$ design matrix of observation group k, $\mathbf{x}$ is the $n \times 1$ vector of unknown coefficients α_i, and $\mathbf{e}_k$ is the $m_k \times 1$ vector of residuals of observation group k. For the p observation groups together, the Gauss-Markov model reads

$$\mathbf{y} = \mathbf{A}\mathbf{x} + \mathbf{e}, \tag{4.14}$$

where

$$\mathbf{y} = \begin{pmatrix} \mathbf{y}_1 \\ \vdots \\ \mathbf{y}_p \end{pmatrix}, \mathbf{A} = \begin{pmatrix} \mathbf{A}_1 \\ \vdots \\ \mathbf{A}_p \end{pmatrix}, \text{ and } \mathbf{e} = \begin{pmatrix} \mathbf{e}_1 \\ \vdots \\ \mathbf{e}_p \end{pmatrix}. \tag{4.15}$$

The stochastic properties of the residuals are described by the stochastic model

$$E\{\mathbf{e}\} = 0,\ E\{\mathbf{e}\mathbf{e}^\mathsf{T}\} = D\{\mathbf{e}\} = \mathbf{Q}_y, \tag{4.16}$$

where $E\{\cdot\}$ denotes the expectation operator, $D\{\cdot\}$ the dispersion operator, and $\mathbf{Q}_y$ is the variance-covariance matrix of the observations.

4.2.2.4 Choices to be made

When using RBFs in gravity field modeling, a number of choices have to be made (Klees et al. 2008):

1. The type of the RBF.
2. The location of the basis function centers, referred to as the network design.
3. The bandwidth (depth) of the RBFs.
4. The number of RBFs.

In the remainder of this subsection, the choices made in this study are described and motivated. The choices 3 and 4 are closely related, and are therefore discussed simultaneously.

Type of the RBF In practice, many different RBFs are used. For some of them, an analytical expression is available. This is attractive, since then the computational load is significantly reduced. Tenzer & Klees (2008) showed by a numerical study that for different types of RBFs comparable accuracies are obtained provided the bandwidth is chosen properly. In their study, they considered the point-mass kernel,

radial multipoles (Marchenko 1998), Poisson wavelets (Holschneider et al. 2003), and the Poisson kernel. For all these kernels, analytical expressions exist. Following Wittwer (2009), we use the Poisson wavelets of order $n = 3$, for which the analytical expression is (Klees et al. 2007)

$$\Psi_n(\mathbf{x},\mathbf{y}) = \frac{1}{4\pi R^2}\left(2\chi_{n+1} + \chi_n\right), \tag{4.17}$$

with

$$\chi_n(\mathbf{x},\mathbf{y}) = \left(|\mathbf{y}|\frac{\partial}{\partial|\mathbf{y}|}\right)^n \frac{1}{|\mathbf{x}-\mathbf{y}|}. \tag{4.18}$$

Note that to simplify the notation, we omitted the index i. The operator $\left(|\mathbf{y}|\frac{\partial}{\partial|\mathbf{y}|}\right)$ takes the partial derivative of $\frac{1}{|\mathbf{x}-\mathbf{y}|}$ with respect to $|\mathbf{y}|$ and multiplies the result by $|\mathbf{y}|$. n indicates how often the operator has to be applied. So,

$$\chi_0(\mathbf{x},\mathbf{y}) = \frac{1}{|\mathbf{x}-\mathbf{y}|}, \tag{4.19}$$

$$\chi_1(\mathbf{x},\mathbf{y}) = |\mathbf{y}|\left(\frac{\partial}{\partial|\mathbf{y}|}\chi_0(\mathbf{x},\mathbf{y})\right), \tag{4.20}$$

$$\chi_2(\mathbf{x},\mathbf{y}) = |\mathbf{y}|\left(\frac{\partial}{\partial|\mathbf{y}|}\chi_1(\mathbf{x},\mathbf{y})\right). \tag{4.21}$$

Klees et al. (2007) provide a recurrence relation for $\Psi_n(\mathbf{x},\mathbf{y})$ that makes use of the recurrence relation derived for radial multipoles (Marchenko 1998) defined as

$$b_n(\mathbf{x},\mathbf{y}) = \left(\frac{\partial}{\partial|\mathbf{y}|}\right)^n \frac{1}{|\mathbf{x}-\mathbf{y}|}. \tag{4.22}$$

For $n \geq 2$,

$$b_n(\mathbf{x},\mathbf{y}) = (2n-1)|\mathbf{x}-\mathbf{y}|b_1\, b_{n-1} - (n-1)^2 b_0^2\, b_{n-2}, \tag{4.23}$$

with

$$b_0(\mathbf{x},\mathbf{y}) = \frac{1}{|\mathbf{x}-\mathbf{y}|}, \tag{4.24}$$

and

$$b_1(\mathbf{x},\mathbf{y}) = \frac{|\mathbf{y}| - |\mathbf{x}|\cos\theta}{|\mathbf{x}-\mathbf{y}|^3}, \tag{4.25}$$

with $\cos\theta = \hat{\mathbf{x}}^{\mathsf{T}}\hat{\mathbf{y}}$. After establishing the relation between $\chi_n(\mathbf{x},\mathbf{y})$ and $b_n(\mathbf{x},\mathbf{y})$, which is

$$\chi_n(\mathbf{x},\mathbf{y}) = \sum_{j=1}^{n} \rho_{n,j}|\mathbf{y}|^j b_j, \tag{4.26}$$

the recurrence relation for $\Psi_n(\mathbf{x},\mathbf{y})$ is given by

$$4\pi R^2\Psi_n(\mathbf{x},\mathbf{y}) = \begin{cases} 2|\mathbf{y}|^{n+1}b_{n+1} + \sum\limits_{j=1}^{n}\beta_{n,j}|\mathbf{y}|^j b_j & \text{for } n \geq 1, \\ 2|\mathbf{y}|b_1 + b_0 & \text{for } n = 0, \end{cases} \tag{4.27}$$

where $\beta_{n,j} = 2\rho_{n+1,j} + \rho_{n,j}$ and the real coefficients $\rho_{n,i}$ fulfill the relations

$$\begin{aligned} \rho_{n,1} &= 1, \quad \text{for all } n, \\ \rho_{n,2} &= \rho_{n-1,1} + 2\rho_{n-1,2}, \\ \rho_{n,3} &= \rho_{n-1,2} + 3\rho_{n-1,3}, \\ &\vdots \\ \rho_{n,j} &= \rho_{n-1,j-1} + j\rho_{n-1,j}, \quad \text{for } j = 2,3,\ldots,n-1. \end{aligned}$$

The factors $\beta_{3,j},\ j = 1,2,3$ needed to construct the Poisson wavelets of order three are $\beta_{3,1} = 3$, $\beta_{3,2} = 17$, and $\beta_{3,3} = 13$.

To build the design matrix, we need to derive $\frac{\partial}{\partial|\mathbf{x}|}\Psi_n(\mathbf{x},\mathbf{y})$ for the gravity anomalies and gravity disturbances, $\frac{\partial}{\partial\varphi_\mathbf{x}}\Psi_n(\mathbf{x},\mathbf{y})$ for the DoV in north direction, and $\frac{\partial}{\partial\lambda_\mathbf{x}}\Psi_n(\mathbf{x},\mathbf{y})$ for the DoV in east direction. Making use of the recurrence relation for $\Psi_n(\mathbf{x},\mathbf{y})$, Klees et al. (2007) derived for $\frac{\partial}{\partial|\mathbf{x}|}\Psi_n(\mathbf{x},\mathbf{y})$

$$\frac{\partial\Psi_n(\mathbf{x},\mathbf{y})}{\partial|\mathbf{x}|} = 2|\mathbf{y}|^{n+1}\frac{\partial b_{n+1}}{\partial|\mathbf{x}|} + \sum_{j=1}^{n}\beta_{n,j}\,|y|^j\,\frac{\partial b_j}{\partial|\mathbf{x}|}, \tag{4.28}$$

where for $n \geq 2$

$$\begin{aligned} \frac{\partial b_n}{\partial|\mathbf{x}|} = (2n-1)b_1\,b_{n-1}\frac{\partial|\mathbf{x}-\mathbf{y}|}{\partial|\mathbf{x}|} + (2n-1)|\mathbf{x}-\mathbf{y}|\left[\frac{\partial b_1}{\partial|\mathbf{x}|}b_{n-1} + b_1\frac{\partial b_{n-1}}{\partial|\mathbf{x}|}\right] \\ -(n-1)^2\left[2b_0\frac{\partial b_0}{\partial|\mathbf{x}|}\,b_{n-2} + b_0^2\frac{\partial b_{n-2}}{\partial|\mathbf{x}|}\right], \end{aligned} \tag{4.29}$$

with

$$\frac{\partial|\mathbf{x}-\mathbf{y}|}{\partial|\mathbf{x}|} = \frac{|\mathbf{x}| - |\mathbf{y}|\cos\theta}{|\mathbf{x}-\mathbf{y}|}, \tag{4.30}$$

$$\frac{\partial b_0}{\partial|\mathbf{x}|} = -\frac{|\mathbf{x}| - |\mathbf{y}|\cos\theta}{|\mathbf{x}-\mathbf{y}|^3}, \tag{4.31}$$

$$\frac{\partial b_1}{\partial|\mathbf{x}|} = \frac{\cos\theta}{|\mathbf{x}-\mathbf{y}|^3} + \frac{3}{|\mathbf{x}-\mathbf{y}|^5}\left(|\mathbf{x}||\mathbf{y}|(1+\cos\theta) - (|\mathbf{x}|^2+|\mathbf{y}|^2)\cos\theta\right). \tag{4.32}$$

The equations for $\frac{\partial}{\partial\varphi_{\mathbf{x}}}\Psi_n(\mathbf{x},\mathbf{y})$, $\frac{\partial}{\partial\lambda_{\mathbf{x}}}\Psi_n(\mathbf{x},\mathbf{y})$, and also $\frac{\partial b_n}{\partial\varphi_{\mathbf{x}}}$ and $\frac{\partial b_n}{\partial\lambda_{\mathbf{x}}}$, are similar to those given in Eq. (4.28) and Eq. (4.29) after replacing $\partial|\mathbf{x}|$ by $\partial\varphi_{\mathbf{x}}$ and $\partial\lambda_{\mathbf{x}}$, respectively. Omitting all intermediate steps, we obtain for $\frac{\partial|\mathbf{x}-\mathbf{y}|}{\partial\varphi_{\mathbf{x}}}$, $\frac{\partial}{\partial\varphi_{\mathbf{x}}}b_0(\mathbf{x},\mathbf{y})$, and $\frac{\partial}{\partial\varphi_{\mathbf{x}}}b_1(\mathbf{x},\mathbf{y})$

$$\frac{\partial|\mathbf{x}-\mathbf{y}|}{\partial\varphi_{\mathbf{x}}} = \frac{x_3\,y_2\,\sin\lambda_{\mathbf{x}} - |\mathbf{x}|\,y_3\,\cos\varphi_{\mathbf{x}} + x_3\,y_1\,\cos\lambda_{\mathbf{x}}}{|\mathbf{x}-\mathbf{y}|}, \tag{4.33}$$

$$\frac{\partial b_0}{\partial\varphi_{\mathbf{x}}} = -\frac{x_3\,y_2\,\sin\lambda_{\mathbf{x}} - |\mathbf{x}|\,y_3\,\cos\varphi_{\mathbf{x}} + x_3\,y_1\,\cos\lambda_{\mathbf{x}}}{|\mathbf{x}-\mathbf{y}|^3}, \tag{4.34}$$

$$\frac{\partial b_1}{\partial\varphi_{\mathbf{x}}} = \frac{1}{|\mathbf{y}|}\frac{\partial b_0}{\partial\varphi_{\mathbf{x}}} + \frac{(3\,|\mathbf{y}| - 3|\mathbf{x}|\cos\theta)\;(x_3\,y_2\,\sin\lambda_{\mathbf{x}} - |\mathbf{x}|\,y_3\,\cos\varphi_{\mathbf{x}} + x_3\,y_1\,\cos\lambda_{\mathbf{x}})}{|\mathbf{x}-\mathbf{y}|^5}, \tag{4.35}$$

where x_1, x_2, and x_3 are related to the spherical coordinates $\varphi_{\mathbf{x}}$, $\lambda_{\mathbf{x}}$, and $|\mathbf{x}|$ by

$$x_1 = |\mathbf{x}|\cos\varphi_{\mathbf{x}}\cos\lambda_{\mathbf{x}}, \tag{4.36}$$

$$x_2 = |\mathbf{x}|\cos\varphi_{\mathbf{x}}\sin\lambda_{\mathbf{x}}, \tag{4.37}$$

$$x_3 = |\mathbf{x}|\sin\varphi_{\mathbf{x}}, \tag{4.38}$$

and y_1, y_2, and y_3 are related to the spherical coordinates $\varphi_{\mathbf{y}}$, $\lambda_{\mathbf{y}}$, and $|\mathbf{y}|$ by similar relations as provided for x_1, x_2, and x_3, respectively. For $\frac{\partial|\mathbf{x}-\mathbf{y}|}{\partial\lambda_{\mathbf{x}}}$, $\frac{\partial}{\partial\lambda_{\mathbf{x}}}b_0(\mathbf{x},\mathbf{y})$, and $\frac{\partial}{\partial\lambda_{\mathbf{x}}}b_1(\mathbf{x},\mathbf{y})$, we obtain

$$\frac{\partial|\mathbf{x}-\mathbf{y}|}{\partial\lambda_{\mathbf{x}}} = \frac{x_2\,y_1 - x_1\,y_2}{|\mathbf{x}-\mathbf{y}|}, \tag{4.39}$$

$$\frac{\partial b_0}{\partial\lambda_{\mathbf{x}}} = -\frac{x_2\,y_1 - x_1\,y_2}{|\mathbf{x}-\mathbf{y}|^3}, \tag{4.40}$$

$$\frac{\partial b_1}{\partial\lambda_{\mathbf{x}}} = \frac{1}{|\mathbf{y}|}\frac{\partial b_0}{\partial\lambda_{\mathbf{x}}} + \frac{(3\,x_2\,y_1 - 3\,x_1\,y_2)\;(|\mathbf{y}| - |\mathbf{x}|\cos\theta)}{|\mathbf{x}-\mathbf{y}|^5}. \tag{4.41}$$

RBF network design The locations of the RBF centers should be determined by the data distribution; for a regular data distribution (without gaps), the RBFs can be on an equal-angular/equal-area grid, for data with gaps, this is not appropriate. In practice, several implementations exist that treat the positioning of the RBFs as an optimization problem (e.g., Barthelmes 1986, Lehmann 1993, Marchenko 1998, Marchenko et al. 2001). However, these approaches are complex and time consuming. Alternatively, one can first place the RBFs on a grid and eventually refine this grid in a second step (Klees et al. 2008).

In this study, we use the data-adaptive approach used by Wittwer (2009); *all RBFs are placed on a grid where individual grid points are omitted if there are no observations available within a distance less than the correlation length of the basis functions.*

Application of this criterion ensures a stable solution provided the grid spacing is chosen properly. Note that we omit the "local refinement" step proposed by Klees et al. (2008). To obtain an as homogeneously as possible distributed set of grid points (as advocated by Eicker 2008), we use a Fibonacci grid (González 2010) of which the number of grid points, i.e., the grid resolution, can be easily adapted.

Contrary to Wittwer (2009), the RBFs are placed on a surface parallel to the topography (offshore this is the bathymetry). As shown by Tenzer et al. (2012), this is superior to the approach of placing them on a constant depth beneath the Bjerhammar sphere. The heights are linearly interpolated from the GEBCO_08 grid (General Bathymetric Chart of the Oceans (GEBCO) 2012); a global $30''$ grid generated by combining quality-controlled bathymetric survey data with interpolation between sounding points guided by altimeter-derived bathymetry and, on land, mainly data acquired by the Shuttle Radar Topography Mission. In generating the GEBCO_08 grid, it was assumed that all data refer to the MSL (General Bathymetric Chart of the Oceans 2012). Since the MSL is not defined on land, ellipsoidal heights are obtained after adding quasi-geoid heights computed using the Earth Gravitational Model 2008 (EGM2008) (Pavlis et al. 2012). As a consequence, the RBFs are not placed exactly on a surface parallel to the topography. This is, however, not significant as the differences between the quasi-geoid and MSL do not exceed 3 meters.

The bandwidth and number of RBFs Following Wittwer (2009), the bandwidth of the RBFs is defined as the correlation length, i.e., the spherical angle where the function decreases to half of its maximum value. It determines their approximation characteristics; the smaller this value, the higher the frequencies it can approximate. For the type of RBFs used in this study (Poisson wavelets of order $n = 3$), the bandwidth is determined by the radial distance $|\mathbf{y}|$ (having fixed the order, the radial distance is the only free parameter) and thus by the depth (the depth equals the height of the topography minus $|\mathbf{y}|$). The challenge is to find a proper value for the bandwidth/depth of the RBFs. This choice is always a trade-off between fit to the data and smoothness of the solution.

Besides the bandwidth, we also need to determine the number of RBFs. This number is controlled by the number of Fibonacci grid points within our computational domain before any grid point is omitted using the criterion specified on page 76 (Section 4.2.2.4). Together with the bandwidth, this number determines the stability and quality of the solution. Indeed, from a numerical point of view it is the number of RBFs that determines whether a bandwidth is too small or too large.

Numerical experiments (not presented here) have shown that it is hard to obtain a proper solution everywhere if we use the same bandwidth for all RBFs and we fix the grid resolution. In itself, this is no surprise; in mountainous areas the signal variance is higher compared to areas without topography. Hence, in these areas we

need to use more RBFs with a smaller bandwidth than elsewhere. By trial-and-error we fixed the depth (bandwidth) to 22.5 km and the grid resolution to 4.08 km. To find proper values for the bandwidth and number of RBFs outside the mountainous areas, we again exploit the fact that a proper quasi-geoid exists that comprises our whole computational region; EGG08. The combination of bandwidth and number of RBFs that provides a solution that best fits EGG08 is used in further computations. The number of Fibonacci grid points over the whole computational region (see Fig. 4.1 for an outline of this region) varies in increments of 5.000 from 60.000 to 90.000 and the depth (bandwidth) varies in increments of 5 km from 20 to 40 km. The quality of the fit is represented by the pointwise root mean square (rms) differences between the computed height anomalies and those obtained from EGG08, both evaluated on a $3' \times 3'$ equal-angular grid. To avoid a contamination of the rms differences by boundary effects, all grid points within 0.5° from the edges of the computational domain are excluded. To reduce the computational load, the rms differences are computed for two subregions of $7.5^\circ \times 7.5^\circ$ of which the one comprises a predominantly flat part of the computational domain (the Netherlands and southern North Sea, referred to as Ω_{A}) and the other a predominantly mountainous part (Scotland and its surrounding waters, referred to as Ω_{B}). See Fig. 4.1 for a geographical outline of both subregions. The results of this procedure are presented in Section 4.5.1.

4.2.3 Data weighting

As different disjunctive observation groups are used (terrestrial, airborne, shipboard, EGG08-derived DoV, and altimeter-derived along-track DoV), proper weight factors need to be derived to prevent over/underweighting of particular observation group(s). In this study, variance component estimation (VCE) is used; for the cofactor matrices of each disjunctive observation group ($\mathbf{Q}_k$) a scale factor (σ_k) is estimated so that the variance-covariance matrix of all observations ($\mathbf{Q}_y$) is given by

$$\mathbf{Q}_y = \sum_{k=1}^{p} \sigma_k^2 \mathbf{C}_k = \begin{pmatrix} \sigma_1^2\mathbf{Q}_1 & \mathbf{0} & \cdots & \mathbf{0} \\ \mathbf{0} & \sigma_2^2\mathbf{Q}_2 & \cdots & \mathbf{0} \\ \vdots & \vdots & \ddots & \vdots \\ \mathbf{0} & \mathbf{0} & \cdots & \sigma_p^2\mathbf{Q}_p \end{pmatrix}, \tag{4.42}$$

with

$$\mathbf{C}_1 = \begin{pmatrix} \mathbf{Q}_1 & \mathbf{0} & \cdots & \mathbf{0} \\ \mathbf{0} & \mathbf{0} & \cdots & \mathbf{0} \\ \vdots & \vdots & \ddots & \vdots \\ \mathbf{0} & \mathbf{0} & \cdots & \mathbf{0} \end{pmatrix} \quad \cdots \quad \mathbf{C}_k = \begin{pmatrix} \mathbf{0} & \mathbf{0} & \cdots & \mathbf{0} \\ \mathbf{0} & \mathbf{0} & \cdots & \mathbf{0} \\ \vdots & \vdots & \ddots & \vdots \\ \mathbf{0} & \mathbf{0} & \cdots & \mathbf{Q}_k \end{pmatrix}. \tag{4.43}$$

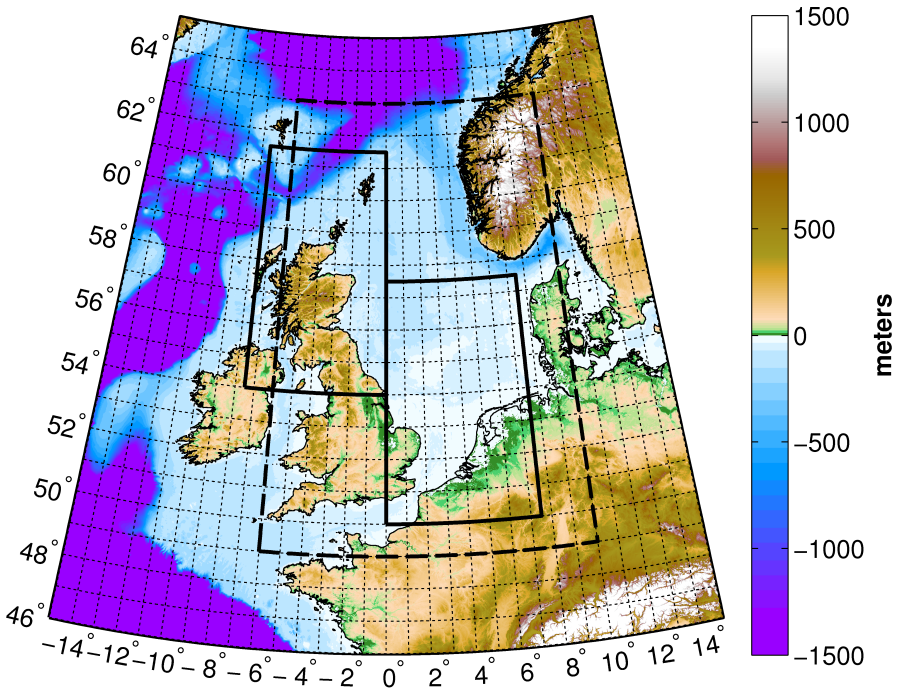

Figure 4.1: Outline of the two subregions used to obtain proper values for the bandwidth and number of RBFs on top of the GEBCO_08 grid (General Bathymetric Chart of the Oceans (GEBCO) 2012). The subregion comprising the Netherlands and southern North Sea is referred to as Ω_{A}, while the region comprising Scotland and its surrounding waters is referred to as Ω_{B}. The subregion indicated by the dashed line is the domain used to quantify the added value of "improved" DT corrections on the quasi-geoid (Section 4.5) and is referred to as Ω_{I}. The region shown in this map is the whole computational domain (Ω).

The variance factor for observation group k is estimated by (Kusche 2003)

$$\hat{\sigma}_k^2 = \frac{\hat{\mathbf{e}}_k^{\mathrm{T}} \mathbf{Q}_k^{-1} \hat{\mathbf{e}}_k}{r_k}, \tag{4.44}$$

with the residuals

$$\hat{\mathbf{e}}_k = \mathbf{A}_k \hat{\mathbf{x}} - \mathbf{y}_k, \quad k = 1, \ldots, p, \tag{4.45}$$

and the partial redundancies

$$r_k = m_k - \frac{1}{\sigma_k^2} \mathrm{tr}\left(\mathbf{A}_k^{\mathrm{T}} \mathbf{Q}_k^{-1} \mathbf{A}_k \mathbf{N}^{-1}\right), \quad k = 1, \ldots, p, \tag{4.46}$$

where m_k is the number of observations in observation group k and $\mathbf{N}$ is the normal matrix computed as

$$\mathbf{N} = \sum_{k=1}^{p} \frac{1}{\sigma_k^2} \mathbf{A}_k^\top \mathbf{Q}_k^{-1} \mathbf{A}_k. \tag{4.47}$$

Because the explicit evaluation of Eq. (4.46) involves a repeated inversion of $\mathbf{N}$, its use is not feasible for large-scale problems such as the one we have at hand. Therefore, we use the Monte-Carlo technique proposed by Kusche (2003). This technique, referred to as Monte-Carlo variance component estimation (MCVCE), is based on stochastic trace estimation (Girard 1989, Hutchinson 1990); the trace operator in Eq. (4.46) is replaced by a pre-multiplication and post-multiplication of a random vector, i.e.,

$$E(\mathbf{z}^\top \mathbf{B} \mathbf{z}) = \operatorname{tr} \mathbf{B}, \tag{4.48}$$

where $\mathbf{B}$ is a symmetric $n \times n$ matrix and $\mathbf{z}$ an $n \times 1$ vector of n independent samples from a random variable Z with $E(Z) = 0$ and $D(Z) = \mathbf{I}$. The entries of $\mathbf{z}$ are samples of a binary distribution, since then $\mathbf{z}^\top \mathbf{B} \mathbf{z}$ is an unbiased estimator of $\operatorname{tr} \mathbf{B}$ and the variance of the approximation errors is minimum (Hutchinson 1990). As numerically shown by Kusche & Klees (2002), for large-scale problems only one sample of the random vector is needed to obtain an accurate estimate of the trace.

Applying Eq.(4.48) to Eq. (4.46) gives an estimate $\hat{r}_k$ of the partial redundancy r_k,

$$\hat{r}_k = m_k - \frac{1}{\sigma_k^2} \mathbf{z}^\top \mathbf{A}_k^\top \mathbf{Q}_k^{-1} \mathbf{A}_k \mathbf{N}^{-1} \mathbf{z}, \quad k = 1, \ldots, p. \tag{4.49}$$

The evaluation of Eq. (4.49) for all p observation groups is formulated as a two-step procedure:

1. Solve
$$\mathbf{N} \mathbf{q}_k = \mathbf{z} \tag{4.50}$$
to obtain the "random parameter solutions" $\mathbf{q}_k$, $k = 1 \ldots p$.
2. Compute an estimate of r_k,
$$\hat{r}_k = m_k - \frac{1}{\sigma_k^2} \mathbf{z}^\top \mathbf{A}_k^\top \mathbf{Q}_k^{-1} \mathbf{A}_k \mathbf{q}_k. \tag{4.51}$$

In general, several iterations are required till the variance factors convergence. Note that in Eq. (4.47) and Eq. (4.51) for the i^{th} iteration

$$\sigma_k^2 = \begin{cases} \sigma_k^2 & \text{for } i = 0, \\ \hat{\sigma}_{k,i-1}^2 & \text{for } i \geq 1. \end{cases} \tag{4.52}$$

In the experiments, no more than five iterations were necessary.

4.3 Data sets and preprocessing

This section provides an overview of the data used to estimate and validate the quasi-geoid. Besides a description of the data sources, the content, and the expected precision, an overview is provided of the data preprocessing.

4.3.1 DGM-1S — a combined GRACE/GOCE gravity model

As reference field we use the optimally combined GRACE/GOCE Delft Gravity Model (DGM-1S) complete to spherical harmonic degree 250 (Hashemi Farahani et al. 2013a,b). It has been computed based on (i) seven years of GRACE K-band ranging data, (ii) four years of GRACE satellites' kinematic orbit data, (iii) fourteen months of GOCE kinematic orbit data, and (iv) ten months of GOCE satellite gravity gradiometry data.

4.3.2 Terrestrial gravity anomalies

The surface gravity anomaly, which is used as data type in the functional model of the gravity data (Eq. (4.3)), is defined as the difference between the observed gravity taken on the Earth's surface and the normal gravity on the telluroid. Terrestrial gravity data sets are commonly provided as free-air gravity anomalies (FAA). The FAA is defined as the difference between the observed gravity taken on the Earth's surface, corrected for the height effect in free air, and the normal gravity taken on the computation point on the level ellipsoid. In Appendix A, we show that the differences between the needed surface gravity anomalies and the FAA are far below the noise level of the FAA data sets used in this study.

Investigations into the application of terrain corrections were outside the scope of this thesis. Therefore, the available terrestrial gravity anomalies are not used in the mountainous areas such as Norway and the UK (instead we use DoV in north and east directions derived from EGG08 (Section 4.3.6)), but confined to the non-mountainous areas comprised by the computational domain; Belgium, Denmark, the Netherlands, and parts of France and Germany. Here, the Belgian data set includes the data points in the Ardennes, since the entire data set was also used to estimate the recent Dutch quasi-geoids NLGEO2004 (Crombaghs & de Bruijne 2004) and NLGEO2007 (Klees et al. 2008). Besides these $14,517$ terrestrial pointwise FAA, the data sets used to estimate NLGEO2004 and NLGEO2007 also include $7,815$ pointwise FAA in the Netherlands (De Min 1996) and $5,465$ block-mean FAA in western Germany. These "in-house" data sets were complemented by pointwise FAA in Belgium, Denmark, France, and Germany. We refer to Table 4.1 for an overview of the meta-information and Fig. 4.2 for a map of the data locations per data provider.

Table 4.1: Meta-information of the terrestrial gravity data sets used in this study.

Provider	Nr. subsets	Nr. pnts	Grav. datum	Point/block	Obs. date	Height	Precision (mGal)
BGI	48	117,730	IGSN71	point	1935–1995	normal/orth.	2.0
BKG	3	2,247	IGSN71	point	1948–2008	DHHN92	2.0
NKG	2	230	-	point	-	orth.	2.0
in-house	3	27,797	IGSN71	point/block	-	SRTM	0.6–2.5
total	56	148,004					

BGI: Bureau Gravimétrique International
BKG: Bundesamt für Kartographie und Geodäsie
NKG: Nordic Geodetic Commission

Building the design matrix requires for each observation point the 3D position of the corresponding telluroid point, where the vertical position of the telluroid point corresponds to the normal height of the observation point. Because the "in-house" data sets do not include height information, the normal heights are obtained from a digital elevation model derived from Shuttle Radar Topography Mission (SRTM) data (Farr et al. 2007, US Geological Survey's EROS Data Center 2009).

As we combine data obtained from different sources, the data need to be harmonized to account for systematic errors introduced by inconsistencies in the gravity, vertical, and horizontal datums being used, as well as by the application of simplified free-air reduction procedures (Heck 1990). Therefore, for each individual survey, which we were able to identify using the provided meta-information, the functional model used to parameterize the data is extended by a bias parameter provided that the survey comprises at least five data points.

Except for the data sets used in the estimation of NLGEO2007 (Klees et al. 2008), no information about the data accuracy is available. Here, we assume an a-priori precision of 2.0 mGal for all other terrestrial data. A-posteriori variances are estimated using MCVCE (Section 4.2.3).

4.3.3 Shipboard gravity data

Shipboard gravity data in the form of FAA are obtained from different global and regional databases. These databases partly contain the same data sets, although differences exist among these "duplicate" data sets in terms of along-track resolution, available meta-information, and/or provided FAA values. The latter points to differences in the post-processing applied to the data (e.g., crossover adjustment). To build a database that contains unique and mutually consistent data sets, from all duplicates of a particular data set the one was selected that provides the highest along-track resolution and/or the most complete data set in terms of available meta-information.

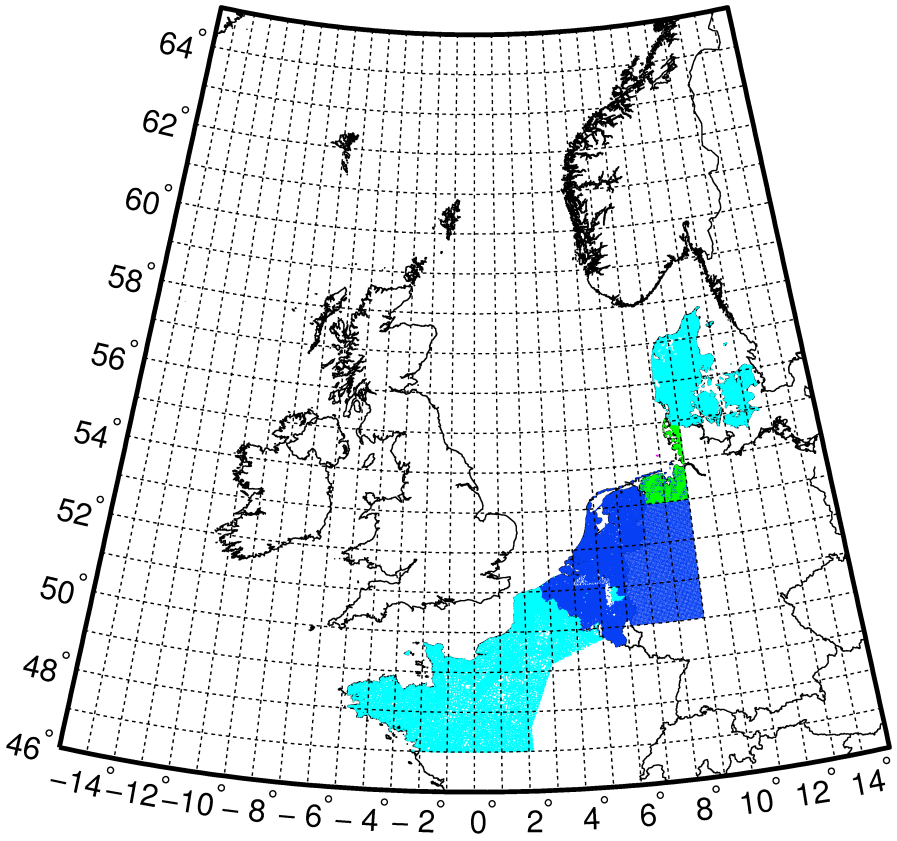

Figure 4.2: Terrestrial gravity data used in the estimation of the quasi-geoid per provider; BGI (cyan), BKG (green), NKG (magenta), and in-house database (blue). Note that the NKG gravity data are hardly visible.

Obviously, the data sets we obtained directly from the principal data owners are preferred over the same data sets extracted from global databases. Table 4.2 provides an overview of the meta-information, while Fig. 4.3 shows a map of the data per data provider. In the remainder of this subsection, we first describe for each data provider the extracted data and, if information is available, the applied preprocessing steps and estimated precision. Second, we describe how systematic errors in the available shipboard gravity data are removed. Note that if no information about the precision is available, we assume a precision of 2.0 mGal. As for the terrestrial data, a-posteriori variances are estimated using MCVCE (Section 4.2.3). In addition, we want to mention that the design matrix related to shipboard data has been computed using zero normal heights.

Table 4.2: Meta-information of the shipboard gravity data sets used in this study.

Provider	Nr. subsets	Nr. cruise lines	Nr. pnts	Grav. datum	Crossover adj.	Obs. date	Precision (mGal)
BGI	18	277	43,979	IGSN71	?	1973–1990	2.0
BGS	2,299	2,299	463,673	IGSN71	y	1962–1992	2.0
IFE	4	87	10,575	IGSN71	y	1983–1993	2.0
NGDC	1	64	26,467	IGSN71	y	1979	2.0
NKG	27	343	21,115	?	?	?	2.0
in-house	2	-	2,358	IGSN71	?	1992	0.36–1.48
total	2,351	3,070	568,167				

4.3.3.1 Overview of the data

From our **in-house database**, we extracted the data acquired by Rijkswaterstaat (the Dutch Department of Public Works) and Shell in the Dutch IJssel Lake and Wadden Sea, respectively. Both data sets have been used to estimate the recent Dutch quasi-geoids NLGEO2004 (Crombaghs & de Bruijne 2004) and NLGEO2007 (Klees et al. 2008). The data set acquired by Rijkswaterstaat is labeled as the WADGRAV data set and described by De Min (1996). Klees et al. (2008) estimated the precisions of the WADGRAV and Shell data to be 1.48 mGal and 0.36 mGal, respectively.

Shipboard gravity data obtained from the **Bureau Gravimétrique International (BGI)** include the publicly available data acquired by Ifremer (French research institute for exploitation of the sea) in the period 1987–1990 (eight cruises), the Deutsches Hydrographisches Institut in the period 1970–1975 (four cruises), Delft University of Technology in 1986 during the "navigation and gravimetric experiment" at the North Sea (Haagmans et al. 1988) (one cruise), the Russian Institute of Physics of the Earth in the period 1973–1979 (three cruises), a, to the author, unknown institute during a cruise in the western Baltic Sea (Plaumann 1979), and another, to the author, unknown institute during a cruise in Danish waters in the period 1970–1975. Since no information about the precision of these data is available, we assume an a-priori precision of 2.0 mGal for all cruises.

The data set obtained from the **British Geological Service (BGS)** contains corrected and smoothed ship gravity measurements acquired by BGS as part of its offshore reconnaissance mapping programme. This programme, funded mainly by the UK's Department of Energy, commenced in 1967. Apart from the data acquired by the BGS, the data set also includes measurements acquired during various commercial and academic cruises between 1965 and 1994. The data were, among others, used (in gridded form) for the computation of the Ordnance Survey Geoid Model 2002 (Forsberg et al. 2003). Note that, in the database, all cruise lines are stored as separate

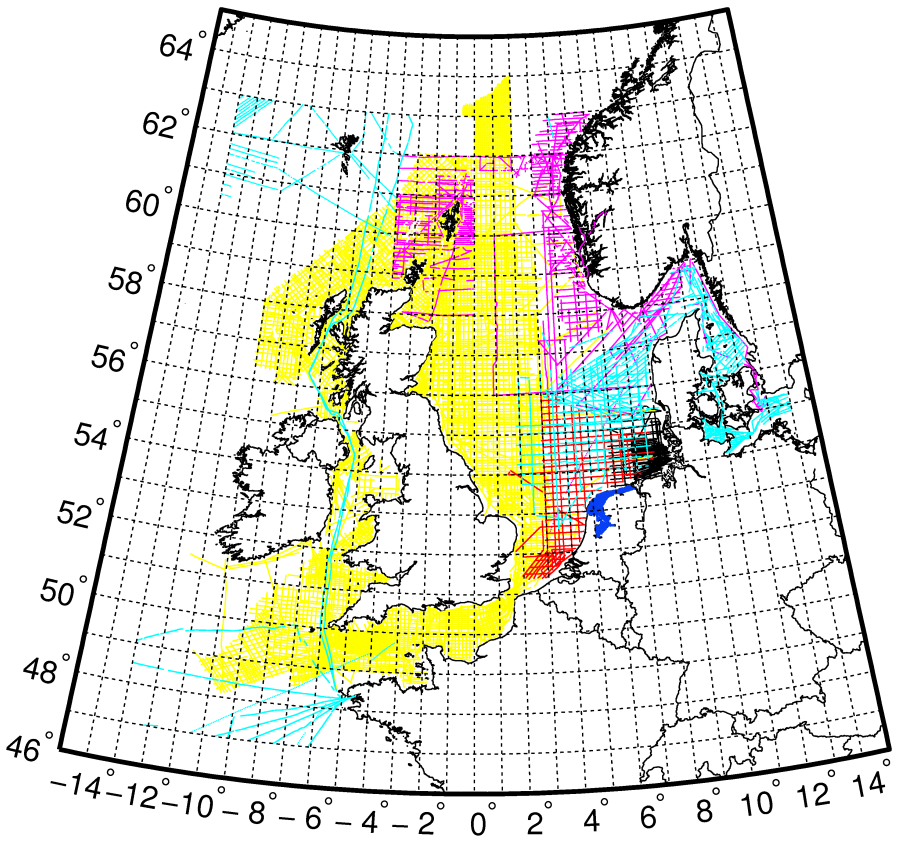

Figure 4.3: Shipboard gravity data used in the estimation of the quasi-geoid per provider; BGI (cyan), BGS (yellow), IFE (black), NGDC (red), NKG (magenta), and in-house database (blue).

cruises, i.e., it is not possible to identify which lines were acquired during the same cruise. No information about the precision of the data is available.

The data have undergone basic processing ("base-tie", Eötvös corrections, etc.) and the corrected data are crossover adjusted (C. P. Royles, personal communication, July 16, 2009). This adjustment involved two separate steps in which errors were treated as either constant or random along the cruise lines. Constant errors were dealt with by an iterative process. In each iteration, the cruise line with the set of largest crossover errors was corrected by a constant value after which the errors throughout the network were re-assessed and the process started again. This process continued until it produced no further improvement of the overall mean crossover error within the cruise grid. The remaining crossover errors were assumed to be random and were corrected for by applying to either line of two intersecting lines a correction

equal to half the crossover error. Between the crossovers, corrections were linearly interpolated.

The **Institut für Erdmessung (IFE)** provided shipboard gravity data acquired during four different cruises, labeled as pg0033, pg0119, pg0131, and pg0132. pg0033 consists of 39 crossover adjusted cruise lines acquired in 1983. The along-track spacing between the data points is about 1 km. The rms of the differences at the crossover locations was originally 2.85 mGal. After the crossover adjustment it reduced to 1.88 mGal. pg0119 contains 180 observations acquired at scattered locations in the shallow water area of the North Sea between Borkum and Sylt from 1992 to 1993. pg0131 contains 23 crossover adjusted cruise lines acquired during the "Victor Hensen" cruise (September 26, 1992 – October 5, 1992) carried out by the Institute of Geophysics of Hamburg University. The along-track data spacing is 0.5 km. Before the crossover adjustment, the data were corrected for a bias of -1.50 mGal. pg0132 is acquired slightly before pg0131; from September 1, 1992 – September 11, 1992 by the Bundesamt für Seeschifffahrt und Hydrographie. This data set consists of 25 crossover adjusted cruise lines, which were corrected for a bias of -3.00 mGal before the adjustment. The precision of all these data is roughly estimated as 1–3 mGal. Here, the a-priori precision is set to 2 mGal. The finally used precision is estimated using MCVCE (Section 4.2.3).

The data set extracted from the US **National Geophysical Data Center's (NGDC)** GEODAS Marine Trackline Geophysics database is acquired during the gravity survey of the Dutch North Sea in 1979. We refer to Strang van Hees (1983) for a detailed documentation of this cruise. He showed that the precision of the crossover adjusted data estimated from the differences at the crossover locations is 1.22 mGal.

The data extracted from the **Nordic Geodetic Commission (NKG)** gravity database, a collection of gravity data used to model the Scandinavian and Baltic geoid, mainly include data in Norwegian waters and around the Shetland Islands. In 2000, this database has undergone a major cleanup; old, erroneous, and inaccurate data were deleted or replaced by new measurements (G. Strykowski, personal communication, November 17, 2008). No information about the precision of the data is available.

4.3.3.2 Removal of systematic errors in shipboard gravity data

Shipboard gravity data are subject to systematic errors introduced by, e.g., gravimeter drift and direct current (DC) offset (Wessel & Watts 1988). Although for the data of many cruises these errors are (partly) removed during the post-processing of the observed data, among the cruises inconsistencies remain, especially since we combine data obtained from different data providers. An estimate of these inconsistencies is shown in Fig. 4.4, where we computed for each cruise the average difference between the shipboard FAA and altimeter-derived FAA obtained from the DTU10 global (on

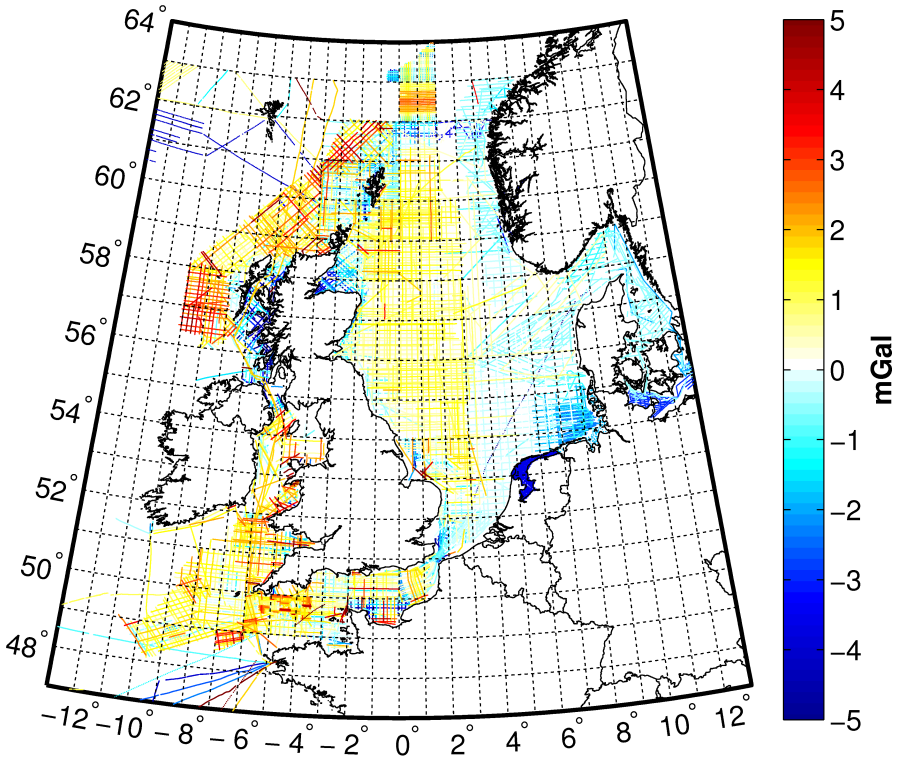

Figure 4.4: Average difference per cruise between the shipboard FAA and altimeter-derived FAA obtained from the DTU10 global gravity field model.

land EGM2008 is used) gravity field model (DTU10-GRA) (Andersen et al. 2010, Andersen 2010). From this map, we conclude that there is an offset of about 1 mGal between the BGS data and the data obtained from BGI, NKG, and NGDC. Also the IFE data is offsetted by about -1 to -2 mGal compared to the data obtained from BGI, NKG, and NGDC. Furthermore, we observe large mean differences between the WADGRAV and Shell data sets in the IJssel Lake and Wadden Sea (obtained from our in-house database) and DTU10-GRA; for both data sets the average difference is about -3.5 mGal. Finally, we conclude that the network adjustment applied by the BGS did not remove all mutual inconsistencies; especially in the data around Scotland we observe large biases of several mGal.

Before a proper quasi-geoid can be estimated, these mutual inconsistencies need to be removed. The most obvious method to do so is to apply a crossover adjustment. In this study, we used the Generic Mapping Tools (GMT) *x2sys* routines (Wessel 2010). A bias is estimated for the data of each cruise; for the BGS data we estimate a bias for each cruise line. Note that since we observed in Fig. 4.4 in some regions

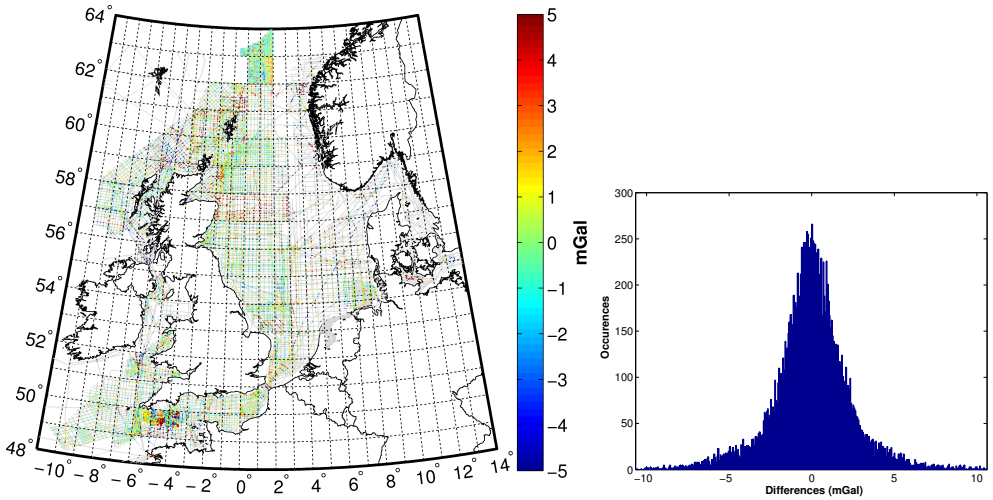

(a) **(b)**

Figure 4.5: Map (a) and histogram (b) of the differences at the crossover locations.

systematic deviations between the BGS data and DTU10-GRA, the adjusted FAA are replaced by the unadjusted ones. Furthermore, it should be noted that all cruise lines that consist of less than five data points are excluded from the crossover adjustment and that there should be at least two crossovers between a particular cruise and all other cruises. The crossover differences are computed by interpolating the values of nearby observations at the crossovers locations using an Akima spline interpolator (Akima 1972).

In Fig. 4.5a and Fig. 4.5b, we show a map and a histogram of the derived crossover differences, respectively. The histogram shows that the differences are normally distributed with a mean of -0.02 mGal and standard deviation of 2.66 mGal. The $16,333$ crossovers are used to estimate $2,224$ biases, see Fig. 4.6. To eliminate the rank deficiency in the design matrix, we assumed a zero bias for the data obtained from the NGDC database, i.e., the data acquired during the gravity survey of the Dutch North Sea in 1979 (Section 4.3.3.1). We assumed a zero bias for *this* data set because no systematic error showed up in the data when they were used in the estimation of the recent Dutch quasi-geoids NLGEO2004 (Crombaghs & de Bruijne 2004) and NLGEO2007 (Klees et al. 2008).

To evaluate whether the inconsistencies among the data acquired during different cruises have been successfully removed, we computed for each cruise the average difference between the shipboard and DTU10-GRA FAA *before* (Fig. 4.7a) and *after* (Fig. 4.7b) applying the crossover adjustment. Note that the difference between Fig. 4.4 and Fig. 4.7a is that in Fig. 4.7a the unadjusted BGS data are used while in Fig. 4.4 the data are used as adjusted by the BGS. Overall, we conclude that for the

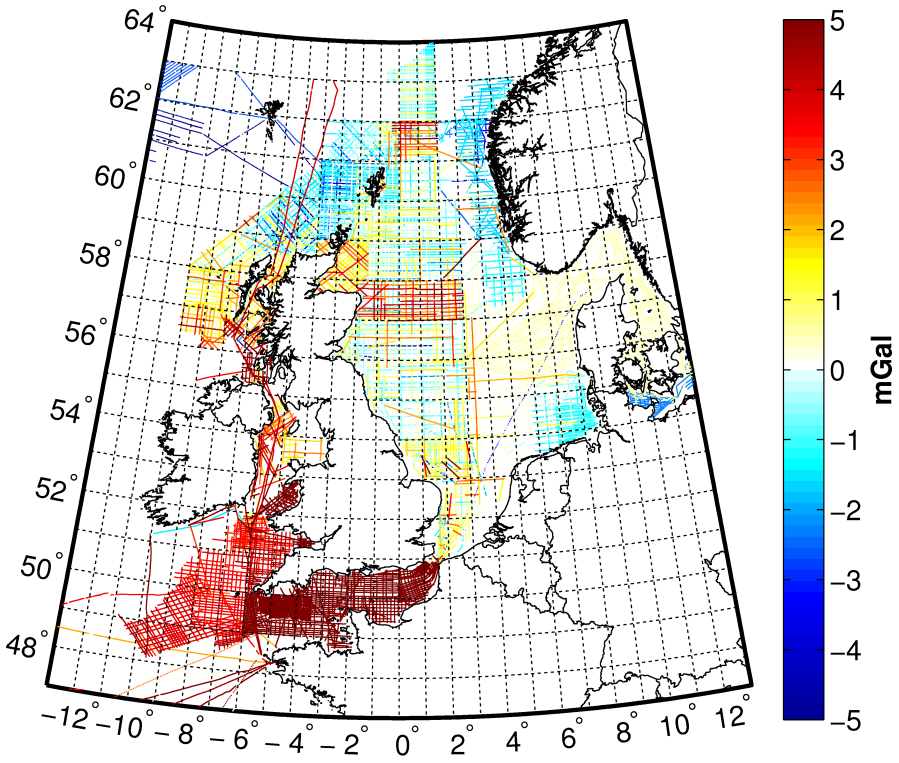

Figure 4.6: Map of the estimated biases in the data of each cruise. The biases are estimated by a crossover analysis. The total number of estimated biases is 2,224, while the number of crossovers is 16,333.

data of many cruises in the North Sea and Skagerrak the mean (per cruise) differences between the shipboard and DTU10-GRA FAA are reduced, while for the data in the Celtic Sea, Irish Sea, St. George's Channel, and English Channel the differences significantly increased. The poor performance of the crossover adjustment in these waters is explained by the fact that the "connection" of the cruises in these waters with the remaining cruises is weak; in the English Channel the connection with the cruises in the North Sea is established by only one cruise line, while in the north of the Irish Sea it is established by the data (two cruise lines) of one BGI cruise. From a comparison of Fig. 4.6 with Fig. 4.7a, we conclude that the estimated bias for this BGI cruise is likely too large, which biases all data in the Celtic Sea, Irish Sea, St. George's Channel, and English Channel. The shift in the estimated biases between the cruises in the English Channel east and west of the -6° meridian (see Fig. 4.6) is caused by the fact that there are almost no connections between these cruises. Note that this cannot be seen from Fig. 4.5a. We also observe a small difference of ~ 1 mGal between the data in the south-eastern North Sea, Skagerrak, and

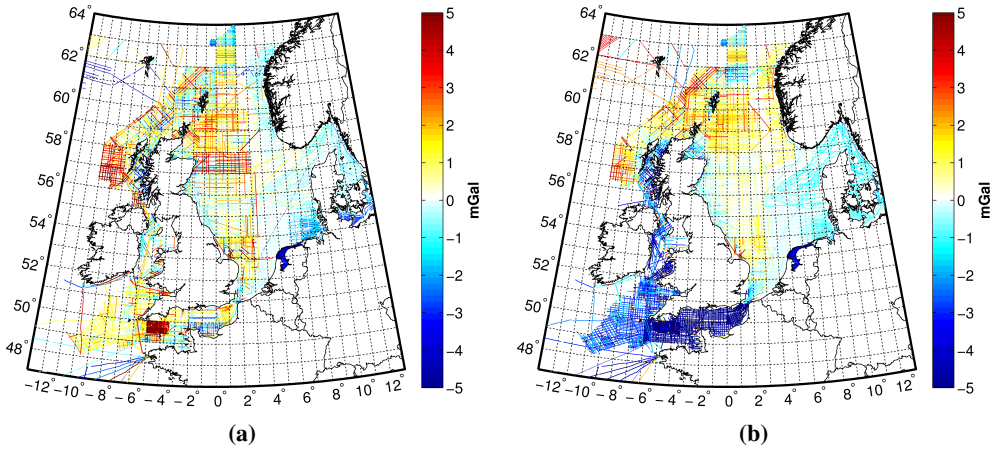

Figure 4.7: Average difference per cruise between the shipboard FAA and altimeter-derived FAA obtained from the DTU10 global gravity field model *before* (a) and *after* (b) applying the crossover adjustment. Note that compared to Fig. 4.4, for these figures the adjusted BGS data were replaced by the unadjusted values.

Kattegat compared to the remaining data in the North Sea. This again shows that after applying the crossover adjustment not all systematic errors in the data are removed.

A better removal of the systematic errors can be obtained by applying a separate crossover adjustment for the data in different regions. However, besides the fact that this is a labor-intensive solution, the main drawback is that not all mutual inconsistencies will be removed. Indeed, among the data of the different regions the inconsistencies remain. As a consequence, post-processing is required or additional bias parameters need to be included into the functional model used to parameterize the data. Mainly restrained by the labor-intensive aspect, in this study, we decided to adjust all shipboard gravity cruises to the altimeter-derived FAA model DTU10-GRA by adding the average differences shown in Fig. 4.7a to the observed FAA. Note that in this way we also "remove" the systematic errors in the data of all "unconnected" cruises, i.e., cruises that have no crossovers with any other cruise. Of course, DTU10-GRA is not error-free. Andersen (2010) showed that the mean and standard deviation of the differences between DTU10-GRA and 321,400 unclassified shipboard gravity observations in the Gulf Stream region with an accuracy of 2–3 mGal are 0.39 and 3.82 mGal, respectively. As discussed by Andersen et al. (2010), the Gulf Stream region introduces an error of 2–3 mGal because of increased sea surface height variability and hence the comparison should not be considered as representative for the general accuracy of DTU10-GRA. Furthermore, one could object that for the data in coastal waters (where we do have many data points) no reliable bias corrections can be computed due to the problems with radar altimeter data (Sec-

Table 4.3: Meta-information of the airborne gravity data used in this study.

Provider	Nr. subsets	Nr. pnts	Grav. datum	Along-track spacing (km)	Crossover adj.	Obs. date	Height	Precision (mGal)
BKG	2	6,699	IGSN71	0.6–1.1	n	2006/2007	ellips.	2.0
NKG	1	1,661	IGSN71	1.2–1.4	n	1996	orth.	2.0
total	3	8,360						

tion 1.3.1). We agree that this is indeed a problem, but want to stress that these problems have been strongly reduced by the fact that DTU10-GRA is computed using retracked radar altimeter data. In addition, for the data sets in the Dutch IJssel Lake and Wadden Sea, where hardly any radar data are available, no adjustment is carried out. Instead, the functional model is extended by a bias term for each of these data sets.

After removing the systematic errors, we used the pointwise differences between the shipboard and DTU10-GRA FAA to remove outliers in the data set. The outliers are identified by using subsequently the 10-sigma and 3-sigma rules, i.e., observations are identified as outliers if the differences between the shipboard and DTU10-GRA FAA are larger than ten/three times the standard deviation of all differences. Here, we first apply the 10-sigma rule to avoid a contamination of the standard deviation by extremely large outliers. By applying these rules, 32 and $9,025$ observations, respectively, were identified and removed.

4.3.4 Airborne gravity data

Airborne gravity data, in the form of gravity disturbances, are obtained from the Bundesamt für Kartographie und Geodäsie (BKG) and the NKG. From the BKG, we obtained the data acquired from 2006–2008 during the BalGRACE and NorthGRACE campaigns (Schäfer et al. 2008). The NKG provided the data acquired as part of the "airborne geoid mapping system for coastal oceanography" project (Forsberg et al. 1997). The latter data set is also used by Alberts (2009, Section 6.1). While originally our computational domain was smaller, we only obtained both from the BKG and NKG the data west to 9° longitude. See Fig. 4.8 for a map of the data locations per data provider and Table 4.3 for an overview of some main features. For a description of the applied data processing, we refer to Olesen (2002).

A comparison of the BalGRACE and NorthGRACE data sets (both in the form of FAA) with independent surface data (terrestrial, shipboard, and altimeter-derived FAA) reveals that the rms and bias values of the differences range between 1.8 to 2.1 mGal and 1.2 to 1.6 mGal, respectively (Schäfer et al. 2008).

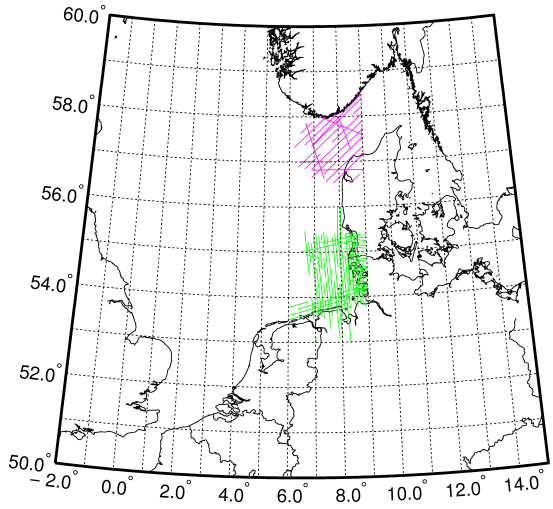

Figure 4.8: Airborne gravity data used in the estimation of the quasi-geoid per provider; BKG (green) and NKG (magenta).

To suppress the high-frequency signals in the data, the data of all tracks are smoothed by a Gaussian filter with a half-width of 3 km. Systematic errors in the data are accounted for by extending the functional model with a single bias parameter per cruise. Remaining errors in the data are assumed to be white Gaussian noise with a standard deviation of 2.0 mGal. As for the terrestrial data, the a-posteriori variances are estimated using MCVCE.

4.3.5 Along-track DoV from radar altimeter data

In this section, we describe the procedure used to derive the along-track deflections of the vertical (DoV) that make up the contribution of satellite altimetry to the quasi-geoid. An outline of this procedure is provided by the flowchart presented in Fig. 4.9, which is a detailed crop of the flowchart presented in Chapter 2 (Fig. 2.1). To structure our description, in the remainder of this section we follow the flowchart.

Figure 4.9 ***(following page)*****:** Flowchart of the procedure used to derive along-track DoV from observed SSHs. The different colors of the blocks refer to the different phases in the overall procedure: (i) green refers to a preprocessing step and (ii) yellow to a step of the iterative phase. The different colors of the arrows refer to the different data flows: RADS data (yellow), EAPRS-ERS1 data (blue), combined (green), and meteorological data (black). The bold capital letters between the brackets refer to Tables 4.6 and 4.7, where we provide an overview of the (removed) number of SSHs/DoV after applying the particular step.

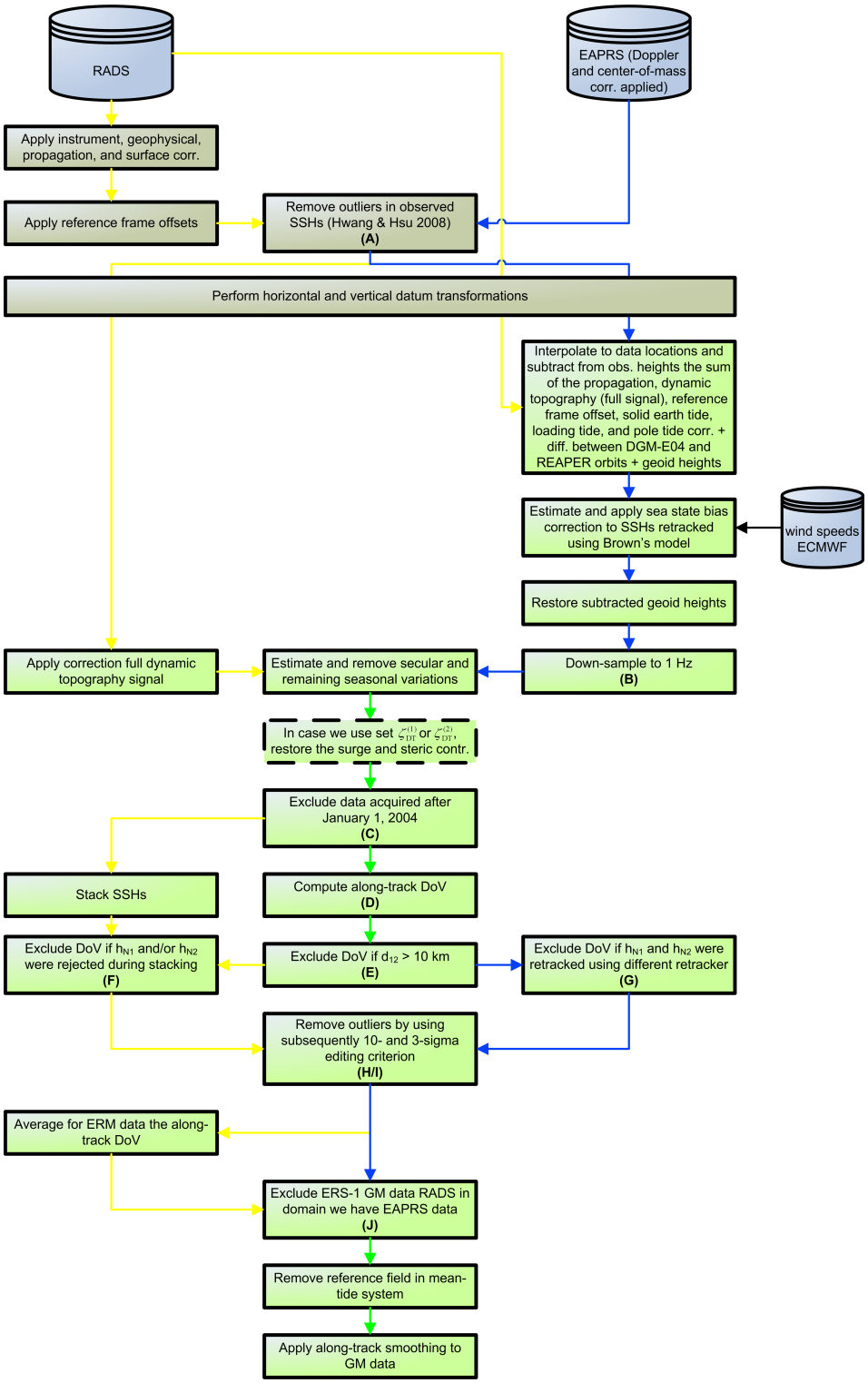
RADS
EAPRS (Doppler and center-of-mass corr. applied)
Apply instrument, geophysical, propagation, and surface corr.
Apply reference frame offsets
Remove outliers in observed SSHs (Hwang & Hsu 2008) (A)
Perform horizontal and vertical datum transformations
Interpolate to data locations and subtract from obs. heights the sum of the propagation, dynamic topography (full signal), reference frame offset, solid earth tide, loading tide, and pole tide corr. + diff. between DGM-E04 and REAPER orbits + geoid heights
Estimate and apply sea state bias correction to SSHs retracked using Brown's model
wind speeds ECMWF
Restore subtracted geoid heights
Down-sample to 1 Hz (B)
Apply correction full dynamic topography signal
Estimate and remove secular and remaining seasonal variations
In case we use set or restore the surge and steric contr.
Exclude data acquired after January 1, 2004 (C)
Stack SSHs
Compute along-track DoV (D)
Exclude DoV if h_{N1} and/or h_{N2} were rejected during stacking (F)
Exclude DoV if d_{12} > 10 km (E)
Exclude DoV if h_{N1} and h_{N2} were retracked using different retracker (G)
Remove outliers by using subsequently 10- and 3-sigma editing criterion (H/I)
Average for ERM data the along-track DoV
Exclude ERS-1 GM data RADS in domain we have EAPRS data (J)
Remove reference field in mean-tide system
Apply along-track smoothing to GM data

Table 4.4: Main characteristics of the radar altimeter missions from which data are used to estimate the quasi-geoid together with an overview of the orbit and background models used to compute the ellipsoidal heights of the instantaneous sea surface. Note that the data of the Envisat and ERS-1/2 missions, as well as the data of the Jason-1/2 and T/P (except the data acquired during the tandem mission phase) missions, are combined.

	Envisat	ERS-1[*1]	ERS-2	GEOSAT[*2]	GFO-1	Jason-1	Jason-2	POSEIDON	TOPEX
ID	n1	e1	e2	gs	g1	j1	j2	pn	tx
Start	9/2002	7/1991	4/1995	3/1985	1/2000	1/2002	6/2008	10/1992	10/1992
End	4/2012	3/2000	7/2011	1/1990	9/2008	7/2013	-	1/2006	1/2006
Inclination	98.5°	98.5°	98.5°	108°	108°	66°	66°	66°	66°
Cycle [days]	35	3/35/336	35	17	17	10	10	10	10
Orbit	EIGEN-GL04S	REAPER	DGM-E04	GDR-C Prime	idem gs	idem n1	idem n1	idem g1	idem g1
Dry Tropo.	ECMWF	idem n1	idem n1	NCEP	NCEP	idem n1	idem n1	idem n1	idem n1
Wet Tropo.	MWR (NN)	idem n1	idem n1	NCEP	MWR	enhanced JMR	enhanced AMR	TMR	TMR
Ionosphere	smth. dual-freq.	NIC09	JPL GIM	NIC09	JPL GIM	idem n1	idem n1	NIC09	idem n1
Sea State Bias	CLS	BM3	BM3	hybrid	idem gs	idem n1	idem n1	BM4	CLS
Load tide	GOT4.7	idem n1	idem n1	idem n1	idem n1	idem n1	idem n1	idem n1	idem n1

[*1] This data set includes data retracked by the EAPRS laboratory.
[*2] Retracked by NOAA.

Data sources 1 Hz radar data acquired by the GEOSAT (geodetic mission (GM) phase), ERS-1 (exact repeat mission (ERM) + GM phases), ERS-2, Envisat, GFO-1, Jason-1/2, and TOPEX/POSEIDON (T/P) satellites during the period March 1985 to September 2011 are extracted from the Radar Altimeter Database System (RADS) (Scharroo 2013). For a part of our computational domain (comprising the whole North Sea), the ERS-1 GM data are replaced by retracked data kindly provided by Prof. P. A. M. Berry from the Earth and Planetary Remote Sensing (EAPRS) Laboratory of the De Montford University (note that the actual replacement is carried out almost at the end of the procedure). These retracked 20 Hz data represent the uncorrected ellipsoidal heights of the instantaneous sea surface, i.e., except for instrumental corrections no other corrections are applied. We refer to these data as the EAPRS-ERS1 data set. Table 4.4 shows the main characteristics of the satellite missions together with an overview of the orbit and background models used to compute the ellipsoidal heights of the instantaneous sea surface.

Computing heights of the instantaneous sea surface (RADS) For the RADS data, ellipsoidal heights of the instantaneous sea surface are computed by correcting the observed SSHs for dry and wet tropospheric refraction, ionospheric refraction, the sea state bias, solid earth tide, loading tide, and pole tide. Reference frame differences among the various altimeters are accounted for by applying reference frame offsets to the data using TOPEX as reference (Andersen & Scharroo 2011).

Remove outliers in observed SSHs Outliers in the 1 Hz RADS and 20 Hz EAPRS-ERS1 data sets are removed using the iterative procedure described in Hwang & Hsu (2008) (see also Section 3.5.4); smoothing of the along-track height differences with

Table 4.5: Overview of the different sets of DT corrections applied to the instantaneous SSHs to obtain geometric quasi-geoid heights.

Set	tide		surge		steric	
	GOT4.7	*DCSM*	*MOG2D*	*DCSM*	*DTU10-MSS-EGG08*	*DCSM*
$\zeta_{\mathrm{DT}}^{(1)}$	x					
$\zeta_{\mathrm{DT}}^{(2)}$ *1		x				
$\zeta_{\mathrm{DT}}^{(3)}$ *2		x		x		x
$\zeta_{\mathrm{DT}}^{(4)}$	x		x		x	

*1 Outside DCSM's model domain we use $\zeta_{\mathrm{DT}}^{(1)}$.
*2 Outside DCSM's model domain we use $\zeta_{\mathrm{DT}}^{(4)}$.

a 1D Gaussian filter using a filter half-width of 5.5 km is repeated until the largest residual between observed and smoothed height differences satisfies the three-sigma criterion, where sigma is the standard deviation of the residuals. Note that contrary to what is done by Hwang & Hsu (2008), we use a filter half-width of 5.5 km for both the ERM and GM data sets instead of using a half-width of 3.5 km for the GM data. Empirically, we found that more outliers in the GM data are removed if we use a filter half-width of 5.5 km.

From SSHs to (biased) geometric quasi-geoid heights (RADS) For the RADS data, geometric quasi-geoid heights are obtained as the differences between the ellipsoidal heights of the instantaneous sea surface and the dynamic topography (DT). Four different approximations to the real DT are used, resulting in four sets of DT corrections that are briefly summarized in Table 4.5. In the first set, referred to as $\zeta_{\mathrm{DT}}^{(1)}$, the DT comprises only the ocean tides derived from the GOT4.7 global ocean tide model (see Ray (1999) and Section 3.5.4). In $\zeta_{\mathrm{DT}}^{(2)}$, the DT comprises the ocean tides from DCSM. Outside the DCSM model domain we use $\zeta_{\mathrm{DT}}^{(1)}$. In $\zeta_{\mathrm{DT}}^{(3)}$, the DT comprises ocean tides, surge, and steric effects taken from DCSM using the experimental setup presented in Section 3.6.1. $\zeta_{\mathrm{DT}}^{(4)}$, that is also used outside the DCSM model domain, comprises the GOT4.7 ocean tides, the surge obtained from the MOG2D model (see Carrère & Lyard (2003) and Section 3.5.4), and water level variations induced by time-averaged spatial variations in water density. The latter are computed as the differences between the DTU10 mean sea surface model (DTU10-MSS) (Andersen 2010) and the EGG08 quasi-geoid (Denker et al. 2008).

Computing 1 Hz geometric quasi-geoid heights for the EAPRS-ERS1 data To reduce the uncorrected EAPRS-ERS1 SSHs to geometric quasi-geoid heights that are consistent with those derived from the RADS data, we need to apply corrections for the tropospheric and ionospheric propagation delays, sea state bias, solid earth tide, loading tide, pole tide, reference frame offset, DT, and differences between the

DGM-E04 (Scharroo & Visser 1998) and REAPER (Rudenko et al. 2012) orbits used for the RADS ERS-1 and EAPRS-ERS1 data, respectively. Except for the sea state bias and the DT corrections derived from DCSM ($\zeta_{\mathrm{DT}}^{(2)}$ and $\zeta_{\mathrm{DT}}^{(3)}$), all corrections are only available at the locations of the RADS data points. The sea state bias corrections (only applied to the SSHs which are obtained making use of a waveform conforming to Brown's model of ocean return (Brown 1977)) are computed using a hybrid sea state bias model for which the parameters are derived using the method presented by Scharroo & Lillibridge (2005). This method uses "SSH residuals" as input, which are computed by removing all corrections including the quasi-geoid heights (here derived from EGG08) from the uncorrected SSHs. Note that in computing the SSH residuals, the *full* DT corrections are applied; $\zeta_{\mathrm{DT}}^{(1)}$ and $\zeta_{\mathrm{DT}}^{(2)}$ are supplemented by the MOG2D surge and the DTU10-MSS-EGG08 steric corrections (these are restored after the estimation and removal of the secular and remaining seasonal variations (next step)). The sum of the corrections that are only available at the RADS data points is interpolated using a cubic spline interpolation to the EAPRS-ERS1 data locations. After applying the sea state bias corrections, the EGG08 quasi-geoid heights are restored and the EAPRS-ERS1 data are down-sampled to 1 Hz to suppress some noise and to make the EAPRS-ERS1 data fully consistent with the RADS data. The down-sampling is performed by estimating from all SSHs (maximum 20) inside a particular bin j the average SSH ($h_{N_j}^{\mathrm{1Hz}}$) using the observation equation

$$h_{N_i}^{\mathrm{20Hz}} = a \cdot \Delta d_{ij} + h_{N_j}^{\mathrm{1Hz}}, \tag{4.53}$$

where $h_{N_i}^{\mathrm{20Hz}}$ is a 20 Hz retracked SSH, a is the slope, and Δd_{ij} is the distance of $h_{N_i}^{\mathrm{20Hz}}$ relative to the center of the bin.

Estimate and remove secular and remaining seasonal variations The geometric quasi-geoid heights computed this way still contain the effect of secular changes in sea level due to, e.g., eustatic and steric sea level changes, self gravitation, and glacial isostatic adjustment. Moreover, if we apply the DT corrections $\zeta_{\mathrm{DT}}^{(1)}$, $\zeta_{\mathrm{DT}}^{(2)}$, or $\zeta_{\mathrm{DT}}^{(4)}$ (for this step, $\zeta_{\mathrm{DT}}^{(1)}$ and $\zeta_{\mathrm{DT}}^{(2)}$ are supplemented by the MOG2D surge and the DTU10-MSS-EGG08 steric corrections), they also contain the signal associated with temporal variations in the steric sea level, while if we apply the DT corrections $\zeta_{\mathrm{DT}}^{(3)}$, they also contain the signal induced by the net steric expansion/contraction of the global oceans. In the next step, these signals are estimated and removed. In the North Sea, the non-secular variations in both the steric sea level and the net steric expansion/contraction signal are mainly seasonal. Therefore, we use the functional model given in Eq. (3.14). The spatially varying trends and seasonal variations are estimated from the T/P and Jason-1/2 geometric quasi-geoid heights over the entire measurement period (1992–2011) in bins of $\sim$6.5 km along the satellite passes and

interpolated to the locations of all data points using GMT's `surface` routine with a tension factor of 1. The corrections are centered to the adopted reference epoch.

If we apply the DT corrections $\zeta_{\mathrm{DT}}^{(1)}$ or $\zeta_{\mathrm{DT}}^{(2)}$, after the estimation and removal of the secular and remaining seasonal variations, the surge and steric contributions are restored to the geometric quasi-geoid heights.

Exclude data acquired after January 1, 2004 The DT corrections $\zeta_{\mathrm{DT}}^{(3)}$ cannot be computed after the end of 2004 as the salinity and temperature fields of POL's hindcast are only available up to that time. Therefore, all data acquired after January 2004 are excluded before we compute the along-track DoV. To remain consistent, these data are also excluded if we apply the other sets of DT corrections. Note that we do not exclude any GM phase data.

Compute along-track DoV The along-track DoV (ε) are approximated using

$$\varepsilon = -\frac{h_{N_2} - h_{N_1}}{d_{12}}, \tag{4.54}$$

where h_{N_1} and h_{N_2} are two successive geometric quasi-geoid heights and d_{12} is the distance between them (about 6.5 km for 1 Hz data). This simple two-point finite difference scheme is applied to each successive pair of geometric quasi-geoid heights. Obviously, this introduces correlations between two successive DoV (correlation coefficient is 0.5), which need to be included in the variance-covariance matrix. Here, we neglect these correlations as the software cannot deal with full variance-covariance matrices. From the obtained set of DoV, we exclude those for which holds that:

1. $d_{12} > 10$ km, i.e., if there is a data gap between two successive points of a track.
2. h_{N_1} and/or h_{N_2} was/were rejected during the stacking operation. During this operation it is evaluated whether (i) the across-track distance between the ground track of a particular satellite fly-over and the average ground track is smaller than half the along-track sampling distance and (ii) the observation is not rejected as an outlier in the computation of the average geometric quasi-geoid heights. As in Hwang et al. (2002), Pope's tau-test (Pope 1976) is used to detect outliers.
3. h_{N_1} and h_{N_2} are retracked by a different retracker.

Remove remaining outliers Remaining outliers in the observation-derived DoV are detected and removed using the method suggested by Sandwell & Smith (2009); DoV are removed as outliers if the differences between the observation-derived and

Table 4.6: Bookkeeping of the number of SSHs/DoV for each (group of) satellite mission(s) (phases) obtained/removed by applying the various data processing steps if we apply the DT corrections $\zeta_{\mathrm{DT}}^{(3)}$. The labels in the first column refer to Fig. 4.9.

Step	e1/b + e1/d	e1/c + e1/g + e2 + n1	e1/a	e1/e	e1/f	g1	gs	tx/a + pn + j1 + j2	tx/b	tx/n	e1/e*1	e1/f*1
Init. # SSHs	22,096	3,110,522	47,913	56,442	57,557	1,185,013	249,047	4,287,814	545,896	17,597	441,967	468,128
A	-125	-24,207	-344	-361	-448	-10,326	-3,044	-40,583	-5,200	-175	-18,315	-17,605
B											19,436	21,066
C	21,971	1,420,575	47,569	56,081	57,109	656,003	246,003	2,281,926	237,437	17,422	19,436	21,066
D	21,755	1,409,710	47,209	55,630	56,649	650,896	244,120	2,264,230	235,452	17,272	19,238	20,863
E	-1,088	-34,739	-2,409	-1,538	-1,530	-22,784	-5,218	-48,140	-4,807	-373	-445	-390
F	-315	-25,514	-414	-0	-0	-7,057	-0	-17,917	-2,085	-0	-0	-0
G											-103	-85
H	-0	-10	-1	-1	-0	-105	-47	-49	-0	-0	-8	-7
I	-584	-23,085	-748	-323	-1,493	-6,848	-1,815	-15,340	-846	-44	-120	-333
J	1,141	14,056	1,272	37,115	35,403	9,277	237,040	6,596	5,552	16,855	18,457	19,344

*1 Data retracked by the EAPRS laboratory.

reference values exceed the three-sigma criterion, where sigma is the standard deviation of the differences. As reference values we use the along-track DoV derived from EGG08 quasi-geoid heights. Just as for the removal of outliers in the shipboard gravity data (Section 4.3.3.2), we use a two-step procedure. First, we remove all observation-derived DoV for which the differences exceed 10 times the standard deviation of the differences. Second, we recompute the standard deviation and remove all observation-derived DoV for which the differences exceed three times the standard deviation.

Final steps In the next step, the DoV for the ERM mission(s) (phases) are averaged. Thereafter we replace the RADS ERS-1 GM data by the EAPRS-ERS1 data. After that, we remove the along-track DoV computed using the DGM-1S GRACE/GOCE model (Section 4.3.1) in the mean-tide system. Finally, we suppress high-frequency noise in the residual along-track DoV derived from GM data by smoothing all passes of the GEOSAT and ERS-1 GM data sets using a Gaussian filter with a half-width that equals the nominal along-track data spacing (6.5 km).

In Table 4.6, we summarize for the case we apply the DT corrections $\zeta_{\mathrm{DT}}^{(3)}$, for all (groups of) satellite missions (phases), the number of SSHs/DoV obtained/removed in each step of the processing. In Table 4.7, we provide the total numbers for all sets of DT corrections. Figures 4.10a and 4.10b provide a map of the residual along-track DoV obtained after applying the DT corrections $\zeta_{\mathrm{DT}}^{(3)}$ for the north-south and south-north passes, respectively.

4.3.6 DoV from EGG08

In the mountainous areas of the computational domain, we use DoV in north and east directions derived from EGG08. This is because investigations into the application

Table 4.7: Bookkeeping of the *total* number of SSHs/DoV obtained/removed by applying the various data processing steps if we apply the four sets of DT corrections summarized in Table 4.5. The labels in the first column refer to Fig. 4.9.

Step	$\zeta^{(1)}_{\mathrm{DT}}$	$\zeta^{(2)}_{\mathrm{DT}}$	$\zeta^{(3)}_{\mathrm{DT}}$	$\zeta^{(4)}_{\mathrm{DT}}$
Org. # SSHs	10,489,992	10,489,992	10,489,992	10,489,992
A (remove outliers in observed SSHs (Hwang & Hsu 2008))	-120,733	-120,733	-120,733	-120,733
B (down-sample to 1 Hz)	9,535,139	9,535,585	9,535,586	9,535,139
C (exclude data acquired after January 1, 2004)	5,082,151	5,082,597	5,082,598	5,082,151
D (compute along-track DoV)	5,042,579	5,043,023	5,043,024	5,042,579
E (exclude DoV if $d_{12} > 10$ km)	-123,378	-123,460	-123,461	-123,378
F (exclude DoV if h_{N_1} and/or h_{N_2} were rejected during stacking)	-54,623	-54,005	-53,302	-54,623
G (exclude DoV if h_{N_1} and h_{N_2} were retracked using different retracker)	-164	-188	-188	-164
H (remove outliers by using 10-sigma editing criterion)	-71	-254	-228	-43
I (remove outliers by using 3-sigma editing criterion)	-50,328	-50,977	-51,579	-50,125
J (exclude ERS-1 GM data RADS in domain we have EAPRS data)	401,767	401,942	402,108	402,005

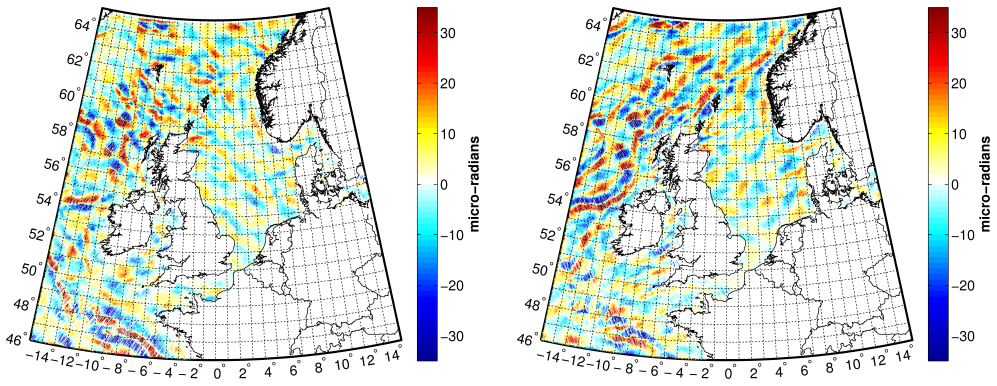

Figure 4.10: Residual along-track DoV obtained after applying the DT corrections $\zeta^{(3)}_{\mathrm{DT}}$ for the "north-south" going tracks (a) and "south-north" going tracks (b).

of terrain corrections were outside the scope of this thesis (Section 4.3.2) and RBF's are not appropriate basis functions to parameterize the uncorrected terrestrial FAA in mountainous areas. In addition, we use these EGG08-derived DoV to fill some data gaps in the continental regions of our computational domain.

The EGG08-derived DoV are sampled at the grid nodes of a tailored Fibonacci grid (the same type of grid we used in the RBF network design (Section 4.2.2.4)). The point of departure is to choose the grid resolution such that it reflects the actual resolution of EGG08, i.e., it should be chosen such that we use the minimum number of "pseudo-observations" from which we still can obtain a reasonable reconstruction of EGG08. Empirically, we found a grid resolution of $\sim$3.8 km for the northern UK and the western part of Norway and $\sim$5.8 km elsewhere. We refer to Figs. 4.11a and 4.11b for maps of the data.

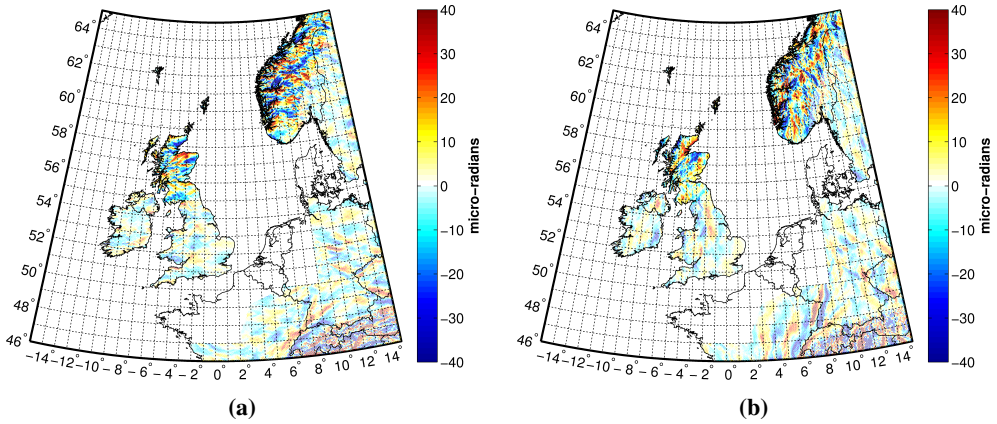

(a) (b)

Figure 4.11: Residual DoV in north (a) and east (b) directions derived from EGG08 at the locations of a tailored Fibonacci grid with a resolution of $\sim$3.8 km in the northern UK and Norway and $\sim$5.8 km elsewhere.

4.3.7 GPS/leveling data

In the framework of this thesis, the GPS/leveling data are exclusively used to validate the quasi-geoid. The data are provided by the Rijkswaterstaat Data-ICT-Dienst and were also used by Klees et al. (2008). The data set contains geometric height anomalies at 81 points covering the Netherlands (see Fig. 4.12). According to Crombaghs & de Bruijne (2004), the quality of these geometric height anomalies is about $0.010 - 0.015$ m.

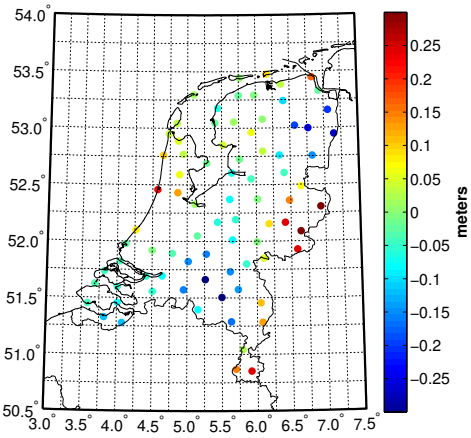

Figure 4.12: Residual geometric height anomalies (after subtraction of the DGM-1S GRACE/GOCE model (Section 4.3.1)) at the locations of 81 GPS/leveling points provided by the Rijkswaterstaat Data-ICT-Dienst.

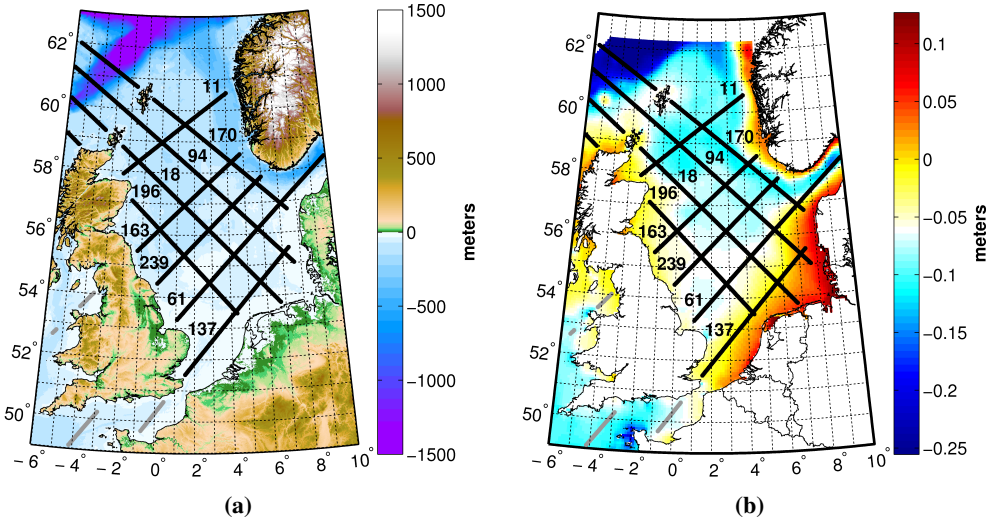

Figure 4.13: The analyzed passes on top of the GEBCO_08 bathymetry (a) and on top of the modeled MDT (b). The figures indicate the pass numbers. The model-derived MDT is the same as the one shown in Fig. 3.2. The grey colored parts of the passes are excluded from the estimation of the PSDs.

4.4 Spectral analysis of the residual along-track DoV

In this section, we present and discuss the first part of the analysis performed to assess the added value of "improved" DT corrections for quasi-geoid determination. The analysis comprises nine case studies. For each case study, we compare the ratios of the mean signal and noise power spectral densities (PSDs) of the residual along-track DoV obtained after applying the four sets of DT corrections to the SSHs (Section 4.3.5).

4.4.1 Case study setup

The PSDs of the residual along-track DoV are computed for data acquired by the TOPEX satellite before cycle 365 when the T/P orbit was changed to the interleave orbit (December 1992 – August 2002). Besides the high accuracy and high temporal resolution (10-day repeat cycle), these data are entirely acquired in the period over which we are able to compute the DT corrections $\zeta_{\mathrm{DT}}^{(3)}$ (Section 4.3.5). Of the 12 TOPEX passes that cross the North Sea, we selected nine representative ones. They are shown on top of the bathymetry and model-derived MDT in Fig. 4.13a and 4.13b, respectively. Both maps give an idea about the locations where larger DoV can be expected.

For each pass, the noise realizations are obtained by differencing the data belonging to different cycles. For P repeated cycles, we can compute $\frac{1}{2}P(P-1)$ noise realizations. Assuming there is no noise cancellation, the differences obtained this way represent the differences between the noise in the data of the two cycles. To obtain the PSD of the noise, we need to divide the PSD of these differences by two.

Due to the presence of data gaps, we use a periodogram-based method to estimate the PSDs. Here, we use a Blackman-Tukey periodogram estimator (Stoica & Moses 2005). As the lag-window, we use a Gaussian. The half-width Q of the Gaussian is derived empirically as the maximum half-width which guarantees a positive PSD at all frequencies for all computed PSDs. This approach was also successfully used by Ditmar et al. (2007). In summary, the procedure applied for each pass and for each set of DT corrections is as follows:

1. Obtain the TOPEX-derived residual along-track DoV (cycle 10–365).
2. Compute the differences between the residual along-track DoV of repeated cycles.
3. Compute for each repeated cycle the signal auto-covariance function. Here, all repeated cycles are excluded for which the distance between the first and last point is less than three-quarters of the pass's arc length (see Table 4.8 for the maximum lag distances ($N_a\Delta d$)). This criterion is a compromise between the need to have a sufficiently large maximum lag distance on the one hand, and a sufficiently large number of realizations when averaging on the other hand.
4. Compute for all $\frac{1}{2}P(P-1)$ differences the empirical auto-covariance function and divide it by two to obtain what we call the noise empirical auto-covariance function. Again, all realizations are excluded for which the distance between the first and last point is less than three-quarters of the pass's arc length.
5. Select a sufficiently large value for the half-width of the Gaussian lag-window function (Q_i).
6. Apply the Gaussian lag-window function with half-width Q_i to all empirical signal and noise auto-covariance functions.
7. Estimate the signal and noise PSDs.
8. As long as any PSD is negative at some frequencies, decrease Q_i and repeat steps 6 and 7.
9. Compute the average signal and noise PSDs.

Table 4.8: Overview of the maximum lag (N_a), maximum lag distance ($N_a\Delta d$), used/total number of cycles, and maximum possible half-width (Q) of the applied lag-window function.

Pass number	N_a	Max lag distance $N_a\Delta d$ (km)	Used/total # of cycles	Q
11	68	417	193/423	22
163	73	448	234/416	20
239	79	485	230/426	21
61	124	766	205/418	22
137	79	485	178/417	19
196	142	877	161/418	29
18	164	1015	188/425	32
94	167	1034	213/423	43
170	148	915	191/418	25

4.4.2 Results

Fig. 4.14 shows the estimated signal and noise PSDs for all passes together with the signal-to-noise ratio (SNR). As can be seen, the shape of all signal PSDs is more or less similar; the signal PSDs peak at a wavelength of about 200 km after which they decrease down to a wavelength of 50–30 km whereafter they stabilize. The decrease for wavelengths $>$ 200 km is caused by the removal of the DGM-1S reference field (Section 4.3.1). Suppose this global model exactly represents the radar altimeter data, than we would not expect any signal at wavelengths above 100–150 km. The fact that we do see signal for larger wavelengths (Fig. 4.14) can be seen as an indication that the global model is not perfect or can be attributed to residual long-wavelength orbit errors, which do not cancel out when taking the difference between two passes. It should be noted that differences among the PSDs that belong to various passes are also introduced by applying different lag-window functions (different half-widths Q) to the empirical auto-covariance functions. As shown in Table 4.8, the derived maximal half-widths vary between 19 (pass 137) to 43 (pass 94), where the smaller Q becomes, the more the PSD is smoothed.

Since we are analyzing the PSDs of the residual along-track DoV, we expect the noise PSDs to increase for higher frequencies. This is what we observe in Fig. 4.14 (note the logarithmic scale); an increase down to a wavelength of $\sim$20 km. The increase is in line with what could be expected based on the observation of Sandwell & Smith (2009) that the SSHs do have a nearly white spectrum; taking the derivative of a white noise signal increases the noise proportional to the frequency.

In general, the SNRs are above 1 down to wavelengths of 30–20 km and far above 1 for longer wavelengths. We also observe for wavelengths around $\sim$200 km slightly higher SNRs for the descending passes (even pass numbers) compared to those for

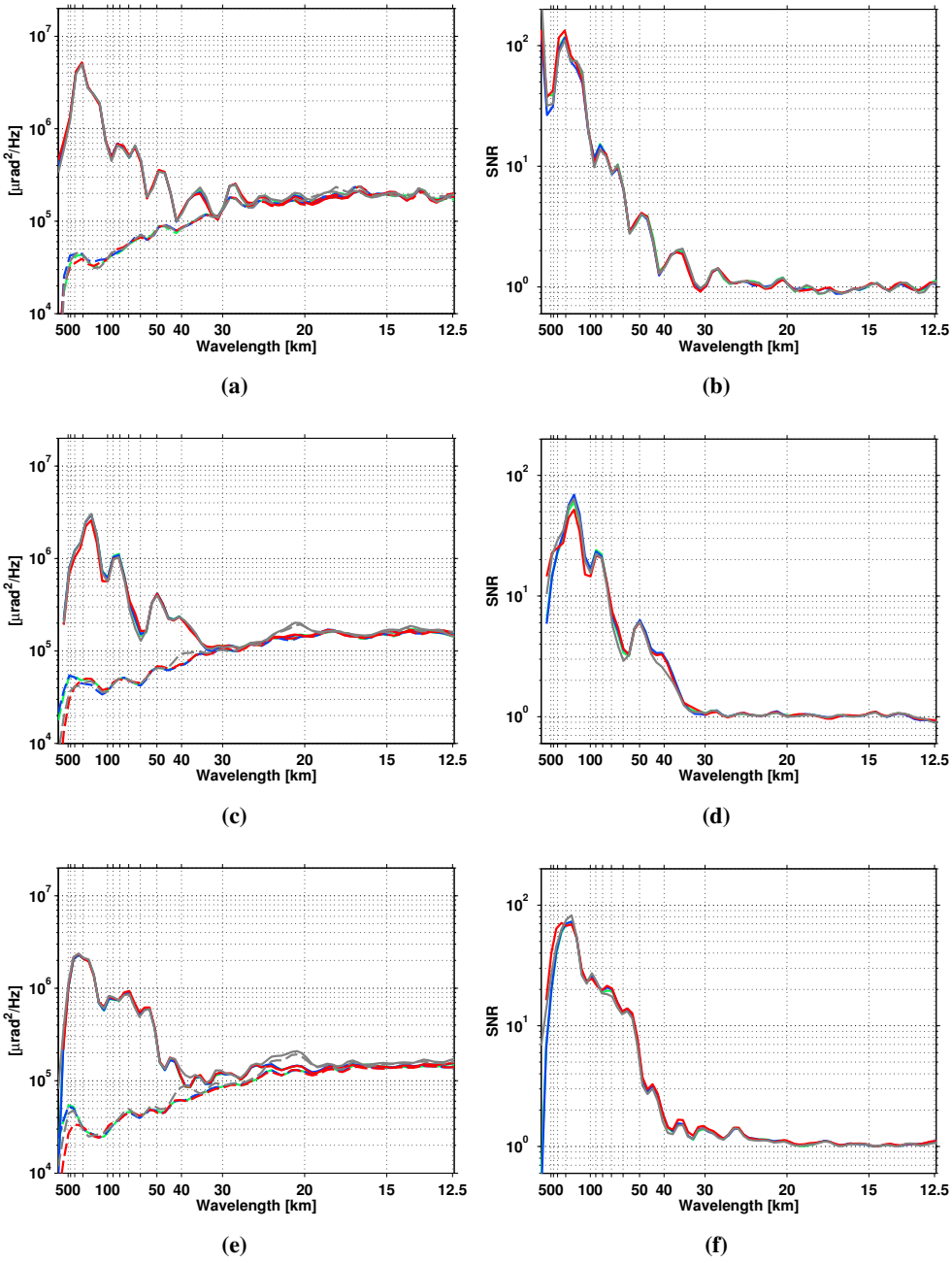

Figure 4.14: The signal (solid line) and noise (dashed line) PSDs (left panels) and the SNR as a function of wavelength (right panels) obtained after applying the DT corrections $\zeta_{\mathrm{DT}}^{(1)}$ (green), $\zeta_{\mathrm{DT}}^{(2)}$ (blue), $\zeta_{\mathrm{DT}}^{(3)}$ (red), and $\zeta_{\mathrm{DT}}^{(4)}$ (grey) for the passes 11 (top), 163 (middle), and 239 (bottom).

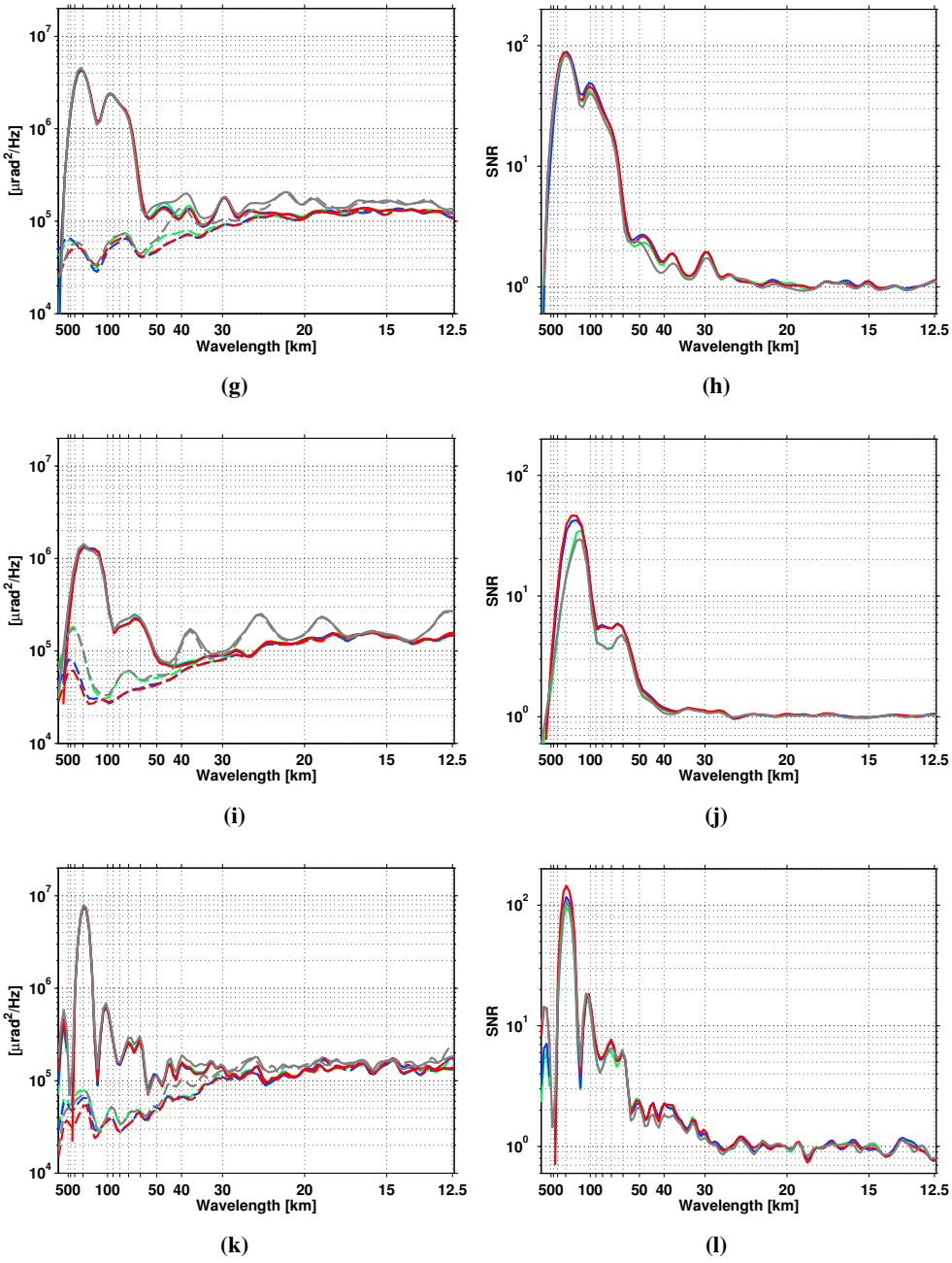

Figure 4.14 (continued): The signal (solid line) and noise (dashed line) PSDs (left panels) and the SNR as a function of wavelength (right panels) obtained after applying the DT corrections $\zeta_{\mathrm{DT}}^{(1)}$ (green), $\zeta_{\mathrm{DT}}^{(2)}$ (blue), $\zeta_{\mathrm{DT}}^{(3)}$ (red), and $\zeta_{\mathrm{DT}}^{(4)}$ (grey) for the passes 61 (top), 137 (middle), and 196 (bottom).

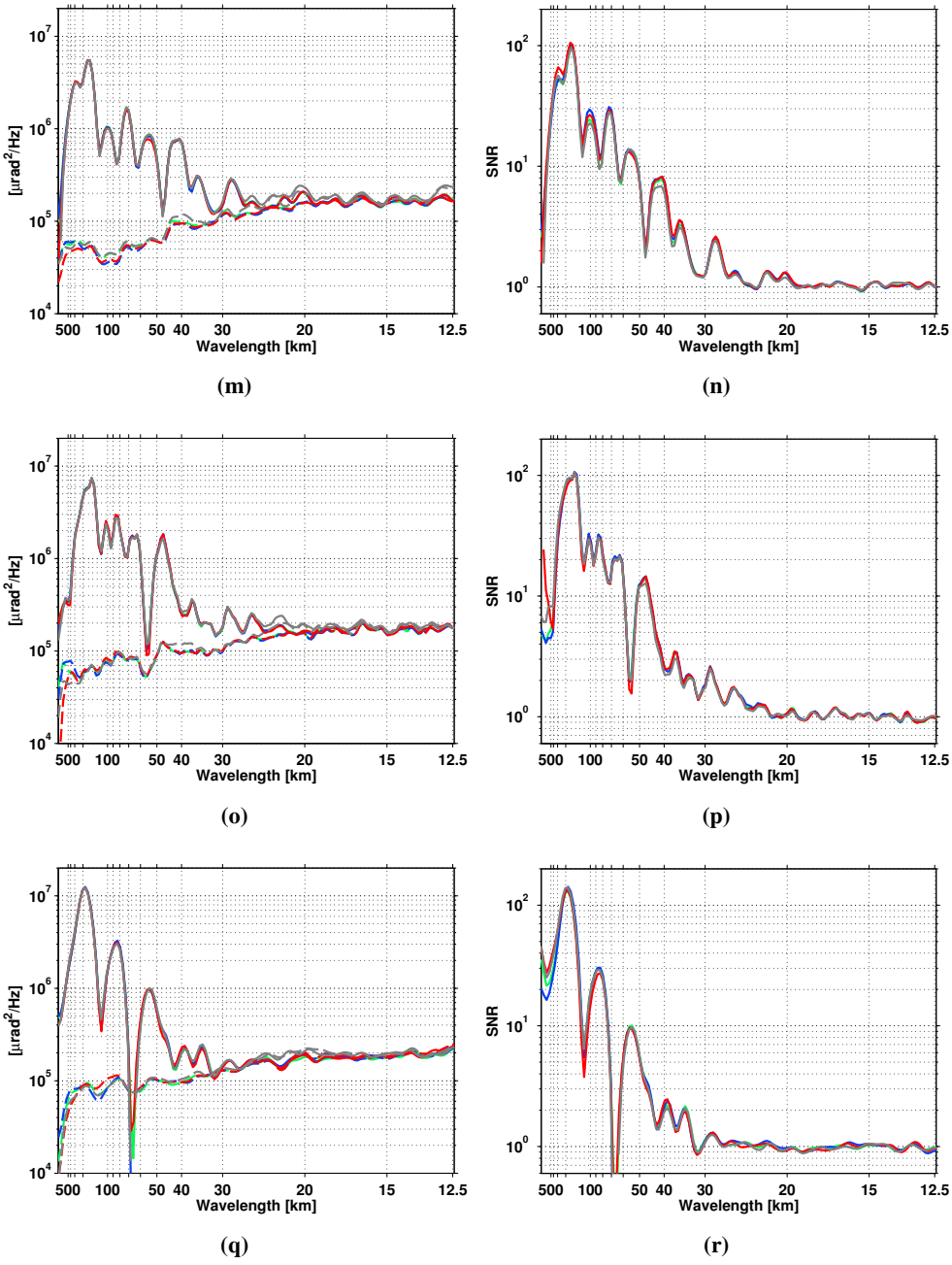

Figure 4.14 (continued): The signal (solid line) and noise (dashed line) PSDs (left panels) and the SNR as a function of wavelength (right panels) obtained after applying the DT corrections $\zeta_{\mathrm{DT}}^{(1)}$ (green), $\zeta_{\mathrm{DT}}^{(2)}$ (blue), $\zeta_{\mathrm{DT}}^{(3)}$ (red), and $\zeta_{\mathrm{DT}}^{(4)}$ (grey) for the passes 18 (top), 94 (middle), and 170 (bottom).

the ascending passes (odd pass numbers). This increased signal variation is explained by the fact that the descending passes cross the shelf edge (steep gradient in the bathymetry (Fig. 4.13a)) and are approximately aligned with the direction of the general trend in the MDT (Fig. 4.13b).

4.4.3 Discussion and conclusions

After these introductory remarks, we turn to the actual analysis that aims to evaluate the impact "improved" DT corrections to the SSHs have on the PSDs/SNRs. Indeed, any improvement is expected to show up by a decrease of the noise level, which in turn improves the SNR in a particular bandwidth. The analysis consists of three parts. First, we assess the impact of deriving the astronomical tide contribution to the DT corrections from the shallow water hydrodynamic model DCSM, compared to deriving this contribution from the global ocean tide model GOT4.7. Second, we assess the added value of including the surge and steric contributions to the DT corrections. Finally, we assess the added value of using DCSM to correct the altimeter-derived SSHs for the full DT signal, compared to using corrections obtained as the sum of the three main contributions to the DT (astronomical tide (GOT4.7), surge (MOG2D), and steric height (DTU10-MSS/EGG08)).

4.4.3.1 Added value of astronomical tide corrections derived from a shallow water hydrodynamic model

First, we assess the impact of deriving the astronomical tide contribution to the DT corrections from the shallow water hydrodynamic model DCSM, compared to deriving this contribution from the global ocean tide model GOT4.7. This assessment is carried out by comparing the PSDs/SNRs obtained after applying the DT corrections $\zeta_{\mathrm{DT}}^{(1)}$ on the one hand, and $\zeta_{\mathrm{DT}}^{(2)}$ on the other hand.

In Fig. 4.14, we observe that for the northerly passes 11, 94, and 170 the SNRs at the long wavelengths (for wavelengths larger than 300 km for pass 170) are more favorable to the DT corrections $\zeta_{\mathrm{DT}}^{(1)}$. At shorter wavelengths, we do not observe (for these three passes) significant differences between both SNR curves. For all other passes, except pass 239, we observe in some parts of the spectrum higher SNRs if we apply the DT corrections $\zeta_{\mathrm{DT}}^{(2)}$. For pass 163, these higher SNRs show up in the wavelength range 200–140 km. For the passes 61 and 18, they are visible in two parts of the spectrum; for wavelengths 150–80 and 55–40 km (pass 61), and 120–70 and 45–36 km (pass 18). The largest relative differences between both SNR curves are observed for the southerly passes 137 and 196 (ranked according to the degree of improvements). For the ascending pass 137, that crosses the southern North Sea just north to the entrance to the English Channel up to the Danish coast (Fig. 4.13), we

observe higher SNRs in the bandwidth $\sim$500–37 km. For the descending pass 196, this bandwidth is $\sim$500–65 km.

Based on these results, we conclude that the added value of using DCSM instead of GOT4.7, i.e., using a shallow water hydrodynamic model instead of a global ocean tide model, is increasing towards the southern North Sea. In addition, we conclude that in the southern North Sea the improvements show up over almost the entire spectrum. The fact that the added value increases towards the southern North Sea could be expected, since in this region the tidal behavior is more complex. Water depths become shallower and the tidal wave through the English Channel joins the tidal wave that has traveled around Scotland.

4.4.3.2 Added value of including the surge and steric contributions

Next, we assess the added value of including the surge and steric contributions to the DT corrections. This assessment is limited to the surge and steric contributions obtained using DCSM as these are expected to be better than those obtained from the MOG2D model and DTU10-MSS/EGG08. So, we compare the PSDs/SNRs obtained after applying the DT corrections $\zeta_{\mathrm{DT}}^{(2)}$ on the one hand, and $\zeta_{\mathrm{DT}}^{(3)}$ on the other hand.

In Fig. 4.14, we observe that for all passes, except pass 61, at longer wavelengths (500–100 km) the SNRs obtained after applying the DT corrections $\zeta_{\mathrm{DT}}^{(3)}$ are higher compared to those obtained after applying the DT corrections $\zeta_{\mathrm{DT}}^{(2)}$. For the passes 163, 239, 18, 94, and 170, these higher SNRs are observed down to wavelengths between 300 and 200 km. For the other passes (11, 137, and 196), the higher SNRs are observed down to wavelengths in the bandwidth 200–100 km. Note that for the passes 163 and 170 the SNRs in the bandwidths 280–80 and 200–80, respectively, are lower if the DT corrections $\zeta_{\mathrm{DT}}^{(3)}$ are applied compared to the ones obtained after applying $\zeta_{\mathrm{DT}}^{(2)}$. The most likely explanation for this decreased performance of the DT corrections $\zeta_{\mathrm{DT}}^{(3)}$ are the errors in these corrections associated with the errors in the used salinity and temperature fields (Section 3.6.1.3). Indeed, by comparing Fig. 3.7b and Fig. 4.13b we conclude that both passes cross that part of the model domain where these errors are visible. We agree that this also applies to pass 11. The reason why we do not see a similar degradation of the SNRs obtained if we apply the DT corrections $\zeta_{\mathrm{DT}}^{(3)}$ is not clear. The degraded performance of the DT corrections $\zeta_{\mathrm{DT}}^{(3)}$ is also observed at wavelengths around 80 km for pass 11, 100 and 70 km for pass 18, and 55 km for pass 94, although here the degradation is small.

So, we conclude that including both the steric and surge parts improves the SNRs at mainly *longer* wavelengths; down to 140–100 km for pass 11, 137, and 196. The fact that the southerly passes 137 and 196 are among the three passes for which we observe higher SNRs over the largest wavelength range supports the conclusion that also here the added value is more significant towards the southern North Sea. We

admit, however, that this increase is marginal. At shorter wavelengths, no significant differences are observed between the PSDs obtained after applying DT corrections that include the surge and steric contributions and those that do not include them. This lack of improvements at shorter wavelengths can be explained as follows. The used ERA-Interim wind and mean sea level pressure fields have a spatial resolution of only $1.5^\circ \times 1.5^\circ$ (nowadays the full resolution data set ($0.75^\circ \times 0.75^\circ$) is available free of charge). Except for a mapping of these low-resolution data to the shorter wavelengths (physics of the model does not necessarily imply that the low-resolution atmospheric wind and pressure forcing leads to only long-wavelength spatial water level fluctuations), the ERA-Interim data are not expected to produce high-resolution surge corrections. Hence, to assess the impact of the surge in the DT corrections at shorter wavelengths, we need to use high-resolution wind and mean sea level pressure fields, e.g., the ones provided by the meteorological high-resolution limited area model (HiRLAM) (Cats & Wolters 1996) (for operational storm surge forecasting with DCSM, HiRLAM data are used with a spatial resolution of 5–15km). Cats & Wolters (1996) showed the strong local variability of wind fields over the North Sea, while Verlaan et al. (2005) reported an improved modeling of the surge when using high-resolution wind and mean sea level pressure fields. Verlaan et al. (2005) referred to numerical experiments where HiRLAM data with a 55 km resolution were replaced by HiRLAM data with a 22 km resolution. Because the ERA-Interim data have a resolution of $1.5^\circ \times 1.5^\circ$ ($\sim 107\times \sim 167$ km in east-west and north-south directions, respectively), it is reasonable to expect some improvements as well if the ERA-Interim data are replaced by HiRLAM data.

4.4.3.3 Added value of using DCSM to correct for the full DT signal

Finally, we assess the added value of using DCSM to correct the altimeter-derived SSHs for the full DT signal, compared to using corrections obtained as the sum of the three main contributions to the DT (astronomical tide (GOT4.7), surge (MOG2D), and steric height (DTU10-MSS/EGG08)). In fact, this is the comparison of applying the "best" available corrections when we *do* and *do not* have access to a shallow water hydrodynamic model. The assessment is carried out by comparing the PSDs/SNRs obtained after applying the DT corrections $\zeta_{\mathrm{DT}}^{(3)}$ (DCSM) on the one hand, and $\zeta_{\mathrm{DT}}^{(4)}$ (GOT4.7, MOG2D, and DTU10-MSS/EGG08) on the other hand.

At the longer wavelengths (500–100 km), we see a mixed picture. For the passes 11, 61, 137, 196, and 18, we observe predominantly higher SNRs if we apply the DT corrections $\zeta_{\mathrm{DT}}^{(3)}$. For the passes 239 and 170, the SNRs after applying the DT corrections $\zeta_{\mathrm{DT}}^{(3)}$ are first higher compared to the ones obtained after applying the DT corrections $\zeta_{\mathrm{DT}}^{(4)}$ (down to 220 km for pass 239 and down to 400 km for pass 170), but lower for the shorter wavelengths in the 500–100 km bandwidth. The degraded performance of the DT corrections $\zeta_{\mathrm{DT}}^{(3)}$ compared to $\zeta_{\mathrm{DT}}^{(4)}$ is observed over the entire bandwidth

500–100 km for the passes 163 and 94. For the passes 163, 94, and 170 (in the bandwidth 200–80 km), we explain this by the, already mentioned, errors in the DT corrections $\zeta_{\mathrm{DT}}^{(3)}$ associated with the errors in the used salinity and temperature fields (Section 3.6.1.3). For the passes 94 and 170, we can additionally add the better representation of the astronomical tide by the GOT4.7 global ocean tide model.

We also find for all passes, except the passes 11 and 170, a somehow higher noise level for wavelengths < 45 km if the DT corrections $\zeta_{\mathrm{DT}}^{(4)}$ are applied. A detailed analysis shows that this increase is caused by the surge corrections as obtained from the MOG2D model which were used in the DT corrections $\zeta_{\mathrm{DT}}^{(4)}$.

We conclude that the added value of obtaining corrections for the full DT signal from DCSM compared to obtaining them as the sum of the three main contributions to the DT is, at the longer wavelengths, more significant towards the southern North Sea. Based on the first two parts of the analysis presented in this section, we conclude that this should be mainly attributed to the improved representation of the astronomical tide in this region by DCSM. Furthermore, we conclude that at shorter wavelengths the surge corrections provided by the MOG2D model turns out to increase the noise level. Apparently, this model is not appropriate to derive proper surge corrections in shallow waters.

It should be noted that in this analysis we compared PSDs obtained by averaging over 161–234 cycles (see Table 4.8). To assess the impact the various signal contributors to a DT correction and the DT correction model have on the GM data, we need to compare the PSDs estimated using the data of a single satellite pass. However, the uncertainty these estimated PSDs will have does not allow to draw any conclusion. Whether improved methods to estimate PSDs in the presence of data gaps compared to the one considered here (e.g., Broersen 2008) allow to carry out such an analysis needs to be investigated.

4.5 Impact of the dynamic topography corrections on the quasi-geoid

The spectral analysis presented in the previous section has shown that improvements due to “improved” DT corrections mainly show up at longer wavelengths and that they are more significant towards the southern North Sea. Here, we investigate the added value of “improved” DT corrections to the altimeter-derived SSHs for quasi-geoid estimation. For the assessment, various quasi-geoid solutions are computed that differ from each other by the set of DT corrections applied to the altimeter SSHs (Section 4.3.5). To exclude the effect different parameterizations of the gravity field may have, the number and bandwidth of the RBFs are fixed to the ones found when using the DT corrections $\zeta_{\mathrm{DT}}^{(3)}$ (Section 4.2.2). This is justified because there are no

indications that the applied set of DT corrections has a significant impact on the parameterization, given the magnitude of the gradients of the corrections compared to the gradients of the residual height anomalies. Furthermore, while it is possible that the contribution of radar altimeter data, and also the contribution of "improved" DT corrections, to the estimated quasi-geoid is suppressed by that of shipboard gravity data, the experiments are repeated without shipboard gravity data. This not only places our findings in a broader context (in other shallow waters less or even no shipboard data might be available), but also makes sense if we consider that the weight of each data set is determined by MCVCE (Section 4.2.3). The outcomes of this estimation cannot be taken for granted since they strongly rely on the underlying assumptions (e.g., the adopted noise model for each observation group). The scenario without shipboard gravity data provides an upper bound on the impact of "improved" DT corrections on the quasi-geoid.

As noted in the introduction of this chapter, we do not need to estimate the quasi-geoid over DCSM's whole model domain. Therefore, to quantify the added value of "improved" DT corrections on the quasi-geoid, the computational domain is defined as the geographic region between 6°W to 10°E and 49°N to 63°N. We refer to this domain as Ω_{I} (Fig. 4.1).

Before we present and discuss the differences among the various quasi-geoid solutions, we first present and discuss the derived values for the bandwidth and number of RBFs as obtained after applying the DT corrections $\zeta_{\mathrm{DT}}^{(3)}$. Note that in deriving these values, shipboard gravity data are included. Furthermore, it should be noted that in this section we only present the *differences* among the various quasi-geoid solutions; the estimated quasi-geoid itself and its validation are addressed in the next section.

4.5.1 Choice of the parameterization of the residual gravity field

The choice of the parameterization is determined using two different subdomains Ω_{A} and Ω_{B}, which are shown in Fig. 4.1. Figures 4.15a and 4.15b show the rms differences between the estimated quasi-geoid and EGG08 as a function of (i) the depth (bandwidth) and (ii) the number of *selected* RBFs (see Section 4.2.2.4 page 76 for the criterion applied to determine whether a particular RBF is used or not) for Ω_{A} and Ω_{B}. The fact that the number of selected RBFs is higher for Ω_{B} than for Ω_{A} is due to the fact that for the parameterization of the data in the mountainous areas of Great Britain (Ω_{B}) and Norway more RBFs are used (Section 4.2.2.4). Furthermore, since we fixed the grid resolution in these areas, the number of RBFs that are added by increasing the number over Ω with 5,000 is less for Ω_{B} than it is for Ω_{A}.

Compared to the rms differences obtained for Ω_{B} (Fig. 4.15b), the rms differences for Ω_{A} (Fig. 4.15a) are lower; for Ω_{A} the values range between 1.6 and 9.6 cm, while for Ω_{B} the values range between 2.6 and 19.2 cm. The smallest rms difference for

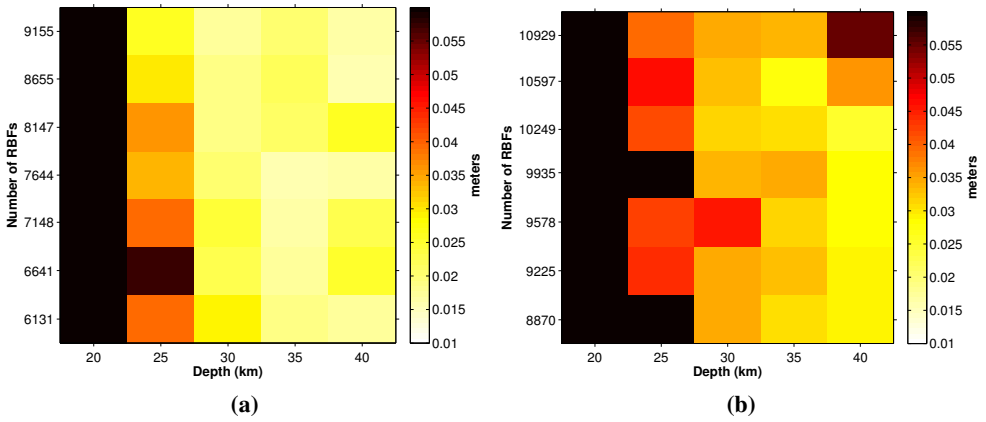

Figure 4.15: The rms differences between the estimated quasi-geoid and EGG08 as a function of the depth (bandwidth) and the number of RBFs over Ω_A (a) and Ω_B (b). The data sets used to estimate the quasi-geoid include shipboard gravity data and altimeter-derived DoV obtained after applying the DT corrections $\zeta_{DT}^{(3)}$.

Ω_A (1.6 cm) is obtained when the depth is 35 km and the number of RBFs equals 7,644, though other choices provide rms differences which are just a few mm larger than this value. In itself this is positive; it shows the solution is quite robust for small changes in the parameterization.

For Ω_B, no clear "optimal" values for the depth and number of RBFs can be identified. We observe that the lowest rms differences are obtained for a depth of 40 km. As 40 km is the maximum depth, this suggest that the "optimum" is somewhere outside the search space. However, another aspect which has to be considered when choosing the depth and number of RBFs is the convergence of the MCVCE (Section 4.2.3). In Figs. 4.16a–4.16h, we show the estimated precisions for each observation group as a function of (i) the depth and (ii) the number of RBFs for Ω_A and Ω_B. In the plots, we masked out all values obtained for a particular combination of depth and number of RBFs if "no convergence" of the estimated variance factors is achieved for one or more observation groups. Here, "no convergence" means that the estimated variance factor in the last iteration differs by more than 20% from the value obtained in the previous iteration. Note that inside Ω_B no airborne and terrestrial data are available. Also note that in Figs. 4.16e–4.16h we show the standard deviations of the EGG08 quasi-geoid heights and the altimeter-derived geometric quasi-geoid heights, and not of the finite difference approximations of the DoV (Eq. 4.54). In this way, the numbers are independent of the distance between the two points involved in the computation of these DoV.

As Figs. 4.16c, 4.16f, and 4.16h show, none of the solutions satisfies our "convergence" criterion for a depth of 40 km. Over Ω_A (Figs. 4.16a, 4.16b, 4.16d, 4.16e, and

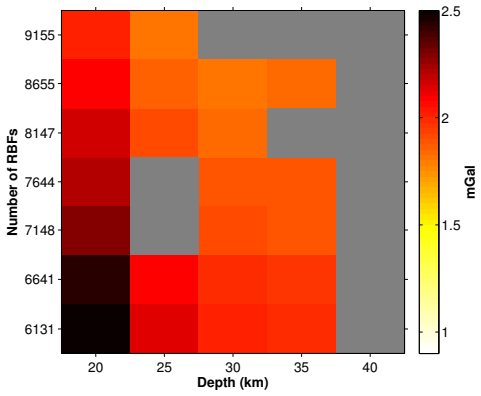

(a)

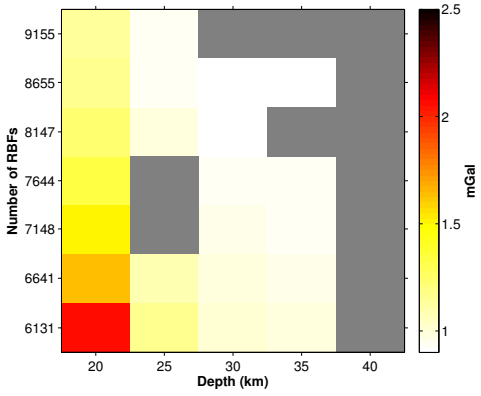

(b)

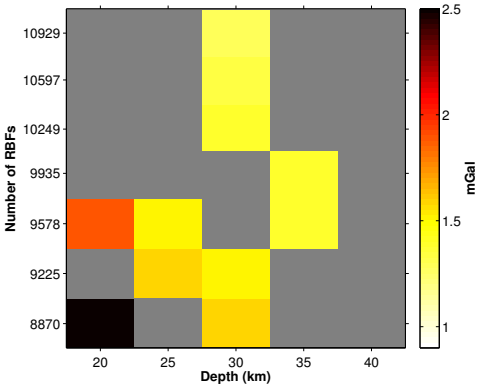

(c)

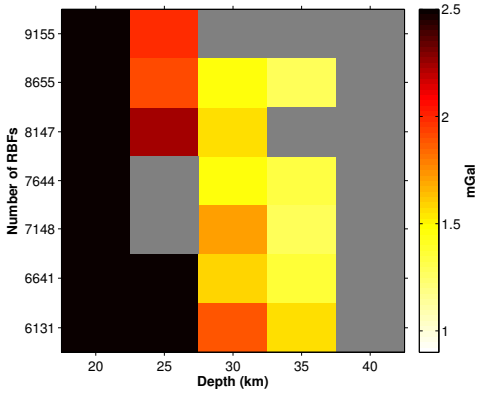

(d)

Figure 4.16: Continued on next page.

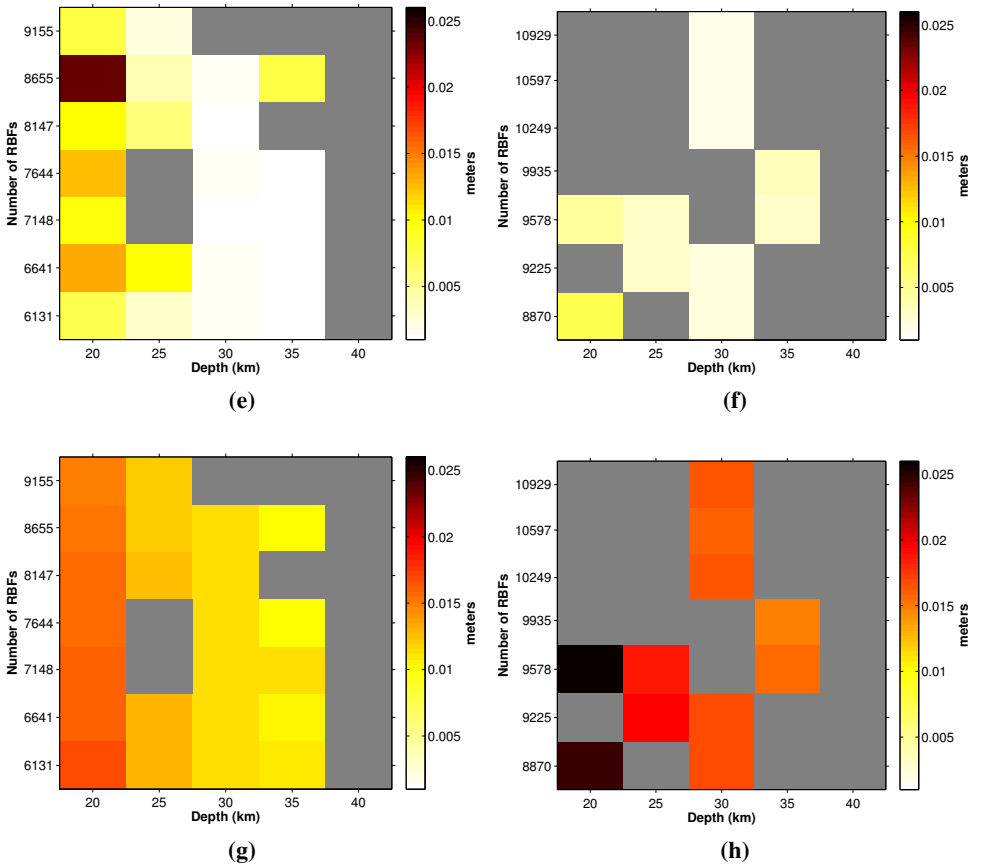

Figure 4.16 (continued): Estimated standard deviations of the terrestrial gravity observation group over Ω_A (a), the shipboard gravity observation group over Ω_A (b) and Ω_B (c), the airborne gravity observation group over Ω_A (d), the EGG08-derived DoV expressed as the standard deviations of the EGG08 quasi-geoid heights over Ω_A (e) and Ω_B (f), and the altimeter-derived along-track DoV expressed as the standard deviations of the geometric quasi-geoid heights over Ω_A (g) and Ω_B (h). The grey color means that "no convergence" of the estimated variance factors is achieved for one or more observation groups. That is, the estimated variance factor in the last iteration differs by more than 20% from the value obtained in the previous iteration. Note that the shown estimated standard deviations for the terrestrial and shipboard gravity observation groups refer to the data sets for which the a-priori standard deviation was set to 2.0 mGal (see Tables 4.1 and 4.2). For the Belgian and Netherlands terrestrial gravity data sets obtained from the in-house database, the estimated standard deviations are a factor 1.25 larger and 3.33 smaller, respectively. For the WADGRAV and Shell shipboard gravity data sets, the estimated standard deviations are a factor 1.35 and 5.56 smaller, respectively.

4.16g) we observe the same, except if the number of RBFs equals $6,641$. Since it is not reasonable to expect that for depths >40 km the estimated weights will converge,

we conclude that the "optimal" values for the depth and number of RBFs should be within our search space. The reason why for Ω_B we obtain the best agreement with EGG08 if the depth equals 40 km is that for this depth especially the EGG08-derived DoV observation group obtains a large weight (note that the obtained solution is determined by the assigned weights estimated in the last iteration before the break). As a consequence, it is no surprise that the rms differences between the estimated quasi-geoid and EGG08 become smaller. In any case, the solution seems to become unstable when the weight of one observation group becomes disproportionately large. This also happens if the depth is 25 km and the number of RBFs $> 10,249$. No specific reason was found for the other "no convergence" cases obtained when the depth was fixed to 20 and 25 km.

Based on these results, we tried various values for the depth and number of RBFs (where the depth was fixed to 30 and 35 km and the number of RBFs over Ω was selected over the range $70,000$ (average distance between the RBF centers is ~ 7.6 km) to $85,000$ (average distance between the RBF centers is ~ 6.9 km)) in estimating a quasi-geoid over Ω_I (not shown here). By comparing the solutions, we conclude that no optimal choice can be made; for some regions a depth of 30 km is most appropriate, while in other regions 35 km provides more reasonable results. Ultimately, we chose a depth of 30 km and a number of $80,000$ RBFs over Ω ($8,147$ and $10,249$ RBFs over Ω_A and Ω_B, respectively). For this choice, the mean distance between the RBF centers is ~ 7.1 km. This is a compromise as it provides in most cases convergence of the MCVCE if we apply other sets of DT corrections and/or exclude shipboard gravity data.

Regarding the estimated standard deviations themselves it is worth to note that, within the investigated ranges of depths and number of RBFs, there is a slight tendency that they decrease when both the depth and number of RBFs increase.

4.5.2 Effect on the quasi-geoid

Having fixed the bandwidth and number of RBFs, we continue to estimate the various residual quasi-geoid solutions over Ω_I using, among others, altimeter-derived residual along-track DoV obtained after applying the various sets of DT corrections. The quasi-geoids are estimated with and without shipboard gravity data. The differences among the various solutions obtained *with* shipboard gravity data are shown in Figs. 4.17a–4.17f, while the differences obtained *without* them are shown in Figs. 4.18a–4.18f.

When comparing Figs. 4.17a–4.17f with Figs. 4.18a–4.18f, we observe that adding shipboard gravity data suppresses the added value of "improved" DT corrections. The reason is that then radar altimeter data contribute much less to the quasi-geoid solution than if shipboard data are excluded. Hence, the DT corrections become less

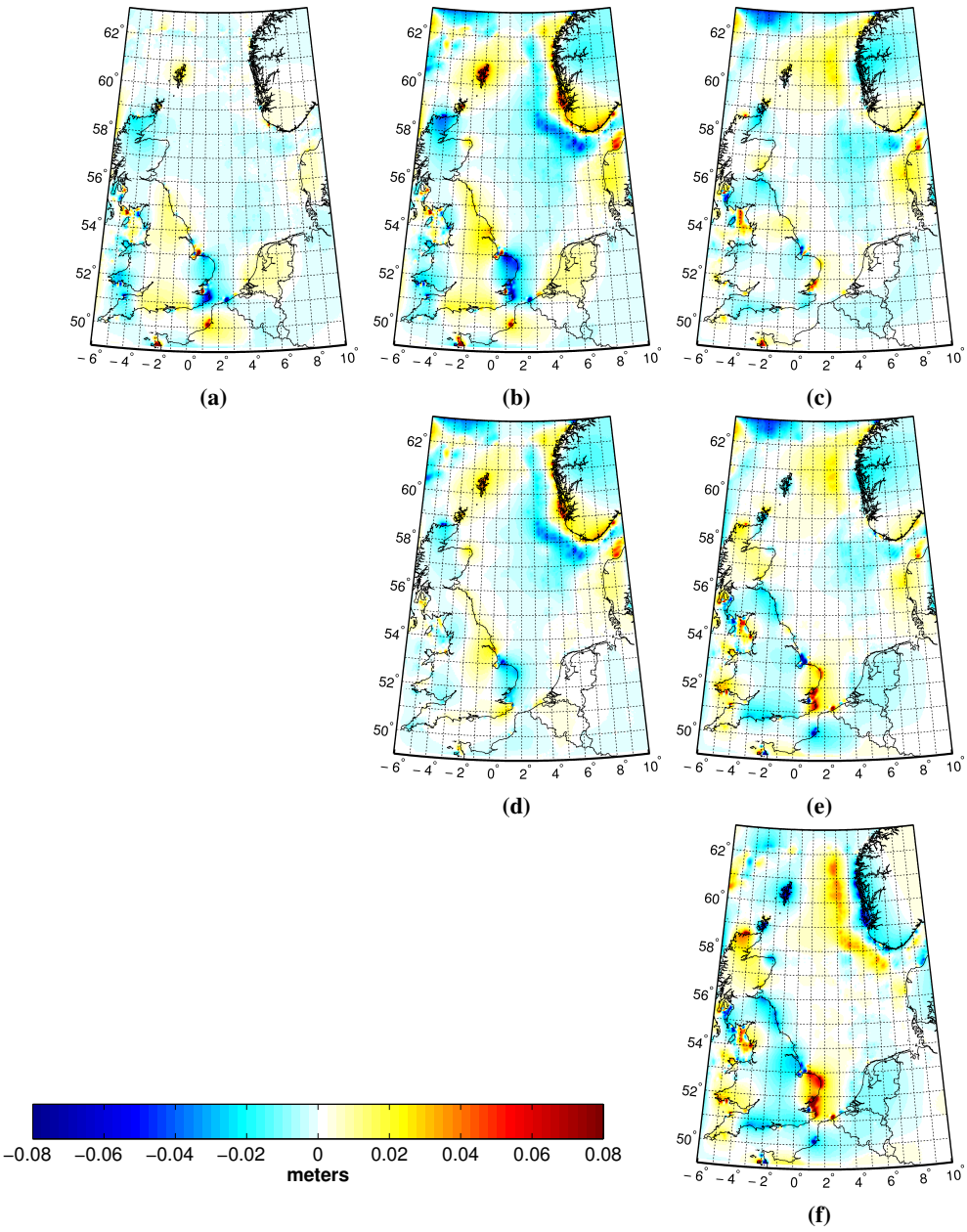

Figure 4.17: Differences among the quasi-geoids estimated *with* shipboard gravity data and after applying the various sets of DT corrections to the observed SSHs. The first row shows the differences between the quasi-geoid obtained after applying the DT corrections $\zeta_{\mathrm{DT}}^{(1)}$ and the ones obtained after applying $\zeta_{\mathrm{DT}}^{(2)}$ (a), $\zeta_{\mathrm{DT}}^{(3)}$ (b), and $\zeta_{\mathrm{DT}}^{(4)}$ (c). The second row shows the differences between the quasi-geoid obtained after applying the DT corrections $\zeta_{\mathrm{DT}}^{(2)}$ and the ones obtained after applying $\zeta_{\mathrm{DT}}^{(3)}$ (d) and $\zeta_{\mathrm{DT}}^{(4)}$ (e)). The last row shows the differences between the quasi-geoids obtained after applying the DT corrections $\zeta_{\mathrm{DT}}^{(3)}$ and $\zeta_{\mathrm{DT}}^{(4)}$ (f).

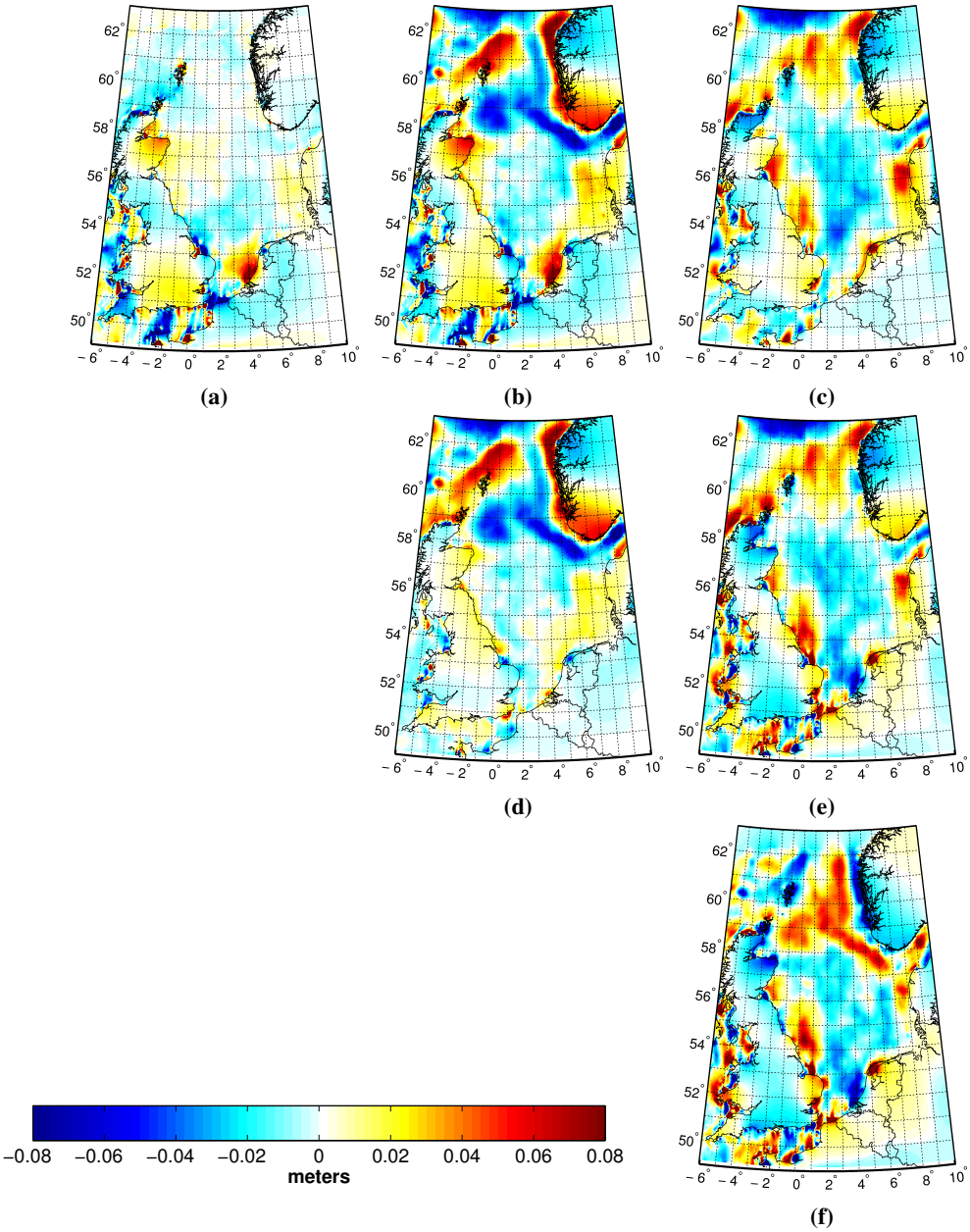

Figure 4.18: Differences among the quasi-geoids estimated *without* shipboard gravity data and after applying the various sets of DT corrections to the observed SSHs. The first row shows the differences between the quasi-geoid obtained after applying the DT corrections $\zeta_{\mathrm{DT}}^{(1)}$ and the ones obtained after applying $\zeta_{\mathrm{DT}}^{(2)}$ (a), $\zeta_{\mathrm{DT}}^{(3)}$ (b), and $\zeta_{\mathrm{DT}}^{(4)}$ (c). The second row shows the differences between the quasi-geoid obtained after applying the DT corrections $\zeta_{\mathrm{DT}}^{(2)}$ and the ones obtained after applying $\zeta_{\mathrm{DT}}^{(3)}$ (d) and $\zeta_{\mathrm{DT}}^{(4)}$ (e)). The last row shows the differences between the quasi-geoids obtained after applying the DT corrections $\zeta_{\mathrm{DT}}^{(3)}$ and $\zeta_{\mathrm{DT}}^{(4)}$ (f).

important. Indeed, the differences among the solutions obtained including shipboard gravity data are within ± 1 cm (even in the southern North Sea), while in Figs. 4.18a–4.18f systematic patterns are observed that reach several centimeters. Exceptions are some isolated spots along the coasts of Belgium, Denmark, France, Great Britain, and the Shetland Islands, and a feature along the Norwegian coast aligned with the Norwegian Trench (Figs. 4.17b, 4.17d, and 4.17f) where larger differences (> 1 cm) are observed.

The apparent suppression of the altimeter-derived DoV with respect to the shipboard gravity data poses the question whether the observation groups have been weighted properly. Table 4.9 provides the estimated standard deviations for the solutions with and without shipboard gravity data. From these values, we first notice that when including shipboard data the estimated standard deviations of the Dutch terrestrial gravity data set (0.56 mGal) and the Shell shipboard gravity data set (0.21 mGal) are in good agreement with the ones estimated by Klees et al. (2008): 0.60 and 0.36 mGal, respectively. For the WADGRAV shipboard data set we obtain 0.85 mGal, which is significantly smaller than the one estimated by Klees et al. (2008) (1.48 mGal). For the other terrestrial gravity data sets, we obtain standard deviations in the range of 1.87 to 2.34 mGal. It is difficult to judge whether this estimate is realistic as we lack any information about the accuracy of the other terrestrial gravity data sets.

On the other hand, the estimated standard deviations of all other observation groups are low to very low. A standard deviation of 1.15–1.17 mGal for the shipboard data sets is feasible nowadays (Nabighian et al. 2005), but not a few decades ago when most of our available data were acquired (often without GNSS navigation). According to Wessel & Watts (1988), the most reliable technique to evaluate the accuracy of shipboard gravity data is to analyze the discrepancies in FAA values at crossover locations. For our edited shipboard gravity data set, this analysis reveals a standard deviation of 2.01 mGal over 17,316 crossovers (mean is < 0.01 mGal). When assuming that the crossover adjustment removed the systematic errors in the shipboard data and that the random errors are statistically uncorrelated, we obtain a standard deviation of a single shipboard gravity measurement of 1.4 mGal. This is close to the MCVCE values of 1.15–1.17 mGal. Nevertheless, it is much lower than the values reported by Wessel & Watts (1988) who assessed the accuracy of the Lamont-Doherty Geological Observatory's global marine gravity data bank. After removing linear drifts and DC shifts, they obtained a standard deviation of 13.96 mGal. Our main explanation for this huge difference is the fact that our data are acquired relatively close to land, while Wessel & Watts (1988) assessed a global data set including data acquired in the middle of the oceans. The estimated standard deviation of the airborne gravity observation group is lower than the reported values for the BalGRACE and NorthGRACE data sets (Schäfer et al. 2008) (rms is 1.8 to 2.1 mGal, see Section 4.3.4). The estimated standard deviations for the EGG08- and altimeter-derived DoV imply a standard deviation of ~ 0.3 cm for the EGG08 quasi-geoid heights and

Table 4.9: Estimated standard deviations for the various observation groups obtained after applying the different sets of DT corrections and with and without shipboard gravity data. For an unambiguous interpretation of the estimated precisions of the EGG08- and altimeter-derived DoV observation groups, the estimated standard deviations are transformed to values that express the standard deviation of the associated (i) EGG08 quasi-geoid heights and (ii) altimeter-derived geometric quasi-geoid heights.

Applied DT corrections	Shipboard data included	**Estimated standard deviations**				
		Terr. (mGal)	*Ship. (mGal)*	*Airb. (mGal)*	h_N *(EGG08) (cm)*	h_N *(radar alt.) (cm)*
$\zeta_{\mathrm{DT}}^{(1)}$	y	1.88[*1]	1.15[*2]	1.37	0.26	1.41
$\zeta_{\mathrm{DT}}^{(2)}$	y	1.88[*1]	1.17[*2]	1.14	0.22	1.35
$\zeta_{\mathrm{DT}}^{(3)}$	y	1.88[*1]	1.14[*2]	1.17	0.29	1.32
$\zeta_{\mathrm{DT}}^{(4)}$	y	1.89[*1]	1.15[*2]	1.20	0.27	1.41
$\zeta_{\mathrm{DT}}^{(1)}$	n	1.85[*1]		0.80	0.28	1.28
$\zeta_{\mathrm{DT}}^{(2)}$	n	1.85[*1]		0.73	0.28	1.21
$\zeta_{\mathrm{DT}}^{(3)}$	n	1.86[*1]		0.99	0.29	1.14
$\zeta_{\mathrm{DT}}^{(4)}$	n	1.86[*1]		0.75	0.27	1.27

[*1] For the in-house data sets the estimated standard deviation is between $\sim$0.56 (Dutch data set) and $\sim$2.34 mGal (Belgian data set).
[*2] $\sim$0.21 and $\sim$0.85 mGal for the Shell and WADGRAV data (Section 4.3.3.1).

1.2–1.4 cm for the altimeter-derived geometric quasi-geoid heights. Both are not realistic. As discussed in Section 1.3.2, the precision of EGG08 is sub-decimeter at continental scales and a few centimeters over a few hundred kilometers. For the data provided by GEOSAT, ERS-1, and TOPEX, the typical accuracies are 3–4 cm (Sandwell & Smith 2009).

However, rather than focusing on the estimated standard deviations for the individual observation groups we should look at their mutual ratios. Indeed, as long as the estimated precisions are too high for all observation groups the fact that they are unrealistic is not a problem. Looking at the ratios, we notice that the standard deviation of the shipboard data (except for the Shell and WADGRAV data sets) is about twice the standard deviation of the Dutch terrestrial gravity data set and 0.5–0.6 times the standard deviation of the other terrestrial gravity data sets. At first glance, the latter is quite unrealistic. On the other hand, we have to consider that the other terrestrial gravity data include high-frequency signals associated with topography (e.g., the Ardennes). They are not modeled well by the chosen RBF parameterization and therefore contribute to the residuals and, in turn, to the estimated standard deviations.

The ratios of the estimated standard deviations of the shipboard to airborne observation groups vary between 1 : 0.97 and 1 : 1.19 depending on the DT corrections applied to the altimeter-derived SSHs (see Table 4.9). Based on the standard deviations of the crossover differences (2.0 mGal shipboard data, 1.69–2.13 mGal for the

BKG airborne data set (Schäfer et al. (2008, Table 2))), we believe that these ratios are reasonable.

If we assume that the resolution of EGG08 in the regions where we use the EGG08-derived DoV is 5 km (half-wavelength), than the standard deviation of the derived DoV is ~ 0.74 mGal ($\sqrt{2 \cdot 0.0026^2/5000^2}$, note that 1.0 µrad $\approx$ 1.0 mGal (Smith 2010)). This is slightly higher than the standard deviation of the Dutch terrestrial gravity data set (~ 0.56 mGal) but much lower than that of the other terrestrial data sets (1.88–2.34 mGal). Compared to the latter, we believe that our estimate is too optimistic. In particular, if we consider that the EGG08-derived DoV are mainly located in the mountainous areas.

Over 7 km, the standard deviation of the altimeter-derived geometric quasi-geoid heights gives a standard deviation of the DoV of 2.77 µrad ($\sqrt{2 \cdot 0.0137^2/7000^2}$). Again using the rule of thumb 1.0 µrad $\approx$ 1.0 mGal (Smith 2010), we obtain a ratio of the weight factor of shipboard gravity data over altimeter-derived DoV of 5.8 : 1. To validate this ratio, we use the standard deviation of the shipboard gravity data derived from the crossover analysis (1.4 mGal) and the results of Section 4.4. That is, the differences between along-track DoV of different cycles are interpreted as the difference of two noise realizations, from which we can compute the noise variance per pass and DT correction assuming noise is time-stationary. Note that to remain consistent with the GM data used in the quasi-geoid computations, the along-track DoV are first smoothed using a Gaussian with a half-width of 6.5 km. This analysis provides estimates of the noise standard deviation in along-track DoV between 1.7 µrad and 2.4 µrad depending on the pass and the DT correction. A value of 2.0 µrad is representative for most passes. For the DT corrections $\zeta_{\mathrm{DT}}^{(2)}$ and $\zeta_{\mathrm{DT}}^{(3)}$, the noise standard deviations are ≤ 2.0 mGal for all passes except the passes 18, 94, and 170. For the DT corrections $\zeta_{\mathrm{DT}}^{(1)}$ and $\zeta_{\mathrm{DT}}^{(4)}$, the noise standard deviations are also > 2.0 mGal for pass 137. From the analysis of the standard deviations of altimeter-derived DoV and the crossover analysis of the shipboard gravity data, we obtain a weight ratio of 2.0 : 1 for most passes. The MCVCE estimate of 5.8 : 1 (for all altimeter-derived along-track DoV) is far beyond this range. From an a-posteriori comparison with the "V18 gravity model", Sandwell & Smith (2009) report rms differences for (retracked) GEOSAT (GM + ERM), retracked ERS-1 (GM + ERM), and TOPEX (interleave + ERM) data after smoothing with a Gaussian with a halfwidth of 18 km between 1.17 (TOPEX) and 3.57 µrad (retracked ERS-1). The latter values correspond to 1.17 and 3.57 mGal, respectively when using the rule-of-thumb of (Smith 2010). Assuming again that a std. dev. of 1.40 mGal for shipboard gravity data is realistic, we obtain weight factor ratios of 0.68 : 1–6.37 : 1. The MCVCE weight ratio of 5.8 : 1 is within this range. Nevertheless, the values in Sandwell & Smith (2009) are likely not be representative for our study, as they refer to a bandpass filtered data set, whereas in this study we applied no smoothing to the repeat-mission data and only a moderate smoothing to the GM data using a Gaussian with a half-width of 6.5 km. Sandwell &

Smith (2009) apply various low- and high-pass filters, which are difficult to reproduce based on the published material.

The estimated standard deviations obtained without the shipboard gravity data are only significantly changed for the observation groups that contain measurements at sea: the airborne gravity data sets and the altimeter-derived DoV data sets. For both observation groups, the estimated standard deviations are smaller compared to the ones obtained when including shipboard gravity data. This improvement can be understood by the fact that the absence of shipboard data allows a better fit of these data sets. That is, the post-fit residuals are smaller and hence the estimated standard deviations decrease. Note that the estimated standard deviation for the altimeter-derived DoV observation group is lowest if we apply the DT corrections $\zeta^{(3)}_{\mathrm{DT}}$.

We conclude that, in an absolute sense, the estimated standard deviations are too optimistic (except for the terrestrial data set) but that with a few exceptions their mutual ratios are reasonable, although we tend to believe that the altimeter-derived DoV observation group is underweighted. Anyway, we have to keep in mind that the estimated standard deviations strongly rely upon the assumed noise models. For all observation groups, we assumed white noise. This was mainly driven by practical constraints as our software cannot handle full variance-covariance matrices. As shown by the noise PSDs in Section 4.4, however, this assumption is not realistic for the altimeter-derived DoV observation group. Remember also the fact that we neglected the correlations between the successive DoV associated with the applied two-point finite difference scheme (see Section 4.3.5). Also for the other observation groups the assumption of white noise is questionable. For the EGG08-derived DoV observation group, this is obvious. For the terrestrial, shipboard, and airborne gravity observation groups, the noise is colored by unremoved systematic errors (e.g., instrumental drift) and/or by the background models used to compute the FAA and gravity disturbances. In a future research, more realistic noise models should be used and their significance should be analyzed. We also should note that we only applied a very moderate smoothing (Gaussian filter with a half-width of 6.5 km) to the altimeter-derived residual along-track DoV and then only to the GM data of GEOSAT and ERS-1. Compare this to the smoothing applied by Sandwell & Smith (2009). They first applied a dedicated low-pass filter (designed in Matlab using the Parks-McClellan algorithm) to the profiles with SSHs with a cut that begins at 26.8 km wavelength, has 0.5 gain at 14.6 km, and is zero at 10 km. Finally, the obtained grids with residual DoV in north and east directions are low-pass filtered using a filter with a 0.5 gain at 16 km. As noted by Sandwell & Smith (2009), the combination of the two filters has a cutoff wavelength of about 20 km. Obviously, increasing the smoothing further suppresses the high-frequency noise, which in turn might improve the relative weight of the altimeter-derived DoV observation group compared to that of shipboard gravity data. This, however, cannot be achieved with the "simple" Gaussian filter we exploited,

but requires a careful filter design, e.g., as the one exploited by Sandwell & Smith (2009).

By comparing the differences among the various quasi-geoids obtained without shipboard gravity data (Figs. 4.18a–4.18f) with the differences between observation-derived and model-derived MDT values (Fig. 3.7b) and the contribution of astronomical tide to MDT (Fig. 5.1b), most features in Figs. 4.18a, 4.18b, 4.18d, 4.18e, 4.18f can be interpreted and hence do not need further discussion. We only want to mention the differences in the English Channel between the solutions obtained after applying the DT corrections that include the DCSM tide corrections on the one hand, and those that include the GOT4.7 tide corrections on the other hand (Figs. 4.18a, 4.18b, 4.18e, and 4.18f). By analyzing the post-fit residuals for the altimeter-derived DoV observation group (not shown here) we conclude these point to errors in the GOT4.7 tide corrections.

Although it turns out that if shipboard gravity data are included the altimeter-derived DoV hardly contribute to the estimated quasi-geoid, we can still show that after applying "improved" DT corrections the systematic errors between both observation groups decrease. In doing so, we computed the differences between the quasi-geoids obtained with and without shipboard gravity data and after applying the same set of DT corrections (see Figs. 4.19a–4.19d). Indeed, since the altimeter-derived DoV hardly contribute if shipboard data are included, the differences shown in Figs. 4.19a–4.19d primarily reflect the differences between the quasi-geoids obtained without radar altimeter data and the ones obtained without shipboard gravity data. Ideally, in both cases the estimated quasi-geoid is the same. However, as shown in Figs. 4.19a–4.19d this is not the case; the differences reach several centimeters. Still, we observe some significant improvements if we apply the sets of DT corrections derived from DCSM ($\zeta_{\mathrm{DT}}^{(2)}$ and $\zeta_{\mathrm{DT}}^{(3)}$) compared to the cases where we apply the other sets ($\zeta_{\mathrm{DT}}^{(1)}$ and $\zeta_{\mathrm{DT}}^{(4)}$). Most pronounced are the systematic differences along the Dutch coast (that even cause a bias over the Netherlands and Belgium) shown in Fig. 4.19a and 4.19d, which are gone in Fig. 4.19b and 4.19c. We also observe improvements along the east coast of Great Britain and in the English Channel. If we compare Fig. 4.19b with Fig. 4.19c, we hardly observe any difference in the southern North Sea. Again, we conclude that the obtained improvements in this area should be attributed to an improved representation of the tide by DCSM. Along the shelf edge, the differences are slightly smaller if we apply the DT corrections $\zeta_{\mathrm{DT}}^{(3)}$. West of Scotland, we again observe in Fig. 4.19c the feature associated with the errors in POL's salinity and temperature fields (Section 3.6.1.3). Furthermore, it is striking that the obtained differences (Fig. 4.19c) are larger if we apply the DT corrections $\zeta_{\mathrm{DT}}^{(4)}$ than those obtained if we apply the DT corrections $\zeta_{\mathrm{DT}}^{(1)}$. Apparently, it is better not to correct for the surge and steric contributions if no proper shallow water hydrodynamic models are available.

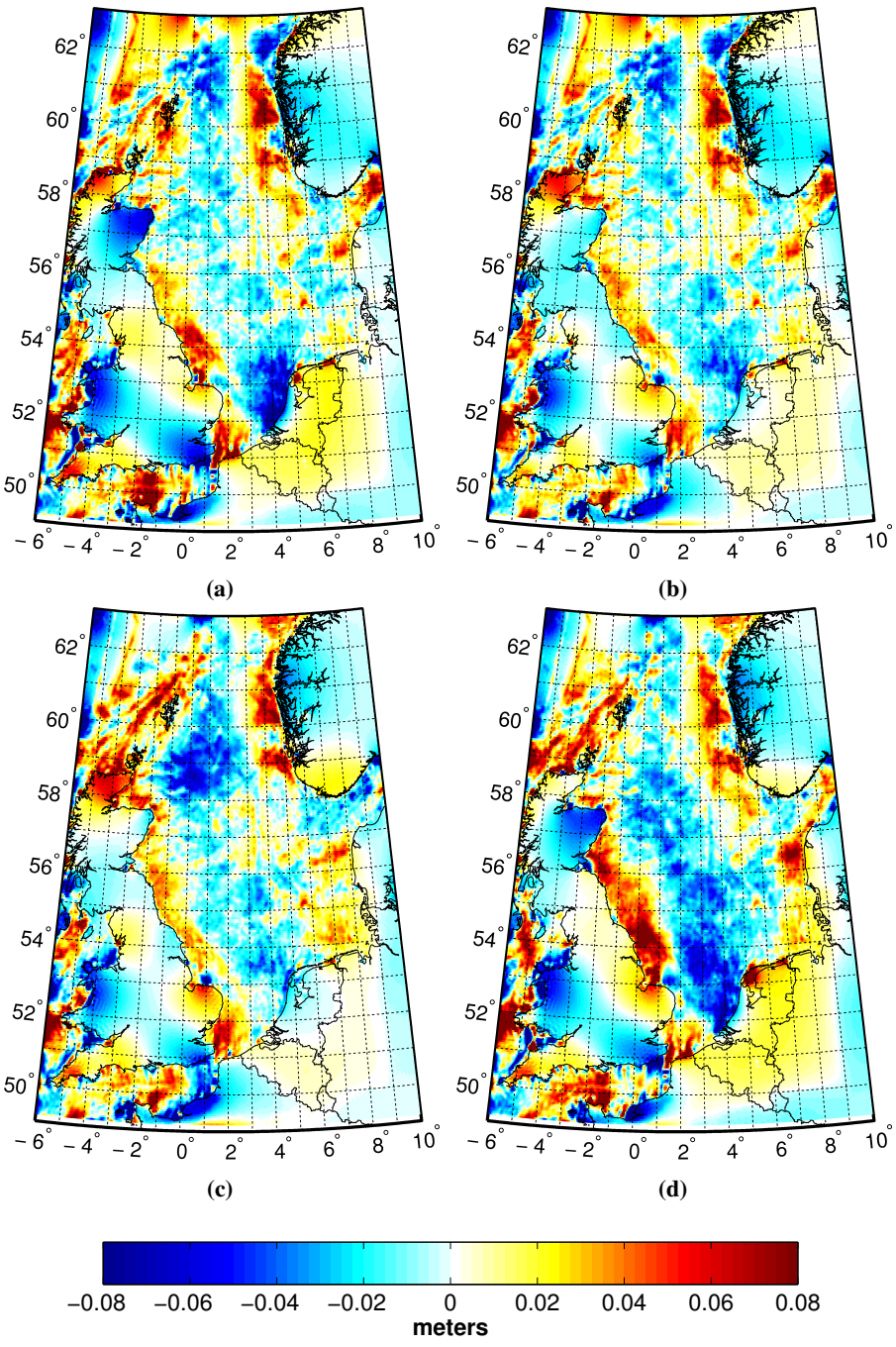

Figure 4.19: Differences between the quasi-geoids estimated *with* and *without* shipboard gravity data, where the altimeter-derived SSHs are corrected using the DT corrections $\zeta_{\mathrm{DT}}^{(1)}$ (a), $\zeta_{\mathrm{DT}}^{(2)}$ (b), $\zeta_{\mathrm{DT}}^{(3)}$ (c), and $\zeta_{\mathrm{DT}}^{(4)}$ (d).

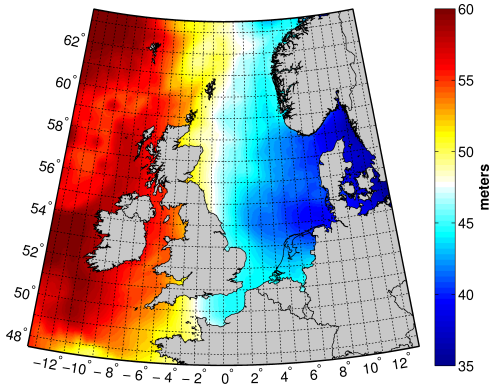

Figure 4.20: NLGEO2013 in the ETRS89/GRS80 reference system (zero-tide system). Note that, in the map, we excluded a strip of 1.5° around the boundaries of the computational domain as this is the region that is mostly affected by boundary effects.

4.6 NLGEO2013

In this last section, we present and validate the quasi-geoid estimated over the whole computational domain (Ω). This quasi-geoid, referred to as NLGEO2013, will be used to compute the ellipsoidal heights of the LAT and MSL surfaces over DCSM's model domain.

To ensure consistency with the model-derived LAT and MDT surfaces, we apply the DT corrections $\zeta_{\mathrm{DT}}^{(3)}$. Indeed, the errors in the representation of the MDT by DCSM (Section 3.6.1.3) affect both the DT corrections and the LAT surface. While, however, their sign is opposite, in the computation of the ellipsoidal heights of LAT they partly cancel out. Note that this also applies to the computation of the ellipsoidal heights of MSL. As can be deduced from the results presented in section 4.5.2, this partial cancellation is best achieved if shipboard gravity data are excluded. Unfortunately, however, we cannot exclude these data entirely; in some parts of Ω we do lack sufficient reliable radar altimeter data (e.g., Irish Sea, English Channel, and Skagerrak). Therefore, shipboard gravity data are included.

In the estimation, we adopt the earlier derived values for the depth and number of RBFs (Section 4.5.1). Based on these, the number of selected RBFs over Ω equals 86,569. The total number of biases, estimated to account for any mutual inconsistencies among the various data sets (Section 4.3), is 64. For performance reasons, an estimation of the variance components by MCVCE is not feasible for this large-scale problem. Therefore, we adopt the weights estimated over Ω_{I} (Table 4.9). The normal equations are solved with an out-of-core solver (Gunter 2004, Gunter & van de Geijn 2005). An out-of-core solver holds the matrix factors in files and may also hold the matrix data and some work arrays in files.

The estimated quasi-geoid NLGEO2013 is shown in Fig. 4.20. To assess its quality, we computed the differences between NLGEO2013 and (i) EGG08, (ii) EGM2008 (Pavlis et al. 2012), and (iii) the gravimetric quasi-geoid solution underlying NL-

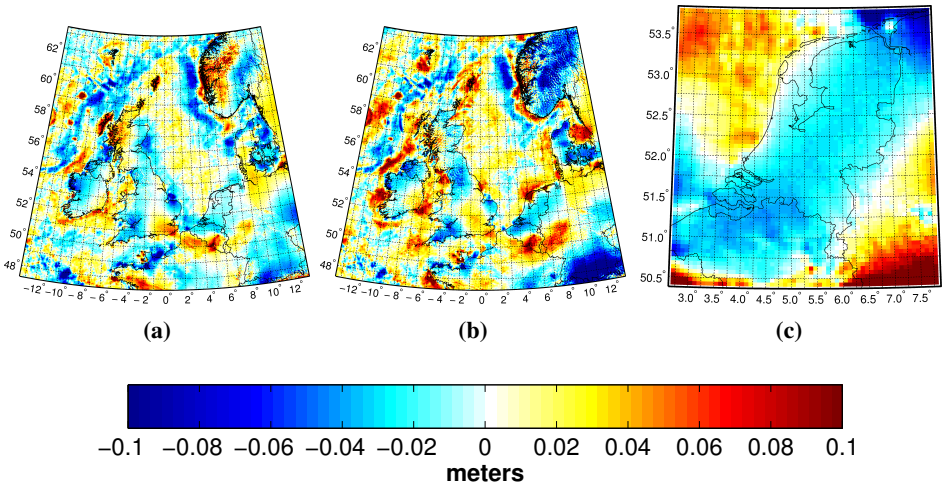

Figure 4.21: Differences between NLGEO2013 and (i) EGG08 (a), (ii) EGM2008 (b), and (iii) NLGEO2004-grav (c). Note that the mean differences are removed. In addition, in the maps (a) and (b), we excluded a strip of 1.5° around the boundaries of the computational domain as this is the region that is mostly affected by boundary effects.

GEO2004 (NLGEO2004-grav) (Crombaghs & de Bruijne 2004). Maps of these differences are shown in Fig. 4.21; the statistics are given in Table 4.10.

Based on these maps and the statistics, we observe that NLGEO2013 agrees best with EGG08. Indeed, this is not entirely a surprise as NLGEO2013 relies on EGG08 in the sense that EGG08-derived DoV are used as data in the continental regions where we lack gravity data and in the mountainous regions comprised by the computational domain (see Fig. 4.11 for a map of the EGG08-derived DoV used to estimate NLGEO2013). Here, one might wonder why in these regions the differences between NLGEO2013 and EGG08 are not equal to zero. The answer is twofold. First, the high-frequency signals in the EGG08-derived DoV are not modeled well by the chosen RBF parameterization. Hence, we cannot reproduce EGG08 exactly. Second, data at sea contribute to the estimated quasi-geoid on land.

We do not attempt to explain all the remaining differences shown in Fig. 4.21 as they may have many causes, for instance:

1. The use of different gravity data sets and the applied preprocessing. This includes the way how systematic errors in the shipboard gravity data are removed. For example, in this study we “removed” them by adjusting all shipboard gravity data to the altimeter-derived FAA model DTU10-GRA (Section 4.3.3.2). In the estimation of EGG08, a crossover adjustment was applied (Denker & Roland 2005).

Table 4.10: Statistics of the differences between NLGEO2013 and (i) EGG08, (ii) EGM2008, and (iii) NLGEO2004-grav). Note that, in computing the statistics, we excluded a strip of 1.5° around the boundaries of the computational domain as this is the region that is mostly affected by boundary effects. All values are provided in cm.

Model	Area	rms	min	max	mean	std
EGG08	oceans+land	2.73	-19.03	28.09	-0.01	2.73
	oceans	2.73	-19.03	28.09	-0.12	2.73
	land	2.74	-13.93	19.75	0.16	2.73
EGM2008*1	oceans+land	3.63	-32.02	32.69	0.16	3.63
	oceans	3.29	-22.19	32.69	1.02	3.13
	land	4.10	-32.02	19.61	-1.15	3.94
NLGEO2004-grav*2	oceans+land	4.22	-12.98	23.18	0.45	4.19

*1 We accounted for the differences between the quasi-geoid's potential values adopted for NLGEO2013 and EGM2008.
*2 We accounted for the differences between the quasi-geoid's potential values adopted for NLGEO2013 and NLGEO2004-grav. For the latter, the value is obtained from Ihde & Augath (2002).

2. The use of a different reference field in the RCR procedure. Note that only for NLGEO2013 the reference field includes both GRACE and GOCE data (Section 4.3.1).
3. Differences in the applied RCR technique. In this study, we applied the classical RCR technique (Section 4.2.1). That is, we did not account for uncertainties in the satellite-based geopotential model. In the estimation of EGG08, the combination of terrestrial gravity data and the EIGEN-GL04C geopotential model (Förste et al. 2008) was done by means of spectral weights, which depend on the accuracy of the input data sets (Denker et al. 2008).
4. Differences in the applied data weighting. In this study, MCVCE was used to estimate the variance factors of the different observation groups (Section 4.2.3). In the estimation of EGG08, a correlated noise model with an error standard deviation of 1 mGal was used for the terrestrial gravity data in the derivation of the spectral weights (Denker et al. 2008).
5. Differences in the used parameterization. This includes the extension of the functional model by extra bias parameters to account for systematic errors in the gravity data sets. In this study, we used a RBF parameterization and added 64 bias parameters. In the estimation of EGG08, the already mentioned spectral combination technique was used (Denker et al. 2008).
6. The use of different altimeter-derived data sets. This includes the form in which radar altimeter data are used when computing the quasi-geoid and the corrections applied for the DT.

Note that the differences along the Norwegian Trench observed in Figs. 4.21a and 4.21b cannot be solely attributed to the errors in the applied DT corrections $\zeta_{\mathrm{DT}}^{(3)}$ as-

Table 4.11: Residual differences of NLGEO2013, EGG08, EGM2008, and NLGEO2004-grav, respectively, at the 81 GPS/leveling points. All values are provided in cm.

Model	rms	min	max	mean	std
NLGEO2013	1.34	-0.61	5.43	0.92	0.98
EGG08	2.29	-0.80	5.53	2.03	1.08
EGM2008[*1]	4.15	-10.90	5.90	2.73	3.14
NLGEO2004-grav[*2]	7.34	-10.20	-3.04	-7.23	1.32

[*1] Here, we accounted for the difference between the quasi-geoid's potential value and the normal potential value.
[*2] Here, we corrected for the average difference of -68 cm mentioned by Crombaghs & de Bruijne (2004).

sociated with the errors in POL's salinity and temperature fields (Section 3.6.1.3). Indeed, the observed differences in Figs. 4.21a and 4.21b are much larger than the ones observed in Fig. 4.17. Furthermore, the differences observed along the shelf edge in the west and north-west parts of the computational domain are most likely explained by differences in the applied DT corrections. The reason is that, in this region, the coverage of shipboard gravity data is poor. We hardly have any shipboard gravity data beyond the shelf edge (Fig. 4.3), and also the map that shows the gravity data used in the estimation of EGG08 shows white spots in this region (Denker et al. 2008, (Fig. 1)). So, there the estimated quasi-geoid should rely on the available radar altimeter data.

We also validated the estimated quasi-geoid over the Netherlands using geometric height anomalies at 81 GPS/leveling points (Section 4.3.7). Maps of the differences between the geometric height anomalies on the one hand, and NLGEO2013, EGG08, EGM2008, and NLGEO2004-grav on the other hand are shown in Fig. 4.22. The statistics of these differences are provided in Table 4.11. From the statistics, we observe that NLGEO2013 has the best performance. Only for this model, the standard deviation is below 1 cm, which is within the uncertainty of the 81 geometric height anomalies ($0.010 - 0.015$ m according to Crombaghs & de Bruijne (2004)). The two outliers in the south of Limburg are probably caused by local errors in the leveling network (Broekman, personal communication, 2013). After removing these two points, the standard deviation between the geometric height anomalies and NLGEO2013 reduces to 0.79 cm. The reduction of the differences for NLGEO2013 observed at the points around the IJssel Lake and Wadden Sea, compared to those observed for EGM2008, NLGEO2004-grav, and to a lesser extent EGG08 is most likely due to incorporating additional bias parameters for the WADGRAV and Shell shipboard gravity data sets. For these data sets, the estimated biases equal -0.45 mGal and -1.18 mGal, respectively.

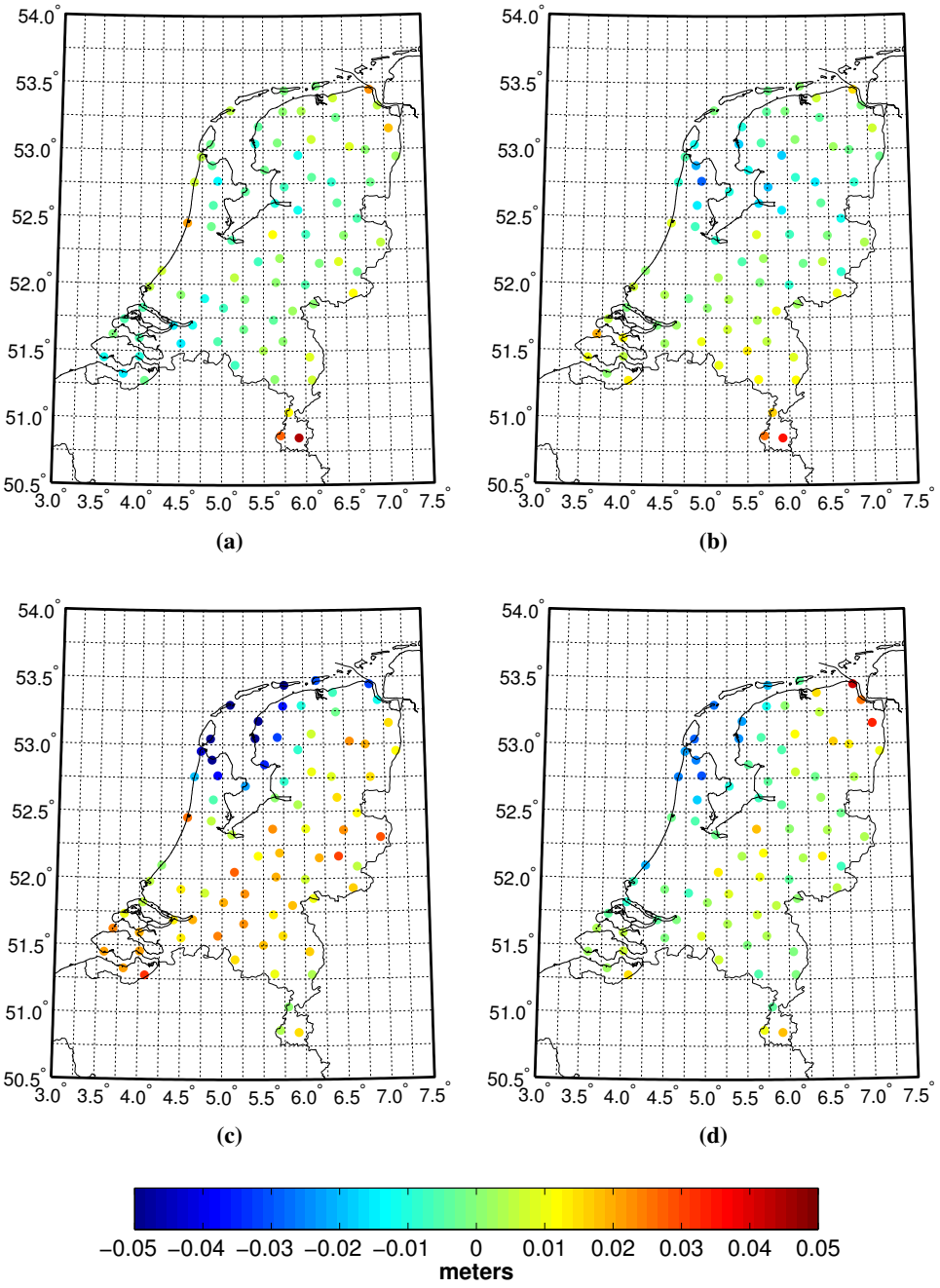

Figure 4.22: Residual differences of NLGEO2013 (a), EGG08 (b), EGM2008 (c), and NLGEO2004-grav (d), respectively, at the 81 GPS/leveling points. Note that the mean differences (Table 4.11) have been removed.

Chapter 5

LAT reference surface

This chapter is based on Slobbe et al. (2013b). The paper treats two closely related, but distinct, topics. The first topic is the derivation of lowest astronomical tide (LAT) in the North Sea from a vertically referenced shallow water model. The second topic is the assessment of the suggested sense of safety of the use of LAT as chart datum.

5.1 Introduction

The first topic (derivation of lowest astronomical tide (LAT) in the North Sea from a vertically referenced shallow water model) attracted the attention of hydrographic surveyors when they realized that the increasing accuracy of 3D positioning with Global Navigation Satellite Systems (GNSS), such as GPS, GALILEO, GLONASS, and/or COMPASS, offers a cost-effective, real-time alternative to the traditional procedures of water level reduction, i.e., the reduction of observed water depths to chart datum (CD). For an explanation of this so-called "water level reduction with GNSS procedure" we refer to Wöppelmann et al. (1999), FIG Commission 4 Working Group 4.2 (2006), and Dodd & Mills (2011). Note that CD is usually a tidal datum, i.e., a particular phase of the tide (Gill & Schultz 2001). As explained in Section 1.1, applying water level reduction with GNSS requires knowledge of the ellipsoidal heights of CD. The bathymetry expressed relative to CD is obtained by subtracting these heights from the ellipsoidal heights of the echo sounder instrument minus the observed water depths, i.e., the ellipsoidal heights of the bottom topography.

Ideally, the ellipsoidal heights of CD are derived from time series of observed water levels by tide gauge instruments, GNSS buoys, and/or radar altimeter satellites. Radar altimeter data are crucial if one aims to derive a coastal-waters-inclusive continuous (CWIC) surface. Indeed, only this data set provides a homogeneous spatial coverage, although at the expense of reduced temporal resolution (sub-hourly sampling at tide

gauges versus 10 days for the TOPEX/POSEIDON and Jason missions). This implies that, especially in shallow shelf waters, not all tidal constituents required to obtain a proper realization of CD, can be derived from radar altimeter data. Consequently, the only data source to derive CD in tidal shelf seas are tide gauges and GNSS buoys, except when the mean sea level (MSL) is defined to be CD.

However, where tides have an appreciable effect on the water level, not MSL but LAT was adopted as CD by the International Hydrographic Organization (IHO). LAT is defined as "the lowest tide level that can be predicted to occur under average meteorological conditions and under any combination of astronomical conditions" (International Hydrographic Organization 2011*a*, Technical Resolution 3/1919). Therefore, in shelf seas, LAT values derived from tide gauge records are combined with LAT values computed by a hydrodynamic model (e.g., Simon 2001, Turner et al. 2010). Here, the model-derived LAT value for each grid point is computed as the minimum modeled water level induced by astronomical tide only over a time span of at least the full nodal cycle (i.e., 18.6 years). As MSL represents the water level under average meteorological conditions, these model-derived LAT values are added to the ellipsoidal heights of MSL, providing ellipsoidal heights of LAT (Wöppelmann et al. 2006).

This last step implies that water levels computed with the hydrodynamic model are identified as water levels relative to MSL, i.e., that the hydrodynamic model's reference surface is MSL (Ballay et al. 2002, Iliffe et al. 2007*b*, Dodd & Mills 2011). However, as the dynamics of a hydrodynamic model usually assumes zero horizontal gravity components, the model's vertical reference surface is an equipotential surface of the Earth's gravity field (a so-called geop) (Hughes & Bingham 2008). Consequently, modeled water levels refer to a geop and so does model-derived LAT. The latter should be added to the ellipsoidal heights of the model's geop surface, unless the impact on the modeled tides of the MSL slope relative with respect to the geop is negligible. Prandle (1978) has shown that the contribution of the M_2 tide to MSL in the southern North Sea varies from -1 to 8 cm, with maximum values along the Dutch coast. Indeed, if we aim to achieve an accuracy of a few centimeters, this contribution cannot be neglected.

Using MSL to derive ellipsoidal heights of LAT is only possible where MSL is known. However, the standard waveform tracking systems onboard the radar altimeter satellites do not provide reliable information about MSL within a distance of 20–25 km off the coastline. Even when using the most advanced retracking schemes, the gap in data coverage may still be a few kilometers (e.g., Deng et al. 2002, Sandwell & Smith 2005, Deng & Featherstone 2006). Bridging this gap is a topic of ongoing research; see Gommenginger et al. (2011) for a recent review. The only other data source from which MSL can be derived are tide gauge data equipped with GNSS and GNSS buoys. For instance, Iliffe et al. (2007*a*) used the data from

385 tide gauges together with radar altimeter data to construct a new model of the mean dynamic topography (MDT) around the British Isles. Nevertheless, tide gauge data (and GNSS buoys) provide pointwise information about MSL. Hence, advanced inter-/extrapolation schemes are required to obtain a continuous MSL surface (see, e.g., Turner et al. (2010) who proposed such a scheme). To reduce the need for interpolation, Pineau-Guillou & Dorst (2011) realized the MSL in the coastal zone by measuring the instantaneous water levels along the tracks of a ship equipped with differential GPS, and correct these heights for tide and surge to obtain the MSL. One major drawback of this method, however, are the costs to carry out such surveys.

Finally, we might question whether the concept of MSL defined over a long period serves practical needs. Indeed, the MSL is subjected to temporal variations on many time scales. Thompson (1980) showed, by means of a multiple regression analysis of 29 tide gauges around the British Isles, that over 80% of the monthly mean sea level variance can be related to seasonal changes, the static pressure effect and the influence of winds over the continental shelf. Seasonal variations cause a lower MSL in spring than in fall; in the North Sea, the difference can be up to a few decimeters. Hence, it makes sense to include these variations into the definition of what is referred to as "average meteorological conditions".

In this study, we propose to derive LAT from a hydrodynamic model directly relative to a geop, which solves the weaknesses of the conventional approach. When following such an approach, we need to explicitly model "average meteorological" (and steric) conditions in combination with the astronomical tide. We suggest using a quasi-geoid as the reference surface. A quasi-geoid is a particular geop, which in some sense is close to MSL. We reference the water levels of the hydrodynamic model to this quasi-geoid following the procedure presented in Chapter 3, where the extended Dutch Continental Shelf Model has been referenced to the European Gravimetric Geoid 2008 (EGG08) in the mean-tide system (Denker et al. 2008). Another advantage of this approach is that the explicit modeling of the average meteorological conditions allows the inclusion of seasonal variations into the definition of the average meteorological conditions.

As for the second topic, nautical charts are not only supposed to be up-to-date and accurate (International Hydrographic Organization 2011*b*, FIG Commission 4 Working Group 4.4 2011), they are also supposed to present depths with respect to a reference that is sufficiently low to support safe navigation. This particularly applies to the southern North Sea as the approach routes to the Ports of Rotterdam and Antwerp run through them. Its sea bed is characterized by sandy sediments with dynamic rhythmic patterns at different scales (Dorst 2009), the water column shows large tidal motions, and there are several severe storms a year. In this environment, ship owners are looking for profit optimization by approximating the safety limits for ship draught, even when carrying harmful substances such as crude oil. It is, for instance, common for

the larger ships to use the incoming tidal wave through the English Channel to create sufficient under keel clearance; when those ships miss the tidal wave they will ground.

The annual review of maritime accidents (European Maritime Safety Agency 2010, Section 5.1) documents that this happens frequently. More than 80% of the accidents in 2010 (411 in total) in the region including the Atlantic Coast, North Sea, and English Channel occurred in the waters around Germany, the Netherlands, Norway, and the UK. From the 411 accidents, there were 88 groundings, which make grounding the second most abundant source of accidents after collision/contact. Though there are many causes for ship grounding, Amrozowicz et al. (1997) concluded that most of the grounding events with oil tankers that were able to follow a safe track (powered groundings) were introduced by fundamental failures in the process of passage planning and piloting. Since nautical charts are the starting point for the planning, the conclusion of Amrozowicz et al. (1997) underlines the importance of accurate and unambiguously interpretable nautical charts. Here, the fact that LAT is used as CD helps the pilots; not only all predicted tidal water levels become positive in sign, but it also provides them with the minimal water depth that can be expected under average meteorological conditions. Since it is recommended by the IHO to compute LAT over a minimum period of 19 years (International Hydrographic Organization 2011*a*, Technical Resolution 3/1919), it provides a sense of safety. Of course, navigators always use an additional safety margin, because they know that in shallow waters surges might generate water levels significantly below LAT. However, a quantification of the amount is not available. Therefore, it would be desirable that the probability of the instantaneous water level to drop below LAT is small. Otherwise, mariners might take more risk than they realize.

Besides the issue of obtaining an accurate representation of the ellipsoidal heights of the LAT surface using hydrodynamic models, obtaining insight into the probability of a lower water level than LAT is the other major topic of this chapter. The model-derived LAT surface is validated by LAT values computed at onshore and offshore tide gauges.

The highest accuracy of the LAT surface is obtained when LAT values at the tide gauges are integrated in the model-derived LAT surface (cf. Turner et al. 2010). As noted in Section 1.4, this can be achieved in several ways. In this study, we rely on the model calibration that has been carried out using both tide gauge and radar altimeter data (Section 3.2). Furthermore, to reduce the numerical complexity, in our experiments we exclude a detailed modeling of the LAT surface in the estuaries and the Wadden Sea.

First, we introduce the tide gauge data set that will be used to validate the obtained LAT surface. Next, we present the results of our numerical experiments. In the first experiment, we quantify the contribution of the astronomical tide to the time-

averaged water levels, which shows up as an error in the ellipsoidal heights of the LAT surface computed following the conventional approach if not accounted for. Thereafter, we present and discuss the results of two experiments designed to investigate the model skill to represent LAT relative to the quasi-geoid both by including the time-averaged meteorological and steric conditions and by including the average month-to-month variations. Next, we present maps that show the probabilities that the instantaneous water level is below LAT and propose a probabilistic method to realize CD. Finally, we conclude by providing a brief summary of the work that has been done, emphasizing the main findings, and adding some concluding remarks.

5.2 Tide gauge data

Tide gauge data are used to validate the model-derived LAT values. From our internal database, we obtained all available data from 92 onshore and 10 offshore gauges covering the time span over which we derive LAT (1984–2004). Note that, except for the French gauges, our database does not contain data prior to 1985. We refer to Table B.1 for an overview of the selected gauges and the main characteristics of the data.

The height transformations required to obtain all observed water levels relative to EGG08 in the mean-tide system were carried out by four different methods, referred to as M_I, M_{II}, M_{III}, and M_{IV}, respectively:

1. Method M_I uses GNSS observations to obtain observed water levels relative to the reference ellipsoid. Then the EGG08 quasi-geoid height is subtracted, which provides water levels relative to the EGG08 quasi-geoid. This method is limited to tide gauges observed with GPS.
2. In method M_{II}, we add the difference between the national (quasi-)geoid height and the EGG08 quasi-geoid height to the observed water levels. Differences between the geoid and the quasi-geoid are assumed to be negligible (Section 1.4).
3. In method M_{III}, observed water levels relative to EGG08 are obtained after a transformation from the national height system to the European Vertical Reference Frame 2007 (EVRF2007) using the EVRF2007 transformation parameters.
4. Method M_{IV} is used for the Dutch offshore tide gauges for which the vertical datum of the data is a local realization of MSL, i.e., the mean water level over a certain measurement period. Here, we first add the ellipsoidal MSL height at the mid-epoch of the time span over which LAT will be derived. Subtracting

the EGG08 quasi-geoid height provides water levels relative to the EGG08 quasi-geoid.

The EVRF2007 transformation parameters are provided by the Bundesamt für Kartographie und Geodäsie. The EVRF2007 heights can be interpreted as heights relative to the EGG08 zero-tide quasi-geoid. Hence, we need to add the difference between the mean and zero-tide quasi-geoid as computed using Eq. (3.11). The MSL heights and the corrections to bring these heights to our reference epoch as used in method M_{IV} are derived from the DNSC08 mean sea surface model (Andersen & Knudsen 2009). If no GNSS data are available and the data refer to the national (quasi-)geoid, we compare for each country the observation- and model-derived MDT values obtained by method M_{II} and M_{III}. For each particular country, we select the method with the smallest root mean square (rms) fit to the model-derived MDT heights. The performance of each method depends on the accuracy of the transformation parameters, the national (quasi-)geoid, and the EGG08 quasi-geoid, and the way systematic errors in the leveling network are accounted for. For instance, the leveling heights in the UK are suspected to contain systematic errors (e.g., Iliffe et al. 2003, Hipkin et al. 2004). To derive orthometric heights (heights relative to the geoid) from GPS measurements, consistent to what would have been achieved through leveling, a correction surface is added to the gravimetric geoid that mainly represents these errors (Iliffe et al. 2003). Hence, in method M_{II} this error cancels out while it remains in method M_{III}.

The procedure to derive LAT at a tide gauge consists of two steps. First, the tidal constituents and a linear trend are estimated from the observed water levels by a harmonic analysis using the functional model

$$\zeta_{\mathrm{O}}(\Delta t) = \overline{\zeta_{\mathrm{O}}} + a\Delta t + \sum_{i=1}^{n} f_i H_i \cos(\omega_i \Delta t + (V_0 + u)_i - G_i) + r(\Delta t), \qquad (5.1)$$

where $\zeta_{\mathrm{O}}(\Delta t)$ is the observed water level relative to EGG08 at time $t - t_0$, t_0 is the reference time (mid-epoch of the period over which $\overline{\zeta_{\mathrm{O}}}$ and $\overline{\zeta_{\mathrm{P}}}$ are computed used to derive $\delta W_{\mathrm{G,P}}$ (Section 3.5.3); January 1, 1999), $\overline{\zeta_{\mathrm{O}}}$ the MDT relative to EGG08, a the linear trend in the observed water levels, n the number of constituents estimated from the data, and $r(\Delta t)$ is the non-tidal residual. Second, the tide signal is reconstructed over the entire computation period (1984–2004) with a sampling rate of 10 minutes (similar to the time step used in the model). From these time series, LAT ($\zeta_{\mathrm{O}}^{\mathrm{L}}$) is derived as the minimum tidal water level that occurs.

Obviously, the derived LAT value depends on the set of constituents included in the harmonic analysis. In principle, this set should be derived for each tide gauge since bathymetry and coastal morphology vary from tide gauge to tide gauge. While such an analysis is not feasible in the course of this project, we apply the analysis for each

tide gauge using both a set of 95 constituents commonly used in the Netherlands and a set of 103 constituents commonly used in the UK. The differences between the two LAT values serve as an indication of the significance of choosing the right set of constituents. In the validation, we use the LAT value derived from the time series generated by the set of constituents that best explains the observed water levels, i.e., for which the rms of the non-tidal residuals (r) is lowest. Both sets of constituents include the *SA* constituent (representing the seasonal variation in water level), which is also included in the reconstruction of the astronomical tide. The latter is consistent with the experimental setup of Experiment III used to derive the LAT surface which we use in the validation (Section 5.3.5). In Experiment III, the monthly signal in the average meteorological and steric contributions is included. Since the seasonal signal dominates, this is approximately what is represented by the *SA* constituent.

Although for almost all gauges we have time series covering more than 18.6 years, we still use the so-called nodal corrections rather than including the nodal modulation terms into the estimation process. According to Foreman et al. (2009), the latter would be more accurate for such long time series, since the nodal corrections to amplitude and phase are time variable rather than constant as is assumed when applying nodal corrections. However, since these nodal corrections are also used to derive the contribution of the astronomical tide to the water levels prescribed at the open sea boundaries (Section 3.4.1), we prefer to remain consistent with the model. The latter ensures a fair comparison between model- and observation-derived LAT values. For the same reason, we ignore the fact that the assumption of stationarity is often invalid in shallow water, i.e., we assume the amplitudes and phases of the tidal constituents are constant over time. Non-stationarity is introduced by, e.g., non-linear interactions between the tide and storm surges or variable river discharge (Foreman et al. 2009), but also by changing ocean bottom topography. Indeed, these processes are not included in the model. On the other hand, Foreman et al. (2009) consider the first two, in general, not to be a serious problem as the effects are often small or of short duration.

5.3 Deriving LAT

In this section, we present and discuss the model-derived LAT surfaces that are derived using various strategies. Although we ultimately aim to derive the ellipsoidal heights of the LAT surface, we present the results with respect to the MSL and quasi-geoid respectively, to enhance visibility. Validation is carried out using LAT values derived from tide gauge records. In all our experiments, summarized in Table 5.1, we model the water levels with a time step of 10 minutes over the period January 1, 1984 to January 1, 2004. The LAT value per grid point is derived as the minimum water level over the entire time series. To distinguish the results of the various experiments,

Table 5.1: Summary of the experiments. Column OBC (open boundary conditions) provides information of how the water levels along the open sea boundaries of the extended DCSM have been computed in the model run. Here, ζ_a is the astronomical tide, ζ_u is the surge, ζ_s is the steric height, and $\delta W_{G,P}$ is the datum shift between the EGG08 quasi-geoid and the model's equipotential reference surface. The overbar is used to denote time averaged values.

Exp.	Objective	OBC	Source ζ_S	Wind and pressure forcing
I	Reference case remaining exp.	$\zeta_a(\vartheta,\lambda,t)$	n/a	n/a
II	Incl. time-avg. wind, pressure, and baroclinic forcings	$\zeta_a(\vartheta,\lambda,t)+\overline{\zeta_u}(\vartheta,\lambda)+\overline{\zeta_s}(\vartheta,\lambda)+\delta W_{G,P}$	POL	ERA-Interim
III	Incl. avg. monthly variations in wind, pressure, and baroclinic forcings	$\zeta_a(\vartheta,\lambda,t)+\zeta_u(\vartheta,\lambda,t)+\zeta_s(\vartheta,\lambda,t)+\delta W_{G,P}$	POL	ERA-Interim
IV	Modeling of instantaneous water levels	$\zeta_a(\vartheta,\lambda,t)+\zeta_u(\vartheta,\lambda,t)+\zeta_s(\vartheta,\lambda,t)+\delta W_{G,P}$	POL	ERA-Interim

they are labeled with Roman numerals. For example, the model-derived LAT for Experiment I is $\zeta^{L}_{D_I}$, where the capital letter D refers to the source from which the water level is derived: the extended DCSM model. The mean water levels derived in Experiment IV will be used to validate the mean water levels derived in Experiment II and Experiment III. The instantaneous water levels will be used in Section 5.4 to compute the probability that the instantaneous water level is below LAT. In Experiment IV, we used POL's time-varying salinity and temperature fields (Section 3.5.3). The steric contribution to the water levels prescribed at the open boundaries is derived from POL's hindcast as well.

5.3.1 Experiment I: LAT relative to MSL

Experiment I serves as a reference case for the remaining experiments. The ellipsoidal heights of the LAT surface are derived using the traditional approach: the model-derived minimum water levels induced by only astronomical tides are added to the ellipsoidal heights of MSL. Note that here we used the original DCSM model, i.e., the model's reference surface is implicitly identified with MSL, though it may be different in reality. We also quantify the contribution of the astronomical tide to the MSL. Unless the model-derived LAT surface is corrected for this contribution, this contribution shows up as an error in the derived ellipsoidal heights of the LAT surface.

The model-derived LAT surface is shown in Fig. 5.1a. Many of the features shown in this map are consistent with oceanographic expectations such as coincidence of the locations where the model-derived LAT values approach zero with the well-known amphidromic system in the northwest European continental shelf. In the North Sea, there are two complete amphidromic systems; one near the center of the southern North Sea at a latitude of 52.5° and one further to the east near 56° latitude. There is also a degenerate system, which has its center in southern Norway (Pugh 1996). All of them can be identified in Fig. 5.1a. We also observe that in the North Sea the

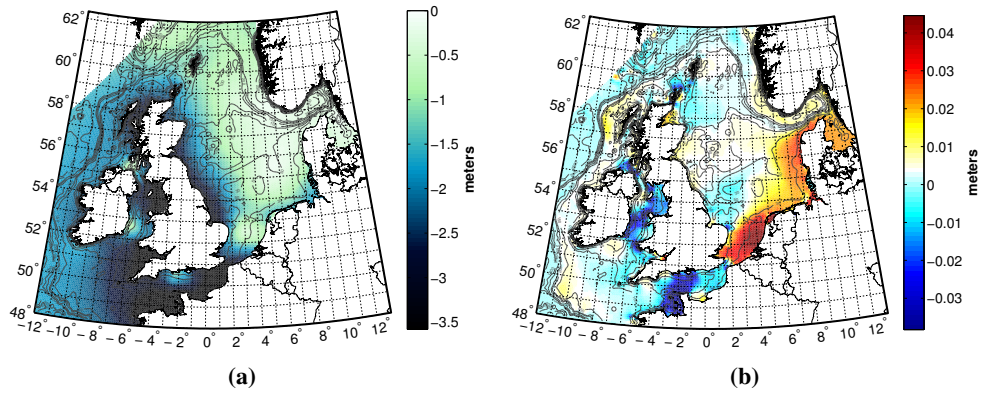

(a) **(b)**

Figure 5.1: Lowest astronomical tide (a) and time-averaged water levels (b) computed over the entire computation period January 1, 1984 – January 1, 2004. The grey lines in both maps show the contour lines of the bathymetry.

magnitude of the LAT values is largest along the British coast, i.e., there where the tidal wave travels southwards. Indeed, along the British coast the shelf is steeper than along the eastern side of the North Sea giving rise to less energy loss due to bottom friction. The large values in the Strait of Dover are due to the confluence of the incoming wave from the Celtic Sea and the wave which has traveled around Scotland and through the North Sea, giving rise to an anti-amphidrome (Pugh 1996). In the English Channel, we observe large magnitudes along the French coast (< -3.5 m) and a degenerate amphidrome off the English coast. Both features agree with the expectations. Following Pugh (1996), the large amplitudes along the French coast are due to Kelvin-wave dynamics and local standing wave resonance. Resonance effects also cause large tidal amplitudes and hence LAT values in the Bristol Channel. Finally, we observe the degenerate amphidrome along the eastern side of the Irish coast (southwest of the Isle of Man) and one between Ireland and the Scottish island of Islay.

One condition that must be satisfied before a straightforward addition of $\zeta^{\mathrm{L}}_{\mathrm{D_I}}$ to the ellipsoidal heights of the MSL surface is allowed, is that for all grid points the mean water level over the entire model run ($\overline{\zeta_{\mathrm{D_I}}}$) is zero. Or, at least, this contribution should be subtracted from $\zeta^{\mathrm{L}}_{\mathrm{D_I}}$. Any time-averaged contribution of the astronomical tide, generated by the non-linear interactions associated with tidal propagation, is part of the observation-derived MSL and shows up as a systematic error in the ellipsoidal heights of the LAT surface.

The time-averaged water levels obtained in Experiment I are shown in Fig. 5.1b. In large parts of the model domain, these mean water levels do not significantly differ from zero (< 1 cm) especially away from the continental shelf. There are, however, a few exceptions. In the Irish Sea and the English Channel, some spots are visible

where the mean water levels range from -2 to -10 cm. Along the south and eastern side of the North Sea, the values are positive. Largest values are observed along the Dutch coast (4.5 cm). Our values are less than those reported by Prandle (1978), which range from -1 to 8 cm when moving from the English to the Dutch coast. Besides differences between the models used (e.g., bathymetry, resolution, and open boundary conditions) and the time span over which the mean water levels are computed (eight complete tidal cycles in Prandle (1978) versus 20 years in this study), there are two other fundamental differences between both studies. While Prandle (1978) only considers the MSL generated by the M_2 constituent, the mean water levels in Fig. 5.1b represent the contribution of the full tidal signal to the MSL. Furthermore, the open boundaries of DCSM are located away from the continental shelf where it is reasonable to assume that the amplitudes of the zero-frequency constituent are zero. For the model used by Prandle (1978), this was not the case. Hence, the variations in MSL due to the M_2 tide are directly dependent on the values prescribed at the open sea boundaries.

5.3.2 Experiment II: LAT relative to the EGG08 quasi-geoid (including the time-averaged meteorological conditions)

In Experiment II, the LAT surface is computed relative to EGG08. Here, we need to include the average meteorological and steric contributions in the modeling of the tidal water levels. In addition, the extended DCSM needs to be vertically referenced, which is realized by prescribing water levels relative to EGG08 at the open sea boundaries. In this experiment, the inclusion of average meteorological and steric conditions means that we include the time-averaged (over 1984–2004) fields of wind stress, mean sea level pressure, and depth-averaged horizontal pressure gradients induced by horizontal variations in water density. Before averaging, the wind speeds are transformed to wind stresses (using Eq. (3.4)). The reason for doing this before the averaging is that the wind drag coefficient (C_d) in Eq. (3.4) depends on the wind speed itself. Hence, the time-averaged wind stress field is not equal to the field obtained by transforming the time-averaged wind speeds to wind stresses. For a similar reason, the time-averaged steric contribution is computed by averaging over the water density fields rather than over the salinity and temperature fields. The time-averaged meteorological and steric contributions to the tidal water levels prescribed at the open sea boundaries, are derived from POL's monthly mean water levels (Section 3.5.3).

We only obtain a proper representation of LAT relative to EGG08 if the inclusion of the time-averaged processes provides a proper representation of the MDT. While in Section 3.6.1 we carried out an extensive validation of the model-derived MDT obtained by using time-variable meteorological and steric contributions (similar experimental setup as in Experiment IV of this chapter), in this part of the study we only need to quantify any degraded performance in the representation of the MDT

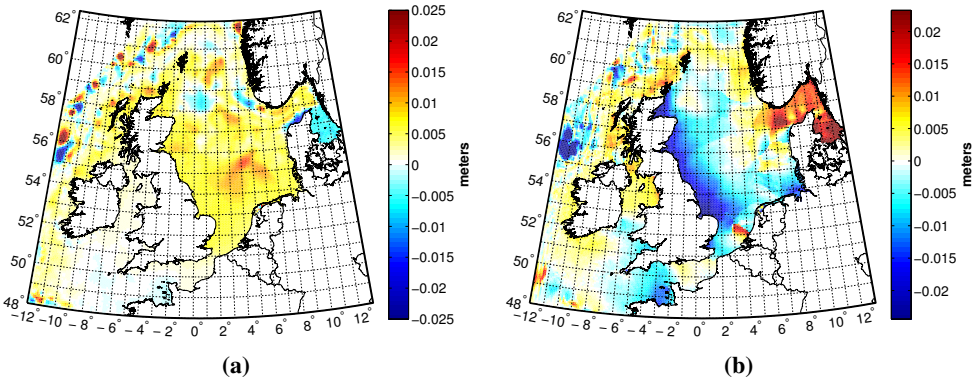

Figure 5.2: Difference in model-derived MDT computed over the entire computation period January 1, 1984 to January 1, 2004 as derived from Experiment II and Experiment IV (a) and the difference between model-derived LAT as derived from Experiment I and Experiment II (b).

Table 5.2: Experiment II: statistics of the differences between the MDT derived in Experiment II and Experiment IV, as well as of the differences between the model-derived LAT of Experiment I and Experiment II, both computed over the whole model domain (Ω_D) and North Sea (Ω_{NS}). Boundaries of the North Sea are taken from International Hydrographic Organization (1953). All values are provided in cm.

differences	dom.	rms	min	max	mean	std
$\overline{\zeta_{D_{IV}}} - \overline{\zeta_{D_{II}}}$	Ω_D	0.57	-3.31	3.78	0.34	0.46
	Ω_{NS}	0.65	-1.33	3.19	0.55	0.34
$(\zeta^L_{D_{II}} - \overline{\zeta_{D_{II}}}) - (\zeta^L_{D_I} - \overline{\zeta_{D_I}})$	Ω_D	0.80	-7.72	3.91	-0.06	0.79
	Ω_{NS}	0.83	-4.43	2.62	-0.33	0.76

compared to the MDT obtained in Experiment IV. Differences are, among others, introduced by a non-linear interaction of the tide with meteorological and steric effects that does not average out. Fig. 5.2a shows a spatial rendition of these differences, while Table 5.2 provides a summary of their statistics.

The mean difference over the whole DCSM domain (Ω_D) equals 0.34 cm while the rms is 0.57 cm. Both values slightly increase when they are computed over the North Sea (Ω_{NS}); to 0.55 cm and 0.65 cm, respectively. The increase of the rms is explained by the increase in the mean as follows from the standard deviations that decrease when we go from Ω_D to Ω_{NS}. From Fig. 5.2a, we observe an irregular pattern of positive and negative differences along the open sea boundaries, which points to boundary effects. On the shelf, the differences are more homogeneous; in the Celtic Sea, Irish Sea, and the English Channel they are nearly zero, while in the North Sea they increase from 0.5 to 1.0 cm with an abrupt decrease in the Skagerrak (-0.5 to -1.0 cm). In general, the differences are small; much smaller than the time-averaged

differences between observed and modeled water levels reported in Section 3.6.1.3. In this section, the same experimental setup was used as in Experiment IV (Section 5.4) to compute the instantaneous water levels over the period January 1, 2000 to January 1, 2003. The time-averaged differences showed spatially correlated patterns up to 6 cm along the open boundaries, 5 cm in the Celtic Sea, and 6 cm in the northern North Sea. They were attributed to boundary effects, quasi-geoid errors, and errors in both the used salinity and temperature fields and the steric water levels prescribed at the open sea boundaries. We conclude that, though the errors shown in Fig. 5.2a are systematic, they are small compared to other errors in the MDT.

The traditional method to compute the ellipsoidal heights of the LAT surface by adding the separation between LAT and MSL to the ellipsoidal heights of MSL assumes that tide and the average meteorological and steric conditions are linearly additive. That is, that there is no non-linear interaction. For tide and surge this is, especially in shallow water, not the case (e.g., Prandle & Wolf 1978, Wolf 1981, Horsburgh & Wilson 2007). In Experiment II, the meteorological conditions are explicitly added to the model, and any interaction becomes part of the model-derived LAT. Indeed, if no interaction occurs, Experiment I and Experiment II should provide identical results. What of the two methods considered in Experiment I and Experiment II is to be preferred depends on the quality of the available MSL/quasi-geoid surfaces and the ability of the model to represent the MDT. The interaction of tide with the average meteorological and steric conditions is quantified by comparing the difference between model-derived LAT and MDT in Experiment I with the corresponding difference obtained in Experiment II, i.e., $\zeta^{\mathrm{L}}_{\mathrm{D_I}} - \overline{\zeta_{\mathrm{D_I}}}$ with $\zeta^{\mathrm{L}}_{\mathrm{D_{II}}} - \overline{\zeta_{\mathrm{D_{II}}}}$. Fig. 5.2b shows a spatial rendition of these differences, while Table 5.2 provides a summary of their statistics. From the latter, we conclude that the maximum absolute differences away from the open boundaries (Ω_{NS}) are < 5 cm. The rms is only 0.83 cm. Fig. 5.2b shows a systematic pattern along the English coast where the differences reach -2.5 cm north of the city Norwich. In the Skagerrak and Kattegat, the sign of the differences changes, but away from the coastal zone they do not exceed 3 cm. Indeed, the order of magnitude of the tide-surge interaction is below the accuracy with which MSL can be derived. For instance, Andersen & Knudsen (2009) report a standard deviation of 4–10 cm for the DNSC08 mean sea surface.

5.3.3 Experiment III: LAT relative to the EGG08 quasi-geoid (including average monthly variations in MSL)

So far, the MSL was defined as the mean water level over a several-year period. In Experiment I, this period is the entire time span of the radar altimeter data that are used, e.g., 17 years for DTU10 (Andersen 2010). In Experiment II, it is the period over which we averaged the wind stress fields, mean sea level pressure fields, and depth-averaged horizontal pressure gradients induced by horizontal variations in wa-

Table 5.3: Experiment III: statistics of the differences between the MDT's derived in Experiment III and Experiment IV, as well as of the differences between the model-derived LAT surfaces of Experiment I and Experiment III, both computed over the whole model domain (Ω_D) and North Sea (Ω_{NS}). All values are provided in cm.

differences	dom.	rms	min	max	mean	std
$\overline{\zeta_{D_{IV}}} - \overline{\zeta_{D_{III}}}$	Ω_D	0.50	-3.45	2.83	0.30	0.41
	Ω_{NS}	0.61	-1.23	2.83	0.53	0.31
$(\zeta^L_{D_{III}} - \overline{\zeta_{D_{III}}}) - (\zeta^L_{D_I} - \overline{\zeta_{D_I}})$	Ω_D	5.49	-15.81	5.86	-4.97	2.33
	Ω_{NS}	6.43	-15.81	-0.52	-6.04	2.20

ter density fields (1984–2004). However, it is well known that the MSL is subject to temporal variations on all time scales (Pugh 1996). On time scales > 1 month, the seasonal signal is most pronounced; from an analysis of 29 tide gauges sited around the British Isles, Thompson (1980) derived an average amplitude of 7 cm. Together with the static pressure effect and the influence of winds over the continental shelf, the seasonal variations account for 80% of the monthly mean sea level variance. Therefore, in Experiment III LAT relative to EGG08 will be recomputed, but now the hydrodynamic model is forced by astronomical tides and the *average monthly* wind stress, mean sea level pressure, and depth-averaged horizontal pressure gradients induced by horizontal variations in water density.

These average monthly forcing fields are computed by averaging for each calendar month all available forcing fields over a period of 20 years (1984–2004). The obtained yearly time series have been used for the twenty-year model run. To avoid jumps in the modeled water levels in the transition from month to month, the obtained time series are interpolated to three-hourly values (the original temporal resolution of the wind speed and mean sea level pressure data) using a cubic spline. Here, we assigned the monthly means to the mid-epochs of each month. The meteorological and baroclinic contributions to the tidal water levels prescribed at the open sea boundaries are obtained in the same way as the average monthly forcing fields. Again, we use POL's monthly mean water levels. Since both the extended DCSM and the POL3DB model make use of the Boussinesq hypothesis, the average monthly net steric expansion/contraction signal of the global oceans is lacking. Here, we applied a post-processing correction (Section 3.4.3) to the modeled water levels that is derived in a similar way as discussed above.

The statistics of the differences between $\overline{\zeta_{D_{IV}}}$ and $\overline{\zeta_{D_{III}}}$ (Table 5.3), and those of the differences between $\overline{\zeta_{D_{IV}}}$ and $\overline{\zeta_{D_{II}}}$ (Table 5.2) do not differ much. Therefore, we conclude that the mean water level in both experiments is equally well represented; allowing time variations in the wind stress, mean sea level pressure, and depth-averaged horizontal pressure gradients induced by horizontal variations in water density forcings does not impact the mean. As could be expected, the differences between

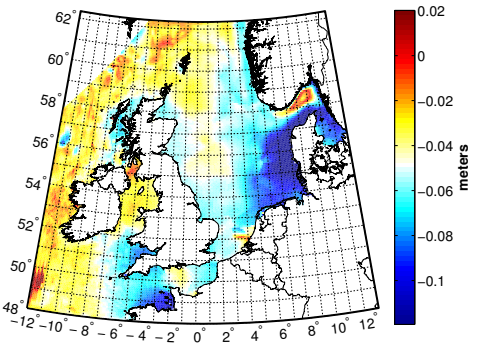

Figure 5.3: Difference between model-derived LAT as derived from Experiment I and Experiment III.

the LAT surfaces of Experiment III and Experiment I, both corrected for the MDT ($(\zeta^{\mathrm{L}}_{\mathrm{D_{III}}} - \overline{\zeta_{\mathrm{D_{III}}}}) - (\zeta^{\mathrm{L}}_{\mathrm{D_I}} - \overline{\zeta_{\mathrm{D_I}}})$), are much larger. Fig. 5.3 shows a map of these differences while the statistics are provided in Table 5.3. Indeed, besides the tide-surge interaction, these differences include the deviation of the MSL at the LAT event (we use time-varying atmospheric wind, pressure, and baroclinic forcing fields) from the MSL defined as the average water level over the entire modeling period. Compared to Fig. 5.2b and the statistics in Table 5.2, the latter contribution dominates. Over the whole model domain (Ω_{D}), the rms and mean of the differences between $(\zeta^{\mathrm{L}}_{\mathrm{D_{III}}} - \overline{\zeta_{\mathrm{D_{III}}}})$ and $(\zeta^{\mathrm{L}}_{\mathrm{D_I}} - \overline{\zeta_{\mathrm{D_I}}})$ compared to the corresponding differences shown in Table 5.2 increased from respectively 0.80 cm to 5.49 cm and -0.06 cm to 4.97 cm. Over the North Sea (Ω_{NS}), the rms and mean increase from respectively 0.83 cm to 6.43 and -0.33 cm to -6.04 cm. The largest differences are observed west to Denmark; almost -15 cm.

5.3.4 LAT and sea level rise

Besides periodic variations, sea level is subjected to secular changes induced by, e.g., eustatic and steric sea level changes, self-gravitation, and glacial isostatic adjustment (GIA). Since the estimated ellipsoidal heights of the LAT surface will be used for several years before it is revised (a decade in the Netherlands) while it refers to a MSL in the past, a correction for these changes is required that is quantified in this section. Here, the time difference between the reference epoch of the model-derived MDT (January 1, 1999) and the mid-epoch of the period the obtained LAT will be used (2012–2022), is 18 years. The secular changes in MSL, estimated from multi-mission radar altimeter data over the period October 1992 – December 2010, are obtained from the publicly available AVISO mean sea level products (CNES/LEGOS/CLS 2011). These trends are not corrected for GIA. The radar altimeter data used to compute the trends are corrected for the inverse barometer effect. Fig. 5.4 shows the changes in MSL over the 18 years that should be added to the model-derived LAT surfaces derived in Experiments I, II, and III. From Fig. 5.4, we conclude that in most

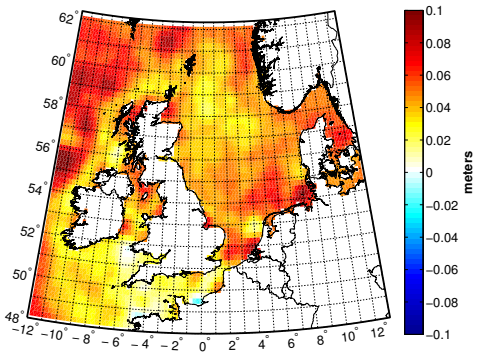

Figure 5.4: Spatial rendition of changes in MSL over 18 years. The changes estimated from multi-mission radar altimeter data over the period October 1992 – December 2010 (CNES/LEGOS/CLS 2011).

regions the corrections are < 5 cm. Away from the continental shelf (mostly outside the model domain of DCSM), along the western and northern Dutch coast, in the German Bight, and in the Kattegat, however, the corrections attain values up to 8 cm.

5.3.5 Validation of the model-derived LAT surface

The model-derived LAT surface of Experiment III ($\zeta^{\mathrm{L}}_{\mathrm{D_{III}}}$) is validated using LAT values derived from 102 tide gauge records (Section 5.2). A summary of the result is given in Table 5.4 while Table C.1 provides the results for each tide gauge.

We start the presentation and interpretation of the results with a comparison of the observation- and model-derived MDT values. These differences reveal problems in either the model skill to represent the MDT, as well as in the vertical referencing of the tide gauges. Indeed, the latter errors show up in the differences between the observation- and model-derived LAT values and hence they hamper the interpretation. From Table 5.4, we conclude that the average error in the representation of the MDT is 3.45 cm while the minimum and maximum errors are -9.49 cm and 19.56 cm, respectively. The errors comprise representation errors in the model-derived MDT values introduced by, e.g., errors in the used salinity and temperature fields (Section 3.6.1.3), but also errors introduced by the applied height transformation. For instance, if method M_{II} is used (Section 5.2), any (quasi-)geoid error in either the national (quasi-)geoid or EGG08 propagates into the observation-derived MDT value. In addition, we should bear in mind that the observation-derived MDT values are point measurements while the model-derived ones represent spatial averages. That is, the model-derived values lack the high-frequency components of the actual MDT signal.

Table 5.4: Experiment III: Summary of differences between observation- and model-derived MDT and LAT values per country (Cnt.), where column Loc. (Location) provides information on the location of the tide gauges (onshore/offshore); column $\varepsilon_{\mathrm{MDT}}$ provides the average, min, and max differences between the observation-derived ($\overline{\zeta_{\mathrm{O}}}$) and model-derived ($\overline{\zeta_{\mathrm{D_{III}}}}$) MDT values; column $\varepsilon_{\mathrm{LAT}}$ provides the average, min, and max differences between the observation-derived ($\zeta^{\mathrm{L}}_{\mathrm{O}}$) and model-derived ($\zeta^{\mathrm{L}}_{\mathrm{D_{III}}}$) LAT values; column rms 1 provides the min and max rms differences between the observation- and model-derived tidal minima; column $\varepsilon_{\mathrm{Amp}} - \varepsilon_{\mathrm{MDT}}$ provides the average, min, and max differences between the observation- and model-derived tidal minima after applying the correction for the MDT error; column std 1 provides the min and max standard deviations of the differences between the observation- and model-derived tidal minima. All values are provided in cm.

Cnt.	Loc.	Nr. tide gauges	$\varepsilon_{\mathrm{MDT}}$			$\varepsilon_{\mathrm{LAT}}$			$\varepsilon_{\mathrm{LAT}} - \varepsilon_{\mathrm{MDT}}$			rms 1		$\varepsilon_{\mathrm{Amp}} - \varepsilon_{\mathrm{MDT}}$			std 1		$\varepsilon_{\mathrm{LAT}} - \varepsilon_{\mathrm{Amp}}$		
			mean	min	max	mean	min	max	mean	min	max	min	max	mean	min	max	min	max	mean	min	max
BE	on	3	2.02	0.18	3.32	6.76	-0.82	18.37	4.74	-3.38	15.05	19.49	26.88	17.97	14.53	22.16	8.57	9.47	-13.23	-17.91	-7.11
	off	5	2.12	-9.47	11.36	-1.73	-9.74	6.22	-3.85	-12.31	4.38	8.28	17.18	5.35	1.24	11.08	8.12	10.77	-9.21	-13.56	-6.70
DK	on	9	5.17	1.76	10.31	19.97	3.59	67.02	14.80	-5.13	56.71	6.43	58.27	10.98	-2.00	46.73	4.36	11.92	3.83	-8.89	10.43
FR	on	8	2.45	-2.70	11.15	-19.07	-36.73	23.57	-21.53	-40.26	16.09	11.90	25.03	1.36	-8.00	15.92	8.86	16.91	-22.89	-35.91	0.17
DE	on	2	-3.85	-9.04	1.33	-17.72	-21.39	-14.04	-13.86	-15.38	-12.35	10.46	11.04	0.61	-1.38	2.60	8.23	11.04	-14.47	-14.94	-14.00
NL	on	23	6.40	-0.68	16.66	1.76	-38.93	19.90	-4.64	-54.70	17.17	6.70	22.14	2.37	-27.25	17.46	5.65	12.36	-7.01	-27.45	6.16
	off	5	0.05	-2.46	1.73	1.38	-15.13	13.78	1.33	-12.66	13.57	3.95	12.23	3.37	-1.93	9.23	3.94	7.77	-2.04	-10.73	4.34
NO	on	4	-3.58	-8.10	-0.06	11.75	5.10	24.03	15.33	7.56	27.72	4.68	11.35	8.89	7.04	12.62	3.89	7.01	6.44	0.52	15.11
SE	on	5	-2.20	-7.94	2.74	9.18	-8.55	22.36	11.38	-5.13	26.10	6.93	14.36	6.61	-8.78	21.61	3.93	7.60	4.77	-2.23	12.87
UK	on	38	4.07	-9.49	19.56	-2.65	-66.21	58.91	-6.73	-74.53	49.50	5.57	63.30	7.64	-34.73	52.72	5.37	24.22	-14.37	-53.64	3.95
All		102	3.45	-9.49	19.56	0.42	-66.21	67.02	-3.03	-74.53	56.71	3.95	63.30	6.10	-34.73	52.72	3.89	24.22	-9.13	-53.64	15.11

To gain more insight into the differences between the observation- and model-derived LAT values, these are corrected for the misfit between the observation- and model-derived MDT values. On average, the results become worse. Before correction, the average misfit between the observation- and model-derived LAT values is 0.42 cm. After correction, this average misfit increases to -3.03 cm. On the other hand, the range of the differences remains more or less the same; -66.21 cm to 67.02 cm and -74.53 cm to 56.71 cm before and after correction, respectively.

To assess the statistical significance of the observed differences, they are compared to the model's ability to represent the tidal minima. The observation-derived tidal minima for a particular tide gauge are derived from the reconstructed tidal water levels obtained by a harmonic synthesis using the estimated amplitudes and phases of the set of constituents that explains the observed water levels best (Section 5.2). Similarly to the time series of the modeled astronomical tide, we use a 10 minutes sampling interval. The tidal minima are derived as the minimum water levels that occur around the epochs the tidal minima are expected. Since we use a sampling of 10 minutes to reconstruct the time series, the error introduced by the fact that we do not sample the exact tidal minima is on the order of a few millimeters and therefore negligible. Before applying the correction for the mismatch in the MDT, the rms differences between observation- and model-derived tidal minima range between 3.95 cm and 63.30 cm. Note that the maximum values are outliers; for 90% of all tide gauges the rms is below 26 cm. A significant contributor to these rms differences is an improper representation of the tidal amplitudes by the model; the average misfit after applying the correction for the MDT error is 6.10 cm with minimum and maximum deviations of -34.73 cm and 52.72 cm, respectively. This also follows from the standard deviations of the differences between observation- and model-derived tidal minima; for all tide gauges they range from 3.89 cm to 24.22 cm, while for 90% of all tide gauges the standard deviation is below 12.41 cm. If we correct the differences between observation- and model-derived LAT also for the average error in the representation of the tidal minima, the average difference over all tide gauges increases to -9.13 cm, while the minimum and maximum deviations decrease to -53.64 cm and 15.11 cm, respectively. These deviations are considered to be statistically significant if their absolute magnitude exceeds three times the standard deviation of the differences between observation- and model-derived tidal minima. Applying this test results in a rejection of only three model-derived LAT values at tide gauges from the UK; Liverpool, Llandudno, and Port Erin. All these tide gauges are located in the Irish Sea where the model performance is known to be less than in the North Sea for which the model was primarily developed. So, we conclude that, though at almost all tide gauges (99 out of 102) the observed differences between observation- and model-derived tidal minima after correction for systematic errors are in agreement within error, the systematic errors have a significant contribution to the overall error budget. Indeed, errors in the representation of the MDT, height transformation, etc.,

as well as errors in the representation of the tidal amplitude, affect the model skill to represent the LAT value relative to EGG08.

In most cases, errors in the representation of the tidal amplitude are attributed to the model's limited spatial resolution (approximately 8×9 km in east-west and north-south directions, respectively) to resolve the tidal behavior in shallow water and complex geometry such as harbors. This is, for instance, the case at the UK tide gauges Hinkley Point (Bristol Channel), Immingham (Humber Estuary), and Millport (Firth of Clyde); the rms differences are 31.98 cm, 36.42 cm, and 54.10 cm, respectively.

The used set of constituents has a significant influence on the obtained results. To illustrate this, we consider the Belgian onshore tide gauges Nieuwpoort, Oostende, and Zeebrugge. Using our criterion defined in Section 5.2, the set of 103 constituents is to be preferred over the set of 95 constituents for all 3 tide gauges. The obtained rms differences between the observation- and model-derived tidal minima after applying the correction for the MDT error are 17.35 cm, 19.33 cm, and 23.76 cm, respectively (Table C.1). Using the set of 95 constituents, these values decrease to 11.07 cm, 12.59 cm, and 18.01 cm, respectively. Though the data are best explained by the set of 103 constituents, the set of 95 constituents is a better choice. Indeed, this illustrates the need for a detailed analysis of each tide gauge to derive the optimal set of constituents to be used. Such an analysis is out of the scope of this study, but needs to be done.

In addition, it should be noted that to derive the observation-derived LAT values, the amplitudes and phases of the tidal constituents are estimated by a least-squares adjustment using all available data over the model period (1984–2004). Hence, they represent the *average* tidal cycle over the data period. For most tide gauges, we have data from 1985 to 2004, but there are some exceptions. For example, for all Belgian offshore tide gauges we have no data prior to February 2000. Furthermore, because the amplitudes and phases are subject to seasonal variations (Leeuwenburgh et al. 1999) and changes due to changes in bottom topography, coastal morphology, etc., they only match the modeled tidal cycle if the average circumstances match the model. Another discrepancy between modeled and "observed" astronomical tide is that in the latter the average seasonal variations are described by including the *SA* constituent in the harmonic synthesis used to reconstruct the tidal water levels. In the modeled tidal water levels, these are induced by the prescribed average monthly forcing fields.

The discrepancy between model-derived LAT and observation-derived LAT is also visible in the timing of the LAT event. Although for almost all tide gauges (97 out of 102) the LAT event occurs within a 3 month bracket, the years in which the event occurs differ up to 18 years. Favorable exceptions are most of the French (6 out of 8) and UK (19 out of 38) tide gauges, for which the timing of the LAT event is on the same day. The tide gauges for which we observe large differences in the

timing of the LAT event are Højer/Vidåslusen, Aukfield platform (offshore), Euro platform (offshore), North Cormorant (offshore), and Port Ellen. The modeling of the astronomical tide at Højer/Vidåslusen is known to be difficult due to tidal flats, which is also reflected by the large rms of the differences between observation- and model-derived tidal minima. At the Aukfield and Euro platforms the modeled tidal water levels at the epoch of the observation-derived LAT event differs only by ~ 1 cm from the model-derived LAT value. This is far below the achievable accuracy of the model-derived LAT and observation-derived LAT. For North Comorant, this difference is 8.4 cm. Here, a possible explanation might be the poor data coverage; we only have four months data in 1990 followed by a gap of almost four years, than almost two years of data, again followed by a gap of more than one year after which no more serious data gaps occur. For Port Ellen (Isle of Islay), the expected tidal variations are low since it is close to an amphidromic point. Probably, this is the explanation for the observed mismatch in the timing of the LAT event.

5.3.6 Comparison with literature

In this section, we compare our statistics with those reported by Turner et al. (2010). Their study includes a comparison of the LAT values derived from the North and Irish Sea and English Channel (NISE10) hydrodynamic tide-surge model, as well as several global ocean tide models, with the LAT values derived at 392 onshore and 187 offshore Admiralty Tide Tables gauges. At the onshore tide gauges, the NISE10 model performed best; the mean and standard deviation of the differences are -16.9 cm and 44.9 cm, respectively. At the offshore tide gauges, the FES2004 model shows the best agreement; the mean and standard deviation of the differences are -3.6 cm and 26.7 cm, respectively. For NISE10, these values are respectively -10.2 cm and 35.8 cm. Note that these numbers do not represent the accuracy of the final LAT surface as they are computed prior to the merging of observation- and model-derived LAT values (see Section 1.2.5). For the onshore tide gauges, we obtain a mean difference between observation- and model-derived LAT of 0.5 cm; the standard deviation is 21.5 cm. Note that both measures are not corrected for the mismatch between the observation- and model-derived MDT's and tidal minima. Since we only have 10 offshore tide gauges, the computation of the mean and standard deviation is too uncertain.

It is tempting to attribute these significant lower values to an improved modeling of LAT by the method suggested in this thesis. There are, however, some significant differences between both studies that make this conclusion difficult to support. Besides the number and locations of the tide gauges, in (Turner et al. 2010) LAT is not derived at all tide gauges, as the available data time span was too short. Instead, a level defined as CD has been used as a proxy of LAT, which was obtained by scaling the available lowest level from the shorter time series through a comparison with identi-

cal time series at nearby primary tide gauges. The rms of the differences between CD and LAT at tide gauges where both are known is already 12 cm. Finally, it should be noted that none of the work carried out by Turner et al. (2010) was aimed at improving the hydrodynamic models. The entire focus was on producing LAT models that are the best possible operational models to be used by mariners and chart developers.

5.4 Assessment of the safety of LAT as a chart datum

Besides the fact that all predicted tidal water levels become positive in sign, another main motivation to use LAT as CD is that LAT provides an indication of the minimal water depth that can be expected under average meteorological conditions and hence provides a sense of safety. Indeed, any surface above LAT results in charted depths that are occasionally greater than the true depth, which might lead to a *false* sense of safety. However, it is well known that meteorological conditions can result in water levels below LAT, especially in shallow waters. Hence, the sense of safety evoked by the use of LAT as CD is only justified if the probability that the instantaneous water level drops below LAT is low. In Experiment IV, these probabilities are computed.

5.4.1 Method

We model the instantaneous water levels using the setup described in Section 3.6.1. For each grid point, an extreme value analysis is performed on the minimum instantaneous water levels that occur during periods of tidal minima over the entire modeling period of 20 years (with a semi-diurnal tide we have $\sim 14,600$ tidal minima). Following Sobey (2005), appropriate probability distributions to apply such an analysis must have a probability density function (PDF) that is asymptotic to a tail at the low end. Since the histograms in Fig. 5.5 suggest that the distribution differs for each location, we use a non-parametric way to estimate the PDFs and cumulative density functions (CDFs). That is, no formal parametric structure is specified. Instead, the model used here consists of a linear combination of kernel functions characterized by a certain bandwidth centered at the original data (Izenman 1991). Here, we used Matlab's `ksdensity` (MATLAB 7.10.0.499, R2010a) with a normal kernel function and the default bandwidth that is optimal for estimating normal densities. Visual inspection of the goodness-of-fit shows that the PDFs provide a good fit over the entire range of observed data, see Fig. 5.5 for some representative examples at typical locations distributed over the whole model domain.

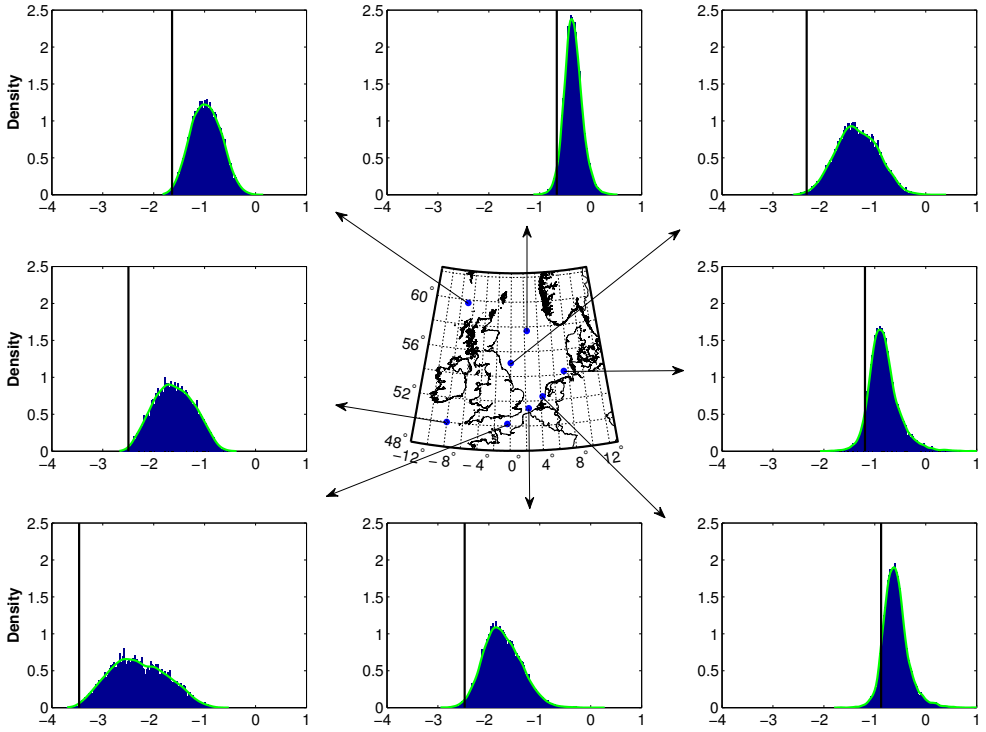

Figure 5.5: Normalized histograms of the model-derived, minimum instantaneous water levels in periods of tidal minima in meters, at eight locations distributed over the model domain. The histograms are fitted by non-parametric probability density functions that are estimated by Matlab's `ksdensity` with a normal kernel function and a bandwidth that is optimal for estimating normal densities.

5.4.2 Results

Using the estimated CDFs, we computed the probabilities that the minimum instantaneous water level in the periods of tidal minima drops below LAT plus a certain threshold. Various thresholds are selected: -1.00 m, -0.50 m, -0.25 m, 0.00 m, and 0.25 m. The probability maps are shown in Figs. 5.6a–5.6e. Except for some grid points in the German Bight, the probabilities that the minimum instantaneous water level in the periods of tidal minima drops 1.00 m below LAT are less than 10^{-4} (i.e., less than once per $5,000$ days). The probabilities increase to $1.5 \cdot 10^{-3}$ off the Dutch coast and to $6 \cdot 10^{-3}$ in the German Bight for a threshold of -0.5 m, i.e., between once per 350–80 days. For a threshold of -0.25 m, the probabilities increase further to values of 0.02 (once per 25 days). A further increase of the probabilities of

almost one order of magnitude is observed if the threshold is set equal to zero (0.18). The probabilities that the minimum instantaneous water levels drop below LAT + 0.25 m are between 0.1 to 1.

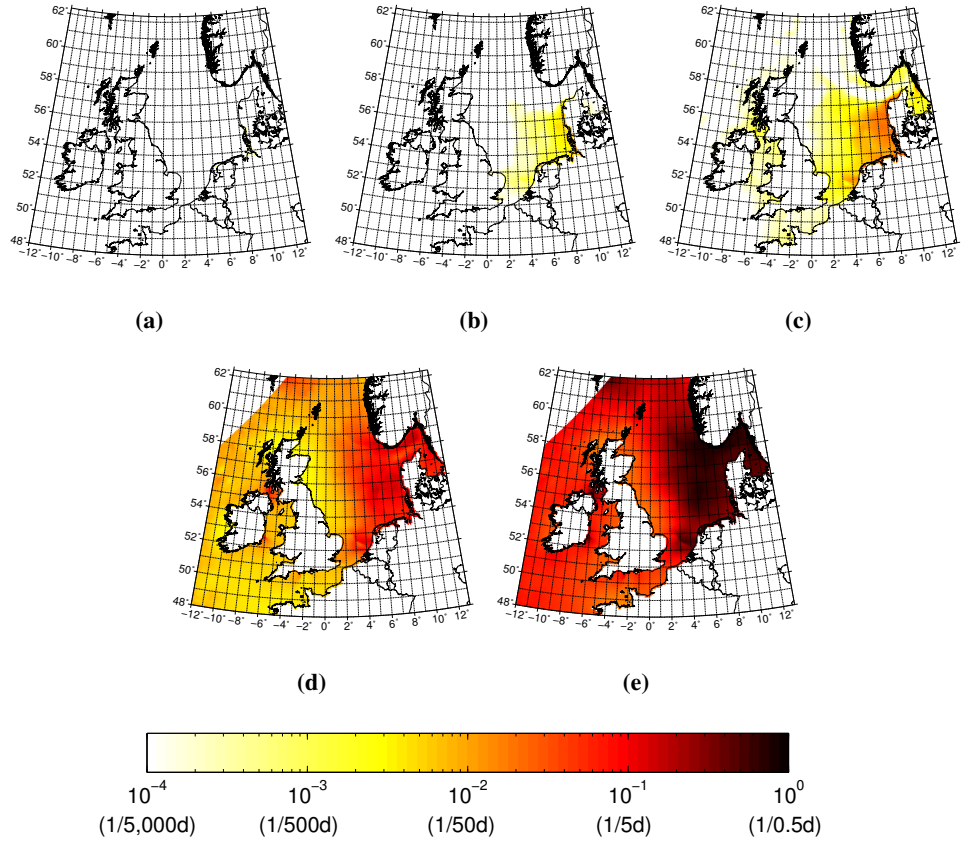

Figure 5.6: Probability that the minimum instantaneous water level in periods of tidal minima drops below: LAT−1.0 m (a), LAT−0.5 m (b), LAT−0.25 m (c), LAT (d), and LAT+0.25 m (e).

So, rather than once per 18.6 years, in the eastern side of the North Sea the probabilities that the minimum instantaneous water level drops below LAT are on the order of once per month to once per week. In comparison with Fig. 5.1a, we observe that the magnitude of LAT is low in this part of the North Sea due to the existence of two complete amphidromic systems and one degenerating one. Indeed, in this region the contribution of the surge dominates the water level variations. Hence, it is reasonable to expect a high probability that the instantaneous water level drops below LAT.

Because storm surge events are not equally distributed over the year (they occur more often in winter than in summer), it is expected that the event that the water level drops below LAT is more likely in winter than in summer. The maps with the probabilities that the minimum instantaneous water level drops below LAT computed over the different seasons are shown in Figs. 5.7a–5.7d. They are computed by repeating the procedure described above for subsets of the entire time series. From Fig. 5.7a and Fig. 5.7c, we conclude that, indeed, the probabilities in winter are much higher than in summer; approximately by a factor of five. In addition, we observe that in spring the probabilities are higher than in fall. This can be explained by the steric contribution to the water level: the water level in spring is lower because the water is colder, while in fall the level is higher due to warmer water.

This experiment has shown that the probability that the instantaneous water level drops below LAT is, at least in the eastern North Sea, a once per month/once per week event, much higher than one may expect from the definition of LAT. As suggested by the IHO resolution (International Hydrographic Organization 2011*a*, Technical Resolution 3/1919), in such a case not LAT but another surface might be used as CD: "*If low water levels in a specific area frequently deviate from LAT, chart datum may be adapted accordingly*". Here, we propose to use a probabilistic approach to realize CD. That is, CD is defined as a level which is exceeded with a given fixed probability. Such a level can be computed using the inverse cumulative density functions (ICDF) of the time series of minimal instantaneous water levels. We computed the levels that are only exceeded once per 18.6 years, once per 10 years, and once per year, and compared these levels with the LAT surface obtained in Experiment III (Figs. 5.8a–5.8c). In all cases, the obtained levels are below LAT. A likelihood of once per 18.6 years (Fig. 5.8a), provide differences up to -1.0 m in the German Bight (at some grid points in this area the differences even reach -1.2 m). For a likelihood of once a year, the differences reduce to -0.6 m to -0.7 m (Fig. 5.8c).

5.4.3 Discussion

Another advantage of using a probabilistic approach to realize CD is that this surface is more easily validated than LAT (cf. Section 5.3.5). Indeed, the same procedure used to compute the probabilities and levels shown in this experiment can be applied to tide gauge records, without the need to make assumptions, e.g, about the set of constituents to be used. Moreover, such an approach might help to reduce the differences in the realizations of CD for the various countries surrounding the North Sea as described by Dorst et al. (2010). The differences are introduced by different views and methods of how to realize LAT from both observations and models. For example, different views exist on the set of constituents to be used and on the time span over which constituents should be estimated. It should be noted that in this study we only considered meteorological and steric effects, because these are recurring phenomena

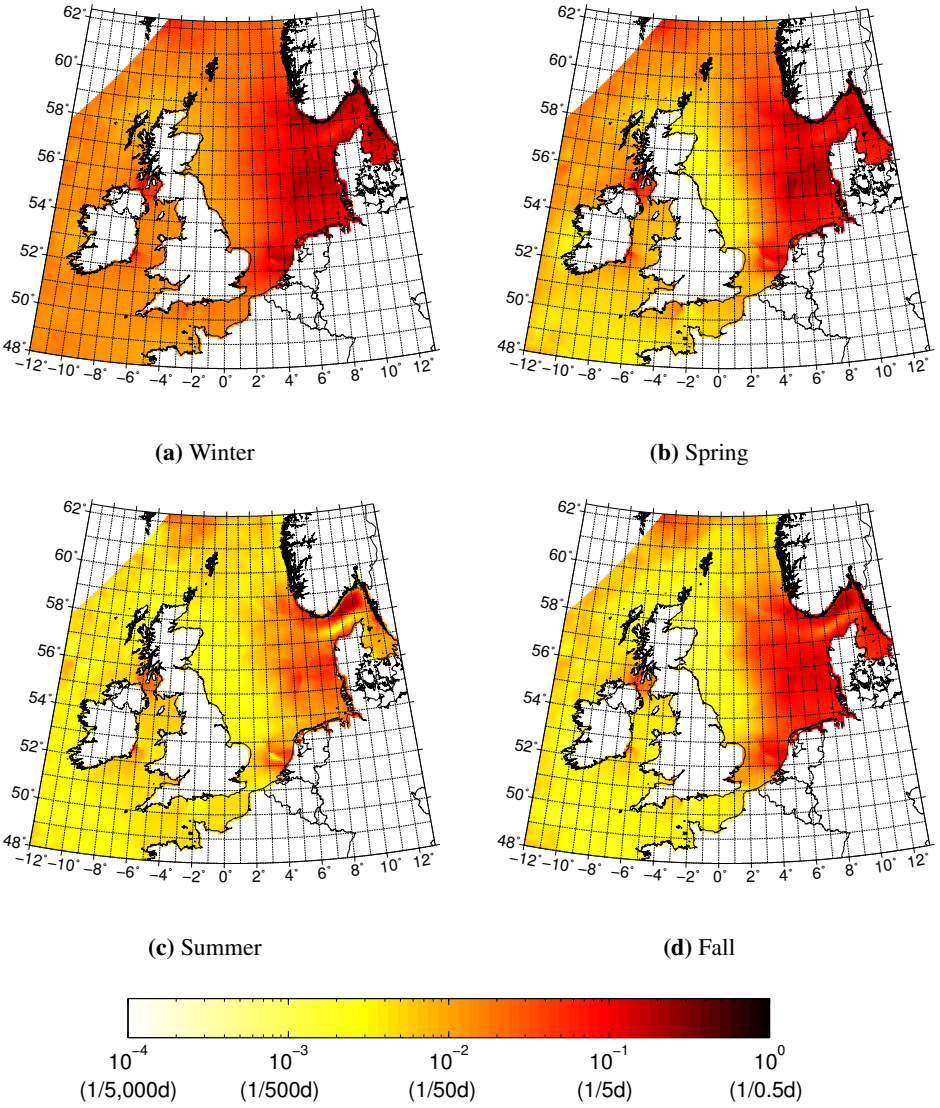

(a) Winter

(b) Spring

(c) Summer

(d) Fall

Figure 5.7: Probability that the minimum instantaneous water level in periods of tidal minima drops below LAT in: winter (a), spring (b), summer (c), and fall (d).

on the time scale we consider (a few decades). However, there are other phenomena that may cause that sea level drops below LAT such as tsunamis. This increases the uncertainty of the computed probabilities depending on the likelihood of the event. Conceptually we could include these phenomena in the realization of the probabilistic CD provided that some information about their probability is available. One issue that needs to be discussed in the hydrographic community is the probability level. On the one hand, this should not be too large to avoid a false sense of safety. From

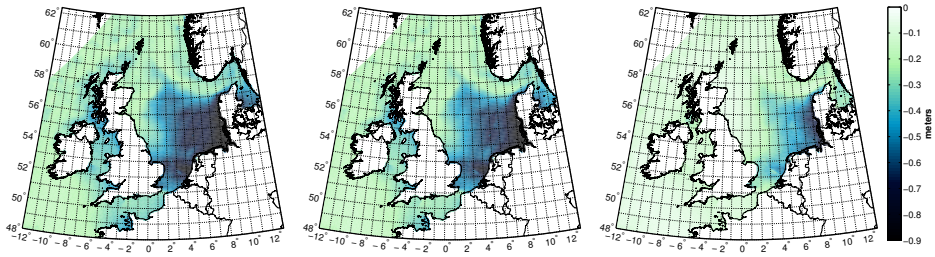

(a) Once per 18.6 years **(b)** Once per 10 years **(c)** Once per year

Figure 5.8: CD realized using a probabilistic approach relative to the LAT obtained in Experiment III. In the probabilistic approach, CD is defined as the level below which the instantaneous water level will drop by a specified fixed probability, This probability is once per 18.6 years in (a), once per 10 years in (b), and once per year in (c).

a commercial point of view, it should not be too small to allow for shorter routes of ships with deeper draughts.

5.5 Summary and conclusions

In this chapter, we evaluated computational strategies to derive the ellipsoidal heights of the LAT surface using a shallow water hydrodynamic model in combination with either ellipsoidal heights of MSL or heights relative to a quasi-geoid. In addition, we conducted an assessment of the suggested sense of safety of LAT as CD. We finish this chapter by giving a brief summary of the work that has been done, by emphasizing the main findings, and by providing some concluding remarks.

5.5.1 LAT derived from a shallow water model

Modeling LAT relative to the quasi-geoid is realized by (i) the explicit modeling of the average meteorological and steric conditions as required by the definition of LAT and (ii) referencing the hydrodynamic model to the quasi-geoid. This approach is conceptually clearer; unlike MSL, both the quasi-geoid and the model's reference surface are equipotential surfaces (indeed, in a strict sense the quasi-geoid is not an equipotential surface, but at sea the differences between the geoid and quasi-geoid are negligible). Moreover, such an approach allows for the inclusion of temporal variations in the definition of the average meteorological conditions and is applicable everywhere (approaches based on the MSL are applicable only where MSL is available).

In a number of numerical experiments using both the original and extended 2D Dutch Continental Shelf Model (DCSM), we first derived LAT relative to MSL and quan-

tified the contribution of the astronomical tide to the MDT. This contribution shows up as an error if not corrected for when the ellipsoidal heights of the LAT surface are computed. Besides some outliers, systematic errors up to 5 cm are observed off the Dutch coast.

In a second experiment, we derived LAT relative to the quasi-geoid by including the time-averaged meteorological and steric contributions. Compared to the model-derived MDT obtained by time-varying meteorological and steric contributions, the obtained MDT is hardly affected; the mean of the differences over the whole DCSM domain (Ω_D) equals 0.34 cm while the rms is 0.57 cm.

Explicit modeling of the average meteorological and steric conditions also implies that the obtained LAT surface includes the interaction of the tide with the average wind field. On average, this effect appears to be small; minimum and maximum deviations range between -7.72 cm and 3.91 cm over the whole model domain, while the rms is only 0.80 cm. Hence, after applying a correction to the model-derived LAT surface obtained with the original DCSM model for the contribution of the astronomical tide to the MDT (Experiment I), we conclude that the traditional approach to compute the ellipsoidal heights of the LAT surface is the preferred method *outside coastal waters*. Indeed, if LAT is derived relative to the quasi-geoid, errors in the model-derived MDT become also part of the total error budget.

If, however, monthly variations in average meteorological and steric conditions are included, the extreme differences between the derived LAT surface and the one obtained using the traditional approach increase to -15.81 cm and 5.86 cm. The rms difference is 5.49 cm. These values are significantly larger than the errors in the model-derived MDT. The largest differences are observed west to Denmark, while the largest errors in the representation of the MDT show up elsewhere.

The LAT surface obtained in Experiment III is validated using LAT values derived from at least 2.5 years and at most 20 years of observed water levels at 92 onshore and 10 offshore tide gauges. The set of constituents used to derive the observation-derived LAT values is that set for which the rms difference between the observed water levels and the reconstructed astronomical tidal water levels is lowest. Two sets were considered; one comprising 103 constituents, the other comprising 95 constituents. For the 92 onshore stations, we found a mean of 0.5 cm and a standard deviation of 21.5 cm. The obtained differences between the observation- and model-derived LAT values reveal a mixture of errors in both model and observations. We found that systematic errors in the representation of the tidal amplitude by DCSM dominate. Using the standard deviation of the differences between observation- and model-derived tidal minima, we conducted a test to evaluate the statistical significance of the differences between the observation-derived LAT values and model-derived LAT values corrected for the mismodeling of the MDT and tidal amplitude. For three tide gauges, the observed differences are larger than three times the stan-

dard deviation and, therefore, are considered statistically significant. All three tide gauges are located in the Irish Sea where DCSM is known to perform less. The hydrodynamic model is considered to be the primary error source for the observed differences between the observation- and model-derived LAT values. In a future work, the hydrodynamic model will be improved in terms of spatial resolution and physics. We also showed that the choice of the set of tidal constituents for each tide gauge has a significant influence on the derived LAT value at this tide gauge. In this study, two sets of tidal constituents were used, but whether those sets are a good choice needs to be investigated.

5.5.2 The safety of LAT as chart datum

In a final experiment, we investigated whether the sense of safety evoked by using LAT as CD is justified. Indeed, since LAT is computed as a once per 18.6 years event under average meteorological conditions, the use of LAT suggests that the instantaneous water level rarely drops below LAT. On the other hand, it is well known that meteorological conditions have a significant influence on the water level in shallow waters. In this study, the probabilities that the minimum instantaneous water level in periods of tidal minima is below LAT are computed using time series of modeled instantaneous water levels. In the eastern North Sea, these probabilities appear to be on the order of once per month to once per week. As could be expected, these probabilities are largest in winter, followed by spring, fall, and summer. The probabilities in winter and summer differ, approximately, by a factor of five. The high probability that the water level is below LAT motivated us to propose a probabilistic approach to realize CD, where CD is defined as the level below which the water falls with a given probability. Without attempting to prescribe how large the probability should be, we realized CD using this approach for different probabilities and quantified the differences to LAT. Even for a probability of once per year, the probabilistic CD would be below LAT by several decimeters. Additional advantages of the proposed method are that it offers an opportunity to realize CD unambiguously and that the obtained CD is much easier to validate.

Chapter 6

The spherical Slepian basis as a means to obtain spectral consistency

This chapter is based on Slobbe et al. (2012). In this paper, we treat the question whether a spherical Slepian basis representation provides spectral consistency in the context of mean dynamic topography (MDT) estimation using the so-called "geodetic approach". That is, by computing the difference between a mean sea surface model obtained from satellite altimetry and a gravimetric geoid. However, as noticed in the paper, the problem of ensuring spectral consistency between two signals before combining them is more general in nature than the specific context in which we presented it. Hence, our conclusions also apply to the problem we have at hand; making the LAT and MDT surfaces spectrally consistent with the geoid. This is needed to compute the ellipsoidal heights of the LAT and MSL surfaces.

6.1 Introduction

Since ocean currents are nearly in geostrophic balance on time scales longer than a few days and spatial scales longer than a few tens of kilometers, the velocity of the surface geostrophic current is proportional to the gradient in the average height of the sea surface expressed relative to the geoid (Wunsch & Gaposchkin 1980). This so-called mean dynamic topography (MDT) can be computed by subtracting a gravimetric geoid from an altimetric mean sea level (MSL) model, provided that both are expressed relative to the same reference ellipsoid and in the same permanent tide system. However, especially in the open ocean, the altimetric MSL has a much higher

spatial resolution than the gravimetric geoid. Consequently, the apparently straightforward computation of the MDT becomes problematic since the high-frequency part that is lacking from the geoid cannot be subtracted from the MSL. This causes a non-random error that can be misinterpreted as a part of the MDT (Losch et al. 2002, Albertella & Rummel 2009). Before the MDT is computed by taking the difference between altimetric MSL and gravimetric geoid, the latter two have to be made "spectrally consistent": they have to cover the same spectral range. Hence, a suitable low-pass filter has to be applied to the altimetric MSL.

The problem of ensuring spectral consistency between two signals before combining them is more general in nature than the specific context in which it appeared above. Indeed, it arises whenever different data sets and/or models with various spatial or temporal resolutions are to be merged for interpretation, e.g., in seismology and geomagnetic studies (Trampert & Snieder 1996, Boschi & Dziewonski 1999, Schachtschneider et al. 2010, Schott & Thébault 2011).

To derive the MDT of the North Atlantic Ocean, Jayne (2006) applied a Hamming window smoother in the spatial domain on both geoid and the MSL. However, since low-pass filtering results in the replacement of the original signal by its weighted spatial average, this operation fails in coastal regions, because the MSL is not defined on land. Alternatively, adaptive filters based on principal component analysis (PCA) over the domain of interest might be used. For example, Vianna et al. (2007) used a singular spectrum analysis (SSA) expansion to filter noise in a GRACE-based MDT for the South Atlantic region. SSA could also be used to obtain spectral consistency of altimetric MSL and gravimetric geoid.

On the other hand, we might make use of the fact that geoid models are bandlimited, i.e., they are expressed as a set of spherical harmonic expansion coefficients, complete to some degree L_g. Likewise, the altimetric MSL could be expanded in spherical harmonics complete to some degree L_r, typically with $L_r > L_g$. Spectral consistency could then be obtained by truncating the MSL expansion at degree L_g. Two problems are inherent in this approach. First, since the spherical harmonics are not an orthogonal basis over incomplete spherical domains such as the oceans, the estimation of the expansion coefficients from radar altimeter data is ill-conditioned (Simons & Dahlen 2006). Second, truncation of the spherical harmonic expansion beyond degree L_g gives rise to Gibbs phenomena that can only be suppressed with appropriate spectral windows.

The first problem, ill-conditioning, is traditionally addressed by regularized least-squares or truncated singular value decomposition (SVD) approaches (e.g., Xu 1998). More recently, truncated Slepian basis representations have been proposed (Simons & Dahlen 2006), about which more is to follow below. Alternatively, as advocated by, e.g., Tapley et al. (2003), missing MSL data on land and in uncovered ocean regions such as the polar gaps can be replaced by geoid information. Rather than es-

timating the spherical harmonic coefficients from a signal defined over a subdomain of the sphere, the estimation is then carried out using the combined whole-sphere signal. The geoid is used to extend the MSL since the two do not differ more than by about 3 m. Despite this small difference, discontinuities persist at the coastlines, introducing Gibbs phenomena. Bingham et al. (2008) suggest to further reduce the Gibbs effects in the MDT by using the same geoid on land as is used to compute the MDT. In an elaboration of the method (Tapley et al. 2003) discussed by Albertella et al. (2008), the transition from land to sea is smoothed by iteratively estimating the spherical harmonic coefficients of MSL up to degree L_r from the combined land-ocean data set. In each iteration, the values over land are replaced by those obtained from a spherical harmonic synthesis of the last derived set of coefficients. This process is repeated until some pre-defined stopping criterion has been satisfied. Finally, low-pass filtering is applied to obliterate the signal above L_g and to reduce Gibbs effects. Albertella et al. (2008) and Albertella & Rummel (2009) use a Gaussian filter, but other (low-pass) filters may be used as well (for more details about the Gaussian filter and alternatives, we refer to, e.g., Jekeli 1981). Generally, however, the low-pass filtered MSL signal still contains energy above degree L_g and will thus not be spectrally consistent with the geoid to which it is compared.

In summary, we might say that no ideal approach currently exists to obtain low-resolution approximations to MSL that are spectrally consistent with the geoid. In studying a one-dimensional version of this problem, Albertella & Rummel (2009) came to the conclusion that extending MSL to the entire globe using, e.g., geoid information unavoidably results in a distortion of its spectral content, even if utmost care is taken to derive smooth transitions from ocean to land. In contrast, they conclude that representing MSL in a basis of Slepian functions, which are suitable for signals of limited bandwidth living on limited intervals (Simons 2010), holds much promise in solving both problems above. Somewhat pessimistically, though, they wrote that "it may prove difficult to apply it to the real world case with the complicated shapes of ocean basins".

Since the efficient generation of Slepian functions on domains of arbitrary geometry, whether in spherical (Simons et al. 2006) or Cartesian (Simons & Wang 2011) coordinates, presents no *intrinsic* difficulties, we are here able to consider their use in the context of the work by Albertella & Rummel (2009), on which we build. Our main goal is to design a bandlimited Slepian basis for the ocean basins in spherical geometry and to evaluate the utility of this basis in solving the problem stated above, which is to derive suitable representations of altimetric MSL while maintaining spectral consistency with the gravimetric geoid. Hwang (1991), see also Hwang (1993) for a shorter version, used another set of orthogonal functions on the oceans to represent the sea surface topography derived from radar altimeter data. This set of orthogonal basis functions has been generated from spherical harmonics using the Gram-Schmidt process, see Golub & Van Loan (1996).

In this chapter, we first summarize some basics about spherical Slepian functions (Section 6.2). Following this, we address the problem of spectral consistency and bandwidth for functions given on a part of the spherical domain (Section 6.3). Next, we describe the setup of several numerical experiments, which were designed to investigate the performance of a Slepian basis representation of the MSL signal which is spectrally consistent with a given gravimetric geoid (Section 6.4). This includes a discussion about the choice of the optimal number of Slepian basis functions. Thereafter, we present and discuss the results of the numerical experiments (Section 6.5). The main result is that all methods discussed in Section 6.5 fail to provide a low-resolution MSL signal with an adequate accuracy. Therefore, in Section 6.6, we reformulate the problem, provide a mathematical solution, and discuss its applicability to high-resolution data. Finally, we conclude by emphasizing the main findings and identifying topics for future research.

6.2 The spherical Slepian basis

The functions now named after David Slepian grew out of the work by Slepian & Pollak (1961) and Landau & Pollak (1961, 1962), who solved a long-standing problem in information theory, namely, that of optimally concentrating a given signal in both the time and frequency domains. Since timelimited functions cannot be simultaneously bandlimited in the frequency domain, nor vice versa, the optimally concentrated signal is considered to be the one with the least energy outside the interval of interest. The concentration problem has been extended and generalized for the purpose of signal estimation, representation, and analysis on geographical domains by Albertella et al. (1999), Pail et al. (2001), and Simons & Dahlen (2006) in geodesy, and by Wieczorek & Simons (2007) and Dahlen & Simons (2008) in more general settings. The quadratic maximization of the spatial energy of bandlimited functions is one way to achieve localization in one domain while curbing leakage in the other. Other constructions may have similarly desirable properties, but even those are often judged on how closely they satisfy quadratic optimality constraints (e.g. Freeden & Michel 1999, Guilloux et al. 2009). We therefore remain faithful to the original approach of Slepian, as transformed into spherical geometry by Simons et al. (2006).

Following the notation of Simons (2010), we use (in this chapter) bold, serifed fonts (e.g., $\mathbf{f}$, $\mathbf{D}$) for vectors or matrices that are entirely composed of spectral quantities, and bold, sans-serif fonts (e.g., f, Y) for those that depend on at least one spatial variable. The colatitude of a geographical point $\hat{\mathbf{x}}$ on the surface Ω of the unit sphere is denoted by ϑ and the longitude by λ, with $0 \leq \vartheta \leq \pi$ and $0 \leq \lambda < 2\pi$. We use Ω_0 to denote a region of Ω, of area $|\Omega_0|$, within we seek to concentrate a bandlimited function of position $\hat{\mathbf{x}}$. Using orthonormalized real surface spherical harmonics $\hat{Y}_{lm}(\hat{\mathbf{x}})$,

whereby

$$\int_\Omega \hat{Y}_{lm}(\hat{\mathbf{x}})\hat{Y}_{l'm'}(\hat{\mathbf{x}})\,d\Omega = \delta_{ll'}\delta_{mm'}, \tag{6.1}$$

we can express a square-integrable real function $f(\hat{\mathbf{x}})$ on the surface of the unit sphere as

$$f(\hat{\mathbf{x}}) = \sum_{l=0}^{\infty}\sum_{m=-l}^{l} f_{lm}\,\hat{Y}_{lm}(\hat{\mathbf{x}}), \quad f_{lm} = \int_\Omega f(\hat{\mathbf{x}})\hat{Y}_{lm}(\hat{\mathbf{x}})\,d\Omega. \tag{6.2}$$

The bandlimited Slepian basis (bandwidth L) that is spatially concentrated to the region Ω_0 is the collection of functions that have no power outside the spectral interval $0 \le l \le L$ but as much of their power as possible concentrated within Ω_0:

$$g(\hat{\mathbf{x}}) = \sum_{l=0}^{L}\sum_{m=-l}^{l} g_{lm}\,\hat{Y}_{lm}(\hat{\mathbf{x}}), \quad g_{lm} = \int_\Omega g(\hat{\mathbf{x}})\hat{Y}_{lm}(\hat{\mathbf{x}})\,d\Omega, \tag{6.3}$$

for which the spatial concentration factor

$$\lambda = \frac{\int_{\Omega_0} g^2(\hat{\mathbf{x}})\,d\Omega}{\int_\Omega g^2(\hat{\mathbf{x}})\,d\Omega} = \text{maximum}. \tag{6.4}$$

Note that by convention, λ is also used to indicate the longitude. Its exact meaning will be clear from the context. Maximizing Eq. (6.4) can be achieved in the spectral domain by solving the algebraic eigenvalue problem:

$$\mathbf{D}\,\mathbf{g} = \lambda\,\mathbf{g}, \tag{6.5}$$

where $\mathbf{g}$ is a $(L+1)^2$-dimensional vector that represents a Slepian eigenfunction expressed in spherical harmonics, i.e. $\mathbf{g} = (g_{00}\cdots g_{lm}\cdots g_{LL})^{\mathrm{T}}$ and $\mathbf{D}$ is the $(L+1)^2 \times (L+1)^2$-dimensional spectral-basis projection operator or localization kernel:

$$\mathbf{D} = \begin{pmatrix} D_{00,00} & \cdots & D_{00,LL} \\ \vdots & & \vdots \\ D_{LL,00} & \cdots & D_{LL,LL} \end{pmatrix}, \tag{6.6}$$

whose elements $D_{lm,l'm'}$ are given by

$$D_{lm,l'm'} = \int_{\Omega_0} \hat{Y}_{lm}(\hat{\mathbf{x}})\hat{Y}_{l'm'}(\hat{\mathbf{x}})\,d\Omega. \tag{6.7}$$

As a consequence of the symmetry $\mathbf{D}^{\mathrm{T}} = \mathbf{D}$, the eigenvectors $\{\mathbf{g}_\alpha : \alpha = 1,\ldots,(L+1)^2\}$ are mutually orthogonal. When choosing them to be orthonormal, we have

$$\mathbf{g}_\alpha^{\mathrm{T}}\mathbf{g}_\beta = \delta_{\alpha\beta} \qquad \text{and} \qquad \mathbf{g}_\alpha^{\mathrm{T}}\mathbf{D}\,\mathbf{g}_\beta = \lambda_\alpha \delta_{\alpha\beta}, \tag{6.8}$$

where $\delta_{\alpha\beta}$ is the Kronecker delta defined as

$$\delta_{\alpha\beta} = \begin{cases} 1 & \text{if } \alpha = \beta, \\ 0 & \text{otherwise.} \end{cases} \tag{6.9}$$

The corresponding spatial Slepian functions,

$$g_\alpha(\hat{\mathbf{x}}) = \sum_{l=0}^{L} \sum_{m=-l}^{l} g_{lm\,\alpha} \hat{Y}_{lm}(\hat{\mathbf{x}}), \quad \alpha = 1,\ldots,(L+1)^2, \tag{6.10}$$

are orthonormal over the whole sphere Ω and orthogonal over the region Ω_0.

Rather than determining *bandlimited* functions that are concentrated in a spatial region of interest Ω_0 we may also find *spacelimited* functions $h(\hat{\mathbf{x}})$ that are concentrated in a spectral interval $0 \le l \le L$. Instead of Eq. (6.5), the $h(\hat{\mathbf{x}})$ satisfy the spatial-domain eigenvalue equation

$$\int_{\Omega_0} D(\hat{\mathbf{x}},\hat{\mathbf{x}}')h(\hat{\mathbf{x}}')\,d\Omega' = \lambda h(\hat{\mathbf{x}}), \quad \text{for} \quad \hat{\mathbf{x}} \in \Omega_0, \tag{6.11}$$

whose kernel is given by the bandlimited delta function

$$D(\hat{\mathbf{x}},\hat{\mathbf{x}}') = \sum_{l=0}^{L} \left(\frac{2l+1}{4\pi}\right) P_l(\hat{\mathbf{x}}\cdot\hat{\mathbf{x}}'), \tag{6.12}$$

and where P_l is the Legendre function of degree l. Eqs. (6.5) and (6.11) have identical eigenvalues λ. In both cases, the eigenvalues are a measure of the quality of the spatiospectral concentration. In the latter case, λ expresses the spectral concentration

$$\lambda = \frac{\displaystyle\sum_{l=0}^{L}\sum_{m=-l}^{l} h_{lm}^2}{\displaystyle\sum_{l=0}^{\infty}\sum_{m=-l}^{l} h_{lm}^2} = \text{maximum}. \tag{6.13}$$

The sum of the eigenvalues, which is known as the Shannon number, K, is given by

$$\begin{aligned} K &= \sum_{\alpha=1}^{(L+1)^2} \lambda_\alpha = \sum_{l=0}^{L} \sum_{m=-l}^{l} D_{lm,lm} = \int_{\Omega_0} D(\hat{\mathbf{x}},\hat{\mathbf{x}})\, d\Omega \\ &= (L+1)^2 \frac{|\Omega_0|}{4\pi}. \end{aligned} \tag{6.14}$$

From Eq. (6.4), it follows that the closer an eigenvalue λ is to 1 the better the corresponding Slepian function $g(\hat{\mathbf{x}})$ is concentrated within Ω_0. If an eigenvalue is small, i.e., $\lambda \ll 1$, the corresponding Slepian function is mostly concentrated in the domain $\bar{\Omega}_0 = \Omega - \Omega_0$. Hence, the Shannon number K, Eq. (6.14), is roughly equivalent to the *number* of well concentrated ($\lambda \approx 1$) eigenfunctions.

If the first K eigenfunctions g_1, g_2, ... , g_K are well concentrated in the region Ω_0, the remaining eigenfunctions g_{K+1}, g_{K+2}, ... , $g_{(L+1)^2}$ are well concentrated in the complementary region $\bar{\Omega}_0$. From Eq. (6.14) it then follows that when the area of region Ω_0 is a small fraction of the sphere, $K \ll (L+1)^2$ holds true. By implication there are many more eigenfunctions with insignificant eigenvalues ($\lambda \approx 0$) than well-concentrated eigenfunctions with significant eigenvalues ($\lambda \approx 1$). If on the other hand the area $|\Omega_0|$ approximates the area of the sphere, $K \approx (L+1)^2$, i.e., there will be many more well concentrated than well-excluded eigenfunctions.

Bandlimited spatially concentrated Slepian functions designed for a given domain Ω_0 form a basis for bandlimited signals *anywhere* on the sphere. When ranked by decreasing eigenvalue λ, the first J members of such a Slepian basis provide efficient constructive approximations to bandlimited functions $s(\hat{\mathbf{x}})$ that are themselves spatially concentrated inside the same region Ω_0:

$$\begin{aligned} s(\hat{\mathbf{x}}) &= \sum_{l=0}^{L} \sum_{m=-l}^{l} s_{lm}\, \hat{Y}_{lm}(\hat{\mathbf{x}}) = \sum_{\alpha=1}^{(L+1)^2} t_\alpha g_\alpha(\hat{\mathbf{x}}) \\ &\approx \sum_{\alpha=1}^{J} t_\alpha g_\alpha(\hat{\mathbf{x}}), \quad \hat{\mathbf{x}} \in \Omega_0, \end{aligned} \tag{6.15}$$

where t_α are the Slepian expansion coefficients. Due to the characteristic flat, and then rapidly declining, shape of the eigenvalue spectrum, taking $J = K$ will provide very reasonable approximations to $s(\hat{\mathbf{x}})$ within the region Ω_0. Equality prevails globally when $J = (L+1)^2$. From an inverse modeling standpoint, the optimal (in the mean-squared error sense) truncation level J in estimating a localized signal from noisy data over the region is determined by the signal-to-noise ratio. In the noiseless case, $J = (L+1)^2$ holds true, while in the special case of white noise contaminating a white signal, the optimal value for J is when the corresponding eigenvalue $\lambda_J = N/S$,

with N the noise variance and S the signal variance. For more details, see Simons & Dahlen (2006).

In geodetic practice we are likely to have M samples of a certain signal $s(\hat{\mathbf{x}})$, which, collected in a vector $\mathbf{s}$, allows us to rewrite Eq. (6.15) as:

$$\mathbf{s} = \mathbf{Y}_L^{\mathrm{T}}\mathbf{s} = \mathbf{Y}_L^{\mathrm{T}}\mathbf{G}\mathbf{t} = \mathbf{G}^{\mathrm{T}}\mathbf{t}, \tag{6.16}$$

where $\mathbf{s} = (s(\hat{\mathbf{x}}_1)\cdots s(\hat{\mathbf{x}}_j)\cdots s(\hat{\mathbf{x}}_M))^{\mathrm{T}}$, $\mathbf{s} = (s_{00}\cdots s_{lm}\cdots s_{LL})^{\mathrm{T}}$, $\mathbf{t} = (t_1\cdots t_\alpha\cdots t_{(L+1)^2})^{\mathrm{T}}$, and, following Simons (2010),

$$\mathbf{Y}_L = \begin{pmatrix} \hat{Y}_{00}(\hat{\mathbf{x}}_1) & \dots & \hat{Y}_{00}(\hat{\mathbf{x}}_j) & \dots & \hat{Y}_{00}(\hat{\mathbf{x}}_M) \\ \vdots & & \hat{Y}_{lm}(\hat{\mathbf{x}}_j) & & \vdots \\ \hat{Y}_{LL}(\hat{\mathbf{x}}_1) & \dots & \hat{Y}_{LL}(\hat{\mathbf{x}}_j) & \dots & \hat{Y}_{LL}(\hat{\mathbf{x}}_M) \end{pmatrix}, \tag{6.17}$$

$$\mathbf{G} = \begin{pmatrix} g_1(\hat{\mathbf{x}}_1) & \dots & g_1(\hat{\mathbf{x}}_j) & \dots & g_1(\hat{\mathbf{x}}_M) \\ \vdots & & g_\alpha(\hat{\mathbf{x}}_j) & & \vdots \\ g_{(L+1)^2}(\hat{\mathbf{x}}_1) & \dots & g_{(L+1)^2}(\hat{\mathbf{x}}_j) & \dots & g_{(L+1)^2}(\hat{\mathbf{x}}_M) \end{pmatrix}, \tag{6.18}$$

$$\mathbf{G} = \begin{pmatrix} g_{00\,1} & \cdots & g_{00\,\alpha} & \cdots & g_{00\,(L+1)^2} \\ \vdots & & g_{lm\,\alpha} & & \vdots \\ g_{LL\,1} & \cdots & g_{LL\,\alpha} & \cdots & g_{LL\,(L+1)^2} \end{pmatrix}. \tag{6.19}$$

In this notation, Eq. (6.3) is rewritten as $\mathbf{G} = \mathbf{G}^{\mathrm{T}}\mathbf{Y}_L$, and the left-hand side of Eq. (6.8) becomes $\mathbf{G}^{\mathrm{T}}\mathbf{G} = \mathbf{I}$, the identity matrix.

6.3 Spectral consistency and the choice of the bandwidth

Suppose we have access to a high-resolution MSL model and a low-resolution geoid model for the oceans or a part of the oceans, e.g., an ocean basin. Then, spectral consistency between MSL and geoid is obtained when both are represented in a bandlimited, spatially concentrated Slepian basis involving the same set of Slepian basis functions. The choice of the bandwidth should be dictated by the signal that has the lowest resolution, in our case the geoid, since this is the resolution at which we need to describe the MSL to compute the MDT reliably. Geoid information is typically

provided in terms of a spherical harmonic expansion complete to some maximum degree, say L_g. This maximum degree describes solely the spatial resolution of the geoid, and, therefore, is also used as a descriptor of the bandwidth.

According to Eq. (6.15), we can transform any given spherical harmonic expansion of the geoid complete to degree L_g into a bandlimited, spatially concentrated Slepian basis invoving $(L_g+1)^2$ Slepian basis functions. Therefore, a natural choice of the bandwidth of the Slepian functions would be L_g. This is definitely correct as long as the geoid is considered as a function on the whole domain Ω. However, when the geoid signal is confined to a part of the domain such as the oceans or an ocean basin, this definition of the bandwidth of the geoid becomes meaningless as we show below. Therefore, the choice of the correct bandwidth of the Slepian basis functions is still open and not necessarily given by the maximum degree of the spherical harmonic expansion of the geoid.

To investigate the choice of the bandwidth for a signal given in a region Ω_0 of the sphere Ω, we design the following experiment. We assume that a certain signal is given in terms of a spherical harmonic expansion complete to degree $L_g = 48$. We try to reconstruct this bandlimited signal from data inside various regions Ω_0 of different size using spherical harmonic expansions complete to degree $L \leq L_g$. In our experiment, the region Ω_0 is always a spherical cap; the radius of the cap varies in increments of 10° between 10° and 180°. The latter case corresponds to the choice $\Omega_0 = \Omega$, the entire sphere. Despite its simplistic geometry, the simple spherical cap is an appropriate choice for a trial region. Its advantage is that the Slepian functions for this particular geometry can be calculated via the painless procedure devised by Grünbaum et al. (1982), as shown by Simons et al. (2006). Furthermore, for complete generality with respect to where we position the cap in the analysis we consider a bandlimited white Gaussian stationary process defined on the region Ω_0, i.e.,

$$w(\hat{\mathbf{x}}) = \begin{cases} \sum_{l=0}^{L_g} \sum_{m=-l}^{l} w_{lm}\, \hat{Y}_{lm}(\hat{\mathbf{x}}) & \text{if } \hat{\mathbf{x}} \in \Omega_0, \\ \text{unknown} & \text{if } \hat{\mathbf{x}} \in \Omega - \Omega_0, \end{cases} \tag{6.20}$$

where

$$\mathrm{E}\{w_{lm}\} = 0, \;\; \mathrm{Cov}\{w_{lm} w_{l'm'}\} = \delta_{ll'}\delta_{mm'}, \quad 0 \leq l, l' \leq L_g, \tag{6.21}$$

and $\mathrm{E}\{\cdot\}$ denotes expectation and $\mathrm{Cov}\{\cdot\}$ denotes covariance. The signal $w(\hat{\mathbf{x}})$ is approximated by a function $\hat{w}(\hat{\mathbf{x}})$, which is given by

$$\hat{w}(\hat{\mathbf{x}}) = \sum_{l=0}^{L} \sum_{m=-l}^{l} \hat{w}_{lm}\, \hat{Y}_{lm}(\hat{\mathbf{x}}), \tag{6.22}$$

for some maximum degree $L \leq L_g$. For continuous data, and using the notation established in Eqs. (6.16)–(6.19), the least-squares estimate of the spherical harmonic

coefficients $\hat{w}_{lm}$ is

$$\hat{\mathbf{w}}_L = \mathbf{D}_L^{-1}\,\mathbf{D}_{L_g}\,\mathbf{w}_{L_g}, \tag{6.23}$$

where $\hat{\mathbf{w}}_L = (\hat{w}_{lm} : l,m \leq L)^{\mathrm{T}}$, $\mathbf{w}_{L_g} = (w_{lm} : l,m \leq L_g)^{\mathrm{T}}$, and $\mathbf{D}_L$ and $\mathbf{D}_{L_g}$ are the matrices with entries $D_{lm,l'm'}$ as in Eq. (6.7) for degrees $l = 0,\ldots,L$ and $l = 0,\ldots,L_g$, in both dimensions or in one of each dimension: $\mathbf{D}_L$ is square, $\mathbf{D}_{L_g}$ is rectangular respectively.

If the signal is known at M points, collected in a vector $\mathbf{w}$, we write Eq. (6.20) as

$$\mathbf{w} = \mathbf{Y}_{L_g}^{\mathrm{T}}\mathbf{w}_{L_g}, \tag{6.24}$$

using the notation established in Eqs. (6.16)–(6.19). The least-squares estimate $\hat{\mathbf{w}}_L$ is given by

$$\hat{\mathbf{w}}_L = (\mathbf{Y}_L\mathbf{Y}_L^{\mathrm{T}})^{-1}\mathbf{Y}_L\mathbf{w}, \tag{6.25}$$

$$= (\mathbf{Y}_L\mathbf{Y}_L^{\mathrm{T}})^{-1}(\mathbf{Y}_L\mathbf{Y}_{L_g}^{\mathrm{T}})\mathbf{w}_{L_g}, \tag{6.26}$$

which is the analogue to Eq. (6.23) for discrete data. Irrespectively of the radius Θ of the spherical cap, when $L = L_g$, we thus in principle recover the input without bias, i.e.,

$$\hat{\mathbf{w}}_{L_g} = \mathbf{w}_{L_g}, \tag{6.27}$$

although the condition number of the normal matrix $\mathbf{Y}_{L_g}\mathbf{Y}_{L_g}^{\mathrm{T}}$ in that case will determine how close we can get. The numerical integration error (i.e., the number and spatial distribution of the samples and the chosen weights) determines how well $\hat{\mathbf{w}}_L$ as defined in Eq. (6.25) matches the elements $\hat{w}_{lm}$ as defined in Eq. (6.23). Assuming that the function of interest $w(\hat{\mathbf{x}})$ is densely sampled inside Ω_0, e.g. on the M nodes of a Fibonacci grid (González 2010), where $M \gg |\Omega_0|\left(\frac{L_g}{\pi}\right)^2$, and the weights are equal to $\Delta\Omega = 4\pi/M$, the normal matrix should be well approximated by (Simons 2010)

$$\mathbf{Y}_L\mathbf{Y}_L^{\mathrm{T}} \approx \Delta\Omega^{-1}\mathbf{D}_L. \tag{6.28}$$

We also note via Eqs. (6.1) and (6.7) that

$$\mathbf{D}_L \to \mathbf{I} \quad \text{for} \quad \Theta \to 180^\circ \quad \text{or} \quad \Omega_0 \to \Omega, \tag{6.29}$$

where $\mathbf{I}$ is the $(L+1)^2 \times (L+1)^2$ unit matrix. When $L < L_g$, the estimate (6.26) contains *broadband leakage* (Simons & Dahlen 2006): high-degree signal contributions to the estimated low-degree coefficients. The broadband leakage is $\hat{\mathbf{w}}_L - \mathbf{w}_L$, which

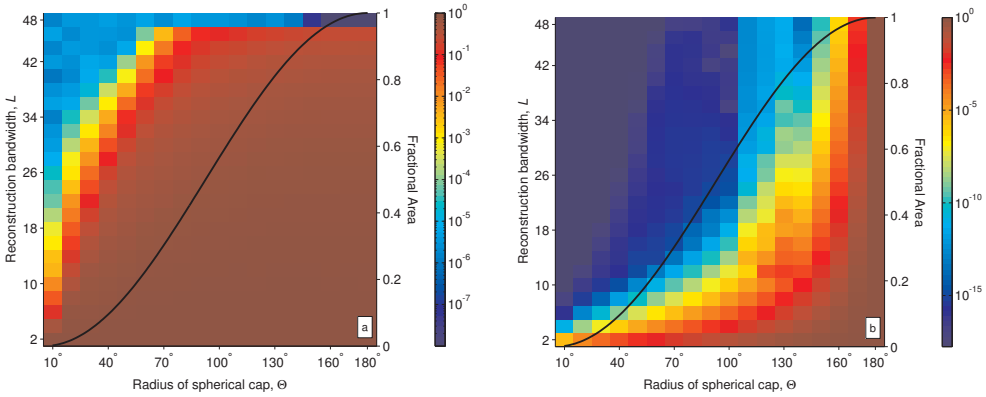

Figure 6.1: Reconstruction, via Eq. (6.33), of a $L_g = 48$ bandlimited white signal, as defined in Eqs. (6.20)–(6.21), from a set of observations made on a Fibonacci grid inside north-polar spherical caps of various radii Θ, for various spherical harmonic reconstruction bandwidths L. Fig. (a) shows the root mean square (rms) error normalized by the rms strength of the signal inside the cap. Note that the rms values are computed at points confined to the cap that are different from the data points. Fig. (b) shows the inverse of the condition number of the matrix $\mathbf{Y}_L$ in Eq. (6.25). The black curves and the markings on the right axes represent the fractional area of the spherical caps, $|\Omega_0|/(4\pi)$.

follows from

$$\begin{aligned}\hat{\mathbf{w}}_L &= (\mathbf{Y}_L\mathbf{Y}_L^{\mathsf{T}})^{-1}\mathbf{Y}_L(\mathbf{Y}_{L_g}^{\mathsf{T}}\mathbf{w}_{L_g}),\\ &= (\mathbf{Y}_L\mathbf{Y}_L^{\mathsf{T}})^{-1}\mathbf{Y}_L(\mathbf{Y}_L^{\mathsf{T}}\mathbf{w}_L + \mathbf{Y}_{\to L_g}^{\mathsf{T}}\mathbf{w}_{\to L_g}),\\ &= \mathbf{w}_L + (\mathbf{Y}_L\mathbf{Y}_L^{\mathsf{T}})^{-1}\mathbf{Y}_L\mathbf{Y}_{\to L_g}^{\mathsf{T}}\mathbf{w}_{\to L_g},\end{aligned} \tag{6.30}$$

where $\mathbf{Y}_{\to L_g}$ is the lower subblock of the matrix $\mathbf{Y}_{L_g}$ that complements $\mathbf{Y}_L$, and $\mathbf{w}_{\to L_g}$ is the lower subportion of $\mathbf{w}_{L_g}$, covering the degrees $L+1 \to L_g$. Hence, the broadband leakage is

$$\hat{\mathbf{w}}_L - \mathbf{w}_L = (\mathbf{Y}_L\mathbf{Y}_L^{\mathsf{T}})^{-1}\mathbf{Y}_L\mathbf{Y}_{\to L_g}^{\mathsf{T}}\mathbf{w}_{\to L_g}. \tag{6.31}$$

Via Eqs. (6.28)–(6.29) we deduce from (6.31) that

$$\hat{\mathbf{w}}_L - \mathbf{w}_L \approx \begin{cases} \Delta\Omega\,(\mathbf{Y}_L\mathbf{Y}_{\to L_g}^{\mathsf{T}})\mathbf{w}_{\to L_g} & \text{for } \Theta = 180^\circ,\\ \Delta\Omega\,\mathbf{D}_L^{-1}(\mathbf{Y}_L\mathbf{Y}_{\to L_g}^{\mathsf{T}})\mathbf{w}_{\to L_g} & \text{for } \Theta < 180^\circ. \end{cases} \tag{6.32}$$

Since the least-squares estimate $\hat{\mathbf{w}}_L$ for the case $\Theta < 180^\circ$ depends on the inverse of the localization kernel $\mathbf{D}_L$, the broadband leakage directly depends on the size and shape of the region of missing data, as well as on the bandwidth $L < L_g$ of the estimate. In the spatial domain, the broadband leakage generates a bias, which Simons & Dahlen (2006) refer to as *broadband bias*.

In practice, it is hard to find a stable inverse of $\mathbf{D}_L$, since for $\Omega_0 \subset \Omega$, the matrix $\mathbf{D}_L$ tends to be poorly conditioned. This problem can be solved either by utilizing a regularized least-squares approach or by using a truncated Slepian basis. The latter refers to a Slepian basis with less than $(L+1)^2$ basis functions, which improves the condition number of the normal matrix. The former may be obtained by a truncated singular value decomposition (SVD) of the matrix $\mathbf{Y}_L^{\mathrm{T}}$ (Xu 1998, Simons 2010). Here, we solve Eq. (6.25) as

$$\hat{\mathbf{w}}_L = \left(\mathbf{Y}_L^{\mathrm{T}}\right)^{+} \mathbf{w}, \tag{6.33}$$

where

$$\left(\mathbf{Y}_L^{\mathrm{T}}\right)^{+} = \mathbf{V}\mathbf{\Sigma}^{+}\mathbf{U}^{\mathrm{T}}, \tag{6.34}$$

and the truncation is accomplished via

$$\Sigma_{ii}^{+} = \begin{cases} \Sigma_{ii}^{-1} & \text{for } |\Sigma_{ii}| > \delta, \\ 0 & \text{otherwise.} \end{cases} \tag{6.35}$$

The singular value decomposition of matrix $\mathbf{Y}_L^{\mathrm{T}} = \mathbf{U}\mathbf{\Sigma}\mathbf{V}^{\mathrm{T}}$, $\delta = \varepsilon M \max(\Sigma_{ii})$, and ε is the machine epsilon. This is in fact implemented in Matlab's `pinv` routine (MATLAB 7.10.0.499, R2010a). Both the regularized least-squares approach and the truncated Slepian approach introduce a bias in the solution, but lower its variance if there is noise (Simons & Dahlen 2006). This so-called *truncation bias* is the third source of misfit in the approximation.

The propagation of errors in $\hat{\mathbf{w}}_L$ to the spatial domain for each combination of bandwidth L and cap size Θ is expressed in terms of the rms error (rmse), which is computed as the rms difference between the original signal and its least-squares estimate at a set of points inside Ω_0 that are different from the points used in the inversion. This metric, normalized by the rms signal, is shown as a function of Θ and L in Fig. 6.1a. For all spherical cap radii Θ the rmse decreases if the bandwidth L increases to meet the original L_g, to relative values on the order of 10^{-5} for radii $\Theta \ll 180^\circ$ and 10^{-14} for radii $\Theta \approx 180^\circ$. This decrease is in line with what we could expect, since increasing the bandwidth means that more basis functions are used to approximate the signal.

We derive insight into the behavior of the rmse shown in Fig. 6.1a via Fig. 6.1b which shows the inverse of the condition number (an estimate of the ratio of the largest to the smallest singular value) of $\mathbf{Y}_L$ as a function of Θ and L. For radii $\Theta \ll 180^\circ$ the condition number is very large and strong truncation (i.e., regularization) is required to solve Eq. (6.25). This explains why the normalized rmse does not drop below a value of about 10^{-5} for spherical cap radii significantly smaller than 180° even if a bandwidth $L = 48$ is chosen. It is the truncation bias that prevents a significantly

smaller rmse. Vice versa, for spherical cap radii close to 180°, the truncation bias is negligible, and the rmse is at the level of numerical round-off errors.

Fig. 6.1a also reveals that the rmse as a function of the bandwidth L drops more rapidly for smaller values of the spherical cap radius Θ (i.e. for smaller regions Ω_0). For example, when $\Theta = 10^\circ$ and $L = 22$, we achieve already a very small normalized rmse of 10^{-4}. For larger spherical cap radii, say, $\Theta > 90^\circ$, a similar reduction of the rmse can only be observed if $L = 48$ is chosen. In general, for large regions Ω_0, the rmse decreases very little if the bandwidth is increased, with an abrupt drop at the transition to full bandwidth.

Counter-intuitive is the behavior of the rmse as function of the spherical cap radius Θ for fixed degree L (cf. Fig. 6.1a). The smaller the spherical cap radius, the smaller the rmse. That is, the bandlimited signal (bandwidth $L = 48$) can be approximated very well by a low-degree ($L < 48$) spherical harmonic expansion provided that the data area is sufficiently small. For fixed degree L, the rmse *increases* with increasing size of the region Ω_0. This suggests that we have a considerable degree of freedom in fitting data from a high-bandwidth model, sampled inside a small region Ω_0, with a low-bandwidth approximation. The smaller the area is, the more freedom we have. This counter-intuitive result is further illustrated in Fig. 6.2. We observe that the least-squares approximation complete to degree and order L is closer to the original signal (complete to degree and order L_g) than the original signal truncated at degree L.

From this experiment, we conclude that if a spherical harmonic expansion is fitted to data given on a part of the sphere, the optimal bandwidth to carry out this procedure is no longer a measure for the spatial resolution of the data set. The smaller the area covered with data is, the larger the difference between the optimal bandwidth and the "true" bandwidth. In general, we can expect that the optimal bandwidth is always smaller than the "true" one.

Note that we would come to the same conclusion if we used an actual signal rather than white noise, data with much higher spatial resolution, a different data distribution rather than a Fibonacci grid or a different region rather than a spherical cap centred at the North Pole. The conclusion also does not change if we repeat the experiment on the circle using series expansions in Legendre polynomials.

The major implication for the main objective of this study (i.e., to get a MSL that is spectrally consistent with a given geoid) is that depending on how closely we want to represent the geoid within a region $\Omega_0 \subset \Omega$, a bandwidth L smaller than the nominal value L_g may be appropriate, depending on the size of the region. Hence, the bandwidth of the Slepian basis functions should be set equal to this optimal bandwidth L instead of the nominal bandwidth L_g. This is contrary to the approach of Albertella & Rummel (2009), who maintained L_g as the bandwidth. In practical applications, the choice of the optimal bandwidth L will also depend on the commission error. That is,

there is no need to obtain an "exact" representation of the given geoid in the presence of noise; any approximation will do as long as the approximation error is smaller than the commission error. This further reduces the optimal bandwidth L to the benefit of a reduced numerical complexity for the computation of the Slepian basis functions and the least-squares estimation of the Slepian basis function coefficients.

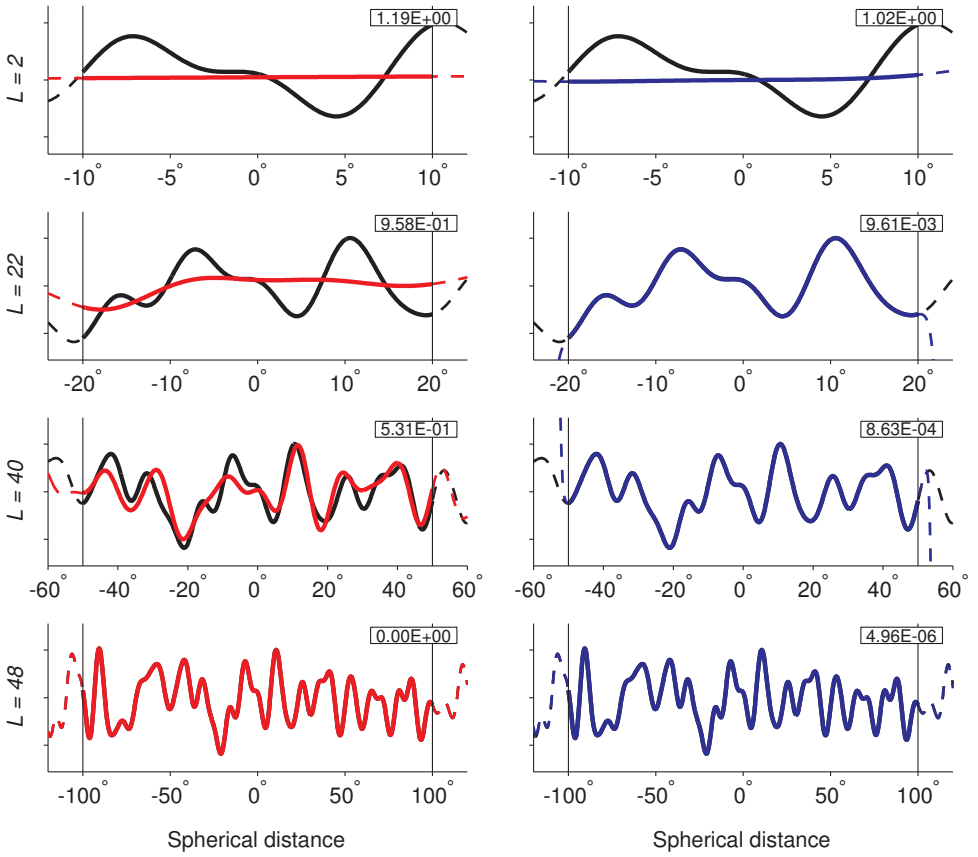

Figure 6.2: The original, bandlimited signal complete to degree 48 (black), the original signal truncated at degree L (red), and the least-squares estimate complete to degree L (blue) for a meridional arc crossing a spherical cap of radius Ψ. From top to bottom: $L = 2, \Psi = 10°$, $L = 22, \Psi = 20°$, $L = 40, \Psi = 50°$, and $L = 48, \Psi = 100°$. The thin black lines indicate the boundary of the spherical cap. Note that within the spherical cap no differences between the original signal and the least-squares approximation are visible for degrees $L \geq 22$. The labels indicate the rms error of the differences between the original, bandlimited signal complete to degree 48 on the one hand and the original signal truncated at degree L (left) or the least-squares approximation complete to degree L (right) on the other hand, normalized by the rms strength of the signal inside the cap.

Another implication of this experiment is that it will be very difficult, if not impossible, to extract a low-resolution signal from high-resolution data given on a part of the sphere. As pointed out before, if a low-resolution spherical harmonic expansion is fitted to data given on a part of the sphere by least-squares, the fit of the model to the data is optimized according to the least-squares principle. Hence, the coefficients representing the low-resolution approximation will explain as much of the signal as possible at the complete set of frequencies to minimize the residual sum of squares, and therefore will not provide a good representation of the true low-resolution signal. In Section 6.5, we investigate whether Slepian functions offer a solution to this problem and, if not, what the alternatives are.

6.4 Experimental setup

In this section, we discuss the setup of the numerical experiments related to the use of a Slepian basis to extract a low-resolution signal from high-resolution data given on a part of the sphere. This comprises the choice of the concentration region and the construction of the Slepian functions, the generation of the sampled geoid, the truncation level in the inversion, and the criteria we use to assess the quality of the results, which are to be presented in Section 6.5.

6.4.1 Concentration region

In the numerical experiments, we consider two concentration regions: (i) a spherical cap with radius 40° centred in the Pacific Ocean and (ii) the union of the world's ocean basins as defined next. Due to the non-polar orbits of all radar altimeter satellites, caps centered on both poles are left without data coverage and therefore are not part of the concentration region. For the TOPEX/POSEIDON (T/P) satellite, the radii of these polar gaps are approximately 24°. For other radar altimetry missions this radius may be smaller, but in our experiments we define Ω_0 as the part of the oceans covered by T/P, i.e:

$$\Omega_0 = \Omega - \bar{\Omega}_0, \tag{6.36}$$

where $\bar{\Omega}_0$ is the union of Eurasia, Africa, North and South America, Antarctica, Greenland, and Australia as defined and shown individually by Simons et al. (2006), Simons et al. (2009), and Simons (2010), with the subsequent addition of the islands New Guinea, Borneo, Madagascar, Sumatra, Honshu, the United Kingdom, and the further exclusion of the two polar gaps. The fractional area of this region on the unit sphere is $|\Omega_0|/(4\pi) \approx 0.67$. Because the bandwidths that we will use to construct the "true" MSL signal and its approximation are relatively small, all islands smaller than 200,000 km^2 are in fact neglected in the localization kernel $\mathbf{D}$. The latter is computed

as the difference of the localization kernel for the latitudinal belt exclusive those continents that are partly located inside the latitudinal belt minus the localization kernels for individual continental regions completely located inside the latitudinal belt.

Spatial expansions of some of the eigenfunctions of $\mathbf{D}$ that result from this procedure, for a bandwidth $L = 36$, are shown with their eigenvalues λ in Fig. 6.3. These are the Slepian functions that we will use as a spatiospectrally localized basis in the forthcoming analysis.

6.4.2 Construction of the sampled geoid and MSL signals

Samples of the geoid and MSL signals are derived from available spherical harmonic models. They are evaluated at a set of M points of a Fibonacci grid, which provides a homogeneous sampling of the region of interest, Ω_0. To avoid sampling errors, M is chosen sufficiently large so that the distance between the sample points does not exceed half of the shortest wavelength contained in the signal. The global geoid signal is derived from the Earth gravitational model EGM2008 (Pavlis et al. 2008, 2012) truncated at degree L_g. The MSL signal is defined as the sum of the MDT model DOT2008A (U.S. National Geospatial-Intelligence Agency EGM Development Team 2010) and the geoid model EGM2008, both truncated at degree L_r, where $L_r > L_g$. In the experiments of Section 6.5, we choose $L_r = 48$, $L_g = 36$, $M \approx 10,000$ (if no land data are used), and $M \approx 13,000$ (otherwise). The number of control points which are used to assess the quality of the various solutions is about $55,000$ randomly distributed over the target area Ω_0. The MSL that is spectrally consistent with the geoid is referred to as the "true" low-resolution MSL. It is defined as the sum of the DOT2008A MDT and the EGM2008 geoid both truncated at degree $L_g = 36$, as displayed in Fig. 6.4.

6.4.3 Optimal truncation level

To compute the MDT as the difference between the MSL (bandwidth L_r) and the geoid (bandwidth L_g) given on Ω_0, where $L_r > L_g$, we need to find a suitable representation of the MSL, which is spectrally consistent with the geoid signal. A Slepian basis with bandwidth L_g comprising $(L_g+1)^2$ basis functions provides such a representation. However, as mentioned in Section 6.2, the number of Slepian basis functions required to obtain a faithful approximation of a given signal on a subdomain of the sphere may be smaller than $(L_g+1)^2$. Simons & Dahlen (2006) have shown that in the presence of noise the optimal number of Slepian basis functions is determined by the signal-to-noise ratio of the data from which the expansion coefficients are derived by inversion, provided this is numerically feasible. In our experiments,

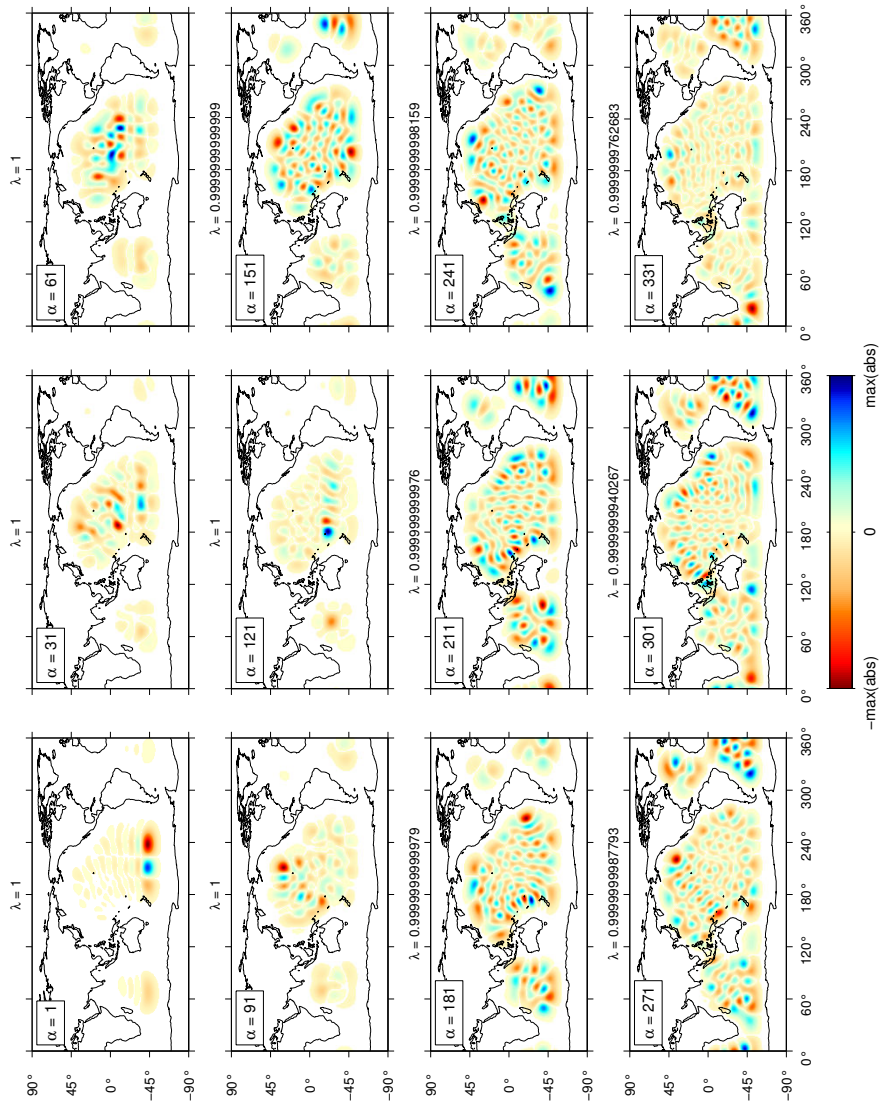

Figure 6.3: Slepian functions that are bandlimited to $L = 36$ but optimally concentrated within the oceanic concentration region Ω_0 as computed via Eqs. (6.4)–(6.7). We integrated Eq. (6.7) using Gauss-Legendre quadrature over the colatitudes and analytically over longitudes. A selection of eigenfunctions g_α is shown with their concentration factors λ_α, as labeled. The rounded Shannon number, from Eq. (6.14), is $K = 918$. Every function was normalized to max(abs(function)). Values smaller than 0.01 on this scale are rendered white. The sign of an eigenfunction is arbitrary since the concentration is quadratic. Altogether the Slepian functions form a complete basis for bandlimited processes anywhere on the sphere. The first K functions provide an approximate basis for bandlimited signals concentrated in the oceanic region Ω_0, as discussed in the text.

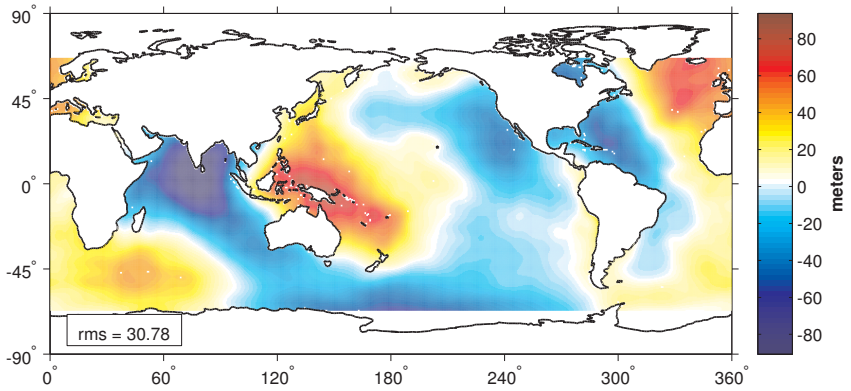

Figure 6.4: The "true" low-resolution MSL signal used in the experiments to be presented in Section 6.5. It is the sum of the EGM2008 geoid and the DOT2008A mean dynamic topography both truncated at degree 36.

however, the sampled geoid and MSL signals are assumed to be noise-free and numerical considerations do come into play. Therefore, we follow another strategy to determine the optimal truncation level $J_\circ$. We evaluate the spherical harmonic expansion of the "true" low-resolution MSL signal at the M points of the Fibonacci grid (these samples serve as data) and at a set of different control points which, however, both cover the target area Ω_0. Then, we fit a Slepian basis function representation comprising J basis functions to the data by least-squares. J is varied between the Shannon number K, defined in Eq. (6.14), and the maximum number of Slepian basis functions, $(L_g+1)^2$. The optimal number $J_\circ$ is found to be the one which minimizes the rms difference between the least-squares solution and the "true" low-resolution MSL signal evaluated at the control points. In the following, the above is referred to as "the Slepian approach", whether data are used on the entire globe Ω or on a subregion Ω_0 will be clear from the context.

6.4.4 Quality assessment

To assess the quality of the Slepian approach we first compute statistics of the differences with respect to the "true" low-resolution MSL as defined in Section 6.4.2. We also compare the estimated Slepian representation of the low-resolution MSL with a low-resolution MSL model obtained using the iterated spherical harmonic and Gaussian smoothing approach. The latter is reported by Albertella et al. (2008) as providing the best results in their experiments. This iterative spherical harmonic approach consists of five steps:

1. A global data set is formed using samples of the high-resolution MSL signal inside the region Ω_0 and samples of the low-resolution geoid in the complementary domain $\bar{\Omega}_0$.
2. A spherical harmonic analysis using the data from step 1 is performed complete to degree L_r.
3. The solution of step 2 is synthesized at the data points in the domain $\bar{\Omega}_0$ and a new data vector is formed.
4. Steps 2 and 3 are repeated until convergence to within error.
5. A Gaussian low-pass filter with half-width Ψ_o is applied to the final set of spherical harmonic coefficients to remove the contributions from the degrees $L_g + 1 \rightarrow L_r$ and to reduce ringing effects. In the experiments, we use an optimal half-width, Ψ_o, of the Gaussian filter, which is empirically derived by minimizing the rms difference between the “true" low-resolution MSL signal and the smoothed MSL signal inside the domain Ω_0.

6.5 Experimental results and discussion

We refer to Table 6.1 for an overview of the statistics of the differences between the “true” and the “approximated” low-resolution MSL signal. The computations in the Slepian basis have been done using open source software provided by F. J. Simons; see `http://www.frederik.net`.

6.5.1 Experiment I: the default case

In Experiment I, the concentration region Ω_0 is identical to the oceans as defined in Section 6.4.1. Fig. 6.5a shows the MSL in the band $37 \leq l \leq 48$, i.e., the difference between the “high-resolution” MSL signal and the “low-resolution” MSL signal. This is exactly the signal that we want to eliminate before computing a reliable MDT.

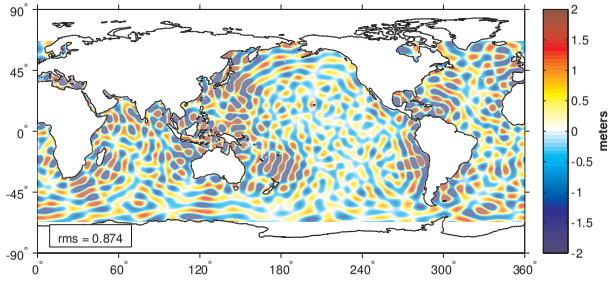

(a) Mean sea level (MSL) in the spherical harmonic band $37 \leq l \leq 48$.

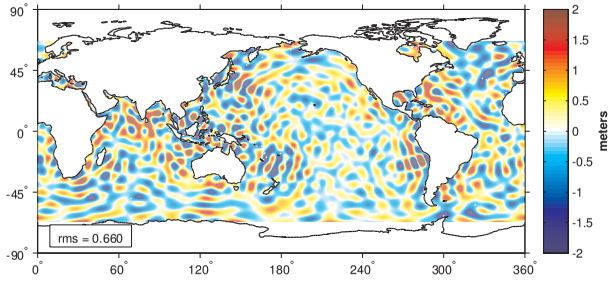

(b) Differences between the iterative spherical harmonic approximation to the low-resolution MSL, with geoid data over the continents and with Gaussian filtering, and the "true" low-resolution MSL shown in Fig. 6.4.

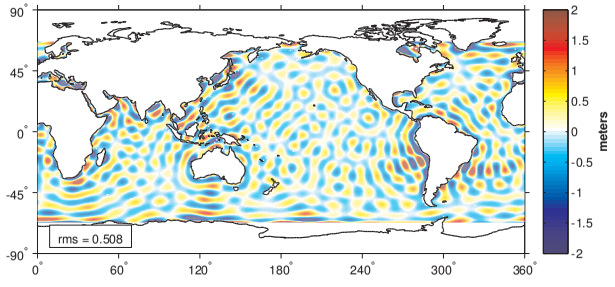

(c) Differences between the $1,180$-term Slepian approximation of the low-resolution MSL and the "true" low-resolution MSL shown in Fig. 6.4.

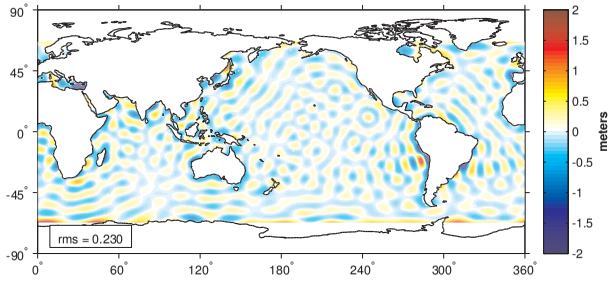

(d) Differences between the $1,322$-term Slepian approximation of the low-resolution MSL, obtained using geoid data on land, and the "true" low-resolution MSL shown in Fig. 6.4.

Figure 6.5: Differences between high-resolution and low-resolution mean sea level (MSL) (top panel) and the differences between the "true" low-resolution MSL and its various approximations.

Using the iterative spherical harmonic approach (with geoid data on land in the first iteration at step 1), 10,303 iterations are required to reduce the maximum absolute residue to 0.01 m. To extract the low-resolution MSL signal, we apply a Gaussian filter with $\Psi_o = 170$ km (cf. Section 6.4.4). Evaluated at a set of random locations, the rms approximation error equals 0.660 m; pointwise errors attain extreme values of several meters (see Table 6.1 for more statistics). Hence, the iterative spherical harmonic approach fails to provide a representation of the low-resolution MSL signal with an accuracy of a few centimeters. Fig. 6.5b shows a geographic map of the approximation errors. They strongly correlate with the MSL signal in the band $37 \leq l \leq 48$, Fig. 6.5a. This is mainly due to the weak performance of the Gaussian filter, which is unable to extract the low-resolution MSL signal from the high-resolution (bandwidth 48) least-squares solution. Too much signal from the band $37 \leq l \leq 48$ is left after filtering. This is confirmed by the rms difference between data and the approximated low-resolution MSL signal (last column of Table 6.1): the rms difference is 0.499 m, which is not close to the 0.874 m rms MSL signal in the band $37 \leq l \leq 48$, which indicates a leakage from the band $37 \leq l \leq 48$ into the low-resolution MSL solution.

Using the iterative spherical harmonic approach with geoid data on land but replacing the Gaussian filter with a boxcar low-pass filter in the frequency domain (i.e., hard truncation at degree $L_g = 36$) provides a much better approximation of the low-resolution MSL signal: the rms approximation error improves from 0.660 m to 0.071 m (cf. Table 6.1). A look at the rms difference between the data and the approximated low-resolution MSL signal confirms this result: it is 0.859 m, close to the 0.87 m rms MSL signal in the band $37 \leq l \leq 48$. Hence, almost no signal in the band $37 \leq l \leq 48$ leaks into the estimated coefficients. This is explained by the fact that Ω_0 covers about 67% of the whole sphere. The main error contributors are the geoid data on land, which are used to initially allow for a global spherical harmonic analysis. Although the rms approximation error is only 0.071 m, the maximum pointwise error is about 1 m, which is far above the target accuracy of a few centimeters. Finally, we will show in Section 6.5.3 that hard truncation performs very poorly if the size of Ω_0 is a much smaller fraction of the whole sphere than the entirety of the ocean basins. Therefore, an ideal low-pass filter cannot generally be the method of choice.

For the Slepian approach that uses only MSL data over the oceans, the rms approximation error of the low-resolution MSL signal is 0.508 m. A spatial rendition of the approximation errors is shown in Fig. 6.5c. This figure represents the optimal solution in the sense explained in Section 6.4.3 whereby $J_\circ = 1,180$ Slepian basis functions. The optimal bandwidth in the sense in which it appeared in Section 6.3 for the oceans is found to be $L = 36$ (i.e., identical to the maximum degree of the global geoid model), which corresponds to 1,369 basis functions and an rmse of 0.596 m (see Table 6.1). We explain the fact that less than the total number of Slepian basis functions provides the smallest rms approximation error by invoking the partial can-

Table 6.1: Experiment I: statistics of the differences between "true" and approximated low-resolution MSL signal, evaluated at a set of control points in the target area Ω_0 (columns 2–5) and the rms difference between data and approximated low-resolution MSL signal in the target area Ω_0 (column 6). $L_r = 48$, $L_g = 36$. The "true" low resolution MSL signal is the sum of the EGM2008 geoid and the DOT2008A mean dynamic topography both truncated at degree 36 (cf. Fig. 6.4). The domain Ω_0 comprises the world's oceans defined in Section 6.4.1. All values are provided in m.

Method	control points rms	min	max	mean	data points rms difference
Iterative SH, $L = L_r$, geoid data outside, Gaussian filter	0.660	-4.76	3.79	-0.017	0.499
Iterative SH, $L = L_r$, geoid data outside, ideal low-pass filter	0.071	-0.963	0.526	0.000	0.859
Direct SH, $L = L_r$, no data outside Ω_0, Gaussian filter	0.660	-4.76	3.79	-0.017	0.499
Direct SH, $L = L_r$, no data outside Ω_0, ideal low-pass filter	$2.71 \cdot 10^{-5}$	$-1.06 \cdot 10^{-4}$	$7.27 \cdot 10^{-5}$	$-2.27 \cdot 10^{-6}$	0.872
Direct SH, $L = L_g$, geoid data outside Ω_0	0.230	-1.50	2.96	0.016	0.773
Direct SH, $L = L_g$, no data outside Ω_0	0.596	-5.38	7.78	0.030	0.610
Slepian functions (bandwidth L_g), no data outside Ω_0, $J_o = 1,180$	0.508	-4.40	6.04	0.025	0.685
Slepian functions (bandwidth L_g), geoid data outside Ω_0, $J_o = 1,322$	0.230	-1.50	2.96	0.016	0.772
MSL signal in the band $37 \leq l \leq 48$	**0.874**	**-7.15**	**6.46**	**-0.040**	

cellation of truncation error and broadband bias. At 0.596 m the rms approximation error for 1,369 Slepian basis functions is only slightly higher than the 0.508 m obtained for $J_o = 1,180$ Slepian basis functions. A positive effect of using fewer Slepian basis functions is a significant improvement of the condition number of the normal matrix: from 10^8 (with 1,369 terms) to only 10 (with 1,180 terms).

The performance of the Slepian approach is not much better than for the iterative spherical harmonic approach (rms error of 0.508 m compared to 0.660 m). The reason for the poor performance of the Slepian approach is the presence of broadband leakage (frequency domain) and broadband bias (spatial domain). Though Slepian functions with the same bandwidth are orthogonal on Ω_0, this does not apply to Slepian functions of different bandwidths. The similarities between the error pattern shown in Fig. 6.5c (Slepian approach) and Fig. 6.5a (MSL signal in the band $37 \leq l \leq 48$) are evidence for the presence of broadband bias and leakage, as they were for the iterative spherical harmonic approach shown in Fig. 6.5b.

The quality of the Slepian approach improves if MSL data on the oceans are complemented by geoid data on land. Then, the solution with minimum rms approximation error is obtained with 1,322 Slepian basis functions. Fig. 6.5d shows a geographic map of the approximation errors in that case, whose rms approximation error has

been reduced from 0.508 m to 0.230 m. Note, however, that this approach is almost identical to a direct least-squares fit to the global data of a spherical harmonic model complete to degree 36 (rms error 0.230 m), which can be understood from the fact that almost all Slepian basis functions are used.

A simple alternative to the approaches discussed so far is a direct least-squares fit of a spherical harmonic expansion complete to degree $L_r = 48$ to the data (no data are used outside Ω_0) followed by a hard truncation at degree $L_g = 36$. The extreme values of the low-resolution MSL approximation error are $-1.06 \cdot 10^{-4}$ m and $7.27 \cdot 10^{-5}$ m, respectively, i.e., at the sub-millimeter level and the rmse is $2.71 \cdot 10^{-5}$ m (cf. Table 6.1). This approach performs by far the best for the current test setup. However, extensive simulations with different target areas Ω_0 and different bandwidths L_r (not shown here) reveal that the performance of this straightforward approach depends critically on (i) the size of the domain and (ii) the bandwidth of the signal. The smaller the domain, the larger the approximation error. Moreover, the larger the bandwidth and the smaller the target area, the larger the condition number of the normal matrix. Then, regularization is indispensable, which introduces an additional bias and reduces the quality of the solution. Therefore, this simple approach works for the oceans in combination with low-resolution MSL data as used here ($L_r = 48$), but fails for smaller target areas and/or MSL data with a higher resolution.

From the results shown in Table 6.1, we can also conclude that the iterative spherical harmonic approach does not depend on the data used on land provided that enough iterations are performed. This has been verified in several numerical simulations. In the limit, it is equivalent to a direct least-squares fit of a high-resolution spherical harmonic model (i.e., complete to degree $L_r = 48$) to the ocean data followed by Gaussian filtering in reaching an rmse of 0.660 m. Expressed differently, neither iteration nor information on land is needed to match the performance of the iterative spherical harmonic approach proposed by Albertella et al. (2008). From Table 6.1, we also conclude that the quality of the iterative spherical harmonic approach and the direct spherical harmonic approach that estimates coefficients complete to degree $L_r = 48$ is solely determined by the performance of the filter. A Gaussian filter is definitely not the preferred choice; we expect that the use of other filters may reduce the errors but will not reduce them down to the level of several centimeters.

6.5.2 Experiment II: a different cost function

Experiment I has demonstrated that the Slepian approach fails to recover the low-resolution MSL with adequate accuracy. This has been explained by broadband leakage and truncation bias. Trampert & Snieder (1996) have proposed a method to suppress leakage, which in fact uses a different cost function than the one being used in the classical least-squares solution. We start with Eq. (6.24), which we split into a

low-degree and a high-degree portion as

$$\mathbf{w} = \mathbf{Y}_{L_g}^{\mathsf{T}} \mathbf{w}_{L_g} = \mathbf{Y}_{L}^{\mathsf{T}} \mathbf{w}_{L} + \mathbf{Y}_{\to L_g}^{\mathsf{T}} \mathbf{w}_{\to L_g}. \tag{6.37}$$

Instead of using the functional model

$$\mathbf{w} = \mathbf{Y}_{L}^{\mathsf{T}} \mathbf{w}_{L} \tag{6.38}$$

in combination with the classical least-squares cost function

$$\Phi(\mathbf{w}) = (\mathbf{w} - \mathbf{Y}_{L}^{\mathsf{T}} \mathbf{w}_{L})^{\mathsf{T}} \mathbf{C}_{w}{}^{-1} (\mathbf{w} - \mathbf{Y}_{L}^{\mathsf{T}} \mathbf{w}_{L}), \tag{6.39}$$

where $\mathbf{C}_w$ is the data noise variance-covariance matrix, we use the cost function

$$\tilde{\Phi}(\mathbf{w}) = \mathbf{v}^{\mathsf{T}} \mathbf{C}_{w}{}^{-1} \mathbf{v} + \mathbf{w}_{L}^{\mathsf{T}} \mathbf{C}_{L}{}^{-1} \mathbf{w}_{L} + \mathbf{w}_{\to L_g}^{\mathsf{T}} \mathbf{C}_{\to L_g}{}^{-1} \mathbf{w}_{\to L_g}, \tag{6.40}$$

where

$$\mathbf{v} := \mathbf{w} - \mathbf{Y}_{L}^{\mathsf{T}} \mathbf{w}_{L} - \mathbf{Y}_{\to L_g}^{\mathsf{T}} \mathbf{w}_{\to L_g}. \tag{6.41}$$

Here, $\mathbf{C}_{L}{}^{-1}$ and $\mathbf{C}_{\to L_g}{}^{-1}$ define weight matrices in model (spectral) space. Minimizing $\tilde{\Phi}(\mathbf{w})$ gives

$$\hat{\mathbf{w}}_{L} = \left(\mathbf{Y}_{L} \mathbf{C}^{-1} \mathbf{Y}_{L}^{\mathsf{T}} + \mathbf{C}_{L}{}^{-1} \right)^{-1} \mathbf{Y}_{L} \mathbf{C}^{-1} \mathbf{w}, \tag{6.42}$$

with the data-space anti-leakage operator

$$\mathbf{C} = \mathbf{Y}_{\to L_g} \mathbf{C}_{\to L_g} \mathbf{Y}_{\to L_g}^{\mathsf{T}} + \mathbf{C}_{w}. \tag{6.43}$$

The advantage of the least-squares solution Eq. (6.42) is that it is not biased by $\mathbf{w}_{\to L_g}$ (Trampert & Snieder 1996).

To investigate the performance of the estimator Eq. (6.42), we use the same data as in Experiment I. We define diagonal covariance matrices in the spherical harmonic domain using Kaula's rule for degrees $l \geq 2$ and the mean variance per coefficient computed from the data for degrees 0 and 1. The diagonal covariance matrix $\mathbf{C}_L$ is propagated into the Slepian domain providing a full covariance matrix (cf. Eq. (6.40)). Numerical instabilities did not allow the computation of a solution for noiseless data. Therefore, zero-mean white noise with a standard deviation of 0.04 m was added to the data (0.04 is the accuracy we expect for MSL from radar altimetry, see e.g., Andersen & Knudsen 2009), and the correct noise-covariance matrix $\mathbf{C}_w$ was used.

Scaling factors for all three matrices were computed using variance component estimation (VCE). For the spherical harmonic approach, the estimated variance components are 0.99 for the data, 103.1 for the spherical harmonic coefficients complete to degree 36, and 201.6 for the spherical harmonic coefficients from degree $37 \leq l \leq 48$. For the Slepian approach, 1,346 basis functions gave the best solution. The corre-

sponding variance components are 0.99 for the data, $2.33 \cdot 10^4$ for the first 1,346 Slepian functions, $3.47 \cdot 10^7$ for the neglected, 23 Slepian functions, and 185.3 for the spherical harmonic coefficients from degree $37 \leq l \leq 48$. Nevertheless, the estimation of the parameters turned out to be very unstable, and the approximation errors are quite large. This can be explained by the fact that we were forced to ignore the correlations among the used and neglected basis functions.

For the direct spherical harmonic approach with geoid data on land this can be explained by the Gibbs effects along the boundary of the domain Ω_0. Note that for this particular experiment the total number of observations was reduced from 13,000 to 10,000 to be able to solve the system of equations. For the direct spherical harmonic approach with only MSL data, there is no straightforward explanation for the poor performance. It is not caused by leakage from the signal in the band $37 \leq l \leq 48$ into the low-resolution MSL solution as shown in the last column of Table 6.2: the rms of the residuals is close to the MSL signal in the bandwidth $37 \leq l \leq 48$. This is not in line with the findings of Trampert & Snieder (1996). We explain the discrepancy by the different set-up of our experiment compared with the experiment considered by Trampert & Snieder (1996). The latter is based on a (moderately) non-homogeneous, but global data distribution. The lack of data on land and in the polar regions as considered in our experiment is an example of an *extremely* non-homogeneous, global data distribution. Our experiment indicates that the method of Trampert & Snieder (1996) is not well suited for this type of data distribution. We conjecture that the method of Trampert & Snieder (1996) will always fail if the diameter of the area without data is large compared to the spatial resolution we aim at. A more precise analysis of the relation between approximation error, spatial resolution, and size of the data gaps requires further research and is beyond the scope of this study. We also tested different power laws to describe the signal behavior in the basis of spherical harmonics, but the quality of the results did not change significantly. We do wish to mention that when we repeated this experiment with $L_r = 18$ and $L_g = 12$, the method of Trampert & Snieder (1996) allowed us to *perfectly* recover the low-resolution MSL signal. No instabilities have been observed and we could also compute without problems a solution with noiseless data. This is in line with the results obtained with the experiment described in Section 6.3 (cf Fig. 6.1b): the condition number depends on the size of the domain Ω_0 *and* on the bandwidth. For a given domain Ω_0, the condition number increases exponentially with increasing bandwidth.

6.5.3 Experiment III: a smaller target domain

In Section 6.5.1, we found that a direct least-squares fit to data over all of the oceans of a spherical harmonic expansion complete to degree $L_r = 48$ allows an almost perfect recovery of the low-resolution (degree $L_g = 36$) MSL signal if an ideal low-pass filter in the frequency domain is applied. The question is whether this also applies

Table 6.2: Experiment II: statistics of the differences between "true" and approximated low-resolution MSL, evaluated at a set of control points and the rms of residuals. All solutions minimize the cost function Eq. (6.40). The "true" low resolution MSL signal is the sum of the EGM2008 geoid and the DOT2008A mean dynamic topography both truncated at degree 36 (cf. Fig. 6.4). The domain Ω_0 comprises the world's oceans defined in Section 6.4.1. All values are provided in m.

Method	control points rms	min	max	mean	data points rms difference
direct SH approach, cost function Eq. (6.40), noisy MSL data, no data on land	0.175	-1.26	1.05	-0.002	0.856
direct SH approach, cost function Eq. (6.40), noisy MSL data, geoid data on land	0.080	-0.671	0.446	0.003	0.875
Slepian approach, cost function Eq. (6.40), noisy MSL data, no data on land	0.262	-2.23	3.52	0.003	0.831
MSL signal in the band $37 \leq l \leq 48$	**0.874**	**-7.15**	**6.46**	**-0.040**	

to smaller areas. Furthermore, we found that for the oceans as target area, almost all Slepian basis functions are needed to obtain a good fit to the data. Using all $(L_g+1)^2$ Slepian functions, however, is equivalent with a spherical harmonic expansion complete to degree L_g. In that case, however, using a Slepian basis does not offer any advantage compared to spherical harmonics. Moreover, the condition number of the normal matrix increases exponentially with increasing bandwidth L_g both for Slepian functions and spherical harmonics, which makes regularization indispensable, at the cost of additional bias. If significantly less than $(L_g+1)^2$ Slepian functions allow a good least-squares fit to the data, this would reduce the computational costs compared to spherical harmonics and would also reduce the condition number, thus making regularization superfluous. To answer these questions, we repeat Experiment I with a smaller target domain Ω_0, which is now a spherical cap of radius 40° in the Pacific Ocean centered at 210° longitude and 5° southern latitude.

Table 6.3 summarizes the main results. First of all, we observe that a direct least-squares fit of a spherical harmonic expansion complete to degree $L_r = 48$ followed by a truncation at degree $L_g = 36$ now has an rms of 0.369 m and thus fails to recover the low-resolution MSL signal with an accuracy of a few centimeters. This is completely different from the results of Experiment I, but in line with what could be expected based on the experiment in Section 6.3. If the size of the domain Ω_0 decreases, the distribution of the energy over the spherical harmonic coefficients is no longer preserved because the spherical harmonics are not orthogonal over Ω_0. Therefore, a hard truncation of the expansion at degree L_g does not allow to recover the original spectrum at degrees $l \leq L_g$, which explains the poor performance of this approach for domains significantly smaller than the whole sphere. The fact that this method still performs better than the iterative spherical harmonic approach and the Slepian approach is due to the fact that a spherical cap of radius 40° is large enough to allow

Table 6.3: Experiment III: statistics of the differences between "true" and approximated low-resolution MSL signal, evaluated at a set of control points (columns 2–5) and the rms difference between the data and the approximated low-resolution MSL signal (column 6). $L_r = 48$, $L_g = 36$. The "true" low resolution MSL signal is the sum of the EGM2008 geoid and the DOT2008A mean dynamic topography both truncated at degree 36 (cf. Fig. 6.4). The domain Ω_0 is a spherical cap with radius 40°. All values are provided in m.

Method	control points rms	min	max	mean	data points rms difference
Iterative SH, $L = L_r$, geoid data outside, Gaussian filter	0.462	-1.66	2.14	0.006	0.317
Iterative SH, $L = L_r$, geoid data outside, ideal low-pass filter	0.153	-0.572	0.589	-0.001	0.525
Direct SH, $L = L_r$, no data outside Ω_0, Gaussian filter	0.462	-1.67	2.14	0.006	0.316
Direct SH, $L = L_r$, no data outside Ω_0, ideal low-pass filter	0.369	-1.37	1.35	0.000	0.637
Direct SH, $L = L_g$, no data outside Ω_0	0.342	-3.91	1.90	0.000	0.430
Slepian functions (bandwidth L_g), no data outside Ω_0, $J_o = 289$	0.499	-3.83	4.31	0.000	0.311
Slepian functions (bandwidth L_g), geoid data outside Ω_0, $J_o = 1,179$	0.342	-3.91	1.90	0.000	0.430
MSL signal in the band $37 \leq l \leq 48$	**0.874**	**-7.15**	**6.46**	**-0.040**	

for this. However, the performance of this approach will further decrease if the size of Ω_0 decreases.

When using Slepian functions, we obtain the lowest rms approximation error if significantly less than the total number of basis functions, which is $1,369$ for $L_g = 36$, are used. The optimal number of Slepian functions turned out to be 289 if only MSL data inside Ω_0 are used and $1,179$ if the MSL data are complemented by geoid data outside Ω_0. Note that the Shannon number of the 40° spherical cap is $K = 161$.

The attempted recovery of a signal complete to degree $L_g = 36$ on a spherical cap of radius 40° from data complete to degree $L_r = 48$ is an unstable problem no matter what basis functions are used and what approach is followed. Strong regularization was necessary in all cases to obtain a solution. We always used a truncated SVD for regularization, which may not be the optimal choice due to its global character. A better choice could be a regularization scheme which constrains the MSL variance over land as used by Kusche & Schrama (2005). The condition number will further increase if higher resolutions are aimed at, with the risk of a larger regularization bias, and, therefore, a reduced accuracy of the recovered low-resolution MSL signal. For completeness, we want to remark that also Experiment II has been executed for the spherical cap of 40° radius. However, the main conclusions are the same as for the world's oceans.

6.6 Reformulation and solution of the problem

So far we defined the MSL data on the domain Ω_0 in terms of a spherical harmonic expansion complete to degree L_r. The "true" low-resolution MSL signal on the domain Ω_0 has been identified with the same spherical harmonic expansion, but now truncated at degree $L_g < L_r$, where L_g is the maximum degree of the expansion of the global geoid in spherical harmonics. Several statistics of the differences between the methods designed to recover the low-resolution MSL signal from the MSL data inside Ω_0 were used to assess the quality of the solutions. We found that more or less all methods fail in the sense that pointwise errors exceed the level of several meters, whereas in practice we would like to recover the low-resolution MSL with errors comparable to the errors in the MSL data and the geoid model, which are at the level of a few centimeters.

This definition of the "true" low-resolution MSL signal is in line with what other authors also used in similar studies (e.g., Tapley et al. 2003, Albertella et al. 2008, Bingham et al. 2008). From the viewpoint of a "globalized" MSL signal (using geoid information on land) this may be justified. If, however, the MSL is considered to be signal which is only defined on a part of the sphere, this definition needs to be reconsidered as the results presented in Section 6.3 have shown. The reason is that on a domain smaller than the whole sphere, the degree of the spherical harmonic representation of a global signal is no longer a measure of its resolution. Usually, a spherical harmonic representation of a lower maximum degree is adequate to reproduce the data within acceptable error bounds. The smaller the size of Ω_0, the lower the maximum degree needed to represent a given signal.

Moreover, when we want to extract a low-resolution signal from high-resolution data given on a domain $\Omega_0 \subset \Omega$, we need to represent the data in a basis orthogonal on Ω_0. We also showed that not every orthogonal basis is equally well suited for this. In particular Slepian functions, which are designed to maximize the concentration of bandlimited functions in a spatial domain Ω_0, are not appropriate here, because every Slepian basis function depends on all spherical harmonics. According to Eq. (6.10), the transformation of a spherical harmonic basis (collected in a vector $\hat{\mathbf{y}}$) into the Slepian basis (collected in a vector $\mathbf{g}$) is given by

$$\mathbf{g} = \mathbf{Q}_\mathrm{S}\,\hat{\mathbf{y}}, \tag{6.44}$$

where the matrix $\mathbf{Q}_\mathrm{S}$ is a full unitary matrix. Hence, every Slepian basis function is a linear combination of *all* spherical harmonics up to the bandwidth L, and all basis functions have the same bandwidth, which is equal to the maximum degree of the spherical harmonic basis. This is why we cannot obtain a low-resolution approximation of a signal represented in a Slepian basis simply by a truncation of the Slepian representation. To obtain such an approximation requires the use of a Slepian

basis with a smaller bandwidth, which involves spherical harmonics of a lower maximum degree. These low-bandwidth Slepian functions are, however, not orthogonal to the Slepian functions representing the full signal. Moreover, the approximation of a high-resolution signal using a low-resolution (i.e., low bandwidth) Slepian basis always causes broadband leakage, which is another consequence of the fact that the Slepian transform matrix $\mathbf{Q}_S$ is a full matrix.

A suitable orthogonal basis on Ω_0 is found if the well-known Gram-Schmidt orthogonalization procedure is applied to spherical harmonics (e.g., Golub & Van Loan 1996). Let L be the maximum degree of the spherical harmonic expansion. Then, the new basis functions, which are orthogonal on Ω_0, are related to the spherical harmonics as

$$q_\alpha(\hat{\mathbf{x}}) = \sum_{l=0}^{L} \sum_{m=-l}^{l} q_{lm\alpha}\, \hat{Y}_{lm}(\hat{\mathbf{x}}), \quad \alpha = 1, \ldots, (L+1)^2, \tag{6.45}$$

where

$$q_{lm\alpha} = 0 \text{ for all } l \geq \alpha. \tag{6.46}$$

In matrix-vector notation, this is written as

$$\mathbf{q} = \mathbf{Q}_{\mathrm{GS}}\, \hat{\mathbf{y}}, \tag{6.47}$$

where, due to Eq. (6.46), $\mathbf{Q}_{\mathrm{GS}}$ is a lower triangular matrix. To compute the coefficients $\{q_{lm\alpha}\}$, we only need to compute the Cholesky decomposition of the Gram matrix of the basis functions $\{\hat{Y}_{lm}\}$, which is proportional to the matrix $\mathbf{D}$ from Eqs. (6.6)–(6.7), namely

$$\frac{1}{|\Omega_0|}\, \mathbf{D} = \mathbf{R}\mathbf{R}^{\mathrm{T}}. \tag{6.48}$$

Then,

$$\mathbf{Q}_{\mathrm{GS}} = \mathbf{R}^{-1}, \tag{6.49}$$

where $\mathbf{R}$ is the lower triangular Cholesky factor. A lower triangular matrix $\mathbf{Q}_{\mathrm{GS}}$ implies that a basis function q_α depends only on spherical harmonics of degree $0 \leq l \leq \alpha - 1$. This is a property Slepian basis functions do not possess (cf. Eq. (6.10)). It has an important practical implication for the problem at hand. Suppose the restriction of the geoid to Ω_0 is represented in terms of spherical harmonics complete to degree L (note that commonly $L < L_g$ as shown in Section 6.3, where L_g is the maximum degree of the *global* representation of the geoid in spherical harmonics). Then,

$$s^{(\mathrm{g})}(\hat{\mathbf{x}}) = \sum_{l=0}^{L_g} \sum_{m=-l}^{l} s^{(\mathrm{g})}_{lm}\, \hat{Y}_{lm}(\hat{\mathbf{x}}) = \sum_{\alpha=1}^{N} s^{(\mathrm{g})}_{\alpha}\, q_\alpha(\hat{\mathbf{x}}), \quad \hat{\mathbf{x}} \in \Omega_0,\ N = (L_g+1)^2. \tag{6.50}$$

In the same way, the MSL data can be written as

$$s^{(\mathrm{MSL})}(\hat{\mathbf{x}}) = \sum_{l=0}^{L_r} \sum_{m=-l}^{l} s_{lm}^{(\mathrm{MSL})} \hat{Y}_{lm}(\hat{\mathbf{x}}) = \sum_{\alpha=1}^{M} s_{\alpha}^{(\mathrm{MSL})} q_{\alpha}(\hat{\mathbf{x}}), \quad \hat{\mathbf{x}} \in \Omega_0,\ M = (L_r+1)^2. \tag{6.51}$$

Due to property (6.46), the low-resolution MSL signal that is spectrally consistent with the restriction of the geoid to Ω_0 is

$$s_{lr}^{(\mathrm{MSL})}(\hat{\mathbf{x}}) := \sum_{\alpha=1}^{N} s_{\alpha}^{(\mathrm{MSL})} q_{\alpha}(\hat{\mathbf{x}}), \quad \hat{\mathbf{x}} \in \Omega_0. \tag{6.52}$$

Hence, the MDT can be computed as

$$s^{(\mathrm{MDT})}(\hat{\mathbf{x}}) = s_{lr}^{(\mathrm{MSL})}(\hat{\mathbf{x}}) - s^{(\mathrm{g})}(\hat{\mathbf{x}}) = \sum_{\alpha=1}^{N} \left(s_{\alpha}^{(\mathrm{MSL})} - s_{\alpha}^{(\mathrm{g})} \right) q_{\alpha}(\hat{\mathbf{x}}), \quad \hat{\mathbf{x}} \in \Omega_0. \tag{6.53}$$

Note that the coefficients $\{s_{\alpha}^{(\mathrm{MSL})}\}$ can be computed from the given MSL data by least-squares. Compared to a least-squares fit of a Slepian representation, the least-squares fit of a representation in the basis $\{q_{\alpha}\}$ does not suffer from broadband leakage, which is a direct consequence of Eq. (6.46).

Table 6.4 shows the result of Experiment I (cf. Table 6.1) with the difference that now the "true" low-resolution MSL is defined in the basis $\{q_{\alpha}\}$ with $N = 1,369$. A geographical plot of the differences between the "true" low-resolution MSL signal of Fig. 6.4, which is used as reference in Table 6.1, and the "true" low-resolution MSL signal in the orthogonal basis $\{q_{\alpha}\}$, which is used as reference in Table 6.4, is shown in Fig. 6.6. Note that if Ω_0 is identical to the oceans as defined in Section 6.4.1, the restriction to Ω_0 of a global geoid model complete to degree 36 requires $(36+1)^2 = 1,396$ basis functions. That is why $N = 1,369$.

For most methods, the fit to the new low-resolution MSL signal $s_{lr}^{(\mathrm{MSL})}$, Eq. (6.52), is not better than to the low-resolution MSL signal used in Section 6.5 (compare Table 6.1 with Table 6.4). However, a direct least-squares fit of a spherical harmonic expansion complete to degree $L_g = 36$ to the MSL data provides an almost perfect fit to $s_{lr}^{(\mathrm{MSL})}$. The same is valid for a least-squares fit of 1,369 Slepian functions of bandwidth $L = 36$, because both solutions are equivalent. This surprising result implies that the unavoidable broadband leakage in the spherical harmonic solution and the Slepian solution, respectively, is negligible for the chosen experimental setup. That is, almost no signal from bandwidth $37 \leq l \leq 48$ leaks into the solution, though spherical harmonics are not orthogonal over Ω_0, and the Slepian solution suffers from broadband leakage as shown in Section 6.2. We suppose that this is due to the fact that in our experiment the "true" low-resolution MSL signal has a moderate maximum degree ($L_g = 36$) and, at the same time, the target area Ω_0 constitutes a sig-

nificant part of the whole sphere. We expect, however, that broadband leakage will become significant for higher spherical harmonic degrees L_g. The latter is relevant for practical applications, because state-of-the-art global geoid models based on data of the dedicated gravity missions CHAMP, GRACE, and GOCE will be complete to degree 200–250. Therefore, we expect that the direct least-squares fit of a spherical harmonic expansion complete to degree L_g and the equivalent Slepian approach using all $(L_g+1)^2$ basis functions do not provide an accurate enough approximation to the low-resolution MSL signal $s_{lr}^{(\mathrm{MSL})}$, Eq. (6.52), for spatial resolutions relevant in practical applications. Instead, the correct solution to the problem at hand needs to be

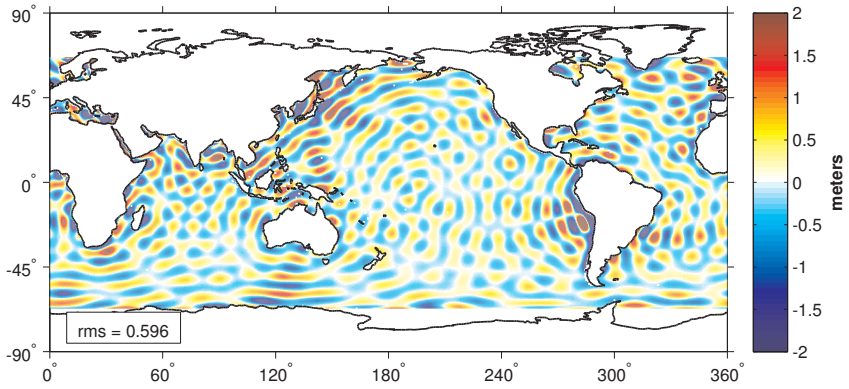

Figure 6.6: Difference between the "true" low-resolution MSL signal used in the experiments of Section 6.5 (cf. Fig. 6.4) and the "true" low-resolution MSL signal in the orthogonal basis $\{q_\alpha\}$.

found as follows: suppose (i) a global geoid model is given in terms of an expansion in spherical harmonics complete to degree L_g; (ii) MSL data are given on a region Ω_0; (iii) the resolution of the MSL data is higher than that of the geoid model. Then,

1. Synthesize geoid data on Ω_0 and compute a least-squares fit of a spherical harmonic expansion complete to degree L. The corresponding spherical harmonic coefficients are denoted $s_{lm}^{(\mathrm{g})}$. Usually, $L < L_g$, in particular for regions with $|\Omega_0| \ll 4\pi$ as found in Section 6.3. The choice of the maximum degree L depends on how well the model should fit the data. In practical applications this depends on the target accuracy of the MDT and/or the accuracy of geoid and MSL data. If the geoid is not given in terms of a spherical harmonic expansion, but as a set of scattered or gridded data, the spherical harmonic synthesis is dropped.
2. Compute the Gram matrix for the spherical harmonics complete to degree L, Eq. (6.48).
3. Compute the Cholesky decomposition of the Gram matrix: $\mathbf{R}\mathbf{R}^{\mathrm{T}}$.

4. Invert the lower triangular Cholesky factor: $\mathbf{Q}_{\mathrm{GS}} = \mathbf{R}^{-1}$.
5. Compute the $N = (L+1)^2$ orthogonal basis functions according to Eqs. (6.47) and (6.49).
6. Compute the N coefficients $s_\alpha^{(\mathrm{MSL})}$ by a least-squares fit to the given MSL data or by numerical integration.

The representation of the MDT is then given as

$$s^{(\mathrm{MDT})}(\hat{\mathbf{x}}) = \sum_{\alpha=1}^{N} s_\alpha^{(\mathrm{MSL})} q_\alpha(\hat{\mathbf{x}}) - \sum_{l=0}^{L} \sum_{m=-l}^{l} s_{lm}^{(\mathrm{g})} \hat{Y}_{lm}(\hat{\mathbf{x}}), \quad \hat{\mathbf{x}} \in \Omega_0. \tag{6.54}$$

Though the correct solution to the problem at hand has been found, the question is whether it is useful in practice. The latter means that it must be possible to construct the orthogonal basis $\{q_\alpha\}$ using Gram-Schmidt for practically relevant target regions Ω_0 and spatial resolutions. Unfortunately, several test computations reveal that the construction of the orthogonal basis fails already for moderate spatial resolutions and/or medium-size target regions Ω_0. For instance, for the oceans as defined in Section 6.4.1 we were able to construct the orthogonal basis $\{q_\alpha\}$ for a maximum degree 36. However, the Cholesky factorization could not be performed anymore for a maximum degree 48. Test computations for a spherical cap of radius 40° failed already for much lower maximum degrees. These problems related to the computation of the orthogonal basis are caused by the ill-conditioning of the Gram matrix, Eq. (6.48). The condition number of the Gram matrix grows exponentially with (i) the maximum degree L and (ii) the size of the target region Ω_0. The higher L and the smaller Ω_0, the larger the condition number. Therefore, for all practically relevant situations, we need to apply regularization to compute the Cholesky factor $\mathbf{R}$ and its inverse. We found, however, that even minimal regularization already destroys the orthogonality of the basis, and the approximation errors attain values of several meters or become even meaningless. Note that Hwang (1991) did extensive numerical experiments for the construction of an orthogonal basis for the oceans using Gram-Schmidt orthogonalization for spherical harmonics. However, successful computations of the basis functions are documented only up to a maximum degree 28.

6.7 Summary and conclusions

In this chapter, we investigated whether the use of bandlimited, spatially concentrated Slepian functions provide a low-resolution MSL signal that is spectrally consistent with a given geoid restricted to an incomplete part of the sphere. The recovered low-resolution MSL signal should have an accuracy that is comparable to the accuracy of the geoid and/or the MSL data, typically on the order of a few centimeters. In a

Table 6.4: Experiment I (repeated): statistics of the differences between "true" and approximated low-resolution MSL signal, evaluated at a set of control points (columns 2–5) and the rms difference between data and approximated low-resolution MSL signal (column 6). $L_r = 48$, $L_g = 36$. The "true" low-resolution MSL is defined in Eq. (6.52). The domain Ω_0 comprises the world's oceans defined in Section 6.4.1. All values are provided in m.

Method	control points rms	min	max	mean	data points rms difference
Iterative SH, $L = L_r$, geoid data outside, Gaussian filter	0.537	-7.23	4.08	-0.047	0.499
Iterative SH, $L = L_r$, geoid data outside, ideal low-pass filter	0.577	-7.67	5.34	-0.030	0.859
Direct SH, $L = L_r$, no data outside Ω_0, Gaussian filter	0.537	-7.14	4.10	-0.047	0.499
Direct SH, $L = L_r$, no data outside Ω_0, ideal low-pass filter	0.596	-7.78	5.38	-0.030	0.872
Direct SH, $L = L_g$, no data outside Ω_0	$1.40 \cdot 10^{-8}$	$-5.29 \cdot 10^{-8}$	$5.77 \cdot 10^{-8}$	$1.57 \cdot 10^{-9}$	0.610
Slepian functions (bandwidth L_g), no data outside Ω_0, $J_o = 1,369$	$1.20 \cdot 10^{-9}$	$-7.87 \cdot 10^{-9}$	$1.19 \cdot 10^{-8}$	$2.94 \cdot 10^{-11}$	0.685
Slepian functions (bandwidth L_g), geoid data outside Ω_0, $J_o = 1,322$	0.457	-6.49	4.48	-0.014	0.772
MSL signal in the band $37 \leq l \leq 48$	**0.874**	**-7.15**	**6.46**	**-0.040**	

number of numerical simulations, we quantified the errors of the Slepian approach and compared them with errors of alternative approaches suggested in the literature.

We showed that Slepian functions are not suited to provide a MSL signal that is spectrally consistent with a given geoid. Though they are orthogonal on the target domain, they lack the important property that the matrix, which transforms a spherical harmonic basis into the Slepian basis, is lower-triangular. Therefore, a least-squares fit of a truncated Slepian basis to given MSL data suffers from broadband leakage, hence, is unable to extract the low-resolution MSL signal with sufficient accuracy.

The iterative spherical harmonic approach proposed by Albertella et al. (2008) performs slightly worse than the Slepian approach, though the differences are not significant for practical applications. Moreover, we could show that this rather time consuming method is equivalent to a direct least-squares fit of a spherical harmonic representation to the given MSL data, which is numerically much easier to implement and less time-consuming.

Several variants of the iterative spherical harmonic approach and the Slepian approach do not provide significantly better results for the world's oceans.

We also showed that the definition of the "true" low-resolution MSL signal on a domain $\Omega_0 \subset \Omega$ requires some care. A reasonable definition requires an orthogonal basis on Ω_0, which is linked to the spherical harmonic basis by a lower-triangular matrix. Then, the "true" low-resolution MSL signal is a truncated version of the

series expansion of the MSL data in the orthogonal basis. This orthogonal basis can be constructed using Gram-Schmidt orthogonalization. In this study, we applied Gram-Schmidt to the spherical harmonics. We showed that the construction of the basis from spherical harmonics is a highly unstable problem in particular for small target areas and/or high-resolution geoid data. Consequently, the Gram-Schmidt orthogonalization for spherical harmonics breaks down already for geoid models of maximum degree, say, 48. The orthogonality of the constructed basis is very sensitive to any regularization, which implies that regularization is not a solution to the instability problem. Using 128 bit arithmetic may allow the Cholesky factorization for somehow higher maximum degrees, but will not be enough for the more recent high-resolution GRACE/GOCE-based geoid models. Whether the application of Gram-Schmidt to other basis functions allows the construction of an orthogonal basis for high-resolution geoid data remains to be investigated.

Chapter 7

Conclusions and recommendations

In this chapter, we answer the four research questions defined in Section 1.4, and we provide some recommendations for future research. Thereafter, we evaluate whether the main research objective defined in Section 1.4 has been achieved.

7.1 Vertical referencing of a shallow water model

The first research question defined in Section 1.4 was: *How can a shallow water model be vertically referenced to a given (quasi-)geoid and to which extent does such a model benefit from an improved (quasi-)geoid? What accuracy can be expected of the modeled instantaneous and mean dynamic topography?* This question is addressed in Chapter 3.

7.1.1 Conclusions

In this study, the vertical referencing of a shallow water hydrodynamic model (here we used the 2D Dutch Continental Shelf Model version 5 (DCSM)) is realized by prescribing water levels along the open sea boundaries referring to the quasi-geoid, which can be unambiguously realized only if all the relevant physics (astronomical tide, surge, and steric effects) is included. While in DCSM, so far, the forcing associated with horizontal variations in water density was neglected, DCSM is extended such that it includes this so-called "baroclinic forcing". This is done by adding the depth-averaged baroclinic pressure gradient terms in east-west and north-south directions as diagnostic variables. In this study, these are computed from temperature and salinity values derived from the Atlantic- European North West Shelf- Ocean Physics Hindcast obtained using the Proudman Oceanographic Laboratory (POL) 3D baroclinic model (POL's hindcast). The reason why we treat it as a diagnostic variable is

that in the North Sea the spatial variations in water density induce a 3D flow structure that cannot be handled by a 2D hydrodynamic model.

Theoretically, also the bathymetry used in the hydrodynamic model should be expressed relative with respect to the quasi-geoid. In the past, bathymetry was interpreted as given relative with respect to mean sea level (MSL). Hence, referring bathymetric data to the quasi-geoid reduces to the application of a correction for the separation between MSL and the quasi-geoid (i.e., the mean dynamic topography (MDT)). However, by a numerical experiment we showed that the errors in the used bathymetry introduced when using MSL rather than the quasi-geoid as the vertical datum have no significant impact on the modeled instantaneous water levels and the model-derived MDT.

The ability of the hydrodynamic model to reproduce both the MDT and the instantaneous water levels is assessed by a comparison with the MDT derived from POL's hindcast, as well as with instantaneous water levels acquired by various radar altimeter satellites. From this comparison, we conclude that our model-derived MDT is in good agreement with the MDT derived from POL's hindcast; the standard deviation of the differences is < 2 cm. Somehow, larger differences are observed when comparing the model-derived MDT with the MDT derived from radar altimeter data. They are attributed to either quasi-geoid errors or errors in the used salinity and temperature fields. The root mean square (rms) differences between observed and modeled instantaneous water levels over the whole model domain vary from 9–11 cm for data acquired by the TOPEX and GFO-1 satellites, respectively. Over the North Sea these numbers improve to 8–10 cm for data acquired by the TOPEX and ERS-2 satellites, respectively. These numbers are a factor two to three larger than the expected accuracy of water levels derived from radar altimeter data ~ 4 cm, (cf. Chelton et al. 2001, Sandwell & Smith 2009). About 25% of these differences can be explained by a bias between the modeled water levels and the observed water levels acquired during a single satellite pass. These biases are, among others, attributed to errors in the applied correction for the net steric expansion/contraction of the global oceans. This effect is not captured by DCSM that makes use of the Boussinesq approximation.

From the experiments, we conclude that the quasi-geoid is only weakly constrained by prescribed water levels along the open sea boundaries. Hence, if another quasi-geoid is chosen as reference surface, the water levels along the open sea boundaries change accordingly, but this change will not propagate much into the model domain. This suggests that from a model quality perspective the hydrodynamic model hardly benefits from an improved quasi-geoid. Note, however, that from this result we cannot conclude that an improved quasi-geoid does not provide any advantage. Indeed, the calibration of the extended DCSM using radar altimeter and quasi-geoid data over the model domain would benefit directly from an improved quasi-geoid. Fur-

thermore, the conclusion only applies to the current procedure used to vertically reference a shallow water hydrodynamic model.

7.1.2 Recommendations

Using the developed procedure to vertically reference a shallow water hydrodynamic model, the model hardly benefits from an improved quasi-geoid. Therefore, we recommend to **study whether the assimilation of instantaneous water levels into the hydrodynamic model improves the vertical referencing**. In this way, we might also be able to suppress errors in the modeled water levels associated with errors in the used salinity and temperature fields. The instantaneous water levels can be computed as differences between sea surface data from radar altimetry and a quasi-geoid model over the model domain and can directly be observed at the locations of the tide gauge stations. The assimilation could be realized using an ensemble Kalman filter (Evensen 1994, 2003); model parameters to be constrained could be identified by a sensitivity analysis.

To achieve further improvements in the representation of the instantaneous and mean dynamic topography by a hydrodynamic model, such as DCSM, we recommend to:

- **Use version 6 of DCSM (DCSMv6), which will become available soon.** Besides an increased spatial (especially in coastal waters) and temporal resolution, DCSMv6 includes more physics (e.g., internal tide) and covers a larger domain. Compared to DCSM version 5, Zijl & Gerritsen (2012) reported improvements of 60% for the tide, 24% for the surge, and 40% for the combined signal.
- **Use wind and mean sea level pressure fields of improved spatial resolution.** In this study, we used the fields provided by the reanalysis ERA-Interim that were originally publicly available with a spatial resolution of $1.5^\circ \times 1.5^\circ$. At this resolution, however, some significant variability of the wind fields in the North Sea (Cats & Wolters 1996) is not captured. An improved representation of the surge after increasing the spatial resolution of HiRLAM wind and mean sea level pressure fields from 55 to 22 km is reported by Verlaan et al. (2005). Hence, it is reasonable to expect improvements by replacing the ERA-Interim data with HiRLAM data (for operational storm surge forecasting, HiRLAM data are used that have a spatial resolution of 5–15 km).
- **Embed the DCSM model into a larger hydrodynamic model that includes the astronomical tide, atmospheric wind and pressure forcing, and baroclinic forcing.** An example of such a model is the POL 3D baroclinic model (Holt & James 2001, Holt et al. 2001), which is part of the POL Coastal Ocean Modeling System. Doing so will improve the current approach where the open

boundary conditions (instantaneous water levels expressed relative to the quasi-geoid) are derived as the sum of three separately derived contributions.

After realizing the above mentioned recommendations, it is worth to **investigate the feasibility to use the shallow water hydrodynamic model to connect the Wadden islands and offshore platforms to the terrestrial height system (NAP)**. Since the facilities to apply hydrostatic leveling are no longer available in the Netherlands, "2D-hydrodynamic leveling" might be used to transfer heights. Essentially, the idea is to use the hydrodynamic model to derive the slope of the MSL with respect to the quasi-geoid between (one or more) mainland tidal stations and island/platform tidal stations. After adding this slope to the NAP height of MSL at the mainland tidal station, we obtain the NAP height of the MSL at the island/platform tidal station(s). Here, for some "transects" a high accuracy can be expected due to foreseeable spatial error correlations of the model-derived MSL. This method might be used to validate results obtained with GPS/leveling or might be used in combination with GPS/leveling to increase the redundancy/accuracy.

7.2 Added value of a shallow water hydrodynamic model in quasi-geoid computations

The second research question defined in Section 1.4 was: *what is the added value of using a shallow-water hydrodynamic model for the reduction of radar altimeter SSHs to quasi-geoid heights when estimating a quasi-geoid for the Netherlands Continental Shelf?* This question is addressed in Chapter 4.

7.2.1 Conclusions

Based on the obtained differences among various quasi-geoids estimated after applying different sets of DT corrections to the observed SSHs, we conclude that if shipboard gravity data are included in the estimation, the added value of using a shallow water hydrodynamic model for the reduction of SSHs to quasi-geoid heights is negligible. This is explained by the fact that radar altimeter data hardly contribute at all to the estimated quasi-geoid. Except at some isolated spots along the coasts of Belgium, Denmark, France, Great Britain, and the Shetland Islands, and a feature along the Norwegian coast aligned with the Norwegian Trench, the differences are below ± 1 cm. Without shipboard gravity data the impact of DT corrections on the quasi-geoid is much larger. By a comparison of the quasi-geoids obtained with and without shipboard gravity data but after applying the same set of DT corrections, we conclude that systematic differences between the various quasi-geoids are reduced if we use a shallow water hydrodynamic model; especially along the coasts

of the Netherlands and Great Britain, and in the English Channel. This indicates that the consistency between the shipboard gravity and the altimeter-derived DoV data sets increases if the DT corrections are obtained from a shallow water hydrodynamic model. The improvements are mainly attributed to an improved representation of the tide by the shallow water hydrodynamic model; surge and steric components of the DT corrections have a negligible impact on the quasi-geoid.

7.2.2 Recommendations

To achieve a more accurate quasi-geoid, we recommend to:

- **Apply terrain corrections to the gravity data.** Investigations into the application of terrain corrections were outside the scope of this thesis. Therefore, the available terrestrial gravity anomalies were not used in the mountainous areas such as Norway and the UK. Instead, we used deflections of the vertical (DoV) in north and east directions derived from the European Gravimetric Geoid 2008 model (EGG08) (Section 4.3.6). Besides the fact that the use of these "pseudo-observations" is conceptually unsatisfactory, the radial basis functions (RBFs) still have problems in modeling the high-frequency signals in these data. Applying accurate, high-resolution terrain corrections will smooth the input data and hence improve their approximation by RBFs. This will also have an impact on the weights assigned to the various data sets, which are estimated using Monte-Carlo variance component estimation (MCVCE).
- **Combine the GRACE/GOCE satellite gravity data and the other data sets (airborne gravity, shipboard gravity, terrestrial gravity, and radar altimeter data) in a joint inversion.** In this study, we applied the classical remove-compute-restore technique, which is suboptimal from a statistical point of view as the available variance-covariance matrix of the satellite-only geopotential model is not used in the estimation process. A joint inversion of all data sets taking into account *all* available stochastic information is expected to provide more realistic weights of the data sets and help suppressing long-wavelength errors in some data sets.
- **Use more realistic noise models.** In this study, the variance-covariance matrices of all data sets used in the estimation of the quasi-geoid were assumed to be diagonal (except the GRACE/GOCE global geopotential model). For most data sets, however, the assumption of white noise is not realistic. For the altimeter-derived DoV, a better noise model can be derived using the noise power spectral densities (PSDs) estimated in this study. For the remaining data sets this will be more difficult. Probably the best we can do is to estimate a variance factor for each individual survey, instead of estimating one variance factor for the entire observation group.

- **Include the correlations between the successive DoV along the satellite's ground track.** Application of the two-point finite difference scheme to the profiles with geometric quasi-geoid heights causes correlations between the successive DoV. In this study, we neglected these correlations as the software cannot deal with full variance-covariance matrices. In a future work, they need to be included. To reduce the numerical complexity introduced when including the correlations, we can make use of the ideas in (Ditmar & Sluijs 2004).
- **Change the functional model of radar altimeter data.** In this study, we used DoV as the altimeter-derived data type. However, since the radar altimeters only provide discrete samples of the quasi-geoid, the DoV can only be approximately computed. Differenced geometric quasi-geoid heights are free from approximation. Hwang & Hsu (2008) have numerically shown that in deriving gravity anomalies from altimeter data the use of this data type compared to DoV and "height slopes" produces the best agreement with shipboard gravity anomalies.
- **Include CryoSat-2 and Jason-1 GM data.** The CryoSat-2 satellite, collecting data since July 2010, has a 369-day repeat cycle resulting in an average ground track spacing of 3.5 km at the equator (Wingham et al. 2006). In April 2012, the Jason-1 satellite was moved to a geodetic orbit (repeat cycle is 406 days). In a future work, these new GM data should be included, because their precision is better than the precision of the GEOSAT and ERS-1 GM data used in this study.
- **Use retracked radar altimeter data in the coastal waters.** In this study, we only had access to retracked GEOSAT GM data and retracked ERS-1 GM data over a part of the computational domain. To further reduce the data gaps along all coastlines and to enhance the quality of radar data in coastal waters, all available radar data in coastal waters need to be retracked using a coastal waveform retracking system (Gommenginger et al. 2011, and the studies cited therein).
- **Improve the reduction of noise in the altimeter-derived residual along-track DoV.** In this study, we applied a very moderate smoothing to the GM-derived residual along-track DoV using a simple Gaussian filter. The use of a more advanced filter is expected to further reduce the high-frequency noise in the altimeter-derived DoV, which in turn might increase the estimated (MCVCE) relative weight of this observation group compared to that of shipboard gravity data.
- **Include DoV derived from kinematic GNSS surveys in coastal regions.** Within a range of 20–25 km off the Dutch coast (and 5–10 km where retracked radar altimeter data are available), the missing radar altimeter data can be replaced by data from the regular kinematic GNSS surveys that are part

of the bathymetric surveys of the Hydrographic Service of the Royal Netherlands Navy, as well as a program of Rijkswaterstaat to monitor bathymetry and sediment transport in Dutch coastal waters. After correction for ship motions and the instantaneous dynamic topography, these data provide geometric quasi-geoid heights along the survey lines. Foster et al. (2009) have shown that instantaneous water levels can be measured with sub-decimeter precision for distances up to 200 km to the coast. Pineau-Guillou & Dorst (2011) showed that under optimal conditions and for shorter distances even 2 cm precision is achievable. This new data set, has not been utilized before in quasi-geoid computations. Therefore, it needs to be investigated whether this data set is consistent with the available shipboard gravity data in this area and whether inclusion of this data set improves the quasi-geoid.

7.3 Deriving LAT relative to the quasi-geoid

The third research question defined in Section 1.4 was: *how, and to which level of accuracy, can we derive the separation between the quasi-geoid and LAT from a shallow water hydrodynamic model?* This question is addressed in Chapter 5.

7.3.1 Conclusions

In this study, modeling the lowest astronomical tide (LAT) relative to the quasi-geoid is realized by (i) the explicit modeling of the average meteorological and steric conditions to which reference is made in the definition of LAT (International Hydrographic Organization 2011*a*, Technical Resolution 3/1919) and (ii) referencing the hydrodynamic model to the quasi-geoid. The explicit modeling of the average meteorological and steric conditions allows for the inclusion of temporal variations in the definition of the *average meteorological conditions*. In this study, we included seasonal variations, which are the most pronounced variations in MSL on time scales > 1 month in the North Sea.

The obtained LAT surface is validated using LAT values at 92 onshore and 10 offshore tide gauges. For the 92 onshore stations, we found a mean of 0.5 cm and a standard deviation of 21.5 cm. The obtained differences between observation- and model-derived LAT reveal a mixture of errors in both model and control data. We found that systematic errors in the representation of the tidal amplitude dominate. Using the standard deviation of the differences between observation- and model-derived tidal minima, we conducted a test to evaluate the statistical significance of the differences between the observation-derived LAT values and model-derived LAT values corrected for the mismodeling of the MDT and tidal amplitude. For three

stations, the observed differences are statistically significant at the 99% confidence level. These are located in the Irish Sea where DCSM is known to perform less.

7.3.2 Recommendations

To improve the accuracy of the model-derived LAT surface, besides the recommendations that follow from our work related to the first research question (Section 7.1.2), it is recommended to:

- **Assimilate tidal water levels at tide gauges and radar altimeter crossovers into the hydrodynamic model.** Current practice is to combine observation- and model-derived LAT values in a post-processing step using some kind of weighted interpolation scheme (e.g., Turner et al. 2010). In doing so, one needs to take care that this weighting scheme accounts for the fact that the measure of representativeness of observation-derived LAT values is strongly anisotropic; the weight assigned to these values is not only a function of the distance (even not if you make use of the concept of "sea distances" as in Turner et al. (2010)). In fact, the representativeness of observation-derived LAT values is determined by the tidal behavior in a particular area, which in turn depends on, e.g., the bathymetry and the bottom friction. By the assimilation of tidal water levels into the hydrodynamic model, this is implicitly taken into account.
- **Improve the reconstruction of tidal water levels from observed ones.** In this study, we did not an attempt to derive an optimal set of tidal constituents per tide gauge. Instead, we used two sets; one commonly used in the Netherlands, the other one commonly used in the UK. We found that, the use of these sets resulted in significant differences between the derived LAT values. In fact, however, a proper set of tidal constituents should be derived for each tide gauge.
- **Use a probabilistic approach to realize CD in the North Sea.** Besides the fact that such an approach contributes to the safety of navigation (if used, nautical maps provide more realistic estimates of the minimal water depths that can be expected), the obtained surface is much easier to validate since the validation becomes independent of, e.g., the used set of tidal constituents in the method to derive LAT values from observed water levels.
- **Use, simultaneously with the GNSS water level reduction method (Section 1.1), a vertically referenced shallow water hydrodynamic model to apply water level reduction.** Apart from using the vertically referenced shallow water hydrodynamic model to realize CD, it can be used as an independent method to obtain water depths relative to CD. Indeed, by subtracting the modeled instantaneous water levels from the observed water depths we obtain

water depths relative to the quasi-geoid. These depths can be reduced to CD as in the water level reduction with GNSS method. As such, it provides a backup system if GNSS fails or is not available. On the other hand, combining both approaches may further increase the accuracy of bathymetric surveys. Note that both methods are complementary; the accuracy of the water level reduction with GNSS is expected to increase towards the coast due to shorter distances to the reference stations, the model performance is likely to be reduced and vice versa.

7.4 Solving spectral inconsistencies using a Slepian basis

The fourth research question defined in Section 1.4 was: *does the use of a Slepian basis representation provides a solution of the spectral inconsistency between a high- (e.g., MSL) and low-resolution (e.g., geoid) data set?* This question is addressed in Chapter 6.

7.4.1 Conclusions

We conclude that a Slepian basis is not suited to make a high-resolution data set spectrally consistent with a given low-resolution data set. Though Slepian functions are orthogonal on the target domain, they lack the important property that the matrix, which transforms a spherical harmonic basis into the Slepian basis, is lower-triangular. Hence, every Slepian basis function depends on all spherical harmonics. Therefore, we cannot obtain a low-resolution approximation of a signal represented in a Slepian basis by a simple truncation of the Slepian representation. To obtain such an approximation, the use of a Slepian basis with a smaller bandwidth is required, which involves spherical harmonics of a lower maximum degree. These low-bandwidth Slepian functions are, however, not orthogonal to the Slepian functions representing the full signal. Moreover, the approximation of a high-resolution signal using a low-resolution (i.e., low bandwidth) Slepian basis always causes broadband leakage, which is another consequence of the fact that the Slepian transform matrix is a full matrix.

A suitable orthogonal basis on the target domain is found if the well-known Gram-Schmidt orthogonalization procedure is applied to spherical harmonics. However, its practical applicability is limited. Numerical experiments demonstrated that the construction of this basis from spherical harmonics is a highly unstable process in particular for small target areas and/or high-resolution data. Consequently, the Gram-Schmidt orthogonalization applied to spherical harmonics breaks down already for models of maximum degree, say, 48, which is far below the maximum degree needed

in today's applications. The orthogonality of the constructed basis is very sensitive to any regularization, which implies that regularization is not a solution to the instability problem.

7.4.2 Recommendations

So far, no proper solution to the spectral inconsistency problem is available that can be implemented in practice. Based on our findings with the Gram-Schmidt orthogonalization applied to spherical harmonics, we recommend to investigate whether the **application of Gram-Schmidt to other basis functions (e.g., piecewise polynomials) allows the construction of an orthogonal basis for high-resolution data**.

7.5 Did we achieve the research objective?

After answering the four research questions, we evaluate to which extent we achieved the main specific research objective defined in Section 1.4 as: *develop a procedure that enables to derive a consistent set of offshore vertical reference surfaces; a quasi-geoid based on, among others, radar altimeter data combined with a shallow water hydrodynamic model and LAT relative to this quasi-geoid, obtained using a shallow water hydrodynamic model*.

Bases on the work presented in this thesis, in particular our conclusion that the quasi-geoid is only weakly constrained by prescribed water levels along the open sea boundaries (Section 7.1.1), we conclude that the developed procedure only partly enables to achieve consistency among the target set of vertical reference frames (VRFs): the quasi-geoid and the LAT surface. In the remainder, we first consider what has been achieved, after which we will show in which respects no full consistency is achieved.

The main achievement is that the developed procedure allows to derive the separation between the LAT surface and the estimated quasi-geoid, which is achieved by the vertical referencing of the hydrodynamic model used to derive this separation. Furthermore, consistency is achieved by the fact that both in the estimation of the quasi-geoid and in the computation of the LAT surface the same hydrodynamic model is used. This implies that all signals introduced by different model representations of the tide, surge, and steric water level variations are avoided.

However, and here we come to the part where we will show in which respects no full consistency is achieved, the contribution of the hydrodynamic model to the realization of the various VRFs, and hence the propagation of model errors to the VRFs, differs. As we have seen, the contribution of the altimeter-derived along-track DoV to the quasi-geoid (the data which establishes a dependency between hydrodynamic

model and quasi-geoid) relies on the weight assigned to this observation group relative to, in particular, the one assigned to the shipboard gravity observation group. Consequently, any error in the representation of the MDT by DCSM that is propagated one-to-one to the model-derived LAT surface does not do this to the estimated quasi-geoid. The one-to-one propagation of errors in the representation of the MDT to the LAT surface is experimentally addressed in Section 5.3.2, where we showed that the non-linear interaction between tide and the *average* surge is small. This implies that the tidal and non-tidal contributions to the model-derived LAT values can be considered as approximately linearly additive. Expressed differently, the model-derived LAT values obtained without modeling the average meteorological and steric contributions (Section 5.3.1) can be approximated as the sum of the MDT values with the LAT values obtained when incorporating the average meteorological and steric contributions (Section 5.3.2). If the errors in the representation of the MDT by DCSM would also have been propagated one-to-one to the quasi-geoid, they would have canceled out in the computation of the ellipsoidal heights of LAT. This also applies if we compute the ellipsoidal heights of MSL as the sum of the estimated quasi-geoid and model-derived MDT. Indeed, if the errors propagated one-to-one to the quasi-geoid and we apply dynamic topography corrections to the observed SSHs that are too large, the resulting geometric quasi-geoid heights will be below the true quasi-geoid heights and vice versa. On the other hand, if the model-derived MDT is too large, the separation between the quasi-geoid and the LAT surface becomes too small and vice versa. Note that since in the estimation of the quasi-geoid radar altimeter data are used in the form of along-track DoV, a bias in the representation of the MDT does not cancel out in the computation of the ellipsoidal heights of LAT. However, as shown by the validation of the model-derived MDT (Section 3.6.1.3), the bias is small ($<$ 1 cm over DCSM's model domain).

Another aspect of consistency not achieved in this study, is the requirement that the quasi-geoid and the model-derived LAT and MDT surfaces should cover the same spectral range before the ellipsoidal heights of LAT and MSL, respectively, can be computed. To enforce this "spectral consistency", we tried the use of a Slepian basis representation as was recently proposed by Albertella & Rummel (2009). As shown in Chapter 6, the use of such a representation turns out to fail. Since the found solution cannot be implemented in practice for the data spatial resolutions at hand, no spectral consistency can be enforced. Nevertheless, although we lack numerical evidence, the errors associated with this inconsistency are expected to be low. The reason why we expect this is that the along-track resolution of radar altimeter data ($\sim$ 7 km) is more or less similar to the spatial resolution of DCSM version 5 (8×9 km).

Appendix A

On the use of free-air gravity anomalies

The free-air gravity anomaly (FAA), which is obtained from the various databases, is defined as the difference between the observed gravity taken on the Earth's surface (P), corrected for the height effect in free air, and the normal gravity taken on the computation point on the level ellipsoid (Q')

$$\Delta g_{\mathrm{FAA}} = g(P) - \alpha H - \gamma(Q'), \tag{A.1}$$

where H is the orthometric height of point P and

$$\alpha = -0.3086 \text{ mGal/m} \tag{A.2}$$

is a representative value of the free-air gravity gradient.

The surface gravity anomaly, which is used as data type in the functional model of the gravity data (Eq. (4.9)), is defined as

$$\Delta g = g(P) - \gamma(Q), \tag{A.3}$$

where Q is a point on the telluroid. The relationship between Δg_{FAA} and Δg can easily be established:

$$\gamma(Q) = \gamma(Q') + \left.\frac{\partial \gamma}{\partial h}\right|_{Q'} H_{\mathrm{N}} + O({H_{\mathrm{N}}}^2), \tag{A.4}$$

where H_{N} is the normal height of point P. Let $\beta := \frac{\partial \gamma}{\partial h}\big|_{Q'}$. Then,

$$\Delta g = g(P) - \gamma(Q') - \beta H_{\mathrm{N}} + O({H_{\mathrm{N}}}^2), \tag{A.5}$$

$$= \Delta g_{\mathrm{FAA}} + \alpha H - \beta H_{\mathrm{N}} + O({H_{\mathrm{N}}}^2), \tag{A.6}$$

$$= \Delta g_{\mathrm{FAA}} + \alpha H - \beta H + \beta H - \beta H_{\mathrm{N}} + O({H_{\mathrm{N}}}^2), \tag{A.7}$$

$$= \Delta g_{\mathrm{FAA}} + (\alpha - \beta) H + \beta (H - H_{\mathrm{N}}) + O({H_{\mathrm{N}}}^2). \tag{A.8}$$

The term $(\alpha - \beta)H$ is at most $1.6911 \cdot 10^{-9}$ mGal for $H = 2000$ m; the term $\beta(H - H_{\mathrm{N}})$ depends on the difference between the orthometric H and the normal height H_{N}, i.e., the separation between geoid and quasi-geoid. At sea, these differences can be neglected (Section 1.4). In the Alps, the differences between the geoid and quasi-geoid are only 30 cm at the highest summit (Flury & Rummel 2009). Hence, in this study $\beta(H - H_{\mathrm{N}})$ does not exceed 0.1 mGal, which is far below the accuracy of the FAA for the data sets used in this study.

Appendix B

Overview tide gauge data

Table B.1: Main characteristics of the tide gauge data used in this study.

Station	Cntry	Source	Data from/to	Sampl.	Vert. datum	Offshore	GPS
Nieuwpoort	BE	VH	Jan 1989–Jan 2004	01:00	TAW		
Oostende							
Zeebrugge							
A2			Feb 2000–Jan 2004	00:05		x	
Bol van Heist						x	
Scheur Wielingen						x	
Wandelaar						x	
Westhinder						x	
Havneby	DK	DCA	Jan 1985–Jan 2004	01:00	DVR90		
Hvide Sande							
Thorsminde							
Thyborøn							
Frederikshavn		DMI	Dec 1991–Jan 2004	01:00	DNN		
Hirtshals			Jan 1992–Jan 2004				
Højer/Vidåslusen			Oct 1989–Jan 2004				
Grenå		DMSA	Jan 1991–Jan 2004	00:15	DNN/DVR90		
Skagen			Dec 1991–Jan 2004				
Boulogne-sur-Mer	FR	SHOM	Jan 1984–Jan 2004	01:00	NGF-IGN69		x
Calais			May 1985–Jan 2004				x
Cherbourg			Jan 1984–Jan 2004				x
Dunkerque							x
Le Conquet							x
Le Havre			Jun 1984–Jan 2004				x
Roscoff			Jan 1984–Jan 2004				x
Saint-Malo			May 1986–Jan 2004				x
Borkum	DE	BSH	Jan 1985–Jan 2004	01:00	TGZ		x
Cuxhaven							x
Brouwershavense Gat 8			Jan 1985–Jan 2004	00:10	NAP		
Cadzand							
Delfzijl							

Continued on next page

Table B.1 – continued from previous page

Station	Cntry	Source	Data from/to	Sampl.	Vert. datum	Offshore	GPS
Den Helder			Jan 1985–Jan 2004				
Harlingen							
Haringvliet 10							
Hoek van Holland							
Huibertgat							
IJmuiden buitenhaven							x
Lauwersoog							
Nes							
Oudeschild							
Petten zuid							
Roompot buiten			Jan 1987–Jan 2004				
Scheveningen			Jan 1985–Jan 2004				
Schiermonnikoog							
Terschelling Noordzee			Mar 1989–Jan 2004				
Texel Noordzee			Jun 1989–Jan 2004				
Vlieland haven			Jan 1985–Jan 2004				
Vlissingen							x
Westkapelle							
West-Terschelling							x
Wierumergronden							
Aukfield platform	NL	RWS	May 1985–Jan 2004		MSL	x	
Euro platform			Jan 1985–Jul 2001			x	
K13a platform			Jan 1985–Jan 2004			x	
Lichteiland Goeree			Jan 1984–Jul 2001			x	
North Cormorant			Mar 1990–Nov 2001			x	
Helgeroa	NO	NHS	Dec 1987–Jan 2004	00:10	NN2000		
Oscarsborg			Sep 1990–Jan 2004				
Tregde			Dec 1987–Jan 2004				
Viker			Nov 1990–Jan 2004				
Göteborg-Torshamnen	SE	SMHI	Jan 1985–Jan 2004	01:00	RH 2000		
Kungsvik							
Ringhals							
Smögen							x
Viken							
Aberdeen	UK	NTSLF	Jan 1985–Jan 2004	00:15	OD (Newl.)		x
Barmouth			Oct 1991–May 2003				
Bournemouth			Jul 1996–Jan 2004				
Cromer			Mar 1988–Jan 2004				
Devonport			Sep 1987–Jan 2004				
Dover			Jan 1985–Jan 2004				x
Felixstowe			Apr 1986–Jan 2004				
Fishguard			Jul 1988–Jan 2004				
Heysham			Nov 1998–Jan 2004				
Hinkley Point			Jun 1990–Jan 2004				
Holyhead			Jan 1985–Jan 2004				
Ilfracombe							
Immingham			Nov 1996–Jan 2004				
Kinlochbervie			Jul 1991–Jan 2004				
Leith			Jan 1989–Jan 2004				
Lerwick (Shetland)			Jan 1985–Jan 2004				x
Liverpool, Gladst. Dock			Dec 1991–Jan 2004				
Llandudno			Jun 1994–Jan 2004				
Lowestoft			Jan 1985–Jan 2004				x
Milford Haven			Dec 1989–Jan 2004				

Continued on next page

Table B.1 – continued from previous page

Station	Cntry	Source	Data from/to	Sampl.	Vert. datum	Offshore	GPS
Millport			Jan 1985–Jan 2004				
Mumbles			Nov 1988–Jan 2004				
Newhaven			Jan 1985–Jan 2004				
Newlyn							x
Newport			Apr 1993–Jan 2004				
North Shields			Jan 1985–Jan 2004				x
Port Ellen			Jun 1991–Jan 2004				
Port Erin			Jun 1992–Jan 2004		OD (local)		
Portpatrick			Jan 1985–Jan 2004		OD (Newl.)		
Portsmouth			Feb 1991–Jan 2004				x
Sheerness			Jan 1985–Jan 2004				x
Stornoway			May 1985–Jan 2004				x
Tobermory			Jan 1990–Jun 2003				
Ullapool			Jan 1985–Jan 2004				
Weymouth			Feb 1991–Jan 2004				
Whitby			Jan 1985–Jan 2004				
Wick							
Workington			Feb 1992–Jan 2004				

VH: Vlaamse Hydrografie, Agentschap Maritieme Dienstverlening en Kust
DCA: Danish Coastal Authority
DMI: Danish Meteorological Institute
DMSA: Danish Maritime Safety Administration
SHOM: Service Hydrographique et Océanographique de la Marine
BSH: Bundesamt für Seeschifffahrt und Hydrographie
RWS: Rijkswaterstaat
NHS: Norwegian Hydrographic Service
SMHI: Swedish Meteorological and Hydrological Institute
NTSLF: National Tidal and Sea Level Facility

Appendix C

Validation of LAT using tide gauge data

Table C.1: Overview of differences between observation- and model-derived MDT and LAT values for each tide gauge, where column Mth. (Method) indicates which height transformation method is used (Section 5.2); column $\varepsilon_{\mathrm{MDT}}$ provides the differences between the observation-derived ($\overline{\zeta_{\mathrm{O}}}$) and model-derived ($\overline{\zeta_{\mathrm{D_{III}}}}$) MDT values; column Const. (Constituents) indicates which set of constituents is used, "S95" refers to the set of 95 constituents commonly used in the Netherlands while "S103" refers to the set of 103 constituents that are commonly used in de UK (Section 5.2); column $\varepsilon_{\mathrm{LAT}}$ provides the differences between the observation-derived ($\zeta^{\mathrm{L}}_{\mathrm{O}}$) and model-derived ($\zeta^{\mathrm{L}}_{\mathrm{D_{III}}}$) LAT values; column $t^{\mathrm{L}}_{\mathrm{O}}$ provides the time of the observation-derived LAT event; column $t^{\mathrm{L}}_{\mathrm{D_{III}}}$ provides the time of the model-derived LAT event; column rms 0 provides the rms differences between the observed water levels and the reconstructed tidal water levels; column rms 1 provides the rms differences between the observation- and model-derived tidal minima; column rms 1a provides the rms differences between the observation- and model-derived tidal minima after correction for the $\varepsilon_{\mathrm{MDT}}$; column $\varepsilon_{\mathrm{Amp}}$ provides the average differences between the observation- and model-derived tidal minima; column std 1 provides the standard deviation of the differences between the observation- and model-derived tidal minima; column Rej. indicates whether $\varepsilon_{\mathrm{LAT}} - \varepsilon_{\mathrm{MDT}} - \varepsilon_{\mathrm{Amp}}$ exceeds three times std 1; All values are provided in cm.

Station	Mth.	$\overline{\zeta_{\mathrm{O}}}$	$\varepsilon_{\mathrm{MDT}}$	Const.	$\zeta^{\mathrm{L}}_{\mathrm{O}}$	$\varepsilon_{\mathrm{LAT}}$	$\varepsilon_{\mathrm{LAT}} - \varepsilon_{\mathrm{MDT}}$	$t^{\mathrm{L}}_{\mathrm{O}}$	$t^{\mathrm{L}}_{\mathrm{D_{III}}}$	rms 0	rms 1	rms 1a	$\varepsilon_{\mathrm{Amp}} - \varepsilon_{\mathrm{MDT}}$	std 1	$\varepsilon_{\mathrm{LAT}} - \varepsilon_{\mathrm{Amp}}$	Rej.
Nieuwpoort	M_{II}	4.63	2.56	S103	-284.2	-0.82	-3.38	Mar 2002	Mar 1989	22.37	19.54	17.35	14.53	9.47	-17.91	
Oostende		2.41	0.18		-269.4	2.72	2.54	Mar 2002	Mar 1989	22.52	19.49	19.33	17.21	8.80	-14.67	
Zeebrugge		6.14	3.32		-241.1	18.37	15.05	Mar 2002	Mar 1989	23.31	26.88	23.76	22.16	8.57	-7.11	
A2		-6.65	-9.47	S95	-264.6	-5.09	4.38	Mar 1997	Mar 1989	21.35	8.28	13.73	11.08	8.12	-6.70	
Bol van Heist		13.78	11.36		-239.0	1.94	-9.42	Mar 1998	Mar 1989	22.50	17.18	10.96	2.04	10.77	-11.45	
Scheur Wielingen		8.92	6.49		-234.8	6.22	-0.27	Mar 1997	Mar 1989	22.62	17.06	12.45	7.25	10.12	-7.52	
Wandelaar		1.92	-0.35		-245.7	-1.99	-1.64	Mar 1997	Mar 1989	20.87	9.74	9.92	5.16	8.47	-6.80	
Westhinder		3.28	2.57		-256.3	-9.74	-12.31	Mar 1997	Mar 1989	18.83	9.83	9.14	1.24	9.06	-13.56	
Havneby	M_{II}	14.96	5.28	S103	-135.7	23.21	17.93	Apr 1998	Apr 2002	38.10	32.81	27.67	26.82	6.83	-8.89	
Hvide Sande		17.71	8.73		-53.8	3.59	-5.13	Apr 1998	Apr 2002	32.73	8.80	4.50	-1.09	4.36	-4.04	
Thorsminde		16.79	7.69		-35.9	13.63	5.93	Apr 1994	May 1986	31.50	12.47	6.22	3.75	4.97	2.19	
Thyborøn		13.27	4.04		-37.2	12.24	8.20	May 2000	May 1990	32.48	12.25	8.85	6.87	5.57	1.33	
Frederikshavn	M_{II}	14.02	5.05	S103	-19.1	11.85	6.81	Apr 1995	May 1988	19.06	6.43	6.01	-2.00	5.66	8.81	
Hirtshals		7.86	1.86		-24.2	19.05	17.19	Apr 1998	May 1988	22.28	10.21	8.69	6.76	5.47	10.43	
Højer/Vidåslusen		19.91	10.31		-87.2	67.02	56.71	Jun 1995	Apr 2002	37.31	58.27	48.22	46.73	11.92	9.99	
Grenå	M_{II}	15.63	1.76	S103	-21.0	15.70	13.93	Apr 1991	May 1988	21.32	10.21	8.81	6.66	5.77	7.27	
Skagen		7.35	1.79		-26.7	13.46	11.67	Apr 1995	May 1988	19.14	7.68	6.35	4.31	4.67	7.36	
Boulogne-sur-Mer	M_I	-7.26	-1.25	S95	-455.3	-8.85	-7.61	Mar 1998	Mar 1998	22.62	12.34	12.35	0.74	12.33	-8.35	
Calais		-6.94	-2.70		-377.9	-25.60	-22.89	Mar 1997	Mar 2002	21.45	14.56	13.41	-4.59	12.60	-18.31	
Cherbourg		-8.78	7.49	S103	-350.3	23.57	16.09	Mar 1997	Mar 1997	14.85	25.03	18.22	15.92	8.86	0.17	
Dunkerque		-2.21	-2.11	S95	-329.5	-24.42	-22.30	Mar 1997	Mar 1989	21.64	11.90	12.00	1.64	11.89	-23.94	
Le Conquet		-12.57	1.17	S103	-374.3	-32.96	-34.13	Mar 1997	Mar 1997	13.48	13.12	13.18	-1.28	13.12	-32.85	
Le Havre		-1.10	2.35		-457.4	-26.51	-28.86	Mar 1997	Mar 1997	17.63	12.11	11.31	2.79	10.96	-31.65	
Roscoff		-7.81	3.53		-505.0	-36.73	-40.26	Mar 1997	Mar 1997	13.75	14.44	15.89	-8.00	13.73	-32.26	
Saint-Malo		-2.11	11.15		-660.1	-21.10	-32.25	Mar 1997	Mar 1998	16.80	22.47	17.30	3.66	16.91	-35.91	

Continued on next page

Table C.1 – continued from previous page

Station	Mth.	$\overline{\zeta_O}$	ε_{MDT}	Const.	ζ_O^L	ε_{LAT}	$\varepsilon_{LAT} - \varepsilon_{MDT}$	t_O^L	$t_{D_{III}}^L$	rms 0	rms 1	rms 1a	$\varepsilon_{Amp} - \varepsilon_{MDT}$	std 1	$\varepsilon_{LAT} - \varepsilon_{Amp}$	Rej.
Borkum	M_I	-3.64	-9.04	S95	-168.1	-21.39	-12.35	Mar 1984	Apr 2003	31.96	10.46	8.63	2.60	8.23	-14.94	
Cuxhaven		13.38	1.33		-189.2	-14.04	-15.38	Mar 2001	Apr 2003	39.03	11.04	11.12	-1.38	11.04	-14.00	
Brouwershavense Gat 8	M_{II}	9.42	4.52	S95	-140.2	16.61	12.09	Mar 1989	Mar 1988	26.68	16.61	12.85	9.98	8.09	2.11	
Cadzand		7.71	5.28		-239.7	1.33	-3.95	Mar 1997	Mar 1989	24.65	11.53	8.92	2.40	8.59	-6.36	
Delfzijl		19.48	15.77		-207.1	-38.93	-54.70	Mar 1997	Apr 2003	34.29	16.87	29.92	-27.25	12.36	-27.45	
Den Helder		9.24	5.69		-112.2	19.60	13.91	Mar 1998	Apr 2003	27.22	20.65	15.78	12.76	9.29	1.16	
Harlingen		14.68	-0.06		-122.3	-19.06	-19.00	Apr 1998	Apr 2002	32.97	8.63	8.61	-3.66	7.79	-15.34	
Haringvliet 10		8.33	2.73		-113.5	19.90	17.17	Mar 1984	Feb 1988	24.19	16.84	14.49	12.05	8.06	5.12	
Hoek van Holland		19.05	12.05		-81.9	17.55	5.50	Jun 1995	Jun 1989	24.57	15.82	8.92	1.06	8.86	4.44	
Huibertgat		10.47	5.90	S103	-163.0	-17.06	-22.96	Apr 1998	Apr 2003	29.02	8.12	7.98	-2.77	7.49	-20.19	
IJmuiden buitenhaven	M_I	10.02	4.29	S95	-92.7	-0.10	-4.40	Jun 1995	May 1992	27.07	11.32	8.71	3.94	7.77	-8.34	
Lauwersoog	M_{II}	12.63	8.89		-159.9	6.34	-2.55	Apr 1998	Apr 2003	31.34	13.22	7.65	2.10	7.35	-4.64	
Nes		15.82	16.66		-158.5	-2.93	-19.59	Apr 1998	Apr 2003	30.69	15.71	8.42	-3.05	7.85	-16.54	
Oudeschild		12.09	8.41		-106.5	12.78	4.36	Mar 1998	Apr 1984	27.63	21.46	13.71	12.00	6.65	-7.63	
Petten zuid		10.89	6.92		-105.1	11.96	5.03	Mar 1984	Apr 1998	26.39	12.71	9.66	1.46	9.55	3.57	
Roompot buiten		9.16	4.87		-166.8	9.18	4.32	Mar 1989	Mar 1988	25.11	8.53	8.18	-1.84	7.97	6.16	
Scheveningen		11.74	5.80		-99.5	-8.86	-14.66	Jun 1995	May 1992	26.13	8.84	11.33	-7.23	8.73	-7.43	
Schiermonnikoog		13.67	9.11		-155.5	-12.40	-21.52	Apr 1998	Apr 2003	30.91	9.47	16.89	-15.29	7.18	-6.23	
Terschelling Noordzee		5.52	1.93		-147.9	-2.68	-4.61	Apr 1998	Apr 2003	25.96	6.70	5.89	1.67	5.65	-6.29	
Texel Noordzee		10.69	8.85		-131.0	16.76	7.91	Mar 1997	Apr 2003	25.58	22.14	14.06	12.10	7.16	-4.19	
Vlieland haven		7.04	3.09	S103	-139.8	-3.43	-6.52	Mar 1998	Apr 2003	26.43	12.26	9.66	7.66	5.89	-14.18	
Vlissingen	M_I	6.12	2.42	S95	-235.3	-10.07	-12.49	Mar 1997	Mar 1989	25.55	14.30	12.68	7.78	10.02	-20.27	
Westkapelle	M_{II}	8.55	5.28		-207.3	9.84	4.56	Mar 1997	Mar 1989	24.44	14.21	10.37	6.30	8.23	-1.74	
West-Terschelling	M_I	3.26	-0.68	S103	-134.3	2.12	2.80	Apr 1998	Apr 2003	27.72	17.80	18.45	17.46	5.97	-14.66	
Wierumergronden	M_{II}	13.81	9.56	S95	-137.5	12.08	2.52	Apr 1998	Apr 2003	27.35	15.66	7.86	4.82	6.21	-2.30	
Aukfield platform	M_{IV}	-5.18	0.72	S103	-89.6	-2.13	-2.85	Aug 1992	Apr 2003	19.50	3.95	3.99	-0.58	3.94	-2.27	
Euro platform		3.06	1.73	S95	-107.0	5.03	3.31	Jun 1987	Feb 1988	22.19	8.39	7.51	3.16	6.81	0.14	
K13a platform		-2.18	0.06	S103	-110.6	5.33	5.27	Mar 1998	Mar 2002	21.86	8.54	8.48	6.97	4.84	-1.70	
Lichteiland Goeree		3.25	0.21	S95	-110.8	13.78	13.57	Feb 1984	Feb 1988	24.08	12.23	12.06	9.23	7.77	4.34	
North Cormorant		-10.81	-2.46	S103	-122.1	-15.13	-12.66	Aug 1988	Apr 2003	19.95	6.97	5.75	-1.93	5.42	-10.73	
Helgeroa	M_{II}	9.57	-0.06	S103	-22.4	11.10	11.15	Apr 1991	May 1988	17.74	8.15	8.20	7.21	3.91	3.94	
Oscarsborg		10.47	-3.70		-25.0	24.03	27.72	Apr 1996	May 1986	21.33	11.35	14.44	12.62	7.01	15.11	
Tregde		2.01	-2.47		-25.2	5.10	7.56	Apr 1991	May 1988	13.87	6.00	8.04	7.04	3.89	0.52	
Viker		5.01	-8.10		-27.3	6.80	14.90	Apr 1991	Apr 1987	20.06	4.68	9.87	8.71	4.64	6.19	
Göteborg-Torshamnen	M_{III}	17.15	2.74	S103	-8.3	3.48	0.74	Apr 1991	Apr 2002	19.33	6.93	4.93	2.97	3.93	-2.23	
Kungsvik		8.74	-3.42		-42.9	-8.55	-5.13	Apr 1991	May 1988	20.82	13.20	10.13	-8.78	5.06	3.65	
Ringhals		16.05	1.36		-4.6	13.41	12.05	Apr 1991	May 1989	18.83	8.33	7.52	4.03	6.35	8.02	
Smögen	M_I	4.32	-7.94		-13.8	15.22	23.16	Apr 1987	May 1988	19.37	14.36	22.05	21.61	4.37	1.54	
Viken	M_{III}	15.53	-3.74		-10.6	22.36	26.10	Apr 1991	May 1988	18.92	12.16	15.25	13.23	7.60	12.87	
Aberdeen	M_I	-2.26	-0.64	S103	-242.2	13.52	14.16	Mar 2002	Mar 2002	15.08	16.02	16.60	15.18	6.72	-1.01	
Barmouth	M_{II}	4.01	7.54		-239.9	-6.22	-13.76	Mar 1984	Mar 2002	20.29	11.33	17.37	-15.25	8.32	1.48	
Bournemouth		1.91	11.12	S95	-153.6	4.13	-6.99	Mar 1997	Mar 1984	13.59	9.76	7.21	-3.62	6.24	-3.37	
Cromer		-8.98	-3.35	S103	-292.3	-14.91	-11.56	Mar 1984	Mar 1984	22.84	9.14	9.25	1.98	9.03	-13.54	
Devonport		-3.60	4.57		-330.5	-13.31	-17.88	Mar 1998	Mar 1998	13.99	13.58	10.47	5.90	8.64	-23.78	

Continued on next page

Table C.1 – continued from previous page

Station	Mth.	$\overline{\zeta_O}$	ε_{MDT}	Const.	ζ_O^L	ε_{LAT}	$\varepsilon_{LAT} - \varepsilon_{MDT}$	t_O^L	$t_{D_{III}}^L$	rms 0	rms 1	rms 1a	$\varepsilon_{Amp} - \varepsilon_{MDT}$	std 1	$\varepsilon_{LAT} - \varepsilon_{Amp}$	Rej.
Dover	M_I	-11.51	-4.88		-355.5	-9.77	-4.89	Mar 2002	Mar 1993	18.55	15.44	19.40	16.55	10.12	-21.44	
Felixstowe	M_{II}	-4.67	-1.20		-213.2	7.37	8.57	Mar 1984	Mar 1989	21.11	13.80	14.85	13.17	6.86	-4.60	
Fishguard		9.87	19.22		-238.6	15.81	-3.41	Mar 1984	Mar 1998	15.06	28.52	11.01	8.39	7.13	-11.80	
Heysham		4.27	5.41		-500.8	-49.66	-55.07	Mar 1984	Mar 1998	22.50	17.07	20.80	-15.75	13.58	-39.31	
Hinkley Point		18.16	19.56		-626.0	23.40	3.85	Mar 1998	Mar 1998	20.15	49.32	31.98	26.25	18.26	-22.41	
Holyhead		-8.65	3.88		-336.7	-16.06	-19.94	Mar 2002	Mar 1998	16.32	11.79	9.42	4.56	8.24	-24.50	
Ilfracombe		-6.50	3.49		-513.2	-14.73	-18.22	Mar 1998	Mar 1998	15.50	14.72	12.80	5.81	11.41	-24.03	
Immingham		2.09	8.68		-399.2	-43.14	-51.81	Mar 1984	Mar 1984	19.14	28.27	36.42	-34.73	10.96	-17.08	
Kinlochbervie		8.61	6.20		-282.6	6.21	0.01	Apr 1985	Apr 1985	19.07	12.59	8.85	3.37	8.19	-3.36	
Leith		1.08	-0.89		-328.3	-30.78	-29.89	Mar 1984	Mar 1984	15.61	18.69	18.16	-10.67	14.69	-19.22	
Lerwick (Shetland)	M_I	-15.53	-9.49		-128.4	-6.93	2.56	Mar 2002	Mar 2002	14.12	5.57	9.66	8.03	5.37	-5.47	
Liverpool, Gladst. Dock	M_{II}	5.13	8.32		-520.3	-66.21	-74.53	Mar 1984	Mar 1998	20.59	19.90	25.97	-20.89	15.43	-53.64	x
Llandudno		-7.22	-1.51		-455.8	-51.67	-50.16	Mar 1984	Mar 1998	18.18	17.73	16.67	-11.32	12.23	-38.84	x
Lowestoft	M_I	-9.23	-4.51		-156.2	9.07	13.58	Mar 1984	Mar 1984	21.46	16.26	20.35	18.85	7.68	-5.27	
Milford Haven	M_{II}	-8.83	1.89		-396.1	-13.77	-15.66	Mar 1998	Mar 1998	15.47	10.03	9.08	3.83	8.23	-19.49	
Millport		11.25	9.41		-193.0	58.91	49.50	Mar 1998	Mar 1998	20.51	63.30	54.10	52.72	12.13	-3.22	
Mumbles		4.80	10.69		-505.2	-1.21	-11.90	Mar 1998	Mar 1998	17.29	21.18	13.45	7.17	11.39	-19.07	
Newhaven		1.05	7.79		-348.9	6.47	-1.32	Mar 1997	Mar 1997	14.46	17.17	11.23	6.93	8.84	-8.25	
Newlyn	M_I	-12.79	-3.07		-306.3	-12.31	-9.23	Mar 1997	Mar 1997	13.40	11.99	14.45	12.14	7.85	-21.37	
Newport	M_{II}	11.04	11.78	S95	-674.4	13.68	1.90	Mar 1997	Mar 1998	25.42	37.38	29.41	16.69	24.22	-14.79	
North Shields	M_I	-8.97	-6.32	S103	-294.3	2.75	9.07	Mar 1984	Mar 1984	16.10	11.10	16.07	13.85	8.16	-4.78	
Port Ellen	M_{II}	-1.38	-0.40		-76.4	-12.41	-12.01	Aug 1991	Apr 1994	19.03	16.82	17.09	11.64	12.52	-23.65	
Port Erin		14.31	16.99		-298.2	-7.45	-24.44	Mar 1984	Mar 2002	17.38	19.26	8.18	0.45	8.16	-24.89	x
Portpatrick		3.90	5.69		-217.8	20.72	15.03	Mar 1998	Mar 2002	18.47	33.24	27.77	26.47	8.40	-11.44	
Portsmouth	M_I	-4.61	5.56		-266.0	19.77	14.22	Mar 1998	Mar 1997	14.72	24.36	19.12	17.72	7.19	-3.50	
Sheerness		-6.43	-1.90	S95	-293.7	-9.69	-7.79	Mar 1997	Mar 1989	23.34	9.59	10.01	3.10	9.51	-10.89	
Stornoway		-6.68	-7.71	S103	-281.6	13.41	21.12	Mar 2002	Apr 1985	16.58	17.48	24.42	22.74	8.91	-1.63	
Tobermory	M_{II}	-2.53	-3.31		-258.0	7.61	10.92	Mar 1993	Mar 1998	18.07	16.38	19.16	16.58	9.60	-5.66	
Ullapool		9.06	6.22		-298.4	5.80	-0.42	Mar 1998	Apr 1985	18.52	13.61	10.77	2.45	10.49	-2.87	
Weymouth		4.27	14.02	S95	-135.6	47.53	33.50	Mar 2002	Mar 1993	13.64	55.09	41.54	39.67	12.33	-6.17	
Whitby		-1.23	2.24	S103	-317.5	-4.96	-7.19	Mar 1984	Mar 1984	17.78	8.17	8.15	-1.03	8.08	-6.16	
Wick		-2.43	-1.81		-203.1	19.21	21.02	Mar 2002	Mar 2002	16.02	17.33	18.94	17.07	8.21	3.95	
Workington		14.82	15.47		-432.5	-11.07	-26.53	Mar 1998	Mar 1998	22.03	22.35	11.29	4.30	10.44	-30.83	

Bibliography

Akima, H. (1972), 'Algorithm 433: interpolation and smooth curve fitting based on local procedures [E2]', *Commun. ACM* **15**(10), 914–918.

Albertella, A. & Rummel, R. (2009), 'On the spectral consistency of the altimetric ocean and geoid surface: a one-dimensional example', *J. Geod.* **83**(9), 805–815.

Albertella, A., Sansò, F. & Sneeuw, N. (1999), 'Band-limited functions on a bounded spherical domain: the Slepian problem on the sphere', *J. Geod.* **73**(9), 436–447.

Albertella, A., Savcenko, R., Bosch, W. & Rummel, R. (2008), Dynamic Ocean Topography – The Geodetic Approach, Technical Report 27, Institut für Astronomische und Physikalische Geodäsie, Forschungseinrichtung Satellitengeodäsie, München.

Alberts, B. A. (2009), Regional gravity field modeling using airborne gravimetry data, PhD thesis, Delft University of Technology. Nederlandse Commissie voor Geodesie Publikatie 70.

Amrozowicz, M. D., Brown, A. J. & Golay, M. (1997), 'A probabilistic analysis of tanker groundings'. Proceedings of the 7th International Offshore and Polar Engineering Conference, Honolulu, Hawaii.

Andersen, O. B. (2010), 'The DTU10 Global Gravity field and mean sea surface - improvements in the Arctic', `http://www.space.dtu.dk/english/Research/Scientific_data_and_models/Global_Marine_Gravity_Field`. Second international symposium of the gravity field of the Earth (IGFS2), Fairbanks, Alaska.

Andersen, O. B. & Knudsen, P. (2000), 'The role of satellite altimetry in gravity field modelling in coastal areas', *Phys. Chem. Earth* **25**(1), 17–24.

Andersen, O. B. & Knudsen, P. (2007), Altimetric Mean Sea Surfaces (DNSC06-MSS) and Ocean Variability. Presented at ENVISAT Symposium 2007, Montreux, Switzerland, 23–27 April 2007.

Andersen, O. B. & Knudsen, P. (2009), 'DNSC08 mean sea surface and mean dynamic topography models', *J. Geophys. Res. (Oceans)* **114**(C11), n/a–n/a.

Andersen, O. B., Knudsen, P. & Berry, P. (2010), 'The DNSC08GRA global marine gravity field from double retracked satellite altimetry', *J. Geod.* **84**(3), 191–199. 10.1007/s00190-009-0355-9.

Andersen, O. B., Knudsen, P. & Trimmer, R. (2005), Improved High Resolution Altimetric Gravity Field Mapping (KMS2002 Global Marine Gravity Field), *in* F. Sansò, ed., 'A Window on the Future of Geodesy', Vol. 128 of *International Association of Geodesy Symposia*, Springer Berlin Heidelberg, pp. 326–331.

Andersen, O. B. & Scharroo, R. (2011), Range and Geophysical Corrections in Coastal Regions: And Implications for Mean Sea Surface Determination, *in* S. Vignudelli, A. G. Kostianoy, P. Cipollini & J. Benveniste, eds, 'Coastal Altimetry', Springer-Verlag, Berlin Heidelberg, pp. 103–145. 1st Edition.

Ballay, A., Simon, B. & Wöppelmann, G. (2002), Towards a globally consistent nautical chart datum definition in France, *in* H. Drewes, A. Dodson, L. Fortes, L. Sánchez & P. Sandoval, eds, 'Vertical Reference Systems', Vol. 124, IAG Symposia, Springer, pp. 270–275.

Barthelmes, F. (1986), 'Untersuchungen zur Approximation des äußeren Gravitationsfeldes der Erde durch Punktmassen mit optimierten Positionen.', *Veröffentlichungen des Zentralinstituts Physik der Erde* **92**. Potsdam, 122 pp.

Bingham, R. J., Haines, K. & Hughes, C. W. (2008), 'Calculating the Ocean's Mean Dynamic Topography from a Mean Sea Surface and a Geoid', *J. Atmos. Ocean. Tech.* **25**, 1808–1822.

Boschi, L. & Dziewonski, A. M. (1999), 'High- and low-resolution images of the Earth's mantle: Implications of different approaches to tomographic modeling', *J. Geophys. Res.* **104**(B11), 25567–25594.

Bouffard, J., Vignudelli, S., Herrmann, M., Lyard, F., Marsaleix, P., Ménard, Y. & Cipollini, P. (2008), 'Comparison of Ocean Dynamics with a Regional Circulation Model and Improved Altimetry in the North-Western Mediterranean', *Terr. Atmos. Ocean. Sci.* **19**(1-2), 117–133.

Brennecke, J. & Groten, E. (1977), 'The deviations of the sea surface from the geoid and their effect on geoid computation', *Bull. Geod.* **51**, 47–51.

Broersen, P. M. T. (2008), 'Spectral Analysis of Irregularly Sampled Data with Time Series Models', *The Open Signal Processing Journal* **1**, 7–14.

Brown, G. (1977), 'The average impulse response of a rough surface and its applications', *IEEE T. Antenn. Propag.* **25**, 67–74.

de Bruijne, A. J. T., Haagmans, R. H. N. & de Min, E. J. (1997), 'A preliminary North Sea geoid model GEONZ97'. MD-report MDGAP-9735.

Carrère, L. & Lyard, F. (2003), 'Modeling the barotropic response of the global ocean to atmospheric wind and pressure forcing - comparisons with observations', *Geophys. Res. Lett.* **30**(6), n/a–n/a.

Cats, G. & Wolters, L. (1996), 'The hirlam project [meteorology]', *IEEE Comput. Sci. Eng.* **3**(4), 4–7.

Chelton, D. B., Ries, J. C., Haines, B. J., Fu, L.-L. & Callahan, P. S. (2001), Chapter 1 satellite altimetry, *in* L.-L. Fu & A. Cazenave, eds, 'Satellite Altimetry and Earth Sciences - A Handbook of Techniques and Applications', Vol. 69 of *International Geophysics*, Academic Press, pp. 1–131, i–ii.

CNES/LEGOS/CLS (2011), 'Multi-Mission Sea Level Trends (period : Oct-1992 to Dec-2010)'. (Accessed June, 2013), `http://www.aviso.oceanobs.com/en/news/ocean-indicators/mean-sea-level/products-images/`.

Crombaghs, M. & de Bruijne, A. (2004), NLGEO2004 - een nieuw geoïdemodel voor Nederland, Technical report, Adviesdienst Geo-informatie en ICT. Report AGI-GAP-2004-25, Delft, 41 p.

Dahlen, F. A. & Simons, F. J. (2008), 'Spectral estimation on a sphere in geophysics and cosmology', *Geophys. J. Int.* **174**, 774–807.

Dee, D. P., Uppala, S. M., Simmons, A. J., Berrisford, P., Poli, P., Kobayashi, S., Andrae, U., Balmaseda, M. A., Balsamo, G., Bauer, P., Bechtold, P., Beljaars, A. C. M., van de Berg, L., Bidlot, J., Bormann, N., Delsol, C., Dragani, R., Fuentes, M., Geer, A. J., Haimberger, L., Healy, S. B., Hersbach, H., Hólm, E. V., Isaksen, L., Kållberg, P., Köhler, M., Matricardi, M., McNally, A. P., Monge-Sanz, B. M., Morcrette, J.-J., Park, B.-K., Peubey, C., de Rosnay, P., Tavolato, C., Thépaut, J.-N. & Vitart, F. (2011), 'The ERA-Interim reanalysis: configuration and performance of the data assimilation system', *QJ Roy. Meteor. Soc.* **137**(656), 553–597.

Deng, X. (2003), Improvement of Geodetic Parameter Estimation in Coastal Regions from Satellite Radar Altimetry, Phd, Curtin University of Technology, Department of Spatial Sciences.

Deng, X. & Featherstone, W. E. (2006), 'A coastal retracking system for satellite radar altimeter waveforms: Application to ERS-2 around Australia', *J. Geophys. Res. (Oceans)* **111**(C6), n/a–n/a.

Deng, X., Featherstone, W. E., Hwang, C. & Berry, P. A. M. (2002), 'Estimation of Contamination of ERS-2 and POSEIDON Satellite Radar Altimetry Close to the Coasts of Australia', *Mar. Geod.* **25**(4), 249–271.

Denker, H., Barriot, J.-P., Barzaghi, R., Fairhead, D., Forsberg, R., Ihde, J., Kenyeres, A., Marti, U., Sarrailh, M. & Tziavos, I. (2008), The Development of the European Gravimetric Geoid Model EGG07, *in* F. Sansò & M. G. Sideris, eds, 'Observing our Changing Earth', Vol. 133 of *International Association of Geodesy Symposia*, Springer Berlin Heidelberg, pp. 177–185.

Denker, H. & Roland, M. (2005), Compilation and evaluation of a consistent marine gravity data set surrounding europe, *in* 'A Window on the Future of Geodesy', Springer Berlin Heidelberg, pp. 248–253.

Dhingra, E. A., Hess, K. W. & White, S. A. (2008), VDatum for the Northeast Gulf of Mexico from Mobile Bay, Alabama, to Cape San Blas, Florida: tidal datum modeling and population of the marine grids, Technical report, U.S. Department of Commerce, National Oceanic and Atmospheric Administration, Silver Spring, Maryland. NOAA Technical Memorandum NOS CS 14, 74 p.

van Dijk, T. A. G. P., van der Tak, C., de Boer, W. P., Kleuskens, M. H. P., Doornenbal, P. J., Noorlandt, R. P. & Marges, V. C. (2011), The scientific validation of the hydrographic survey policy of the Netherlands Hydrographic Office, Royal Netherlands Navy, Technical report, Deltares. Available online at: `http://www.defensie.nl/marine/hydrografie/geodesie_en_getijden/dieptemeten/` (accessed April 12, 2012).

Ditmar, P., Klees, R. & Liu, X. (2007), 'Frequency-dependent data weighting in global gravity field modeling from satellite data contaminated by non-stationary noise', *J. Geod.* **81**(1), 81–96. 10.1007/s00190-006-0074-4.

Ditmar, P. & Sluijs, A. A. v. E. v. d. (2004), 'A technique for modeling the earth's gravity field on the basis of satellite accelerations', *J. Geod.* **78**(1-2), 12–33.

Dodd, D. & Mills, J. (2011), 'Ellipsoidally referenced surveys: issues and solutions', *Int. Hydrogr. Rev.* **6**, 19–29.

Dodd, D., Mills, J., Battilana, D. & Gourley, M. (2010), 'Hydrographic Surveying Using the Ellipsoid as the Vertical Reference Surface'. FIG Congress 2010, Sydney, Australia, 11–16 April 2010.

Dorst, L. L. (2004), 'Survey plan improvement by detecting sea floor dynamics in archived echo sounder surveys', *Int. Hydrogr. Rev.* **5**(2), 49–63.

Dorst, L. L. (2009), Estimating sea floor dynamics in the Southern North Sea to improve bathymetric survey planning, PhD thesis, University of Twente. ISBN 978-90-365-2878-8. NCG Publication on Geodesy 69, ISBN 978-90-6132-311-2.

Dorst, L. L., Slobbe, D. C., Klees, R., Verlaan, M. & Ligteringen, T. (2010), Unifying vertical reference surfaces in the North Sea: an overview of developments. Proceedings of Hydro 2010, Rostock-Warnemünde, Germany, 2–5 November 2010.

Drinkwater, M. R., Floberghagen, R., Haagmans, R., Muzi, D. & Popescu, A. (2003), 'VII: CLOSING SESSION: GOCE: ESA's First Earth Explorer Core Mission', *Space Sci. Rev.* **108**, 419–432.

Eicker, A. (2008), Gravity field refinement by radial basis functions from in-situ satellite data, PhD thesis, Universität Bonn, Bonn.

Ekman, M. (1989), 'Impacts of geodynamic phenomena on systems for height and gravity', *Bull. Geod.* **63**, 281–296.

Ekman, M. & Mäkinen, J. (1996), 'Mean sea surface topography in the Baltic Sea and its transition area to the North Sea: A geodetic solution and comparisons with oceanographic models', *J. Geophys. Res.* **101**, 11993–12000.

Ellmer, W. & Goffinet, P. (2006), Tidal correction Using GPS - Determination of the chart datum. Proceedings of the XXIII International FIG Congress, Munich, Germany, 8–13 October 2006.

Engedahl, H. (1995), Implementation of the Princeton Ocean Model (POM/ECOM3D) at the Norwegian Meteorological Institute, Technical report, DNMI. Research Report No. 5.

European Maritime Safety Agency (2010), 'Maritime Accident Review 2010'. (Accessed June, 2013), `http://www.emsa.europa.eu/implementation-tasks/accident-investigation/item/1219.html`.

Evensen, G. (1994), 'Sequential data assimilation with a nonlinear quasi-geostrophic model using Monte Carlo methods to forecast error statistics', *J. Geophys. Res.* **99**(C5), 10143–10162.

Evensen, G. (2003), 'The Ensemble Kalman Filter: theoretical formulation and practical implementation', *Ocean Dynamics* **53**(4), 343–367.

Farr, T. G., Rosen, P. A., Caro, E., Crippen, R., Duren, R., Hensley, S., Kobrick, M., Paller, M., Rodriguez, E., Roth, L., Seal, D., Shaffer, S., Shimada, J., Umland, J., Werner, M., Oskin, M., Burbank, D. & Alsdorf, D. (2007), 'The Shuttle Radar Topography Mission', *Rev. Geophys.* **45**(2), n/a–n/a.

FIG Commission 4 Working Group 4.2 (2006), FIG Guide on the Development of a Vertical Reference Surface for Hydrography, Technical Report 37, The International Federation of Surveyors (FIG), Frederiksberg, Denmark.

FIG Commission 4 Working Group 4.4 (2011), Report on the Economic Benefits of Hydrography, Technical Report 57, The International Federation of Surveyors (FIG), Copenhagen, Denmark. ISBN: 978-87-90907-94-5.

Flather, R. A. (2000), 'Existing operational oceanography', *Coast. Eng.* **41**(1-3), 13–40.

Flury, J. & Rummel, R. (2009), 'On the geoid-quasigeoid separation in mountain areas', *J. Geod.* **83**(9), 829–847.

Foreman, M. G. G., Cherniawsky, J. Y. & Ballantyne, V. A. (2009), 'Versatile Harmonic Tidal Analysis: Improvements and Applications', *J. Atmos. Ocean. Tech.* **26**, 806–817.

Forsberg, R. Hehl, K., Mayer, U., Gidskehaug, A. & Bastos, L. (1997), Development of an airborne geoid mapping system for coastal oceanography (AGMASCO), *in* 'Proc. Int. Symposium on Gravity geoid and Marine Geodesy, Japan', pp. 130–142.

Forsberg, R., Strykowski, G., Iliffe, J. C., Ziebart, M., Cross, P. A., Tscherning, C. C., Cruddace, P., Stewart, K., Bray, C. & Finch, O. (2003), OSGM02: A new geoid model of the British Isles, *in* I. N. Tziavos, ed., 'Gravity and Geoid: Proceedings of 3rd Meeting of the International Gravity and Geoid Commission', Editions ZITI, pp. 132–137. Thessaloniki, Greece, August 2002.

Förste, C., Schmidt, R., Stubenvoll, R., Flechtner, F., Meyer, U., König, R., Neumayer, H., Biancale, R., Lemoine, J.-M., Bruinsma, S., Loyer, S., Barthelmes, F. & Esselborn, S. (2008), 'The GeoForschungsZentrum Potsdam/Groupe de Recherche de Gèodésie Spatiale satellite-only and combined gravity field models: EIGEN-GL04S1 and EIGEN-GL04C', *J. Geod.* **82**(6), 331–346.

Foster, J. H., Carter, G. S. & Merrifield, M. A. (2009), 'Ship-based measurements of sea surface topography', *Geophys. Res. Lett.* **36**(11), n/a–n/a.

Freeden, W. & Michel, V. (1999), 'Constructive approximation and numerical methods in geodetic research today – an attempt at a categorization based on an uncertainty principle', *J. Geod.* **73**, 452–465.

General Bathymetric Chart of the Oceans (2012), 'GEBCO Frequently Asked Questions, GEBCO's grids and vertical datum', `http://www.gebco.net/general_interest/faq/`. Accessed March 7, 2013.

General Bathymetric Chart of the Oceans (GEBCO) (2012), 'General Bathymetric Chart of the Oceans (GEBCO)', `http://www.gebco.net/`. Accessed March 7, 2013.

Gerritsen, H., de Vries, H. & Philippart, M. (1995), The Dutch Continental Shelf Model, *in* D. R. Lynch & A. M. Davies, eds, 'Quantitative Skill Assessment for Coastal Ocean Models, Coastal Estuarine Stud.', Vol. 47, AGU, Washington, D. C., pp. 425–467.

Gill, S. K. & Schultz, J. R. (2001), Tidal datums and their applications, Technical report, U.S. Department of Commerce, National Oceanic and Atmospheric Administration. NOAA Special Publication NOS CO-OPS 1, 111p.

Girard, A. (1989), 'A fast 'Monte-Carlo cross-validation' procedure for large least squares problems with noisy data', *Numerische Mathematik* **56**(1), 1–23. 10.1007/BF01395775.

Golub, G. H. & Van Loan, C. F. (1996), *Matrix computations*, 3rd edn, John Hopkins University Press, Baltimore, MD.

Gommenginger, C., Thibaut, P., Fenoglio-Marc, L., Quartly, G., Deng, X., Gómez-Enri, J. Challenor, P. & Y., G. (2011), Retracking Altimeter Waveforms Near the Coasts, *in* S. Vignudelli, A. G. Kostianoy, P. Cipollini & J. Benveniste, eds, 'Coastal Altimetry', Springer-Verlag, Berlin Heidelberg, pp. 61–101. 1st Edition.

González, Á. (2010), 'Measurement of Areas on a Sphere Using Fibonacci and Latitude-Longitude Lattices', *Math. Geosc.* **42**(1), 49–64.

Greatbatch, R. J. (1994), 'A note on the representation of steric sea level in models that conserve volume rather than mass', *J. Geophys. Res.* **99**, 12767–12771.

Greatbatch, R. J., Lu, Y. & Cai, Y. (2001), 'Relaxing the Boussinesq Approximation in Ocean Circulation Models', *J. Atmos. Ocean. Tech.* **18**, 1911–1923.

Grünbaum, F. A., Longhi, L. & Perlstadt, M. (1982), 'Differential operators commuting with finite convolution integral operators: Some non-abelian examples', *SIAM J. Appl. Math.* **42**(5), 941–955.

Guilloux, F., Faÿ, G. & Cardoso, J.-F. (2009), 'Practical wavelet design on the sphere', *Applied and Computational Harmonic Analysis* **26**(2), 143–160.

Gunter, B. C. (2004), Computational methods and processing strategies for estimating Earth's gravity field, PhD thesis, The University of Texas at Austin. Available at `http://repositories.lib.utexas.edu/handle/2152/1318`.

Gunter, B. C. & van de Geijn, R. A. (2005), 'Parallel out-of-core computation and updating of the QR factorization', *ACM Trans. Math. Softw.* **31**(1), 60–78.

Haagmans, R. H. N., Husti, G. J., Plugers, P., Smit, J. H. M. & Strang van Hees, G. L. (1988), NAVGRAV Navigation and Gravimetric Experiment at the North Sea, Technical Report 32, Netherlands Geodetic Commission, Delft.

Hashemi Farahani, H., Ditmar, P., Klees, R., Liu, X., Zhao, Q. & Guo, J. (2013a), 'The static gravity field model DGM-1S from GRACE and GOCE data: computation, validation, and an analysis of GOCE mission's added value', *J. Geod.* . In press.

Hashemi Farahani, H., Ditmar, P., Klees, R., Teixeira da Encarnação, J., Liu, X., Zhao, Q. & Guo, J. (2013b), 'Validation of static gravity field models using GRACE K-band ranging and GOCE gradiometry data', *Geophys. J. Int.* . In press.

Heaps, N. S. (1983), 'Storm surges, 1967-1982', *Geophys. J. Roy. Astr. S.* **74**(1), 331–376.

Heck, B. (1990), 'An evaluation of some systematic error sources affecting terrestrial gravity anomalies', *J. Geod.* **64**(1), 88–108.

Heemink, A. W., Mouthaan, E. E. A., Roest, M. R. T., Vollebregt, E. A. H., Robaczewska, K. B. & Verlaan, M. (2002), 'Inverse 3D shallow water flow modelling of the continental shelf', *Cont. Shelf Res.* **22**, 465–484.

Hess, K. W., Schmalz, R. A., Zervas, C. & Collier, W. (2004), Tidal constituent and residual interpolation (TCARI): A new method for the tidal correction of bathymetric data (Revised), Technical report, U.S. Department of Commerce, National Oceanic and Atmospheric Administration, Silver Spring, Maryland. NOAA Technical Report NOS CS 4, 112 p.

Hipkin, R., Haines, K., Beggan, C., Bingley, R., Hernandez, F., Holt, J. & Baker, T. (2004), 'The geoid EDIN2000 and mean sea surface topography around the British Isles', *Geophys. J. Int.* **157**, 565–577.

Hofmann-Wellenhof, B. & Moritz, H. (2005), *Physical Geodesy*, Springer-Verlag, Berlin.

Holschneider, M., Chambodut, A. & Mandea, M. (2003), 'From global to regional analysis of the magnetic field on the sphere using wavelet frames', *Phys. Earth Planet. Inter.* **135**(2-3), 107–124.

Holt, J. & Proctor, R. (2008), 'The seasonal circulation and volume transport on the northwest European continental shelf: A fine-resolution model study', *J. Geophys. Res. (Oceans)* **113**(C6), n/a–n/a.

Holt, J. T., Allen, J. I., Proctor, R. & Gilbert, F. (2005), 'Error quantification of a high-resolution coupled hydrodynamic ecosystem coastal ocean model: Part 1 model

overview and assessment of the hydrodynamics', *J. Marine Syst.* **57**(1-2), 167–188.

Holt, J. T. & James, I. D. (2001), 'An s coordinate density evolving model of the northwest European continental shelf, 1, Model description and density structure', *J. Geophys. Res.* **106**, 14015–14034.

Holt, J. T., James, I. D. & Jones, J. E. (2001), 'An s coordinate density evolving model of the northwest European continental shelf, 2, Seasonal currents and tides', *J. Geophys. Res.* **106**, 14035–14054.

Horsburgh, K. J. & Wilson, C. (2007), 'Tide-surge interaction and its role in the distribution of surge residuals in the North Sea', *J. Geophys. Res.* **112**(C8), n/a–n/a.

Hounjet, M., Bijlsma, A., Verlaan, M. & Dorst, L. L. (2012), Accurate water levels using PREMO: Tool for reduction of hydrographic measurements, Hydrographic Society Benelux. Topic J: accurate hydrodynamics. Available at `http://proceedings.utwente.nl/243/`.

Hughes, C. W. & Bingham, R. J. (2008), 'An Oceanographer's Guide to GOCE and the Geoid', *Ocean Sci.* **4**, 15–29.

Hutchinson, M. F. (1990), 'A stochastic estimator of the trace of the influence matrix for laplacian smoothing splines', *Commun. Statist. Simulat. Comput.* **19**(2), 433–450.

Huthnance, J. M., Holt, J. T. & Wakelin, S. L. (2009), 'Deep ocean exchange with west-European shelf seas', *Ocean Sci.* **6**, 1061–1092.

Hwang, C. (1991), Orthogonal Functions over the Oceans and Applications to the Determination of Orbit Error, Geoid and Sea Surface Topography from Satellite Altimetry., Technical Report 414, Department of Geodetic Science and Surveying, The Ohio State University, Columbus, Ohio.

Hwang, C. (1993), 'Spectral analysis using orthonormal functions with a case study on the sea surface topography', *Geophys. J. Int.* **115**, 1148–1160.

Hwang, C. (1997), 'Analysis of some systematic errors affecting altimeter-derived sea surface gradient with application to geoid determination over Taiwan', *J. Geod.* **71**(2), 113–130.

Hwang, C., Guo, J., Deng, X., Hsu, H.-Y. & Liu, Y. (2006), 'Coastal Gravity Anomalies from Retracked Geosat/GM Altimetry: Improvement, Limitation and the Role of Airborne Gravity Data', *J. Geod.* **80**, 204–216.

Hwang, C. & Hsu, H.-Y. (2008), 'Shallow-water gravity anomalies from satellite altimetry: Case studies in the east china sea and Taiwan strait', *J. Chin. Inst. Eng.* **31**(5), 841–851.

Hwang, C., Hsu, H.-Y. & Jang, R.-J. (2002), 'Global mean sea surface and marine gravity anomaly from multi-satellite altimetry: applications of deflection-geoid and inverse Vening Meinesz formulae', *J. Geod.* **76**, 407–418.

Ihde, J. & Augath, W. (2002), 'The European vertical reference system (EVRS), its relation to a World height System and to the ITRS', *Vistas for geodesy in the new millennium* pp. 78–83.

Iliffe, J. C., Ziebart, M., Cross, P. A., Forsberg, R., Strykowski, G. & Tscherning, C. C. (2003), 'Osgm02: A new model for converting gps-derived heights to local height datums in great britain and ireland', *Surv. Rev.* **37**(290), 276–293.

Iliffe, J. C., Ziebart, M. K. & Turner, J. F. (2007*a*), 'A New Methodology for Incorporating Tide Gauge Data in Sea Surface Topography Models', *Mar. Geod.* **30**(4), 271–296.

Iliffe, J. C., Ziebart, M. K. & Turner, J. F. (2007*b*), 'The derivation of vertical datum surfaces for hydrographic applications', *Hydrographic Journal* (125), 3–8.

International Hydrographic Organization (1953), 'Limits of Oceans and Seas', available at `www.iho.int`. Special Publication S-23, Third Edition.

International Hydrographic Organization (2005), 'Manual on Hydrography', available at `www.iho.int`. Publication C-13, 1st Edition, 2005, (Corrections to December 2010).

International Hydrographic Organization (2008), 'IHO Standards for Hydrographic Surveys', available at `www.iho.int`. Special Publication S-23, Third Edition.

International Hydrographic Organization (2011*a*), 'Resolutions of the International Hydrographic Organization', available at `www.iho.int`. Publication M-3, 2nd ed., 2010, Updated to August 2011.

International Hydrographic Organization (2011*b*), 'The Need for National Hydrographic Services', available at `www.iho.int`. Publication M-2, Version 3.0.1.

IOC, SCOR and IAPSO (2010), *The international thermodynamic equation of seawater - 2010: Calculation and use of thermodynamic properties*. Intergovernmental Oceanographic Commission, Manuals and Guides No. 56, UNESCO (English), 196 pp. Available online at: `http://www.teos-10.org/pubs/TEOS-10_Manual.pdf` (accessed September 29, 2011).

Izenman, A. J. (1991), 'Recent Developments in Nonparametric Density Estimation', *J. Am. Stat. Assoc.* **86**(413), 205–224.

Jayne, S. R. (2006), 'Circulation of the North Atlantic Ocean from altimetry and the Gravity Recovery and Climate Experiment geoid', *J. Geophys. Res.* **111**(C3), n/a–n/a.

Jekeli, C. (1981), Alternative methods to smooth the Earth's gravity field, Technical report, Ohio State University, Ohio. Technical report #327.

Journal of Geodesy (2011), 'Special issue: Goce-the gravity and steady-state ocean circulation explorer'. Guest editor: R. Rummel, 85(11) 747-884.

Keysers, J. H., Quadros, N. D. & Collier, P. A. (2012), Vertical Datum Transformations across the Littoral Zone, Technical report, Cooperative Research Centre for Spatial Information. Available at `http://www.crcsi.com.au/Documents/UDEM-Project3-FinalReport_1-2.aspx`.

Klees, R., Prutkin, I., Tenzer, R. & Wittwer, T. (2007), Development of a technique for combining parameters of the Earth's gravity field for quasi-geoid determination on the territory of the Federal Republic of Germany and Europe, Technical report, Delft University of Technology.

Klees, R., Tenzer, R., Prutkin, I. & Wittwer, T. (2008), 'A data-driven approach to local gravity field modelling using spherical radial basis functions', *J. Geod.* **82**, 457–471.

Kusche, J. (2003), 'A Monte-Carlo technique for weight estimation in satellite geodesy', *J. Geod.* **76**, 641–652.

Kusche, J. & Klees, R. (2002), 'Regularization of gravity field estimation from satellite gravity gradients', *J. Geod.* **76**(6), 359–368. 10.1007/s00190-002-0257-6.

Kusche, J. & Schrama, E. J. O. (2005), 'Surface mass redistribution inversion from global GPS deformation and Gravity Recovery and Climate Experiment (GRACE) gravity data', *J. Geophys. Res.* **110**(B9), n/a–n/a.

Kwanten, M. C. (2007), 'Memorie Noordzee reductiematrix 2006 (in Dutch)'. Ministerie van defensie, Koninklijke Marine, Dienst der Hydrografie.

Landau, H. J. & Pollak, H. O. (1961), 'Prolate spheroidal wave functions, Fourier analysis and uncertainty - II', *Bell Syst. Tech. J.* **40**(1), 65–84.

Landau, H. J. & Pollak, H. O. (1962), 'Prolate spheroidal wave functions, Fourier analysis and uncertainty - III: The dimension of the space of essentially time- and band-limited signals', *Bell Syst. Tech. J.* **41**(4), 1295–1363.

Leendertse, J. J. (1967), *Aspects of a Computational Model for Long-period Water-wave Propagation*, Rand Corporation for the United States Air Force Project Rand.

Leeuwenburgh, O., Andersen, O. B. & Huess, V. (1999), 'Seasonal tide variations from tide gauges and altimetry', *Phys. Chem. Earth* **24**(4), 403–406.

Lehmann, R. (1993), 'The method of free-positioned point masses — geoid studies on the Gulf of Bothnia', *Bull. Geod.* **67**, 31–40.

Lemoine, F. G., Zelensky, N. P., Chinn, D. S., Beckley, B. D. & Lillibridge, J. L. (2006), 'Towards the GEOSAT Follow-On Precise Orbit Determination Goals of High Accuracy and Near-Real-Time Processing'. AAS paper 2006-6402, AIAA/AAS Astrodynamics Specialist Conference. Am. Inst. of Aeronaut. Astronaut., Keystone, Colorado, Aug 21-24.

Losch, M., Sloyan, B. M., Schröter, J. & Sneeuw, N. (2002), 'Box inverse models, altimetry and the geoid: Problems with the omission error', *J. Geophys. Res.* **107**(C7), 15–1–15–13.

Luettich, R. A., Westerink, J. J. & Scheffner, N. W. (1992), ADCIRC: an advanced three-dimensional circulation model of shelves, coasts and estuaries, Report 1: theory and methodology of ADCIRC-2DD1 and ADCIRC-3DL, Technical report, Department of the Army, Vicksburg, MS. Technical Report DRP-92-6.

Lyard, F., Lefevre, F., Letellier, T. & Francis, O. (2006), 'Modelling the global ocean tides: modern insights from FES2004', *Ocean Dynamics* **56**, 394–415.

Mäkinen, J. & Ihde, J. (2008), The Permanent Tide In Height Systems, *in* F. Sansò & M. G. Sideris, eds, 'Observing our Changing Earth', Vol. 133 of *International Association of Geodesy Symposia*, Springer Berlin Heidelberg, pp. 81–87.

Marchenko, A. N. (1998), *Parametrization of the Earth's gravity field: point and line singularities.*, Lviv Astronomical and Geodetical Society, Lviv.

Marchenko, A. N., Barthelmes, F., Meyer, U. & Schwintzer, P. (2001), Regional geoid determination: An application to airborne gravity data in the Skagerrak, Technical report, GeoForschungsZentrum, Potsdam.

Martin, R. J. & Broadbent, G. J. (2004), 'Chart Datum for Hydrography', *Hydrographic Journal* (112), 9–14.

Mellor, G. L. & Ezer, T. (1995), 'Sea level variations induced by heating and cooling: An evaluation of the Boussinesq approximation in ocean models', *J. Geophys. Res.* **100**(C10), 20565–20577.

Meyer, T. H., Roman, D. R. & Zilkoski, D. B. (2006), 'What does height really mean? Part III: Height Systems', *Surveying and Land Information Science* **66**(2), 149–160.

Milbert, D. G. & Hess, K. W. (2001), Combination of topography and bathymetry through application of calibrated vertical datum transformations in the tampa bay region, Proceedings of the Second Biennial Coastal GeoTools Conference, Charleston, South Carolina, 8–11 January 2001.

de Min, E. J. (1996), De geoide voor Nederland, PhD thesis, Delft University of Technology, Delft. Nederlandse Commissie voor Geodesie Publikatie 34.

Moritz, H. (2000), 'Geodetic Reference System 1980', *J. Geod.* **74**(1), 128–162. 10.1007/s001900050278.

Mouthaan, E. E. A., Heemink, A. W. & Robaczewska, K. B. (1994), 'Assimilation of ERS-1 altimeter data in a tidal model of the continental shelf', *Deutsche Hydrographische Zeitschrift* **46**, 285–319.

Myers, E. P., Wong, A., Hess, K. W., White, S. A., Spargo, E., Feyen, J., Yang, Z., Richardson, P., Auer, C., Sellars, J., Woolard, J., Roman, D., Gill, S., Zervas, C. & Tronvig, K. (2005), 'Development of a National VDatum, and its Application to Sea Level Rise in North Carolina', Downloaded from `http://www.thsoa.org/hy05/09_3.pdf`. technical paper presented at the U.S. Hydro 2005 Conference.

Myers, E. P., Yang, Z., Xu, J., Hess, K. W. & Dhingra, E. A. (2010), Tide Modeling in Support of NOAA's National VDatum Program, *in* M. L. Spaulding, ed., 'Estuarine and Coastal Modeling (2009)', ASCE, pp. 514–526. 10.1061/41121(388)31.

Nabighian, M. N., Ander, M. E., Grauch, V. J. S., Hansen, R. O., Lafehr, T. R., Li, Y., Pearson, W. C., Peirce, J. W., Phillips, J. D. & Ruder, M. E. (2005), 'Historical development of the gravity method in exploration', *GEOPHYSICS* **70**(6), 63ND–89ND.

National Geodetic Survey (2012), 'The official NGS GEOID Page', `http://www.ngs.noaa.gov/GEOID/`. Accessed January 22, 2013.

National Ocean Service (2012), 'Estimation of Vertical Uncertainties in VDatum', `http://vdatum.noaa.gov/docs/est_uncertainties.html`. Accessed January 22, 2013.

Olesen, A. V. (2002), Improved airborne scalar gravimetry for regional gravity field mapping and geoid determination, PhD thesis, University of Copenhagen, Copenhagen, Denmark.

O'Reilly, C., Parsons, S. & Langelier, D. (1996), A Seamless Vertical Reference Surface for Hydrographic Data Acquisition and Information Management. Proceedings of the Canadian Hydrographic Conference 1996, Halifax, N.S., pp. 26–33.

Pail, R., Plank, G. & Schuh, W.-D. (2001), 'Spatially restricted data distributions on the sphere: the method of orthonormalized functions and applications', *J. Geod.* **75**, 44–56.

Parker, B., Milbert, D., Hess, K. & Gill, S. (2003), National vdatum - the implementation of a national vertical datum transformation database, U.S. Hydrographic Conference 2003 Proceedings/Technical Papers.

Pavlis, N., Holmes, S., Kenyon, S. & Factor, J. (2008), 'An Earth Gravitational Model to Degree 2160: EGM2008'. presented at the 2008 General Assembly of the European Geosciences Union, Vienna, Austria, April 13–18, 2008.

Pavlis, N. K., Holmes, S. A., Kenyon, S. C. & Factor, J. K. (2012), 'The development and evaluation of the earth gravitational model 2008 (egm2008)', *J. Geophys. Res.* **117**(B4), n/a–n/a.

Philippart, M. E., Gebraad, A. W., Scharroo, R., Roest, M. R. T., Vollebregt, E. A. H., Jacobs, A., van den Boogaard, H. F. P. & Peters, H. C. (1998), DATUM2: Data assimilation with Altimetry Techniques Used in a tidal model, 2nd program, Technical report, Netherlands Remote Sensing Board.

Pineau-Guillou, L. & Dorst, L. L. (2011), 'Creation of vertical reference surfaces at sea using altimetry and GPS', *Annales hydrographiques* **8**(777), 10–1–10–7. Available at `http://www.shom.fr/fr_page/fr_prod_annales/777/777-ZTL.pdf`.

Pingree, R. & Lecann, B. (1989), 'Celtic and Armorican slope and shelf residual currents', *Prog. Oceanogr.* **23**, 303–338.

Plaumann, S. (1979), *Eine seegravimetrische Vermessung in der westlichen Ostsee*, Schweizerbart'sche Verlagsbuchhandlung, Stuttgart. Geologisches Jahrbuch Reihe E, Band E 14.

Pope, A. J. (1976), The statistics of residuals and the detection of outliers, NOAA Technical Report NOS65 NGS1, U.S. Department of Commerce, National Geodetic Survey, Rockville, Maryland.

Prandle, D. (1978), 'Residual Flows and Elevations in the Southern North Sea', *Proc. R. Soc. Lond. A* **359**, 189–228.

Prandle, D. & Wolf, J. (1978), 'The interaction of surge and tide in the North Sea and River Thames', *Geophys. J. Int.* **55**, 203–216.

Pugh, D. T. (1996), *Tides, surges, and mean sea-level (reprinted with corrections)*, J. Wiley, Chichester; New York.

Rapp, R. H. & Yi, Y. (1997), 'Role of ocean variability and dynamic ocean topography in the recovery of the mean sea surface and gravity anomalies from satellite altimeter data', *J. Geod.* **71**(10), 617–629.

Ray, R. D. (1999), A global ocean tide model from TOPEX/POSEIDON altimetry: GOT99.2, Technical report, Goddard Space Flight Center, Greenbelt. NASA Tech. Memo 209478, 58 pp.

Rijkswaterstaat-Waterdienst & Deltares (2009*a*), 'Modelbeschrijving kuststrook-fijn model', `http://www.helpdeskwater.nl/publish/pages/22751/kuststrook-fijn-1999-v4.pdf`. Accessed January 22, 2013. (In Dutch).

Rijkswaterstaat-Waterdienst & Deltares (2009*b*), 'Modelbeschrijving kustzuid model - incl nevla', `http://www.helpdeskwater.nl/publish/pages/22751/kustzuid-2004-v4.pdf`. Accessed January 22, 2013. (In Dutch).

Roblou, L., Lamouroux, J., Bouffard, J., Lyard, F., Le Hénaff, M., Lombard, A., Marsaleix, P., de Mey, P. & Birol, F. (2011), Post-processing Altimeter Data Towards Coastal Applications and Integration into Coastal Models, *in* S. Vignudelli, A. G. Kostianoy, P. Cipollini & J. Benveniste, eds, 'Coastal Altimetry', Springer-Verlag, Berlin Heidelberg, pp. 217–246. 1st Edition.

Roelvink, J. A., van der Kaaij, R. M. & Ruessink, G. (2001), Calibration and verification of large-scale 2D/3D flow models, Phase 1, Technical report, Delft Hydraulics. Project No. Z3029.10 ONL Coast and Sea Studies.

Rudenko, S., Otten, M., Visser, P., Scharroo, R., Schöne, T. & Esselborn, S. (2012), 'New improved orbit solutions for the ers-1 and ers-2 satellites', *Adv. Space Res.* **49**(8), 1229–1244.

Sandwell, D. T. & Smith, W. H. F. (2005), 'Retracking ERS-1 altimeter waveforms for optimal gravity field recovery', *Geophys. J. Int.* **163**, 79–89.

Sandwell, D. T. & Smith, W. H. F. (2009), 'Global marine gravity from retracked Geosat and ERS-1 altimetry: Ridge segmentation versus spreading rate', *J. Geophys. Res.* **114**(B1), n/a–n/a.

Schachtschneider, R., Holschneider, M. & Mandea, M. (2010), 'Error distribution in regional inversion of potential field data', *Geophys. J. Int.* **181**, 1428–1440.

Schäfer, U., Liebsch, G., Schirmer, U., Ihde, J., Olesen, A. V., Skourup, H., Forsberg, R., Pflug, H. & Neumeyer, J. (2008), Improving gravity field modelling in the German-Danish border region by combining airborne, satellite and terrestrial

gravity data, *in* 'IAG International Symposium on Gravity, Geoid and Earth Observation (Chania, Greece 2008)'.

Scharroo, R. (2013), *RADS version 3.1: User Manual and Format Specification*, Delft University of Technology. (Accessed June, 2013), `http://rads.tudelft.nl/rads/radsmanual.pdf`.

Scharroo, R. & Lillibridge, J. (2005), Non-Parametric Sea-state Bias Models and Their Relevance to Sea Level Change Studies, *in* 'Envisat & ERS Symposium', Vol. 572 of *ESA Special Publication*.

Scharroo, R. & Visser, P. (1998), 'Precise orbit determination and gravity field improvement for the ERS satellites', *J. Geophys. Res.* **103**(C4), 8113–8127.

Schmidt, M., Fengler, M., Mayer-Gürr, T., Eicker, A., Kusche, J., Sánchez, L. & Han, S.-C. (2007), 'Regional gravity modeling in terms of spherical base functions', *J. Geod.* **81**(1), 17–38.

Schott, J.-J. & Thébault, E. (2011), Modelling the earth's magnetic field from global to regional scales, *in* M. Mandea & M. Korte, eds, 'Geomagnetic Observations and Models', Vol. 5 of *IAGA Special Sopron Book Ser.*, Springer.

Simon, B. (2001), *Niveaux caractéristiques et coefficient de marée: calcul direct à l'aide des constantes harmoniques*, Vol. 2 of *Rapport d'étude - Service hydrographique et océanographique de la marine*, Service hydrographique et océanographique de la marine, Paris, FRANCE. Français.

Simons, F. J. (2010), Slepian functions and their use in signal estimation and spectral analysis, *in* W. Freeden, M. Z. Nashed & T. Sonar, eds, 'Handbook of Geomathematics', Vol. 30, Springer, pp. 891–923.

Simons, F. J. & Dahlen, F. A. (2006), 'Spherical Slepian functions and the polar gap in geodesy', *Geophys. J. Int.* **166**, 1039–1061.

Simons, F. J., Dahlen, F. A. & Wieczorek, M. A. (2006), 'Spatiospectral Concentration on a Sphere', *SIAM Rev.* **48**(3), 504–536.

Simons, F. J., Hawthorne, J. C. & Beggan, C. D. (2009), Efficient analysis and representation of geophysical processes using localized spherical basis functions, *in* 'Society of Photo-Optical Instrumentation Engineers (SPIE) Conference Series', Vol. 7446 of *Presented at the Society of Photo-Optical Instrumentation Engineers (SPIE) Conference*.

Simons, F. J. & Wang, D. V. (2011), 'Spatiospectral concentration in the Cartesian plane', *Int. J. Geomathematics* **2**(1), 1–36.

Sjöberg, L. E. (2005), 'A discussion on the approximations made in the practical implementation of the remove-compute-restore technique in regional geoid modelling', *J. Geod.* **78**(11-12), 645–653.

Slepian, D. & Pollak, H. O. (1961), 'Prolate spheroidal wave functions, Fourier analysis and uncertainty - I', *Bell Syst. Tech. J.* **40**(1), 43–63.

Slobbe, D. C., Klees, R., Verlaan, M., Dorst, L. L. & Gerritsen, H. (2013b), 'Lowest Astronomical Tide in the North Sea Derived from a Vertically Referenced Shallow Water Model, and an Assessment of its Suggested Sense of Safety', *Mar. Geod.* **36**(1), 31–71.

Slobbe, D. C., Simons, F. J. & Klees, R. (2012), 'The spherical Slepian basis as a means to obtain spectral consistency between mean sea level and the geoid', *J. Geod.* **86**(8), 609–628.

Slobbe, D. C., Verlaan, M., Klees, R. & Gerritsen, H. (2013a), 'Obtaining instantaneous water levels relative to a geoid with a 2D storm surge model', *Cont. Shelf Res.* **52**(0), 172–189.

Smith, W. H. F. (2010), The Marine Geoid and Satellite Altimetry, *in* V. Barale, J. F. R. Gower & L. Alberotanza, eds, 'Oceanography from Space Revisited', Springer, pp. 181–193. 1st Edition.

Sobey, R. J. (2005), 'Extreme low and high water levels', *Coast. Eng.* **52**(1), 63–77.

Spargo, E. A. & Woolard, J. W. (2005), VDatum for the Calcaseiu River from Lake Charles to the Gulf of Mexico, Louisiana: tidal datum modeling and population of the grid, Technical report, U.S. Department of Commerce, National Oceanic and Atmospheric Administration, Silver Spring, Maryland. NOAA Technical Memorandum NOS CS 19, 26 p.

Stelling, G. S. (1984), On the construction of computational methods for shallow water flow problems, PhD thesis, Delft University of Technology, Delft. Rijkswaterstaat Communications 35.

Stoica, P. & Moses, R. (2005), *Spectral analysis of signals*, Pearson/Prentice Hall Upper Saddle River, NJ.

Strang van Hees, G. L. (1983), 'Gravity survey of the north sea', *Mar. Geod.* **6**(2), 167–182.

Tapley, B. D., Chambers, D. P., Bettadpur, S. & Ries, J. C. (2003), 'Large scale ocean circulation from the GRACE GGM01 Geoid', *Geophys. Res. Lett.* **30**(22), n/a–n/a.

Tenzer, R. & Klees, R. (2008), 'The choice of the spherical radial basis functions in local gravity field modeling', *Stud. Geophys. Geod.* **52**(3), 287–304.

Tenzer, R., Prutkin, I. & Klees, R. (2012), A Comparison of Different Integral-Equation-Based Approaches for Local Gravity Field Modelling: Case Study for the Canadian Rocky Mountains, *in* S. Kenyon, M. C. Pacino & U. Marti, eds, 'Geodesy for Planet Earth', Vol. 136 of *International Association of Geodesy Symposia*, Springer Berlin Heidelberg, pp. 381–388.

Thompson, K. R. (1980), 'An analysis of British monthly mean sea level', *Geophys. J. Int.* **63**, 57–73.

Todd, P., Martin, R. J. & Broadbent, G. J. (2004), Infrastructure supporting mapping of tidal planes and lines. Proceedings of the 2004 Trans Tasman Surveyors Conference. Auckland, New Zealand.

Tomczak, M. & Stuart, G. J. (1994), *Regional oceanography: An introduction*, 1st edition edn, Pergamon, Oxford, England and New York.

Trampert, J. & Snieder, R. (1996), 'Model Estimations Biased by Truncated Expansions: Possible Artifacts in Seismic Tomography', *Science* **271**(5253), 1257–1260.

Turner, J. F., Iliffe, J. C., Ziebart, M. K., Wilson, C. & Horsburgh, K. J. (2010), 'Interpolation of Tidal Levels in the Coastal Zone for the Creation of a Hydrographic Datum', *J. Atmos. Ocean. Tech.* **27**, 605–613.

United Kingdom Marine Monitoring and Assessment Strategy (UKMMAS) (2010), Charting Progress 2 Feeder Report: Ocean Processes (Ed. Huthnance, J), Technical report, Department for Environment Food and Rural Affairs on behalf of UKMMAS. 279pp.

US Geological Survey's EROS Data Center (2009), 'SRTM Topography', `http://dds.cr.usgs.gov/srtm/version2_1/Documentation/SRTM_Topo.pdf`. Accessed March 7, 2013.

U.S. National Geospatial-Intelligence Agency EGM Development Team (2010), 'EGM2008 - Files & Products for Oceanographic Applications', Downloaded from `http://earth-info.nga.mil/GandG/wgs84/gravitymod/egm2008/oceano.html`. (Accessed July, 2010).

Verboom, G. K., de Ronde, J. G. & van Dijk, R. P. (1992), 'A fine grid tidal flow and storm surge model of the North Sea', *Cont. Shelf Res.* **12**, 213–233.

Verlaan, M., Zijderveld, A., de Vries, H. & Kroos, J. (2005), 'Operational storm surge forecasting in the Netherlands: developments in the last decade', *Philos. Trans. Royal Soc. Math. Phys. Eng. Sci.* **363**, 1441–1453.

Versteeg, H. A. (2000), 'Tidal reduction on fairsheet level – a modern approach to onboard prediction of water levels', *Hydro Int.* **4**(7), 6–9. available at `http://www.defensie.nl/marine/hydrografie/over_hydrografie/artikelen/`.

Vested, H. J., Nielsen, H. R., Jensen, H. R. & Kristensen, K. B. (1995), Skill assessment of an operational hydrodynamic forecast system for the North Sea and Danish Belts, *in* D. R. Lynch & A. M. Davies, eds, 'Quantitative Skill Assessment for Coastal Ocean Models, Coastal Estuarine Stud.', Vol. 47, AGU, Washington, D. C., pp. 373–396.

Vianna, M. L., Menezes, V. V. & Chambers, D. P. (2007), 'A high resolution satellite-only GRACE-based mean dynamic topography of the South Atlantic Ocean', *Geophys. Res. Lett.* **34**(24), n/a–n/a.

de Vries, H. (2011), 'Maritime Modelling', `http://www.knmi.nl/research/maritime_modelling/WAQUA/`. Accessed March 20, 2013.

de Vries, H., Breton, M., de Mulder, T., Krestenitis, Y., Ozer, J., Proctor, R., Ruddick, K., Salomon, J. C. & Voorrips, A. (1995), 'A comparison of 2D storm surge models applied to three shallow European seas', *Environ. Softw.* **10**(1), 23–42.

Wells, D., Kleusberg, A. & Vaníček, P. (1996), A seamless vertical-reference surface for acquisition, management and display of ECDIS hydrographic data, Technical report, Department of Geodesy and Geomatics Engineering, University of New Brunswick, Fredericton, New Brunswick, Canada. Final contract report for the Canadian Hydrographic Service, Technical Report No. 179, 64 pp.

Wessel, P. (2009), 'A general-purpose Green's function-based interpolator', *Computers and Geosciences* **35**, 1247–1254.

Wessel, P. (2010), 'Tools for analyzing intersecting tracks: The x2sys package', *Computers and Geosciences* **36**, 348–354.

Wessel, P. & Smith, W. H. F. (1995), 'New version of the generic mapping tools', *EOS Transactions* **76**, 329–329.

Wessel, P. & Watts, A. B. (1988), 'On the accuracy of marine gravity measurements', *J. Geophys. Res.* **93**, 393–413.

Wieczorek, M. A. & Simons, F. J. (2007), 'Minimum-variance spectral analysis on the sphere', *J. Fourier Anal. Appl.* **13**(6), 665–692.

Wingham, D. J., Francis, C. R., Baker, S., Bouzinac, C., Brockley, D., Cullen, R., de Chateau-Thierry, P., Laxon, S. W., Mallow, U., Mavrocordatos, C., Phalippou, L., Ratier, G., Rey, L., Rostan, F., Viau, P. & Wallis, D. W. (2006), 'Cryosat: A mission to determine the fluctuations in earth's land and marine ice fields', *Adv. Space Res.* **37**(4), 841–871.

Wittwer, T. F. (2009), Regional gravity field modelling with radial basis functions, PhD thesis, Delft University of Technology. Nederlandse Commissie voor Geodesie Publikatie 72.

Wolf, J. (1981), Surge-tide interaction in the North Sea and River Thames, *in* D. H. Peregrine, ed., 'Floods due to High Winds and Tides', Elsevier, New York, pp. 75–94.

Wöppelmann, G., Allain, S., Bahurel, P., Lannuzel, S. & Simon, B. (1999), 'Zéro hydrographique: vers une détermination globale', *Revue XYZ* (79), 27–34.

Wöppelmann, G., Zerbini, S. & Marcos, M. (2006), 'Tide gauges and Geodesy: a secular synergy illustrated by three present-day case studies', *Comptes Rendus Geoscience* **338**, 980–991.

Wunsch, C. & Gaposchkin, E. M. (1980), 'On using satellite altimetry to determine the general circulation of the oceans with application to geoid improvement', *Rev. Geophys.* **18**, 725–745.

Wunsch, C. & Stammer, D. (1997), 'Atmospheric loading and the oceanic "inverted barometer" effect', *Rev. Geophys.* **35**, 79–107.

Wunsch, C. & Stammer, D. (1998), 'Satellite Altimetry, the Marine Geoid, and the Oceanic General Circulation', *Annu. Rev. Earth Pl. Sc.* **26**, 219–254.

Xu, P. (1998), 'Truncated SVD methods for discrete linear ill-posed problems', *Geophys. J. Int.* **135**(2), 505–541.

Yang, Z., Myers, E. P., Jeong, I. & White, S. A. (2012), VDatum for the coastal waters from the Florida Shelf to the South Atlantic Bight: tidal datums, marine grids, and sea surface topography, Technical report, U.S. Department of Commerce, National Oceanic and Atmospheric Administration, Silver Spring, Maryland. NOAA Technical Memorandum NOS CS 27, 107 p.

Ziebart, M. K., Iliffe, J. C., Turner, J. F., Oliveira, J. & Adams, R. (2007), VORF - The UK Vertical Offshore Reference Frame: Enabling Real-time Hydrographic Surveying. In: (Proceedings) ION GNSS2007, Fort Worth, Texas, USA.

Zijl, F. Verlaan, M. & Gerritsen, H. (2012), Calibration of a New Generation Flood Forecasting Model for the Northwest European Shelf and North Sea using Data Assimilation Techniques (OpenDA). Presented at JONSMOD 2012, Brest, France, 21–23 May 2012, available at `http://publicwiki.deltares.nl/download/attachments/77240930/JONSMOD_2012_3-2_ZIJL.pdf`.

About the author

Dirk Cornelis Slobbe was born in Capelle aan den IJssel, the Netherlands, on January 7, 1983. He attended the Gomarus Scholengemeenschap in Gorinchem, where he received his VWO diploma in 2001. Then, he studied Geodesy and Geoinformatics at the University of Applied Sciences Utrecht. As part of his studies, he did two internships. One for the municipality of 's-Hertogenbosch, where he studied the usability of geographic information systems in daily work processes. The other one was for a survey company where he implemented a Kalman filter. In his graduation thesis, he studied the relation between the configuration of bathymetric survey lines in a watercourse and the uncertainty caused by geostatistical interpolation to a whole-area model. In June 2005, he received his Bachelor of Applied Sciences in both the direction of Geodesy and Geoinformatics (cum laude).

After finishing, he continued his MSc Geomatics at Delft University of Technology. Here, he was involved in the technical feasibility study on the potential of satellite radar interferometry for monitoring dikes of the Netherlands. In his graduation project, he combined GRACE and ICESat data to estimate Greenland's ice sheet mass balance. In November 2007, he received his Master of Science (cum laude).

In November 2007, he started his PhD research at Delft University of Technology. During this project, he participated in the Interreg IVB North Sea Region Programme, project "Bringing Land and Sea Together" (BLAST).